Dynamics of downdraughts and cold pools: an experimental and numerical study

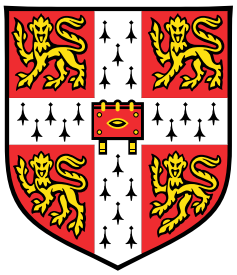

Emily Susan Kruger

Department of Applied Mathematics and Theoretical Physics
University of Cambridge

This dissertation is submitted for the degree of
Doctor of Philosophy

Magdalene College

November 2019

Somebody said that it couldn't be done
But he with a chuckle replied
That "maybe it couldn't," but he would be one
Who wouldn't say so till he'd tried.
So he buckled right in with the trace of a grin
On his face. If he worried he hid it.
He started to sing as he tackled the thing
That couldn't be done, and he did it.

Somebody scoffed: "Oh, you'll never do that;
At least no one ever has done it;"
But he took off his coat and he took off his hat
And the first thing we knew he'd begun it.
With a lift of his chin and a bit of a grin,
Without any doubting or quiddit,
He started to sing as he tackled the thing
That couldn't be done, and he did it.

There are thousands to tell you it cannot be done,
There are thousands to prophesy failure,
There are thousands to point out to you one by one,
The dangers that wait to assail you.
But just buckle in with a bit of a grin,
Just take off your coat and go to it;
Just start in to sing as you tackle the thing
That "cannot be done," and you'll do it.

-Edgar Albert Guest

Declaration

This dissertation is the result of my own work and includes nothing which is the outcome of work done in collaboration except as declared below and specified in the text. It is not substantially the same as any that I have submitted, or, is being concurrently submitted for a degree or diploma or other qualification at the University of Cambridge or any other University or similar institution except as declared below and specified in the text. I further state that no substantial part of my dissertation has already been submitted, or, is being concurrently submitted for any such degree, diploma or other qualification at the University of Cambridge or any other University or similar institutions except as declared below and specified in the text.

Emily Susan Kruger
November 2019

Acknowledgements

Firstly, I would like to express my sincere gratitude to my supervisor Paul Linden for his continuous support, motivation, and immense knowledge. His guidance helped me in all the time of research and writing of this thesis. Secondly, to Dr. Henry Burridge for his patience and support throughout the last four years and in particular during the writing of this thesis.

I would also like to thank those in the GK Batchelor lab, especially Jamie Partridge for all the support both in and out of the laboratory, and the amazing technicians for all their help with my experimental setup. It has been a privilege being part of such an amazing group of people. In particular I would like to thank David, Katherine and all the other PhD students in Pav H for always making a day in the office entertaining.

The work was generously funded by an NERC iCASE award with the Met Office. At the Met Office, I would particularly like to thank Gabriel Rooney (my industrial supervisor) for sharing his insight in how this work relates to industry, and Adrian Hill for always being available to answer my questions about MONC.

Throughout my PhD studies, I have been fortunate enough to have been surrounded by friends outside the department too. In particular, I would like to thank those in Magdalene BC, Cantabridgian RC and CUCPSC. In particular, I'd like to thank Amy Webster, Evie Taylor, Stephanie Turnello, Olive Turner and Anthony Kane who were always supportive and there when I needed a distraction. I would also like to thank my aunt and uncle Rosemary and John Gates who have always found the time to proof read my work. Finally, I would like to thank my parents, for all their love and support over the years.

Abstract

Downward moving cold air within a thunderstorm, known as a downdraught, can be an additional storm hazard, and also prolong the convective lifecycle. An understanding of downdraughts is therefore useful for weather forecasting. Typically, in weather forecasting downdraughts are modelled using the theory of a plume from Morton et al. [43], which inherently assumes that the plume is long and thin. However, downdraughts are often wider than their height and hence deviate from the Morton, Taylor and Turner theory. More recently they have been compared to thermals rather than plumes, and their flow along the ground after impact as axisymmetric gravity currents, for example in the study performed by Rooney [49].

In this thesis both numerical and laboratory experiments have been performed by releasing finite volumes of dense fluid from cylinders of varying lengths. In the laboratory the cylinders were perspex tubes submerged in a tank filled with sodium chloride at a fixed height above the base of the tank. The tubes were sealed at the base using a latex sheet and filled with sodium nitrate solution which was dyed using methylene blue. The fluid was released by bursting the latex sheet and was analysed using an extension to the dye attenuation technique developed by Cenedese & Dalziel [15]. Red, green and blue LEDs were used to address the need for a larger range of dye concentration than provided by red LEDs alone. The numerical experiments were performed in MONC, the Met Office's large eddy model. Some basic testing of the model, and comparison with Rooney [49] was done to determine the set up needed to best reproduce both Rooney [49] and the laboratory experiments. Edge detection and tracking was used for both sets of experiments to see how the vertical and radial velocities, and shape of the releases change when changing both the length of the cylinder, and height of the cylinder from the ground. Velocities and shape information from edge detection, and information on the volume from dye attenuation was also used to give information on the entrainment of the thermals.

Changing the height and length of the tube determined whether or not the dense release had developed into a self-similar thermal, was still draining from the tube, or transitioning between the two, upon impact with the ground. It was found that the slumping phases and heights of the resulting gravity currents behave differently depending on both the height

and length of the tube. Theory for the evolution of the flow during the draining of the tube was developed and compared to both the numerical and laboratory experiments. This model combined with existing thermal theory has been used to define more realistic initial conditions for a gravity current model.

Table of contents

Chapter 1

Introduction

Weather has a huge impact on all aspects of life, from infrastructure to every day life, many people rely on weather forecasting. In particular severe weather can have disastrous effects causing flash floods and hurricanes. Thunderstorms are a common feature of weather around the world especially in monsoon rainfall. Variations in rainfall intensities and patterns associated with monsoons can cause severe problems for agriculture, ecology and economics. It is therefore important to be able to predict the heavy rainfall and strong winds produced by thunderstorms.

1.1 Atmospheric Processes That Cause Thunderstorms

1.1.1 Structure of the Atmosphere

The atmosphere is the gas and aerosol envelope that extends from the surface of Earth outward into space. Within the atmosphere a variety of coupled, and complex dynamical, chemical, radiative and other processes are active. These processes determine the overall structure of the atmosphere and drive various flow patterns on many length and time scales which set both our weather and climate. Within this thesis we focus on processes with time scales from seconds to minutes and length scales from $\approx 10\,\mathrm{m} - 10^4\mathrm{m}$. The dynamic state of the atmosphere on these scales is focussed on individual weather events like thunderstorms. A full description of the make up and structure of the atmosphere can be found in Andrews [4]. The following serves only as a brief overview in order to describe the processes in the atmosphere that cause thunderstorms to form, and explain the structure of a thunderstorm.

In principle the atmosphere can behave dynamically differently depending on the latitudinal range of interest due to the vertical component of the Earth's angular velocity changing

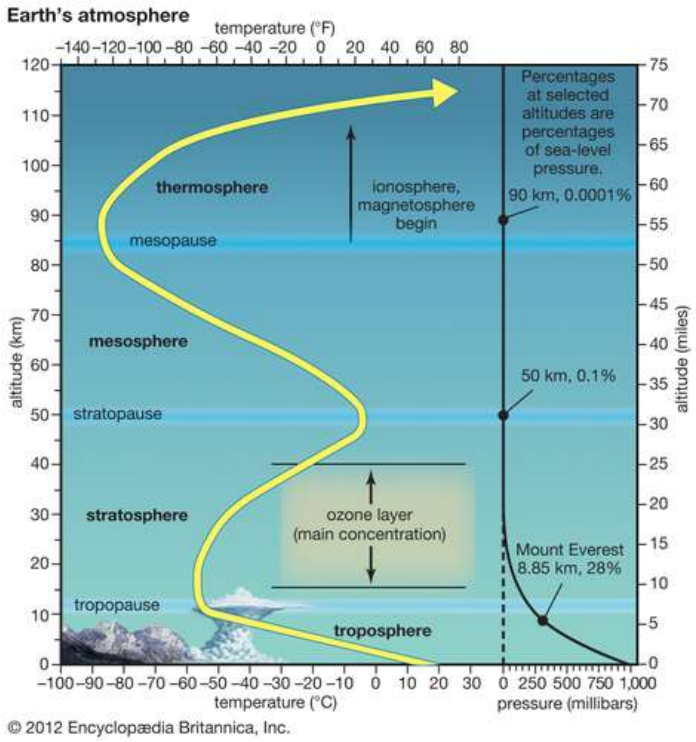

Fig. 1.1 Vertical layers of the atmosphere including the both the temperature and pressure profile of each layer. (Encyclopaedia Britannica, Inc.)

with latitude. Over the length scales we are interested in however, this does not play a significant role [43].

The density of the atmosphere decreases outward, due to the gravitational attraction of the planet. Gravity pulls the gases and aerosols (microscopic suspended particles of dust, soot, smoke, or chemicals) inward, meaning the density is at its greatest closest to the surface of the planet. The atmosphere is characterised by a number of vertical layers which are defined by the vertical temperature profile. These layers, shown in figure 1.1, are defined by a sign change in temperature gradient. The exact vertical height of each layer of the atmosphere differs between the tropics and the poles, but the overall qualitative structure remains the same.

The lowest layer of the atmosphere is called the troposphere. In this layer both the pressure and temperature generally decrease with height. This layer is significant as it contains most of Earth's clouds and is the layer where weather primarily occurs. As we go higher the atmospheric layers have increasingly less of a dynamical impact on the troposphere and hence on weather systems [4]. This thesis will be focussing on dynamical processes within the troposphere.

1.1.2 Atmospheric Stability

The vertical temperature gradient in the atmosphere is known as the lapse rate. The lapse rate (LR) is considered positive when the temperature decreases with altitude, zero when the temperature is constant with altitude, and negative when the temperature increases with altitude and is given by

$$LR = -\frac{\mathrm{d}T}{\mathrm{d}z},$$

where T is the temperature, and z the altitude. There are three important measurements of lapse rate: the dry adiabatic lapse rate (DALR), the saturated (or moist) adiabatic lapse rate (SALR) and the environmental lapse rate (ELR) [4].

When a parcel of air expands, it pushes on the air around it, doing thermodynamic work. An expansion or contraction of an air parcel without inward or outward heat transfer is called an adiabatic process. Since the upward-moving and expanding parcel does work but gains no heat, it loses internal energy and therefore its temperature decreases. The dry adiabatic lapse rate (DALR) is the rate at which such a rising unsaturated parcel of air cools. Its value is given by.

$$DALR = \frac{g}{c_p} \tag{1.1}$$

where g is the acceleration due to gravity and c_p the specific heat capacity of air.

When the air parcel contains moisture, the rate that a rising parcel of air cools is known as the saturated (or moist) adiabatic lapse rate (SALR). The value of the SALR is always less than the DALR due to condensation within the parcel inhibiting cooling. When an air parcel that is saturated with water vapour rises, some of the vapour within will condense and release latent heat. This process causes the parcel to cool slower than it would if it was not saturated. The SALR rate varies considerably because the amount of water vapour in the air is highly variable. The greater the amount of water vapour, the smaller the SALR. As an air parcel rises and cools, it may eventually lose its moisture through condensation; its SALR then increases and approaches the DALR.

Finally, the environmental lapse rate (ELR), is the rate of decrease of temperature with altitude in the stationary atmosphere at a given time and location. It is the most important of the three rates as it is used to compare to the both the DALR and SALR in order to determine what in known as the stability of the atmosphere [4].

The three lapse rates are used to determine if a parcel of rising air will be able to rise high enough for its water vapour to condense and form clouds. The difference between the environmental lapse rate in the atmosphere and the dry and saturated adiabatic lapse rates determines the vertical stability of the atmosphere. That is, if an air parcel when displaced vertically will return to, or accelerate away from, its original position. This is

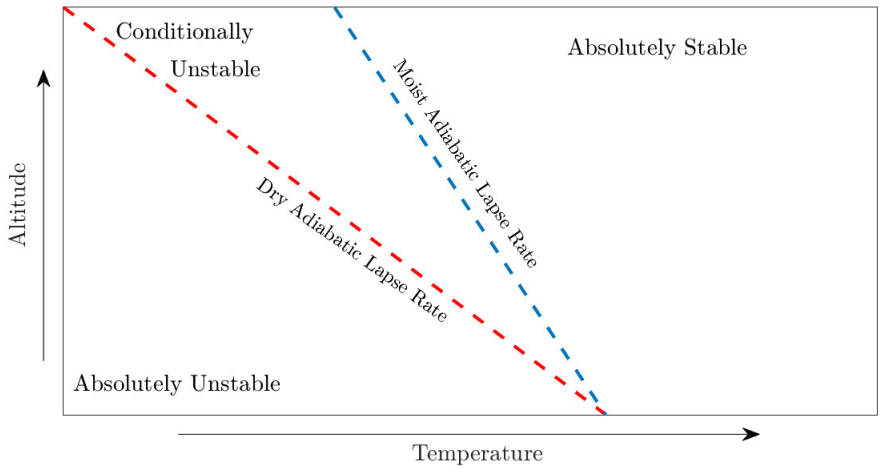

Fig. 1.2 Regions of absolute (in)stability and conditional instability in relation to the saturated and dry adiabatic lapse rates.

known as the stability of the atmosphere. It is for this reason that the lapse rate is of great importance to meteorologists in forecasting certain types of cloud formations, the incidence of thunderstorms, and the intensity of atmospheric turbulence.

The atmosphere is broadly either: absolutely stable, conditionally unstable, or absolutely unstable. Figure 1.2 shows the ranges of environmental lapse rates for which the atmosphere is either absolutely unstable, conditionally unstable or absolutely stable in relation to the moist and dry adiabatic lapse rates.

The atmosphere is said to be absolutely stable when a parcel is moved upward forces act to return the parcel to its original position. In these situations the air parcel will be colder and thus denser than the air around it. It will therefore sink back to its original position provided any upward forcing ceases. In these cases the ELR is less than the SALR. In a stable environment any vertical mixing is inhibited and although one may expect clouds to develop, their vertical growth will be limited [4].

Conditional instability is more complicated, and the stability depends on how saturated an air parcel is. The atmosphere is said to be conditionally unstable when the ELR is between the DALR and the SALR. The stability of such an air parcel is solely determined by the moisture content within the parcel. In this condition, a parcel of dry air will return to its original level if it is pushed upward. On the other hand, a parcel of saturated air will continue to rise as it still will be warmer, and hence lighter, than the surrounding air. In general, the atmosphere is in a conditionally unstable state. In a conditionally stable environment vertical

mixing will be inhibited in the same way as an absolutely stable environment but to a lesser extent. Similarly, for a conditionally unstable environment vertical mixing is enhanced just as in an absolutely stable environment but again, to a lesser extent [4].

The atmosphere is said to be absolutely unstable when a parcel is moved upward forces act to accelerate it away from its original altitude. This occurs when the ELR is greater than the DALR and therefore the parcel will be warmer and less dense than air around it. The larger the initial temperature difference the faster the parcel will rise. In an unstable environment vertical mixing exists through the rising and sinking of air parcels. In this scenario cumuliform clouds can potentially form if there is enough moisture. One may also expect clouds to develop with significant vertical extent, and may observe: cumulus congestus or cumulonimbus which are the types of clouds associated with weather events such as thunderstorms [4].

1.1.3 Life-cycle of Thunderstorms

Thunderstorms are known to occur in almost every region of the world, though they are rare in polar regions and infrequent at latitudes higher than 50° North or South. The temperate and tropical regions of the world, therefore are more prone to thunderstorms. A thunderstorm develops when the atmosphere becomes unstable. For example, as the sun heats up the Earth's surface, the air above it heats up. This means that relatively warm, light air is overlain by cooler, and therefore heavier air. Under such conditions the cooler air tends to sink, displacing warmer air upward. If a sufficiently large volume of air rises, an updraught will be produced. If the updraught is also moist, the water will condense and form clouds; condensation will release latent heat energy, further fuelling upward motion. This forms cumulonimbus clouds and, eventually, precipitation occurs. Columns of cooled air called downdraughts then sink earthward, striking the ground with strong downward and horizontal winds. The cooled air then spreads radially forming what is known as a cold pool. As these cold pools spread they force the warm air on the surface upwards creating more updraughts. This cycle of updraughts-downdraughts-cold pools-updraughts creates what is known as the convective cycle of a thunderstorm. A full description of all the processes that happen in the creation and propagation of thunderstorms can be found in Houze [32].

Convection is the process by which motion is induced in parcels of a liquid or gas through heating (or cooling), causing a difference in temperature. These temperature differences cause the warmer, less dense areas to rise, and the cooler, more dense areas to sink. Often the areas of heating and cooling are fixed on the Earth's surface, and allow convective cycles or currents to become established [32].

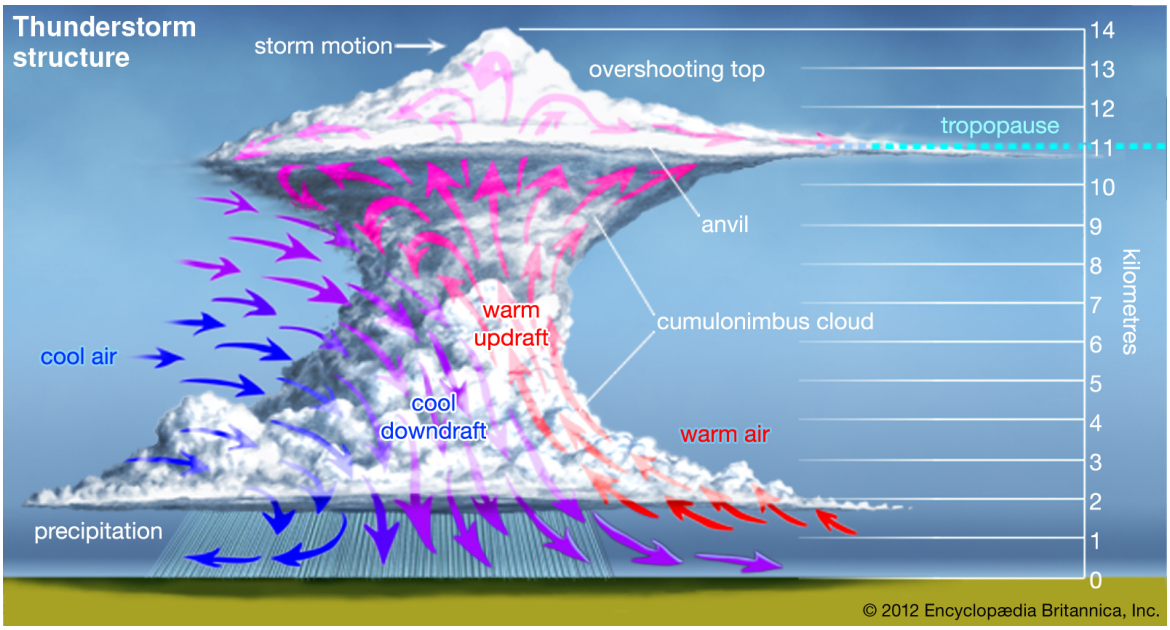

Fig. 1.3 Diagram of a typical cumulonimbus cloud created through moist convection. (Encyclopaedia Britannica, Inc.)

Convection is a vital process in the atmosphere which helps redistribute energy away from warmer areas to cooler areas of the earth. This aids temperature circulation and reduces sharp temperature differences. As previously discussed, in unstable conditions vertical mixing, convection, occurs in the atmosphere. This process of mixing is also sometimes referred to as turbulence [32].

Convection occurs in the atmosphere in two forms. Firstly, when the surface is substantially warmer than the overlying air, and therefore unstable, convection will spontaneously occur in order to redistribute the heat. This process, referred is to as free convection or convective turbulence.

Convection can also occur from forced convection, which is the combination of radiative heating and mechanical turbulence. Mechanical turbulence is due to shear stresses caused by the wind on the surface becoming large enough to induce vertical mixing. Shear stress is the pulling force of a fluid moving in one direction as it passes close to a fluid or object moving in another direction. As a result of surface friction, the average wind the velocity at Earth's surface must be zero unless that surface is itself moving. Winds above the surface decelerate, then when the vertical wind shear becomes large enough the result is vertical mixing [32].

Areas of the atmosphere where vertical motion is relatively strong due to either free or forced convection are called cells. When cells carry air to the upper troposphere, they are

known as deep cells. Thunderstorms develop when deep cells of moist convection become organised and merge [32].

Upward motions to create these deep cells can be initiated in a variety of ways. A common mechanism is by the heating of a land surface and the adjacent layers of air by sunlight. If the heating of a surface is sufficient, the temperatures of the lowest layer of air will rise faster than those layers above, and the atmosphere will become unstable. The ability of the ground to heat up quickly, due to low albedo, is why most thunderstorms form over land rather than oceans. Instability can also occur when layers of cool air are warmed from below after they move over a warm ocean surface or over layers of warm air. Mountains can also trigger upward motion by acting as barriers that force cool winds to rise. Mountains can also act as high altitude sources of heat and instability when their surfaces are heated by the sun [32].

Once upward motions have been initiated in an unstable atmosphere, rising parcels of warm air accelerate as they rise through their cooler surroundings, because they have a lower density and are more buoyant. These rising pockets of warm air are known as updraughts. Updraughts characterize a storm's early development, and the warm parcels of air rise to the level where condensation can begin and clouds can form [32].

Clouds are formed when parcels have ascended, expanded and cooled adiabatically enough such that the water vapour in the parcel condenses, or deposition of water vapour on aerosols occurs. Under these conditions water undergoes a change of state, from gas to liquid, since the cooler air can hold less water vapour than warmer air. Without the presence of aerosols the spontaneous conversion of water vapour into liquid water or ice crystals requires conditions with relative humidity greater than 100%, known as supersaturation, which only occurs in a controlled laboratory setting. The presence of aerosol particles reduces the amount of saturation required for water vapour to change phase. The larger the size or concentration of aerosol particles the lower the saturation percentage required for the particle to serve as a condensation particle [32].

The clouds associated with thunderstorms typically start as isolated cumulus clouds, formed by convection, that develop vertically into domes and towers. If there is enough instability in the atmosphere, and moisture in the parcel, the heat released by condensation will further enhance the buoyancy of the rising air parcel. The cumulus clouds will grow and merge with other cells to form cumulus congestus clouds extending even higher into the atmosphere. Ultimately, a cumulonimbus cloud will form, with its characteristic anvil-shaped top, billowing sides, and a dark base as depicted in figure 1.3. Cumulonimbus clouds typically produce large amounts of precipitation [32].

Cumuliform clouds will form if a saturated parcel of air is warmer than the surrounding ambient atmosphere. Since this air parcel is warmer than its surroundings it will accelerate upward, creating the saturated turbulent bubble characteristic of a cumuliform cloud. Cumuliform clouds are known as cumulus humulus when they are randomly distributed, and as stratocumulus when they are organized into lines. Cumulus congestus clouds extend into the middle troposphere, while deep, precipitating cumuliform clouds that extend throughout the troposphere are called cumulonimbus. Cumulonimbus clouds are also called thunderstorms, since they usually have lightning and thunder associated with them [32].

The evolution of clouds that follows the initial formation depends on the phase of water that occurs. A cloud in which only liquid water occurs, even at negative temperatures, is referred to as a warm cloud. In such a cloud, the growth of a liquid water droplet to a raindrop begins with condensation. This process continues until the droplet has attained a radius of about $10\,\mu m$. The mass of a droplet increases according to the cube of its radius, and so above this size further growth increases due to condensation are very slow. Subsequent growth, therefore, occurs only when cloud droplets develop at slightly different rates. Differences in growth rates have been attributed to differences in the initial aerosol sizes, solubility, and magnitudes of supersaturation. Cloud droplets of different sizes will fall at different velocities and will collide with droplets of different radii. If the collision is hard enough to overcome the surface tension between the two colliding droplets, coalescence will occur and result in a new and larger single droplet. This process of cloud-droplet growth is referred to as collision-coalescence. Warm-cloud rain results when the droplets attain a sufficient size to fall to the ground. The typical radii of raindrops resulting from this type of precipitation process range up to several millimetres and have fall velocities of around 3 to $4\,m\,s^{-1}$. This type of precipitation is very common from shallow cumulus clouds over tropical oceans [32].

A cloud that contains ice crystals is referred to as a cold cloud. In this type of cloud, ice crystals grow directly from the deposition of water vapour. This water vapour may be supersaturated with respect to ice, or it may be the result of evaporation of supercooled water and subsequent deposition onto an ice crystal. Ice crystals will grow using the available liquid water, which results in a rapid conversion of liquid water to ice. This rapid change of phase permits large ice crystals to grow quickly from small ice crystals to create snowflakes. These snowflakes are large enough to fall by this depositional growth alone. Ice crystals that grow by deposition have a much lower densities than solid ice because of the air pockets occurring within the volume of the crystal. This lower density differentiates snow from ice [32].

Ice crystals can also grow large enough to precipitate either by aggregation or by riming. Aggregation occurs when the arms of the ice crystals interlock and form a clump. This

collection of intermingled ice crystals can occasionally reach several centimetres in diameter. Riming is the process where supercooled water freezes directly onto the crystal to form a kind of ice known as rime. With greater accumulation of dense ice on the crystal, the crystal grows and its fall velocity increases. When the riming is substantial enough, the form of the snowflake is lost and replaced by a spherical particle called graupel. Smaller-sized graupels are generally referred to as snow grains. In cumulonimbus clouds during conditions where graupels are repeatedly wetted and then injected back toward high altitudes by strong updraughts, very large graupels called hail result [32].

Frozen precipitation which falls to levels of the atmosphere that are much warmer than 0°C often melts and reaches the ground as rain. Such cold-cloud rain at the ground is usually distinguished from warm-cloud rain by its larger size. Melted hailstones, in particular, make a large-radius impact when they strike the ground [32].

Deep precipitating convective clouds, such as those seen in thunderstorms, can produce downward moving flows that are known as downdraughts. Downdraughts are small localised flows of relatively heavy cold air which rush downward and spread radially outward as they near the ground. The downflow shaft is often circled by a horizontal vortex ring which is responsible for intense outward winds both during the descent and at the ground [2]. They originate at heights where the air temperature is cooler than at ground level. The parcel of cold air is kept cooler than the environment as it sinks by rapid evaporation of moisture or melting of hail [3]. The associated negative buoyancy, and/or momentum transfer from the evaporated precipitation, accelerates the downward motion [49]. An example of a downdraught in the atmosphere can be seen in figure 1.4 which shows a downdraught from a thunderstorm over Phoenix, Arizona.

When the convective cloud forms in a wet, humid environment, the downdraught will be accompanied by intense rainfall at the ground. Severe multiple-cell and supercell storms can produce torrential rain and hail and cause flash floods. However, if the cloud forms in a dry environment, the precipitation may evaporate before it reaches the ground and the downdraught will be dry resulting in a dry thunderstorm [32].

Not only is the sinking air more dense than its surroundings, but it carries a horizontal momentum that is different from the surrounding air. If the descending air originated high enough above the ground it might reach the ground with a horizontal velocity much higher than the wind at the ground [41].

The touch down of such downdraughts has long been associated with the creation of hazardous gust fronts. The descending cold air impacts the ground and spreads out to form a gravity current, known as a cold pool. When such air hits the ground, it moves outward ahead of the storm potentially at a higher speed than the storm itself. The fronts of the spreading

Fig. 1.4 A downdraught released from a thunderstorm over Phoenix, Arizona and the resulting cold pool. (Bruce Haffner/Andrew Park/Jerry Ferguson)

cold pools can move at over $20 \mathrm{ms}^{-1}$, with gusts of wind up to twice this speed behind the front. The cold pool can be some 500 to 2.000 m deep, and often there is a distinct boundary between the cool air and the warm, humid, air in which the storm developed [32]. Also visible in the figure 1.4 is the cold pool formed by the downdraught after impact with the ground.

As these negatively buoyant cold pools spread out radially they push up warmer air at their edge and thereby trigger new convective updraughts, or reinforce existing ones. In particular, cold pools are responsible for triggering updraughts that are wide enough to convect deeply leading to a chain reaction of deep convection: downdraughts, cold pools, updraughts, cloud formation, precipitation and so on as depicted in figure 1.3 [48].

Types of Thunderstorm

Violent weather at the ground is usually produced by organized multiple-cell storms, squall lines, or a supercell. All of these tend to be associated with a mesoscale weather system i.e. 10 to 1,000 km in horizontal extent [32].

Isolated thunderstorms tend to occur where there are light winds that do not change dramatically with height and where there is an abundant moisture at low and middle levels of the atmosphere (0-10 km). These storms are sometimes called local thunderstorms. They

are mostly vertical in structure, are relatively short-lived, and usually do not produce violent weather at the ground.

Aircraft and radar measurements show that such storms are composed of one or more convective cells, each of which goes through a well-defined life cycle. At maturity, the cell contains both updraughts and downdraughts in close proximity. In its later stages, the downdraft spreads throughout the cell and diminishes in intensity as precipitation falls from the cloud. Solar heating is an important factor in triggering local, isolated thunderstorms. As such these storms occur in the late afternoon and early evening, when surface temperatures are highest.

The updraughts and downdraughts in isolated thunderstorms are typically between about 0.5 and 2.5 km in diameter at altitudes of 3 to 8 km. The updraught diameter may occasionally exceed 4 km. Closer to the ground, draughts tend to have a larger diameter and lower speeds than higher in the cloud. Updraught speeds typically peak in the range of 5 to 10 metres per second, and speeds exceeding 20 metres per second are common in the upper parts of large storms.

Isolated thunderstorms contain one or more convective cells in different stages of evolution. Frequently, the downdrafts and associated outflows from a storm trigger new convective cells nearby, resulting in the formation of a multiple-cell thunderstorm, which have several updraughts and downdraughts in close proximity to one another. They occur in clusters of cells in various stages of development moving together as a group. Within the cluster one cell dominates for a time before weakening, and then another cell repeats the cycle.

Supercell storms have one intense updraught and downdraught. When environmental winds are favourable, the updraught and downdraught of a storm become organized and reinforce each other. The result is a long-lived supercell storm. These storms are the most intense type of thunderstorm. Updraught speeds in supercell storms can exceed 40 metres per second and are capable of suspending hailstones as large as grapefruit. Supercells can last between two to six hours. They are the most likely storm to produce wind and hail damage as well as powerful tornadoes.

1.2 Motivation

As mentioned previously thunderstorms are a common feature of weather around the world especially in monsoon rainfall. Monsoon seasons occur over the majority of the world covering Africa, North America, Asia and Australia. The most severe of these seasons being the West African and Asia-Australian monsoons, with the West African monsoon of 2012 causing one of the largest flood crises to hit the region in the last seven years

[17]. Most summer monsoons have a strong tendency to produce copious rainfall and thunderstorms, which occurs as a result of the condensation of water vapour in the rapidly rising air. Therefore updraughts, downdraughts and cold pools are prominent features. The horizontal winds produced by the expanding downdraught, and the spreading cold pool can even be strong enough to cause structural damage and even have severe implications for aviation [55].

In November 2016, Melbourne, Victoria experienced severe thunderstorm activity triggering what is known as an epidemic thunderstorm asthma event. This caused a greater than 600% increase in asthma admissions to hospitals across Victoria over a 30 hour period, putting a strain on available resources. It has been proposed that this epidemic was due to cold pools collecting and transporting grass pollen into the clouds via updraughts where the pollen ruptured and released allergens, which were then transported back to the ground via the downdraughts. These allergens were small enough to trigger asthmatic reactions and increase the number of asthmatic events across the city [18].

The forces generated by downdraughts of cooler air and the resulting cold pools play a significant role in the structure and regeneration of severe storms. We know that cold pools trigger new updraughts by mechanical forcing. Therefore, understanding cold pool dynamics is one of the keys to understanding tropical precipitation [48]. Not only this but, the severe horizontal winds associates with both downdraughts an cold pools have implications for aviation, engineering infrastructure and weather prediction [55].

It is therefore important that downdraughts and cold pools are understood and included in forecasting models to improve the accuracy of weather predictions, and warning systems for events like flooding and health effects such as thunderstorm triggered asthma. We therefore chose to focus this study on the dynamics of downdraughts and cold pools. We will do this both experimentally and using numerical simulations. The details of how these experiments and simulations are performed are presented in chapter 2 and 5 respectively. In the following section we discuss how we recreate the scales and physics we see in the atmosphere in the laboratory.

1.3 Modelling Atmospheric Flows Experimentally

Many assumptions are made when atmospheric flows are modelled in the laboratory or by numerical methods. In general, flows within the atmosphere are high Reynolds and Peclet number, stratified rotational flows on a sphere and so it is impossible to capture the full dynamics in the laboratory. However, relevant analogues can be made by making a number of simplifications.

As briefly discussed previously, the atmosphere is made of layers, all of which have their own pressure and temperature stratifications. Both downdraughts and cold pools occur at heights within the troposphere, the lowest layer of the Earth's atmosphere, and so only the temperature and pressure profile within this layer needs to be considered.

For atmospheric convection within the troposphere the vertical extent of the motion will be large enough such that it is impossible to treat the air as an incompressible fluid. A useful quantity to describe the vertical structure of the atmosphere is the potential temperature, θ. The potential temperature of a parcel of air is defined as the temperature that air would have if it were expanded or compressed adiabatically from its existing pressure and temperature to a standard pressure p_0 (normally taken as 1000 hPa). Potential temperature is conserved by dry adiabatic processes. It should be noted that the quantity is not conserved when considering moist adiabatic processes. Since atmospheric processes are often close to adiabatic, potential temperature remains essentially conserved in the atmosphere, akin to mass which is the conserved quantity in an incompressible fluid [57]. Within the troposphere the potential temperature is only constant within the boundary layer, and there exists an increase in potential temperature with height. The boundary layer typically ranges between $2-3$ km in height over land. Further details on the properties of potential temperature can be found in Andrews [4].

Motions in a compressible fluid, which are described by velocities, potential temperatures, and potential densities, can therefore be described in an incompressible fluid by velocities, absolute temperatures, and densities. Hence, potential temperatures and potential densities can be substituted for absolute temperatures and densities, and the analysis of laboratory experiments can be used to inform the dynamics of atmospheric flows [43].

In order to simplify the problem and study downdraughts and cold pools within the laboratory, we choose to ignore the effects of both the background potential temperature stratification. We must also assume a single layer model of the Earth's atmosphere with a uniform constant potential temperature and density. The mechanisms that create the downdraught are both complex and happen at scales too small to be measured or controlled in the laboratory. The larger length scales associated with downdraughts are reduced from kilometres to centimetres when studied in a laboratory. As described above it is the falling and evaporation of rain that causes the density difference. The largest rain drops may be as large as several millimetres in the atmosphere are will be at the micrometre scale in the laboratory.

1.3.1 Typical Length and Time Scales

From around 3000 observations from over two years, Giangrande et al. [23] found that downdraughts are formed at heights mostly below $\sim$ 5km with diameters of ranging from $2-20$ km. We know that the formation of downdraughts occurs within clouds through the evaporation and drag of falling precipitation. Cumulonimbus clouds form with heights from 3 km, but rarely exceeding 15 km.

In order to make comparisons with previous laboratory and numerical studies the size of a storm can be characterised by two non-dimensional numbers: the ratio of the height of the cloud base above the ground and the radius of the downdraught (H/D), and the ratio of the height of the cloud and the radius of the downdraught (L/D). Using the observations by Fujita [21, 22], Giangrande et al. [23] we can estimate the values of L/D and H/D in the atmosphere: $0.15 \leq L/D \leq 7.5$ and $H/D \leq 2.5$. In the laboratory we have the ability to perform experiments with $1 \leq L/D \leq 5$ and $2 \leq H/D \leq 8$.

The cooling of the air within the downdraft due to the evaporation of precipitation is around 5°C compared to the ambient potential temperature of the surrounding atmosphere [32]. It is therefore a Boussinesq flow since $\frac{\nabla\rho}{\rho} = \frac{\nabla\theta}{\theta} \sim \frac{5}{300}$, where ρ is the density, and θ the potential temperature. The density difference in downdraughts is therefore small. Meaning density differences are negligible except where they appear in terms multiplied by the acceleration due to gravity, g. For reasons that that will be explained fully in the following chapter it is necessary in the laboratory to consider larger density differences with $\frac{\nabla\rho}{\rho} \sim \frac{0.1}{1}$. However, since the density difference is still small the flow within the laboratory remains Boussinesq.

Lundgren et al. [41] developed and validated an important scaling law to relate the simulated structures, produced by the release of relatively dense cylinders of fluid into a uniform quiescent ambient fluid, to much larger atmospheric downdraughts. These length and time scales depended on the initial volume V_0 of the release and on the reduced gravity $g'_0 = g\frac{\rho_0-\rho_a}{\rho_a}$ where ρ_0 and ρ_a were the densities of the release and ambient fluid, respectively. Or, when considering temperature differences, $g'_0 = g\frac{\theta_0-\theta_a}{\theta_a}$ where θ_0 and θ_a are the potential temperatures of the downdraught and ambient air respectively. The length and time scales are given by

$$R_0 \sim V_0^{1/3}, \tag{1.2a}$$

$$T_0\, R_0^{1/2}(g'_0)^{-1/2} \sim V_0^{1/6}(g'_0)^{-1/2}. \tag{1.2b}$$

Using these scalings Scorer [53] showed that laboratory measurements of the radius and vertical position of the simulated downdraughts replicated measurements of real downdraughts in Fujita [22]. When applied to measurements of downdraughts in the atmosphere these scalings

give a characteristic length scale $R_0 \sim (O)(1\,\mathrm{km})$ and timescale $T_0 \sim (O)(1\,\mathrm{minute})$. For comparison the typical length and time scales considered in the laboratory are $R_0 \sim (O)(1\,\mathrm{cm})$ and timescale $T_0 \sim (O)(0.1\,\mathrm{s})$.

Using the observations from Fujita [21, 22], the Reynolds number of downdraughts has been calculated to be of the order $\mathrm{Re} = R_0 u_0/\nu = O(10^8)$, where u_0 is the velocity scale $u_0 = R_0/T_0$ and ν the kinematic viscosity. In the atmosphere the Peclet number is $\mathrm{Pe} = \mathrm{RePr} = O(10^7)$ where $\mathrm{Pr} \approx 0.7$ is the Prandtl number. However, in the laboratory $\mathrm{Pe} = \mathrm{ReSc} = O(10^{10})$ where $\mathrm{Sc} \approx 500$ is the Schmidt number.

It is impossible to create Reynolds numbers of this order in the laboratory but Lundgren et al. [41] has shown that when using a saline solution in fresh water their measurements from laboratory experiments agree with measurements from observations of downdraughts when the Reynolds number $\mathrm{Re} = R_0 > 3 \times 10^3$. Therefore, it is sufficient to produce experiments with $\mathrm{Re} > 3 \times 10^3$ to obtain comparable dynamics to that of the atmosphere. In the experiments produced in this study $4 \times 10^3 < \mathrm{Re} < 1.5 \times 10^4$ and $1 \times 10^6 < \mathrm{Pe} < 1 \times 10^7$. To obtain these values of the Reynolds number it is easier to use salt solutions rather than heat to create density differences. Working with density differences in salt solutions allows for larger values of reduced gravity and has smaller values of kinematic viscosity and molecular diffusivity than using heat in air, and so larger values of the Reynolds and Peclet numbers can be achieved this way [40].

1.4 Previous Work

Downdraughts were first qualitatively described from observations by Fujita [21, 22]. He described them as a downward flow surrounded by a horizontal vortex which forms a vortex ring during the descent. In most following studies of downdraughts the mechanisms that create the potential temperature and density differences that cause downdraughts are ignored. This approach has been adopted when studying the macro-properties of a downdraught in the laboratory by Alahyri & Longmire [2], Lundgren et al. [41], Nagata et al. [44], Sengupta & Sarkar [54] and Yao & Lundgren [59].

Previous work has instead considered downdraughts as either thermals [41, 49], or has used the classical plume theory of Morton et al. [43] to describe them. However, Morton et al.'s plume theory inherently assumes that the downdraughts are tall and thin, and thermal theory requires heights above the ground (values of H) larger than the geometries associated with downdraughts in order that the dynamics become self-similar. The impact of plumes and jets on a horizontal surface has already been considered by Rooney & Linden [51] and Linden & Simpson [39], and the impact of self-similar thermals by Lundgren et al. [41], Yao

& Lundgren [59] and Rooney [49]. It is therefore worth studying what happens when a thermal impacts the ground before a thermal has become self-similar as we believe that these are the geometries that will be significant in the atmosphere.

In this study we will investigate how finite buoyancy-driven releases impacting a horizontal boundary resulting in gravity currents behave depending on the aspect ratio of the initial release and relative height above the surface. We will use both laboratory experiments and numerical simulations to consider thermals impacting on a boundary and spreading as axisymmetric gravity currents to represent downdraughts impacting the ground and the subsequent spreading cold pools.

Thermals

In early laboratory studies e.g. Scorer [53], thermals were initiated by turning over a hemispherical cup, meaning that the vertical and horizontal length scales were comparable. However, more recent studies have used submerged tubes temporarily sealed at the base which were then released and the fluid was left to drain out, e.g. Bond & Johari [8], Hart [30], Lundgren et al. [41]. A typical cylindrical tube used as a release mechanism for thermals can be seen in figure 1.5. The image also shows the three length scales which affect the dynamics of the developing flow. Namely, the diameter of the cylinder D, the length of the cylinder L, and the height above the ground H. We chose to investigate the effects of these length scales through the nondimensional parameters L/D and H/D.

Scorer [53] showed that after some initial adjustment phase, the dynamics of a thermal reach a self-similar behaviour for which the initial conditions of the release no longer affect the evolution of the thermal. Scorer [53] determined during this self-similar phase, and this will be shown in chapter 3, that the radius of the thermal grows linearly with the vertical position. The vertical position z can be written as a function of time t as follows:

$$z \sim t^{1/2}. \tag{1.3}$$

To obtain the similarity solution in (1.3) Scorer [53] made two assumptions. The first was an approximation, which has been widely adopted since, that the shape of an isolated thermal may be represented by an oblate spheroid. The radii r (equivalent to the horizontal axis of its cross-section) and h (equivalent to the vertical axis of its cross-section) determine its volume and surface area.

The second assumption is the entrainment assumption proposed by Morton et al. [43]. For plumes Morton et al. [43] determined that the velocity u_e of ambient fluid being entrained by the plume was proportional to the local vertical velocity w of the plume. They, therefore,

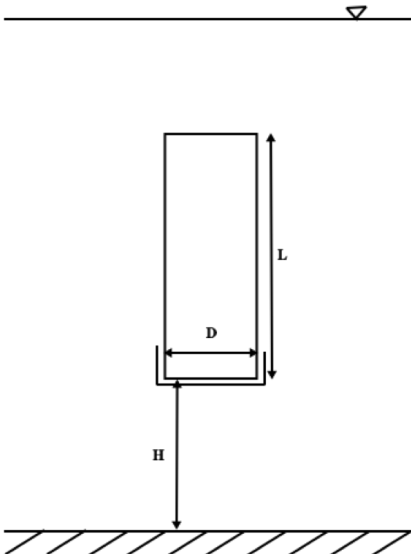

Fig. 1.5 Diagram of a typical cylindrical release mechanism for a thermal. Shown are the three length scales most commonly varied: the diameter of the cylinder D, the length of the cylinder L, and the height above the ground H.

wrote $u_e = \alpha w$ where α is the entrainment coefficient. For a thermal an equivalent assumption is that the rate of change of the volume is proportional to its surface area, A_s, multiplied by its vertical velocity i.e.

$$\frac{\mathrm{d}V}{\mathrm{d}t} = \alpha a r^2 \frac{\mathrm{d}z_c}{\mathrm{d}t}, \tag{1.4}$$

where V is the volume of the thermal, ar^2 is the surface area of the thermal under the assumption that it is a spheroid and z_c is the vertical position of the centre of mass. Lundgren et al. [41] conducted experiments and numerical simulations on the descent and gravity current phases of the elevated release of a cylinder of dense fluid. They used two diameters of tube, where for both tubes $L/D = 1$. As discussed above, they found that their experimental measurements and data from field observations of downdraughts collapsed onto the similarity solutions found by Scorer [53], when scaled by a length scale R_0 and time scale T_0 given by equation (1.2). Lundgren et al. [41] concluded that their experimental measurements of the radial and vertical positions were independent of Reynolds number above $\mathrm{Re} = 3000$, where $\mathrm{Re} = R_0 u_0/\nu$ with the velocity scale $u_0 = R_0/T_0$. From direct numerical simulations they showed that the circulation in the vortex ring that forms during the descent rapidly increased before reaching a constant value. They found that these results were approximately independent of the release height which they varied in the range $1.4 \leq H/D \leq 1.9$.

Bond & Johari [8] studied the evolution of cylindrical releases with aspect ratios in the range $2 \leq L/D \leq 8$. The cylinders were released at heights in the range of $25 \leq H/D \leq 55$ with Reynolds number Re approximately in the range 1350 to 3140. Both light induced fluorescence (LIF) and particle image velocimetry (PIV) measurements were taken in a region $7-11$ source diameters away from the source. They concluded that the distance required for the initial release to become self-similar increases linearly with the length scale R_0 provided by Lundgren et al. [41] and given in (1.2). They concluded that the descent could be viewed in two phases: the initial acceleration phase and the self-similar phase. The duration of the initial acceleration phase was found to last from one to two times T_{drain}, where T_{drain} is the time taken for the source fluid to leave the cylinder. After the initial acceleration phase the flow decelerated and displayed the properties of a self-similar thermal. In the second stage the front of the buoyant parcel advanced close to $\hat{z}_f(t) \propto \hat{t}^{1/2}$, characteristic of self-similar thermals, nondimensionalised by the length and time scales given in (1.2).

Lai et al. [37] performed numerical simulations on the role of the aspect ratio on the radial spreading rate of a falling finite volume dense release. They used OpenFOAM and a numerical solver of the Unsteady Reynolds averaged Navier-Stokes equations (URANS), using the $k-\varepsilon$ turbulence closure to simulate the release of cylinders of dense fluid with varying initial volumes. They varied both the length and diameter of the cylinder producing ranges of height $21 \leq H/D \leq 44$ and aspect ratio of the cylinder $0.125 \leq L/D \leq 4$. They found that both the vertical z and radial r positions of the thermals from their numerical simulations agreed well with the previous experimental work of Hart [30] and Zhao et al. [60]. Lai et al. [37] concluded that the initial aspect ratio was a key factor affecting the thermal spreading rate $n = (\mathrm{d}r/\mathrm{d}t)/(\mathrm{d}z/\mathrm{d}t)$, and that an increase in initial aspect ratio, L/D, led to a decrease in the constant value of the spreading rate, n. Increasing the initial aspect ratio above $L/D = 2$ had no effect on the radius of the thermal during the descent however, it was observed that for values of $L/D > 2$ a thin trailing stem was ejected from the thermal. This value of L/D is known as a formation number and relates to the maximum vorticity that can be incorporated into a vortex ring before a trailing stem forms. In the case of buoyant vortex rings the formation number has been shown to be about 4–5 [37]. In the case of thermals, which are a form of buoyant vortex ring produced with no initial momentum, the trailing stem seen for the simulations performed at $L/D = 2$ indicates that some of the fluid could not be incorporated into the vortex head and that the formation number is lower at $L/D \approx 2$. For the experiments with $L/D \leq 2$ they found that the spreading rate of the thermal decreased from 0.31 to 0.13 as the cylinder increased in length from $L/D = 0.125$ to 2. As with the study performed by [8], all the simulations were performed with large values of

H/D and as a result of this Lai et al. [37] did not report any results for the acceleration phase of the thermal.

In a numerical study by Rooney [49], large eddy simulations (LES) were performed using the Met Offices large eddy model (LEM). Spherical releases with 6 different radii r_0 ranging between 238 to 756 m were initiated by an initial temperature perturbation in the potential-temperature field at two release heights. This gave rise to a range of H/D which varied between 1.5 and 18. Also varied were the initial buoyancies, which were varied to give rise to a large range in estimated impact times i.e. the time it took for the thermal to reach the ground. The 'cold bubble' was allowed to develop, impact on the boundary below and spread radially as a gravity current. The results showed that the descent was observed to follow the similarity solution from thermal theory, (1.3) i.e. $z \sim t^{1/2}$ with the introduction of a virtual origin z_v. The virtual origin was defined as $z_v = n^{-1} r_0$, where $n = (\mathrm{d}r/\mathrm{d}t)/(\mathrm{d}z/\mathrm{d}t)$ is the spreading rate of the thermal, which gives the vertical position where $r_0 = 0$. Rooney [49] also observed that the thermal required an initial adjustment period during which the geometry of the release influences the flow, before reaching the self-similarity.

The studies by Lundgren et al. [41] and Yao & Lundgren [59] kept the ratio of the cylinder $L/D = 1$ the same for all experiments. Therefore, they did not compare the effect of the ratio of the release on a thermal at a height applicable to downdraughts. However, experiments with varied release ratios have been performed separately for a thermal by Bond & Johari [8] and Lai et al. [37]. Both of these studies have focused on the properties of a self-similar thermal and have not considered the effect on a gravity current. The flow directly after release is referred to as the acceleration phase of thermal development. The duration of this initial acceleration phase has been considered by Bond & Johari [8] using the criteria that the vertical position evolves as $z \sim t^{1/2}$. This similarity solution relies on the two assumptions: that the thermal is a spheroid, and the entrainment assumption from Morton et al. [43]. It can be inferred from the findings of Bond & Johari [8] and Lai et al. [37], for $L/D > 2$ the thermal develops a significant trailing tail and the shape assumption therefore no longer holds. From observations we know that downdraughts are formed at heights mostly below $\sim$ 5km with diameters of around 2 km [49] i.e. $H/D \approx 2.5$. According to Bond & Johari [8] below this height we would expect all releases with $L/D > 1$ to be in the acceleration phase. A better understanding of the acceleration phase of a thermal and the effect of increasing L/D on the acceleration phase is required, since it is significant for applications to atmospheric downdraughts. In particular the shape assumption for a thermal for $L/D > 2$, and the entrainment assumption during the initial acceleration phase needs to be considered.

Gravity Currents

Gravity currents have been studied in considerable detail both numerically and in the laboratory. In the laboratory, gravity currents are usually initiated using a lock release/exchange experiment. In a lock release/exchange experiment a portion of a tank is sectioned off using a lock gate, the density of one side of the lock is then increased or decreased before releasing the lock to let the gravity current evolve. In the case of axisymmetric gravity currents this is either done using a cylindrical tank with a cylindrical lock, or by using a sector tank which gives a sector of the cylindrical set-up.

Grundy & Rottman [27] proposed a similarity solution of the shallow water equations for the front speed u_f of an axisymmetric gravity current in terms of the radius r

$$u_f \propto B^{1/2} r^{-1}, \tag{1.5}$$

where $B = g_0' V_0$ is the conserved total buoyancy. Since $u_F = \mathrm{d}r/\mathrm{d}t$, in terms of the radius this gives

$$r \propto B^{1/4} t^{1/2}, \tag{1.6}$$

as expected from previous work, such as Simpson [55, p.172]. The analysis of Rooney [50] shows it is possible to obtain (1.5) without using the shallow water equations, but instead from the Boussinesq–Euler equation. It also follows from dimensional analysis.

Huq [35] performed experiments on axisymmetric gravity currents to find the effect of the initial aspect ratio h_0/r_0 of the initial height, h_0, and radius, r_0, of a lock release, and the effect of the fractional depth h_0/h_{max}, where h_{max} is the depth of the ambient fluid, of the current on the entrainment rates. They showed that their data collapsed with the similarity solution given by (1.6) using the length scale and time scales given in (1.2) i.e. based on the initial volume and reduced gravity. For the smallest aspect ratios considered, with $h_0/r_0 < 0.2$, the entrainment velocity u_e, which is the volume flux of ambient fluid entrained per unit area, was found to be proportional to the velocity of the head of the gravity current u_F. However, for higher aspect ratios the entrainment velocity was shown not to vary with the velocity of the head in a proportional manner.

As with a thermal, a gravity current goes through an initial adjustment phase immediately after release before it reaches the similarity solution given by (1.6). This initial adjustment phase is known as the slumping phase, and for axisymmetric gravity currents, this phase has been studied in works such as Huppert & Simpson [34] and Hallworth et al. [29]. Hallworth et al. [29] performed experiments on axisymmetric gravity currents using a sector of a cylindrical tank. They found that the radius of the slumping phase r_s was three times the

initial radius of the lock r_0, i.e. $r_s/r_0 = 3$, only when the initial height of the release was equal to that of the ambient fluid.

In the study performed by Rooney [49], gravity currents were initiated by the impact of a thermal on a solid boundary. The radii of the gravity currents were shown to compare well with the similarity solution of a gravity current produced by a lock release experiment when considering $r - r_i$, where r_i is the radius of the thermal at impact with the ground. Rooney [49] concluded that there was no major flow adjustment during impact with the ground and that if the thermal transitions to a gravity current in a 'spun up' state, i.e. a self-similar thermal, then the radius of the gravity current was allowed to evolve, and attain self-similarity.

Both Lundgren et al. [41] and Yao & Lundgren [59] conducted experiments to produce axisymmetric gravity currents initiated by a thermal impacting on the ground. Their experiments involved releasing cylinders of dense fluid with aspect ratio $L/D = 1$ at a height $H/D \approx 2$. They applied the scalings found by Lundgren et al. [41] and show that at some time after impact with the ground the radial position of the gravity current agrees with the observations of axisymmetric gravity currents performed by Huppert & Simpson [34]. However, during the adjustment phase of the gravity current, the velocity of the current is set by radial velocity of the thermal which is slower than expected from a self-similar gravity current. They concluded from observations and velocity measurements that this phase, where the thermals radial speed set the speed of the thermal, was due to the development of gravity current directly after impact being impeded by the vortex ring within the thermal. Directly after impact this vortex ring carried the radially spreading current backwards over its top until the vortex ring was eventually weakened by wall friction and the current became self-similar [59].

The studies by Lundgren et al. [41] and Yao & Lundgren [59] kept the ratio of the cylinder, $L/D = 1$, the same for all experiments, and therefore did not compare the effect of the ratio of the release on a gravity current. However, experiments with varying release ratios have been performed separately for an axisymmetric gravity current but only when produced by a lock release, by Huq [35]. The flow directly after release of a gravity current is referred to as the slumping phase, the duration of which has been found to be between 3 and 10 lock lengths for an axisymmetric lock release experiment [33]. However, Rooney [49] found that this phase was reduced when the gravity current was initiated by a thermal impacting on a surface. Similarly, the experiments of Lundgren et al. [41] and Yao & Lundgren [59] found that this phase occurred within 1 and 2 times the impact radius. By definition the self-similar phase of the gravity current will be unaffected by the shape of a thermal that has impacted on the ground. However, as shown by Rooney [49] the slumping phase will be affected by

the initial geometry of the release. An understanding of how the slumping phase is affected by changing the geometry of the release of a thermal is therefore required since it may have implications for cold pools.

1.5 Outline and Aims

The aim of this study is to investigate downdraughts and cold pools using cutting edge experiments and numerics. Overall the summary above shows that the macro properties of downdrafts and cold pools in the atmosphere, although complex, can be represented by the release of thermals which then impact with the ground and spread as axisymmetric gravity currents. As discussed, thermals released from cylindrical tubes have been shown to require an adjustment region before becoming self-similar. The duration of these adjustment periods are dependent on the length of the tube that the thermals have been released from. However, from field observations of downdraughts it is likely that most would impact the ground not in a self-similar phase. Much is still unknown about the details of the initial acceleration period of thermals and how, if they were to impact the ground in this phase, this may affect the resulting gravity currents.

Here our objectives are, first, to extend the current understanding of the development of the shape and dynamics of thermals from release to the self-similar state. We will find that to obtain accurate measurements of thermals a novel extension to an existing experimental technique is required. To extend the current understanding of the initial development of a thermal we will consider ranges of L/D at two different heights not previously considered: these ranges are outlined in table 1.1 and shown in figure 1.6. Figure 1.6 shows the ranges of L/D and H/D considered by previous studies, the range seen in real downdraughts, and the values of L/D and H/D that we will consider in this thesis. We can see that the values of L/D considered by us at $H/D = 2$ spans a range of cases that we might expect to see in the atmosphere. At the higher value of H/D the same values of L/D are also studied which covers a range that has not previously been considered by any other study.

Secondly, we aim to investigate the impact of a thermal with the ground and transition to a self-similar gravity current and see how both of these are affected by the aspect ratio and relative height of the release of a thermal. Finally, we wish to determine whether the existing self-similar theory for thermals can be applied to those produced here. This will be achieved using the experimental measurements and numerical simulations performed in the Met Office's new large eddy model (MONC).

Chapter 2 introduces the experimental techniques used throughout the subsequent chapters to investigate thermals impacting on a boundary and the resulting gravity current. In particular,

Reference	H/D range	L/D range	description
Alahyri & Longmire [3] −−	$1.75 \leq H/D \leq 2.7$	$L/D = 1.4,\ 2$	experiments on thermals and gravity currents
Lundgren et al. [41] −−	$1.4 \leq H/D \leq 1.9$	$L/D = 1$	experiments on thermals and gravity currents
Yao & Lundgren [59] ×	$H/D \approx 2$	$L/D = 1$	experiments on thermals and gravity currents
Rooney [49] −−	$1.5 \leq H/D \leq 18$	L/D=1 (spheres)	simulations of thermals and gravity currents
Bond & Johari [8] □	$25 \leq H/D \leq 55$	$2 \leq L/D \leq 8$	experiments on thermals only
Lai et al. [37] □	$21 \leq H/D \leq 44$	$0.125 \leq L/D \leq 4$	simulations of thermals only
Huq [35] −−		$0.04 \leq L/D \leq 0.62$	experiments on gravity currents only
This Study ○	$H/D = 2$ and 8	$1 \leq L/D \leq 5$	experiments and simulations of thermals and gravity currents
Downdraughts □	$0.25 \leq H/D \leq 2.5$	$0.25 \leq L/D \leq 2.5$	

Table 1.1 A summary of the ranges of L/D and H/D for previous works on both gravity currents and/or thermals. Also included are the symbols that represent the studies in figure 1.6.

we will outline a novel extension to the dye-attenuation technique, which was developed to address the problems that arose during the process of this work in order to study the development of the shape of a thermal.

Chapter 3 examines the thermals produced in the laboratory experiments. A more detailed background of thermal theory is provided and extended to include the initial acceleration phase. The results of the laboratory experiments are presented and compared to the solutions for both theoretical models. It is observed that the initial acceleration period of a thermal can be split into two further phases and adaptations of the self-similar theory are made to model these two phases. Finally, the validity of the assumptions made on the shape and entrainment of thermals are examined during both of these phases, and in self-similar phase.

Chapter 4 examines the gravity currents produced in the laboratory experiments. A gravity current model is determined, and the results of the laboratory experiments are presented and

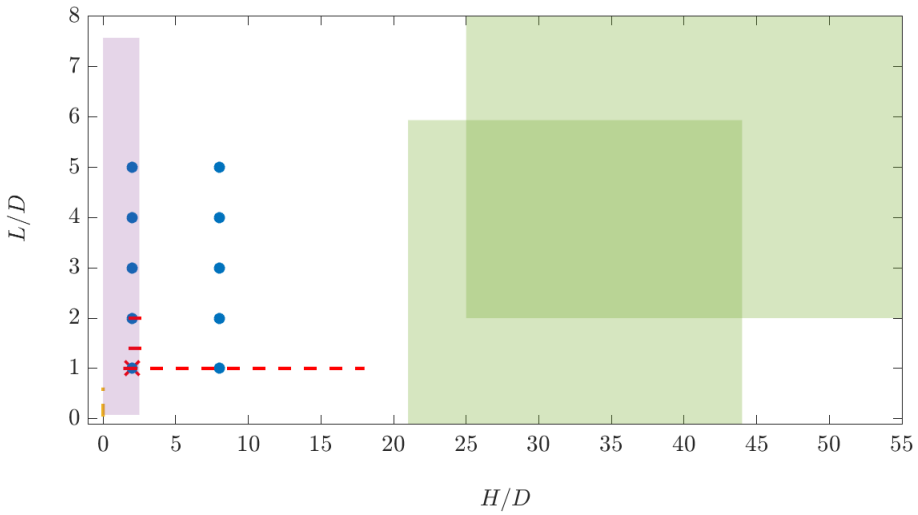

Fig. 1.6 Phase diagram showing the ranges of L/D and H/D considered by previous studies, as well as the range seen in the atmosphere. The studies plotted here are given in table 1.1 along with the given markers. Also plotted are the values of L/D and H/D of the experiments and simulations performed in this study (blue dots).

compared to the theory. The transitions of the radii from a thermal to a gravity current are considered and linked to conditions of the thermal at impact. Implications for collisions of cold pools are also briefly discussed.

Chapter 5 presents the results from MONC, the Met Office large eddy model. A description of MONC is provided and compared to its predecessor the LEM. Testing of the set-up of MONC was performed in order to best replicate the laboratory conditions. A subset of simulations performed by Rooney [49] in the LEM have been compared to exact replicas run in MONC in order to compare the two large eddy models. The effects of the initial geometry have then been considered, by comparing both cylindrical and spherical releases of equal volume. The results of cylindrical releases imitating the laboratory experiments are then presented and compared to the experimental results of both thermals and gravity currents. Finally, the assumptions on the shape and entrainment of thermals made in the development of the theory for thermals are discussed further. Here a general version entrainment assumption is considered in order to remove any assumptions made on the shape of a thermal. Finally, the conclusions of this study are given in chapter 6.

Chapter 2

Experimental Methods

2.1 Experiments on Thermals and Gravity Currents

Early experiments initiated thermals by turning over a hemispherical cup, e.g. Scorer [53]. However, more recent studies have been using submerged tubes temporarily sealed at the base which are then burst and the fluid is allowed to drain out, e.g. Bond & Johari [8], Hart [30], Lundgren et al. [41]. It is the later method that will be used in this study. Similarly gravity currents are traditionally formed using lock-release experiments, and there are only a limited number of studies considering a thermal impacting a boundary [41, 49]. Herein,we carry out experiments designed to enable robust measurements of thermals impacting a boundary and the resulting gravity currents. In this chapter the general set-up of the laboratory experiments will be described in detail as well as the measurement techniques used to obtain the results for the following chapters.

2.1.1 Experimental Set Up

The experimental set up used for this study was designed to make the initiation of thermals as repeatable as possible. Two measurement techniques were used to analyse the thermals and gravity currents, both of which require the same basic set up. All of the experiments were performed in a tank of horizontal cross-section 80 cm ($y-$direction) x 250 cm ($x-$direction) horizontal cross section and depth 75 cm ($z-$direction). The tank was filled with sodium chloride solution of uniform density around $\rho_a = 1.10\,\mathrm{gcm}^{-3}$ to a depth 5 cm above the top of the submerged tube used to provide the source of the downdraught. In the base of the tank a raised false bottom was added. This false base was raised 7 cm from the base of the tank and was a 66 cm $\times$ 66 cm square. The run-out from experiments created a dense layer at the base of the tank, i.e. below the false bottom, which enabled us to perform multiple

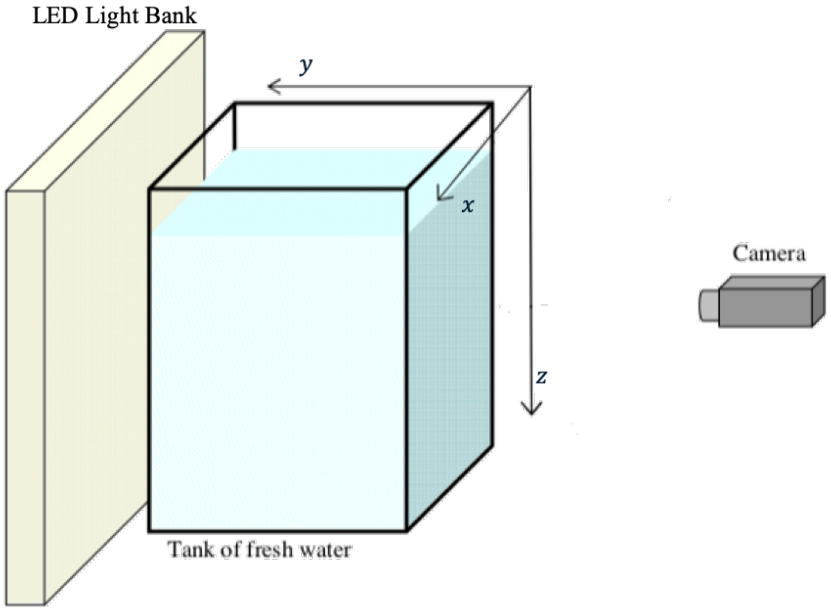

Fig. 2.1 Position of camera and LED light bank relative to the tank.

experiments without the need to drain and refill the tank. The tank was illuminated from behind with a tricolour (red, green and blue) LED bank which measured 190 cm × 99 cm and consisted of alternating rows of red, green and blue LED strips. The strips were separated by 4 cm and a light diffuser was positioned 13 cm in front of the LED strips to ensure that, for each of the colours, the lighting was uniform. This allowed us to illuminate the tank with the individual colours as well as using white light by having all three colours turned on. To image the thermals, and subsequently the gravity currents, an ISVI Dalsa Falcon 12 megapixel camera with a 60 mm lens was positioned in front of the tank, as shown in the schematic in figure 2.1, and images were recorded at 90 Hz.

The thermals were initiated by releasing dyed sodium nitrate of density ρ_0 from perspex tubes into sodium chloride ambient of density ρ_a. The densities of the fluids were measured using a DMA 500 density meter with an accuracy of $\pm 1 \times 10^{-6}$gcm^{-3}. The tubes themselves were made of perspex, had inner diameter $D = 5$ cm and lengths varying from $L = 5$ cm to $L = 25$ cm. This range of lengths of tube was chosen in order to cover the ranges of L/D considered by Bond & Johari [8], Lai et al. [37] and Lundgren et al. [41]. The heights, H, were chosen to fill in the gaps left by these studies. For Lundgren et al. [41] only $L/D = 1$ at $H/D \approx 2$ was considered, so a larger range will be considered here. In order to make comparisons with Bond & Johari [8] and Lai et al. [37] the height of $H/D = 8$ was chosen as it was expected that for tubes with values of $L/D = 1$ and 2 the thermal would impact the ground in the self-similar thermal phase. Using the heights at which a thermal becomes

L/D	H/D	number of repeats	range of g_0' (g/cm^3)	Reynolds Number (Re$= R_0 u_0/\nu$)
1	2	7	44.84 48.95 51.41	6609 – 7077
2	2	7	44.84 48.95 55.46	9346 – 10394
3	2	7	32.94 44.84 48.95 55.46	9811 – 12730
4	2	5	48.23 51.42 55.46	13708 – 14700
5	2	5	45.36 48.23 51.42	15326 – 15825
1	8	9	24.17 35.59 41.32 42.21	4852 – 6412
2	8	7	32.94 36.94 42.30 45.36	8010 – 9400
3	8	7	32.94 34.52 42.30 42.52 45.36	9811 – 11147
4	8	5	41.32 42.21 42.52	12688 – 12871
5	8	5	34.52 41.32 42.21 42.52	12966 – 14391

Table 2.1 Details of the experiments performed in this study.

self-similar from Bond & Johari [8], we would expect to have experiments that impact the ground while draining, in the acceleration phase of a thermal and as a self-similar thermal. Therefore, the range of heights and lengths of tube chosen will produce gravity currents formed with three different impact conditions. The diameter of the tube was chosen to enable us to perform experiments at the height $H/D = 8$ in the tank used whilst still being able to have the longest tube submerged by at least one source diameter under the free surface. The details of all the experiments performed here are given in table 2.1. Included in the table are the values of L/D and H/D considered, the number of repeat experiments performed for each length of tube at each height, and the values of g_0' used.

The perspex tubes were positioned directly above the centre of the false bottom and were rigidly held in place by a structure fixed to the top of the tank. This structure included a winch that allowed for the tube to be moved vertically in order to change the release height H. The tubes were submerged 5 cm under the free surface of the ambient fluid, and temporarily sealed at the bottom with a 0.2 mm thick sheet of latex. The latex was held in place by being stretched over 6 nylon pins placed around the bottom edge of the tube. The base of the tube was curved and smoothed to ensure that the latex could be stretched over the base of the tube without tearing. For each experiment a 10×10 cm square of latex was cut and a 1×1 cm cross drawn in the center. The latex was then stretched over the base and secured on the nylon pins. The latex was stretched until the edges of the cross drawn in the center was at the edge of the tube. This was done to ensure that the latex was stretched with a similar tension in every experiment. The tube was then slowly filled using a syringe and needle with sodium nitrate dyed using methylene blue. The tubes were always completely filled as it was found that using a partially filled tube affected some of the measurements of the vertical position of the thermal. More details of this procedure can be found in appendix A.

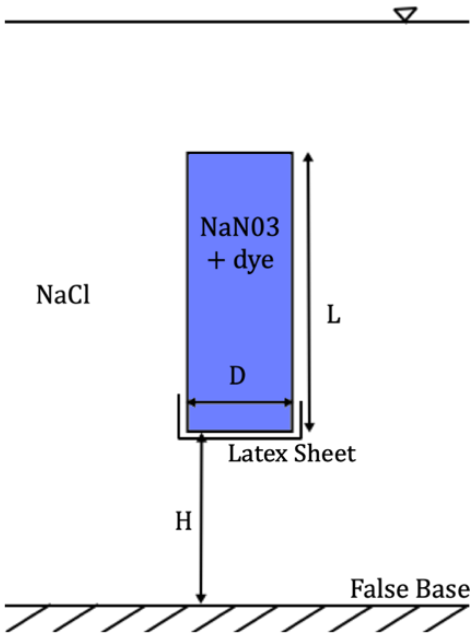

Fig. 2.2 The set-up of the tube in the laboratory experiments

The experiment was initiated by piercing the latex with a needle positioned at the center of the cross drawn on the latex. It was found that the latex had ruptured and fully retracted from the tube within 2-3 camera frames, i.e. within $0.022-0.033\,\mathrm{s}$ and $0.051-0.099T_0$, where T_0 is the time scale based on the initial volume and reduced gravity. Insignificant volumes of dyed fluid were initially propelled sideways by the latex, and either entrained by the main body of the thermal or had no further interaction with it. Once released the thermals took between 1 and 7 s to impact with the ground. This time depended on the length of the tube and height at which the tube was held above the ground, with the thermals produced by the longest tube being the fastest. The thermal then impacted with the false bottom and started to spread as an axisymmetric gravity current. The entire experiment, including both the thermal and gravity current, lasted from 4 to 17 s. The duration of the experiments varied with the value of both L/D and H/D, with the longest experiment being performed with $L/D=1$ at $H/D=8$ and the shortest performed with $L/D=5$ at $H/D=2$.

2.2 Dye Attenuation

Dye attenuation measures the integral of dye along light rays and may be used to infer either the concentration of dye in a fluid or the width of a fluid in the $y-$direction (figure 2.1). It is based on an image processing technique developed by Dalziel in 1989 as part of the

image processing system DigImage. The methodology behind this process was outlined by Cenedese & Dalziel [15]. The technique uses Beer-Lambert theory of light absorption combined with careful calibration to relate the light intensity seen by the camera to the width-integrated, in the $y-$direction, concentration of dye. This calibration is a critical part of the process and will be discussed in detail in section 2.2.2. The technique is illustrated here with measurements of thermals. Due to the large dilution of dye in a thermal, and subsequent gravity current as a result of entrainment, the technique presented by Cenedese & Dalziel [15] is herein extended in order to cover the larger range of dye concentrations required and is presented in section 2.2.4.

2.2.1 Light Attenuation Theory

Beer-Lambert theory gives the following equation for intensity $I(l,c)$, which is a function of the distance along a ray of light l and concentration c,

$$\frac{\mathrm{d}I}{\mathrm{d}l} = -\eta I, \tag{2.1}$$

where $\eta = \eta(c)$ is the rate of absorption and is some function of concentration c only. If we suppose that the concentration is constant along a ray of light, i.e. $c(l) = c$, then integrating along the ray gives

$$I(h,c) = \hat{I}_0 e^{-\eta(c)h}, \tag{2.2}$$

where h is the distance of the dyed water travelled through by the ray of light, $\hat{I}_0$ is the intensity before the light has travelled through the tank, and $\eta(c)$ is the absorbency of the dye. The absorbency function $\eta(c)$ is assumed to be a function of the concentration only, and is determined by the calibration outlined in section 2.2.2. For low concentrations of dye the absorbency function $\eta(c)$ is approximated to be linear in concentration

$$\eta(c) = Ac + b, \qquad A,\, b > 0, \tag{2.3}$$

where the constant A determines how increasing the concentration affects the attenuation, and the constant b is the attenuation of undyed water. In practice, we take

$$\frac{I}{I_0} = e^{-Ach}, \tag{2.4}$$

where $I_0 = I(0,h) = \hat{I}_0 e^{bh}$, which takes into account any of the light attenuated by other factors e.g. the air, tank walls and ambient water etc. However, this analysis ignores any

effects due to the difference in refractive indices within the dyed fluid, which we will return to in section 2.2.4.

Wavelength Dependence

In the derivation of (2.4) it is assumed that the absorbency, $f(c)$, of the dye is a function of concentration only. The absorbency is actually a function of both the concentration and the wavelength of light. The wavelength dependency of the absorbency function is due to the absorption spectrum of a dye, meaning that a dye will absorb different wavelengths of light in different amounts.

The impact of the wavelength dependence has been looked at in detail by Cenedese & Dalziel [15]. They showed that if the absorption function $f(c,\lambda)$ depends on the wavelength λ then (2.4) will no longer be valid. In practice, to make the absorption function approximately independent of wavelength, two things can be done: a colour filter can be put on the camera so as to allow only a narrow band of wavelengths through, or coloured lights with a narrow spectrum of light (e.g. coloured LEDs) can be used to illuminate the tank. We chose to exploit the latter.

2.2.2 Calibration of Methylene Blue Dye

A common dye used for dye attenuation is methylene blue as it is safe and the concentration is easily controlled between batches unlike other dyes such as food colouring. By choosing a single colour to illuminate the tank the effects of the wavelength dependence on the absorbency function $f(c,\lambda)$ are reduced. For methylene blue the colour red is chosen since there is a peak in the absorption spectrum of methylene blue near the red wavelengths of light, shown in figure 2.3. A peak in the absorbance spectrum means that the dye will absorb a large amount of red light and, therefore, only a small amount of dye is needed to create a large difference in light intensity recorded by the camera. As mentioned above, light attenuation theory requires the concentration of dye to be small in order to make a linear approximation of the absorption function (2.3), further making red a valid choice. Indeed, any function can be chosen provided the function is known and calibrated for, however, in order to maximise accuracy we chose to stay in the region where one can make a linear approximation.

To perform the calibration two tanks with known lengths were used: the first had dimensions $x = 30\,\text{cm}$, width $y = 15\,\text{cm}$ and depth $z = 20\,\text{cm}$ the second tank with length $x = 10\,\text{cm}$ width $y = 10\,\text{cm}$ and depth $z = 24\,\text{cm}$. The two tanks were chosen since they both had different widths in the $y-$direction this gave two different values of h in (2.4) to ensure that the value of A is consistent at different widths and concentrations. Both tanks

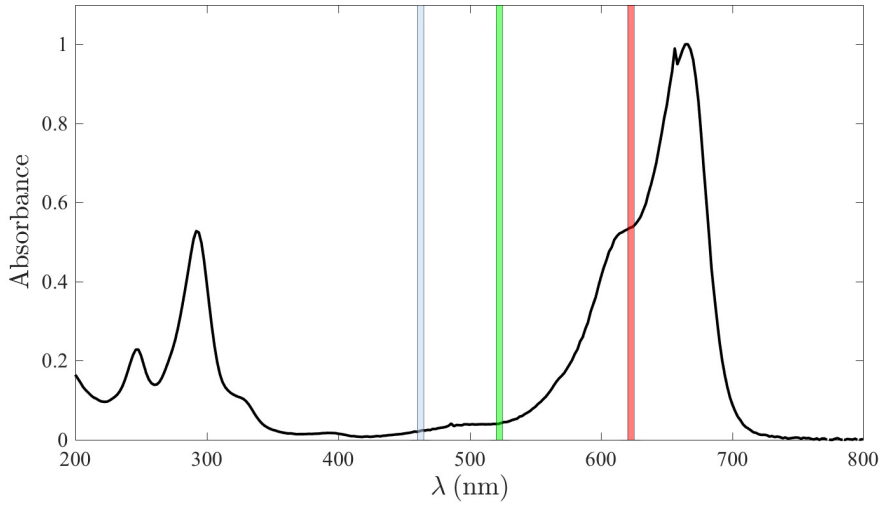

Fig. 2.3 Absorbance spectrum of methylene blue dye. The absorbance has been normalised by the maximum absorbance. The coloured vertical lines represent the bands of wavelengths produced by the blue, green and red LEDs available to us. Spectrum provided by Scott Prahl, Oregon Tech, USA.

were partially submerged in the larger main tank of water. The two smaller tanks were then filled with a known volume of water, and using red LEDs to illuminate the tanks from behind, a background image is taken of the tanks containing no dye. Known volumes of dye were then added incrementally to the tanks and after each addition of dye the tanks were recorded. More dye was then added and the process repeated until the image recorded was saturated and the intensity could no longer be reliably measured with the recorded image. Each recorded image was normalised by the background image and the average value of the intensity I/I_0 is taken over an area of dyed fluid for both of the tanks. The average value of this intensity gives the value of I/I_0 for a known concentration c of dye and a fixed width h in the y-direction. By using (2.4) it is possible to find a value of A.

Figure 2.4 shows the calibration of methylene blue with red LEDs performed in the two tanks with $h = 10\,\text{cm}$ (circles) and $h = 15\,\text{cm}$ (triangles). The values of ch for both widths of tank used, collapse onto one curve implying that the use of (2.4) is valid. The figure shows the value of I/I_0 for each ch cm g/l, as well as the fitted curve used to find A. Also shown on figure 2.4 are the upper and lower values of I/I_0 (dashed lines) within which the noise level of the image or the error in the fit to the calibration is insignificant. The lower limit was chosen to be the value of $I/I_0 = 0.16$ where the calibration curve no longer had a large gradient meaning that large changes in ch would only make small changes to I/I_0. For the upper bound on I/I_0, it is important that $I/I_0 \neq 1$, i.e. the camera is not saturated, so

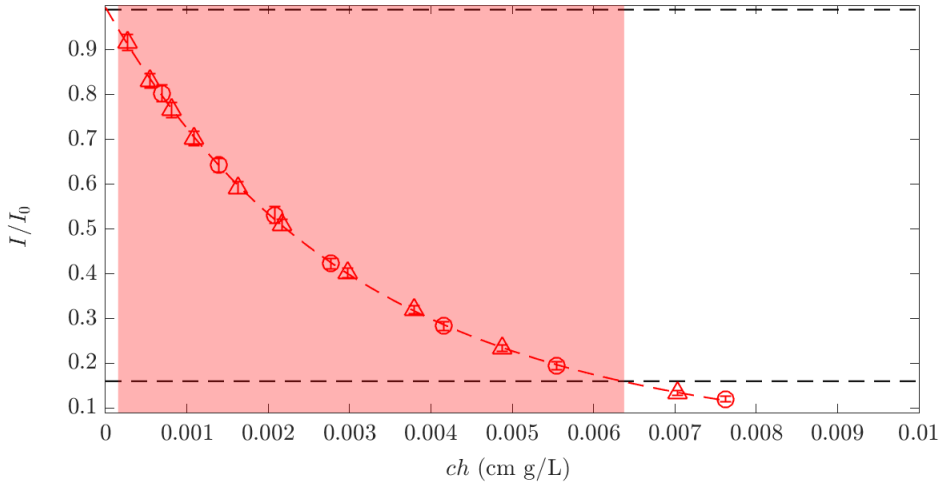

Fig. 2.4 Calibration of methylene blue with red LEDs performed in two tanks with $h = 10\,\text{cm}$ (circles) and $h = 15\,\text{cm}$ (triangles). The red dashed line shows the theoretical fit that will be used to apply the calibration. The black dashed lines show the minimum and maximum intensity to achieve an intensity not contaminated by high levels of dye or the noise of the camera. The red shaded region represents the range of ch that our calibration can accurately cover.

the value of $I/I_0 = 0.99$ was chosen. The shaded red area shows the range of ch accurately covered by the calibration fit under these two bounds.

2.2.3 Problems with Red LEDs and Methylene Blue Dye

In this section the problems of using a single background colour for dye attenuation is discussed. For flows which dilute significantly a large range of calibrated dye concentrations are needed for accurate dye attenuation measurements. Thermals are an example of a flow which dilute sufficiently that dye attenuation is rendered inaccurate when using a single background colour. As the thermal develops and entrains ambient fluid, the dye concentration was diluted by a factor between 2 and 10 depending on the length of the tube and the distance the thermal falls. For the thermals produced in this study there are two factors that combine regarding the dye concentration that can make measurements inaccurate; the high entrainment rates associated with thermals, and the distance the thermal falls.

Examples of these two scenarios are shown in figures 2.5 and 2.7. The first of these scenarios occurs when the initial concentration of dye is too small to give accurate measurements of the thermals at later times. An example of such an experiment is given in figure 2.5. For

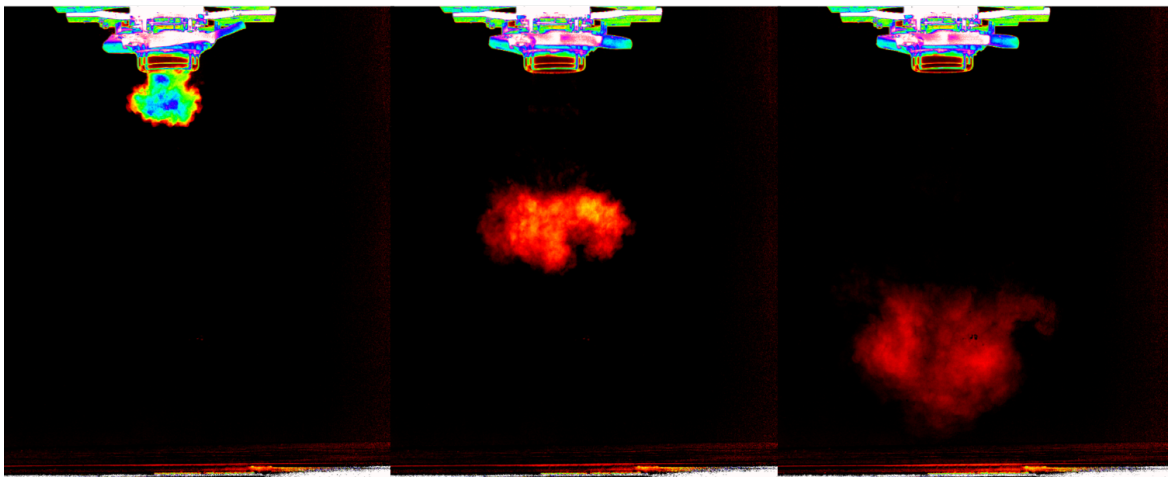

Fig. 2.5 Example snapshots of the concentration field of an experiment using methylene blue and red LEDs. In this experiment the initial dye concentration is too low for the thermal to be completely resolved at the latter stages of its descent.

this experiment the initial concentration of dye is within the range found by the calibration in figure 2.4. Due to the large fall height the final dye concentration is so low that the resulting attenuation is comparable to the noise level of the camera. This effect is illustrated further by measurements of the total mass from a set of experiments where this occurs. Figure 2.6 shows the total mass found by taking an average of 7 experiments all of which have a tube of length $L/D = 1$, at a height $H/D = 8$ and have an initial dye concentrations $c = 0.002\,\mathrm{g\,l^{-1}}$. The measured mass M_{tot} is then compared to the value of $c_0 V_0$ which gives the actual initial mass. The figure shows two problems: firstly there is a decrease in the measured mass caused by the dye becoming too dilute to be reliably picked up by the camera (note the gradient for $\hat{t} > 5$). Secondly the value of the measured mass is less than half the actual initial mass: this could be caused by a number of factors and was observed by Hart [30]. Hart found that it is most likely caused by the large error in c_0 that comes from measuring such small amounts of dye, in our case from 1 to 2 ml at a time. However, in this case that would mean an error of 58% in the dye measurement which is improbable, so more likely comes from a large portion of the dye being not visible to the camera.

The second scenario arises when the initial concentration of dye is too large for accurate dye attenuation measurements. An example of such an experiment is given in figure 2.7. For this experiment the initial concentration $c = 0.004\,\mathrm{g\,l^{-1}}$ of dye is twice that of the experiment shown in figure 2.5. There is a maximum concentration of dye above which the image is saturated and the intensity cannot be reliably measured by the camera. The white areas of the experimental images in figure 2.7 show where dye is above this maximum concentration and the image is saturated.

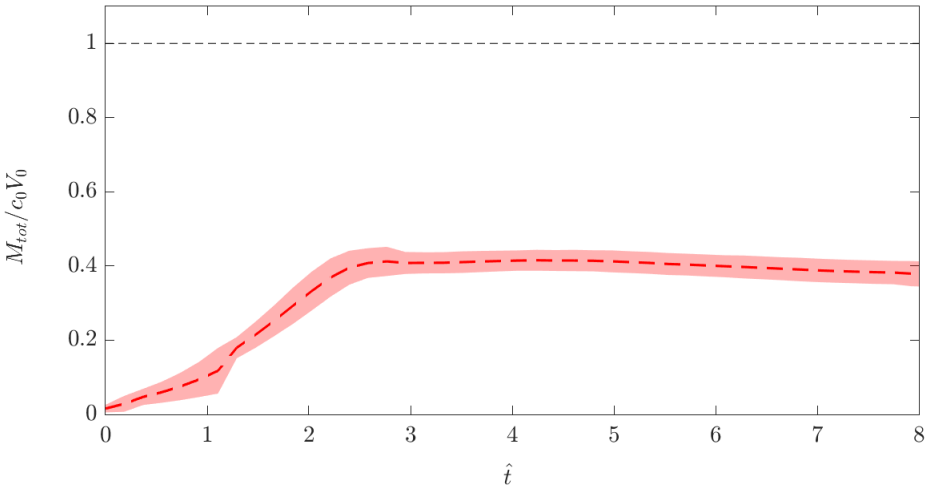

Fig. 2.6 The average total mass from 7 experiments where $L/D = 1$ compared to the actual mass. The shaded region is plus and minus one standard deviation around the average shown by the dashed line. The horizontal dotted line is at one, i.e. where the predicted value of $M_{tot} = c_0V_0$, the actual mass in the experiment.

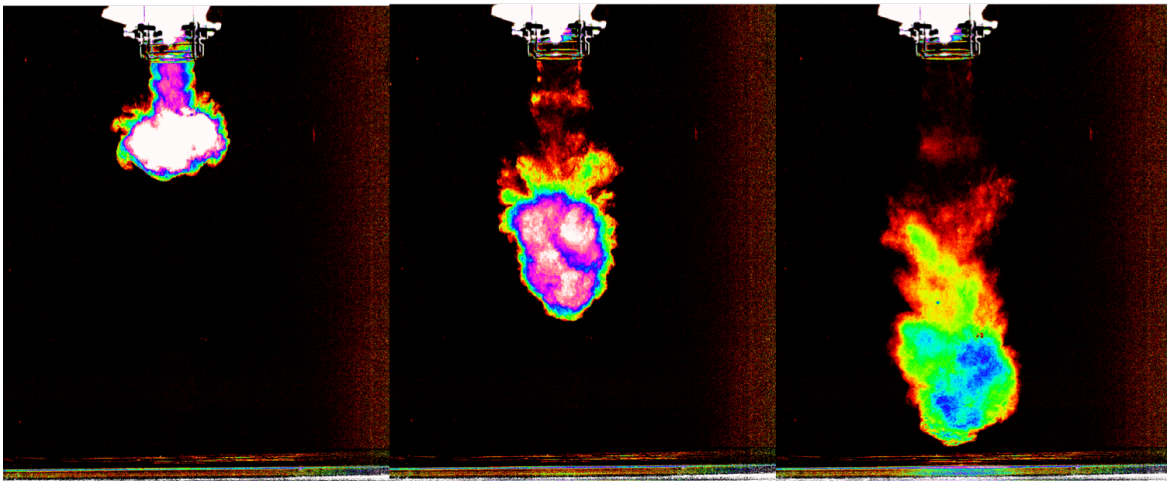

Fig. 2.7 Example snapshots the concentration field of an experiment using methylene blue and red LEDs. In contrast to figure 2.5 in this experiment there is too much dye initially resulting in saturation of the image and hence prohibiting the initial concentration to be accurately measured.

To gain reliable measurements for the whole flow, i.e. the descent and gravity current phases, we need the camera to be able to reliably record lower and higher concentrations of dye. Consequentially, an increase in the range of dye concentrations that can be measured by the camera is needed.

2.2.4 Extending the Range of Dye Concentration

Cenedese & Dalziel [15] showed that the attenuation of a dye depends on the wavelength of light passing through it. For methylene blue it is possible to use the wavelength dependence to increase the range of dye that can be measured by the camera accurately. The absorption spectrum of methylene blue in figure 2.3 shows the amount of light absorbed by methylene blue depending on wavelength. The absorption spectrum has a peak near red, meaning that methylene blue will absorb the most light from a red light source. So, if for a given dye concentration no dye is visible to the camera using red lights then there is no other wavelength of light that can be used so that the dye can be visible to the camera. It is, therefore, not possible to make the range of dye concentration larger by including smaller dye concentrations. Hence we need to be able to measure the dye concentrations that are above the maximum concentration accurately measured by the camera using red LED's.

In order to measure the larger concentrations of dye, we required the dye to absorb less light. This was achieved by using wavelengths of light with a lower absorption e.g. green or blue. Figure 2.3 shows the absorption spectrum of methylene blue with the bands of wavelengths of the red, green and blue LEDs available to us. There is a large reduction in absorption between red and green LEDs and a further reduction for the blue LEDs. Using either the green or the blue LEDs can therefore increase the maximum range of dye concentration possible to measure accurately. We chose to use three colours of LED: red, green and blue. Blue LEDs were chosen since they give the largest increase in measurable dye concentration. However, they will be ineffective at the lower dye concentrations covered by the red LEDs. The green LEDs were chosen as they will be used ensure that dye concentrations can be accurately measured by at least two colours, either the red/green or green/blue, over most of the dye concentrations applicable.

The same calibration method that was described in section 2.2.2, was performed using the green and blue LEDs. Figure 2.8 shows the three calibration curves for the red, green and blue LEDs. As with the previous calibration the lower limit was chosen to be the value of $I/I_0 = 0.16$ where the calibration curve no longer had a large gradient meaning that large changes in ch would only make small changes to I/I_0. For the upper bound on I/I_0, it is important that $I/I_0 \neq 1$, i.e. the camera is not saturated, so the value of $I/I_0 = 0.99$ was chosen. The shaded red area shows the range of ch accurately covered by

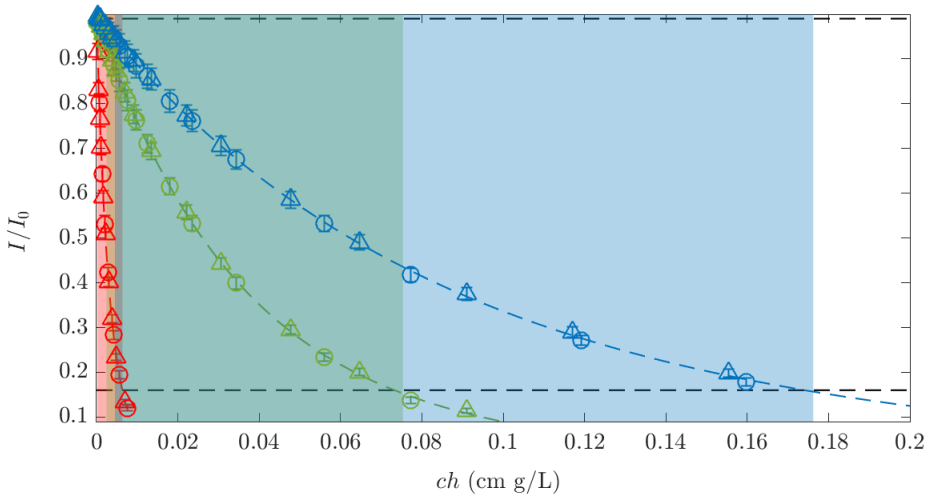

Fig. 2.8 Calibration of methylene blue with red, green and blue LEDs performed in two tanks with $h = 10\,\mathrm{cm}$ (circles) and $h = 15\,\mathrm{cm}$ (triangles). The coloured dashed lines represent the theoretical fits that will be used to apply the calibrations to the experimental images. The black dashed lines show the minimum and maximum intensity to achieve an intensity not contaminated by high levels of dye or the noise of the camera. The coloured shaded regions represents the range of ch that our calibration can accurately cover for each colour of LED.

the calibration fit under these two bounds. Using red LEDs only, figure 2.4 showed that the range of dye concentration covered was $0.001\,\mathrm{cm\,g\,l^{-1}} < ch < 0.006\,\mathrm{cm\,g\,l^{-1}}$. By adding the green and blue LEDs this novel technique increased the range of dye concentration to $0.001\,\mathrm{cm\,g\,l^{-1}} < ch < 0.16\,\mathrm{cm\,g\,l^{-1}}$.

Using the tricolour LEDs a typical experiment is performed with an initial dye concentration of $c = 0.01\,\mathrm{g\,l^{-1}}$, well beyond the range of dye concentration that single colour red LEDs are capable of measuring. An example of an experiment at three different times (rows), using the three colours of LEDs (columns) is shown in figure 2.9. The first column (red LEDs) is similar to the experiment shown in figure 2.7, with areas within the core of the thermal containing too much dye to be accurately measured by the red LEDs. The second (green LEDs) and third columns (blue LEDs) are similar to the experiment shown in figure 2.5, with areas of dye too weak to be accurately measured. However, the areas of the flow, which are not accurately measured by one colour LED, can now be accurately measured by at least one of the other colour LEDs.

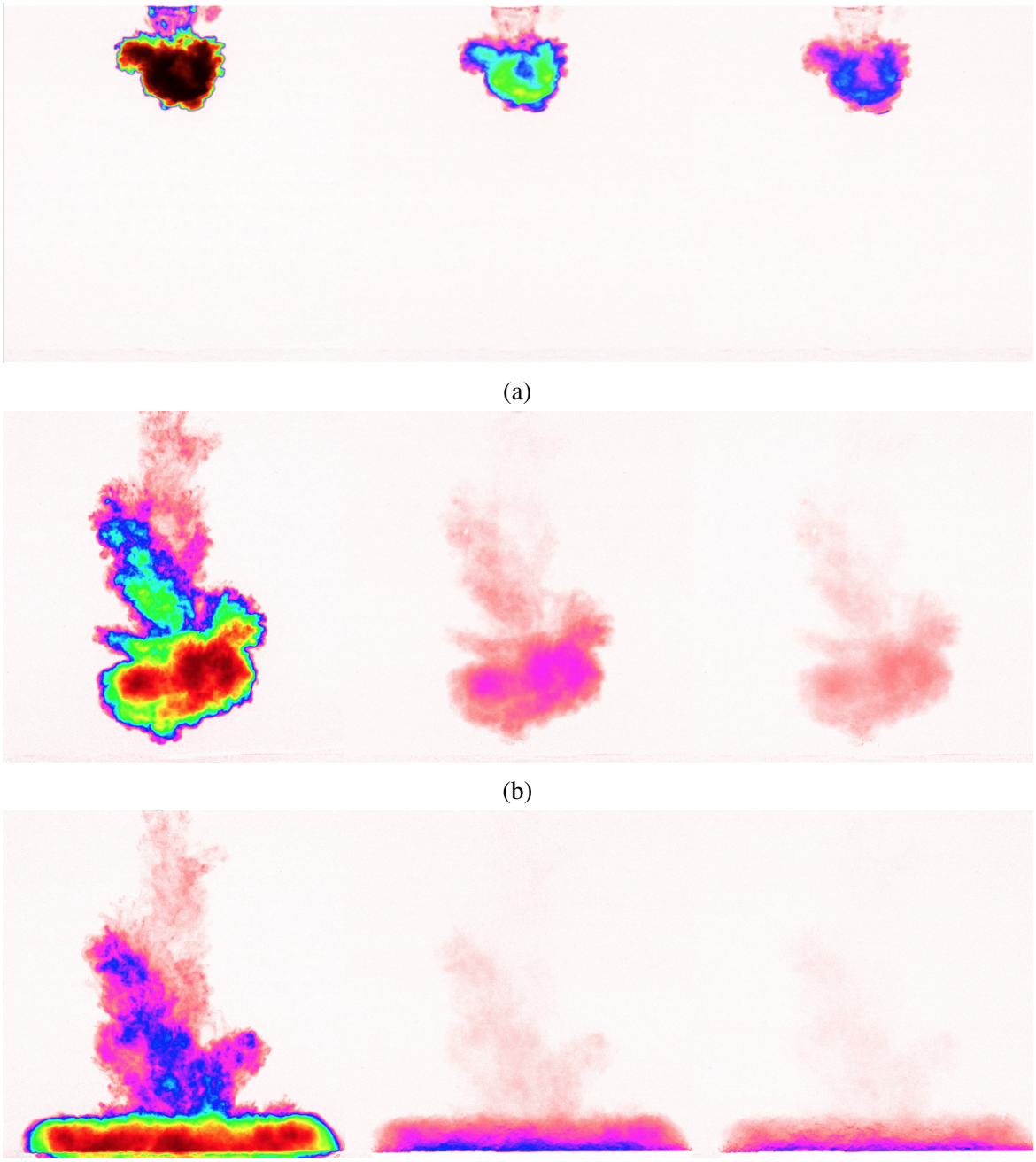

(a)

(b)

(c)

Fig. 2.9 Example raw images of one experiment with the three colour LEDs. Columns represent one colour, from left to right red, green and blue respectively, and rows show the three colours at different times.

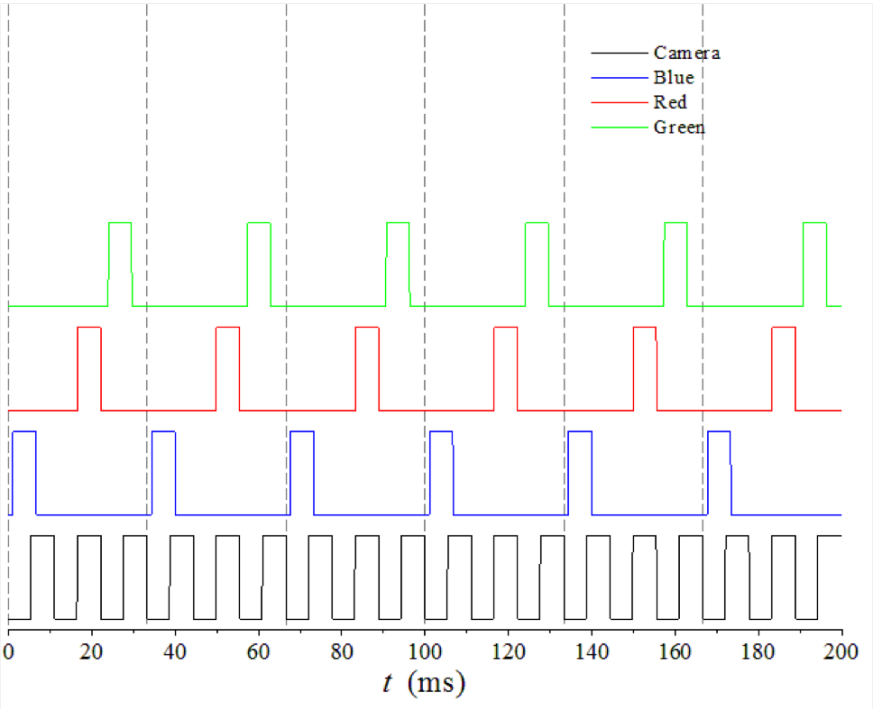

Fig. 2.10 The timing signals sent to the LEDs and the camera.

Tricolour Dye Attenuation Set-Up

To perform the dye attenuation experiments using the three colours of LED the set up is the same as described in section 2.1.1. As described in the previous section the three colours of the light bank were chosen to take advantage of the different absorbance spectrum of methylene blue dye.

The LEDs were pulsed rapidly (30 Hz for each colour), alternating between the colours sequentially, i.e. the colours were out of phase as shown figure 2.10. For a given pulse width of the LEDs, the light intensity measured by the camera varied between the colours (due to the efficiency of the LEDs themselves and the fact that the camera has a different response depending on the wavelength of the light it receives). To mitigate this, the pulse width of each of the LEDs was varied so that, in a tank of fresh water, the background intensity was constant between the different coloured LEDs and close to saturating the camera. Also shown on figure 2.10 is the signal that was sent to the camera to keep it phase locked to the pulsing of the LEDs. Given the three colours, all pulsing at 30 Hz out of phase, the frame rate required by the camera was 90 Hz.

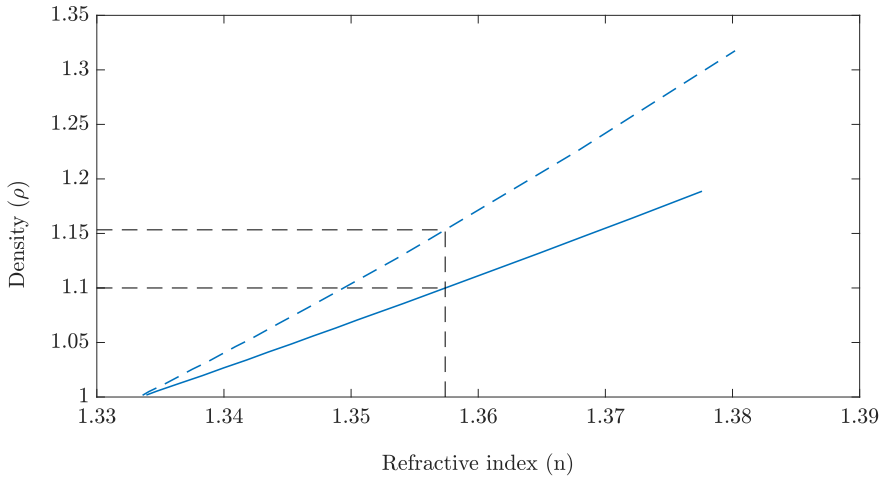

Fig. 2.11 Refractive index n vs density ρ for NaCl (solid line) and $NaNO_3$ (dashed line). Black dashed lines represent the densities of the two solutions where the refractive index is the same for approximately a 5% density difference. Data from Rumble [52].

Matching Refractive Indices

The refractive index (n) of a fluid is the dimensionless quantity that describes how fast light travels through the fluid. The refractive index also determines how much the path of the light is bent. When sodium chloride (NaCl) is added to water, it changes the refractive index of the solution. Therefore if the ambient fluid has a different refractive index to that of the falling thermal, the light travelling through the dyed portion of the thermal will have an altered path. When using dye attenuation this can change the length of the path taken by the light. This effect was found to reduce the accuracy of the dye attenuation measurements. Thus, it is necessary to find a method of minimizing refractive index variations.

To mitigate the effects of differences in refractive index we rely on the refractive index of a solution of sodium nitrate ($NaNO_3$) to have a different scaling with concentration than a solution of sodium chloride (NaCl). This salt-solution methodology is similar to that employed by Olsthoorn [45] for studying vortex rings in a stratified fluid. Figure 2.11 plots the density of both salt solutions versus its refractive index (n). In order for the refractive index of both salt solutions to match, the salt concentrations, and hence the densities, will be different. We exploit this and generate thermals using a source fluid ($NaNO_3$) with refractive index equal to the ambient fluid (NaCl). In principle, the refractive index will depend not only on its respective salt concentration, but on the temperature of the fluid and the wavelength of the incident light. In practice, for a near uniform temperature profile within the tank, and narrow banded wavelength light source, these additional dependencies are negligible in the experiments presented here [45].

It should be noted that it is unclear to what extent the refractive index is linear with mixing of solutes. That is, a mixture of NaCl and $NaNO_3$ solutions which have equivalent refractive indices may not be matched to the refractive index of the two separate solutions. However, by limiting ourselves to low density differences between the salt solutions for practical purposes, this was not an issue for our experiments [45].

Olsthoorn [45] commented on the effect of the cross-diffusivities of the two different salt solutions. They concluded that over the time of their experiments (6 hours) double diffusive effects will not affect their experiments. This was due to the time scale of the experiments being significantly smaller than the diffusion time scale. Since the experiments presented here are significantly shorter than those performed by Olsthoorn [45] (from 4 s to 17 s) double diffusion should also not play a role here.

For other experiments, another approach has been used to match the refractive indices: Alahyri & Longmire [2] used glycerol as the solute. However, glycerol spills are challenging to clean up, and also have a significant viscosity difference to sodium chloride. We therefore chose to use sodium nitrate as it is easily disposed of, has minimal safety concern and is cost effective.

The tank was filled with sodium chloride of density $\rho_0 \approx 1.10\,\mathrm{g/cm^3}$ and well mixed. To ensure the tank was well mixed, measurements of density were taken from the bottom of the tank and the surface of the water, this process was continued until the two density measurements were within $0.001\,\mathrm{g/cm^3}$ of one another. The required density of sodium nitrate was then calculated by first calculating the value of the refractive index for the measured density of the ambient fluid from a cubic fit of the data for sodium chloride shown in figure 2.11. The value of the refractive index was then to calculate the corresponding density of sodium nitrate from a quartic fit of the sodium nitrate data also shown in figure 2.11.

The range of densities of sodium nitrate and sodium chloride used for the experiments are shown in figure 2.12 (circles). Also shown are the values of both densities required for both solutions to have the same refractive index (dashed line). From the figure we see that most of the pairs of densities agree well with the dashed line, with the largest difference between the actual and required value of ρ_0 being approximately 2% smaller than the required density. This resulted in an average difference between the refractive indices of 0.05% (shown in figure 2.13). For comparison the difference in refractive index for sodium chloride with a 5% density difference from water is approximately 1.15%, marked on figure 2.13 as a red circle.

Post-Processing

To process the images, the respective calibration for each colour LED is applied to each intensity image, I/I_0, in the sequence so there are three distinct sets of concentration images,

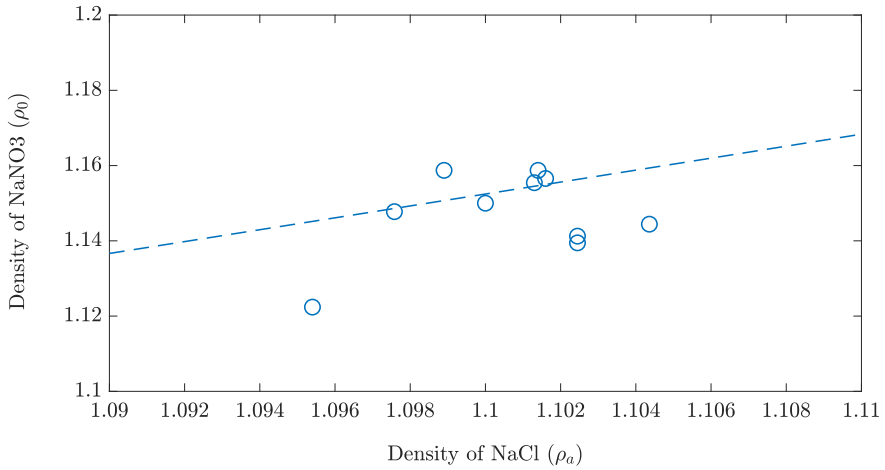

Fig. 2.12 The density of sodium nitrate and of sodium chloride used for the experiments (circles) compared to the values of the density of both solutions required to have the same refractive index (dashed line).

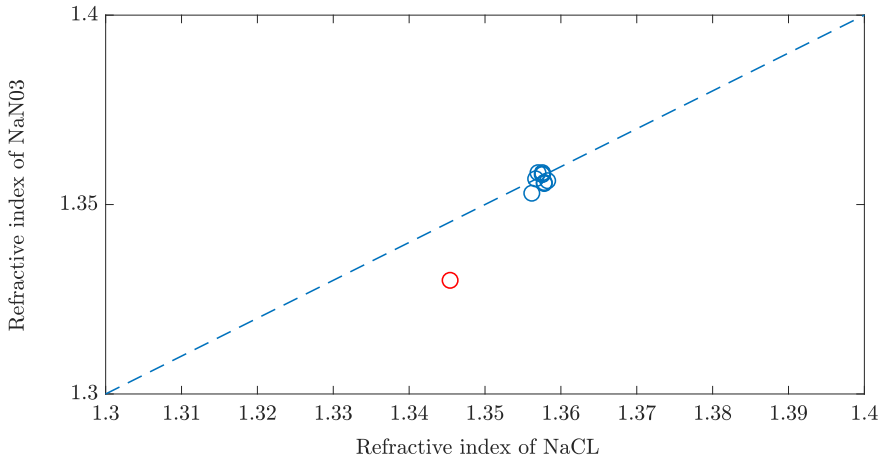

Fig. 2.13 The density of sodium nitrate and of sodium chloride used for the experiments (blue circles) compared to the values of the density of both solutions required to have the same refractive index (dashed line). Also plotted is the refractive index for sodium chloride with a 5% density difference from water against the refractive index of water (red circle).

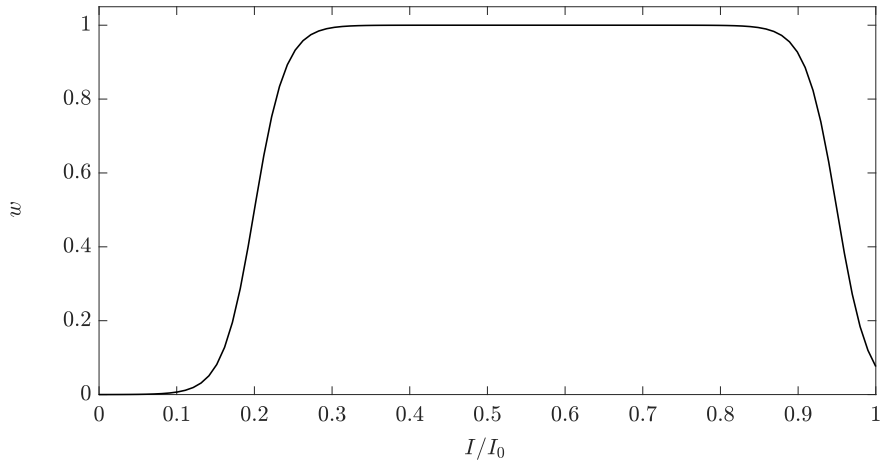

Fig. 2.14 The weighting function applied to I/I_0 used both to: remove the range of values of I/I_0 which were contaminated with high levels of dye (relative to the colour of illumination) or where the noise level of the calibration is relatively high, and for the weighted averaging process.

ch (one for each colour). The three distinct set of concentration images are then combined using a weighted average at each time step. Before this average can be taken, each colour series of images are multiplied by a weighting function, $w(I/I_0)$. Figure 2.14 shows the form of the chosen weighting function, a sigmoid function. The function was chosen as we require the function to do two things: firstly, to have a value of one for the range of intensities best covered by each colours calibration and zero elsewhere. This ensures that the weighted images were not contaminated by areas of the image that contained high levels of dye (relative to the colour of illumination), $I/I_0 > 0.99$, or where the noise level of the calibration is relatively high (i.e. to the far right of figure 2.8, $I/I_0 < 0.16$). Secondly, we require the function to be continuous to ensure a smooth transition between the colours.

An example of the weighting function applied to the experimental images shown in figure 2.9, are shown in figure 2.15. The weighted concentration images from the three colours are then combined to form one concentration image by

$$ch = \frac{w(I_r/I_{0,r})ch_r + w(I_g/I_{0,g})ch_g + w(I_b/I_{0,b})ch_b}{w(I_r/I_{0,r}) + w(I_g/I_{0,g}) + w(I_b/I_{0,b})}.$$

To detect the centre of mass of the combined images, the total mass can be found by integrating the following over the entire image

$$M_{tot} = \int_0^{\Delta z} \int_0^{\Delta x} \frac{\rho_0}{c_0} ch \, \mathrm{d}x \, \mathrm{d}z$$

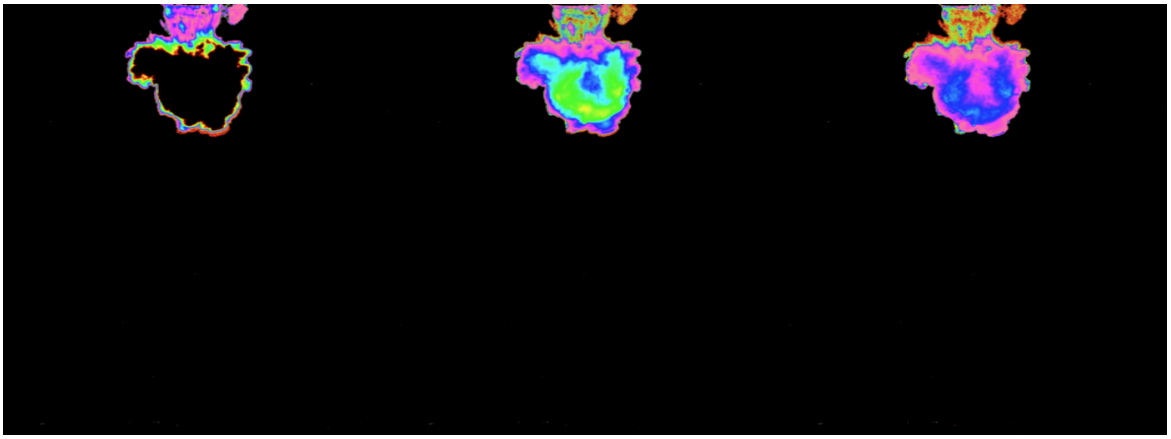

(a)

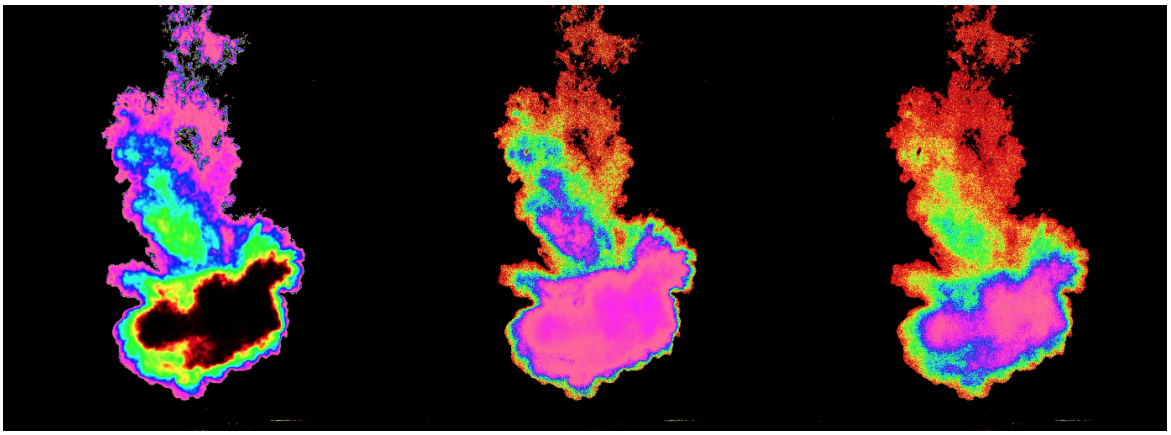

(b)

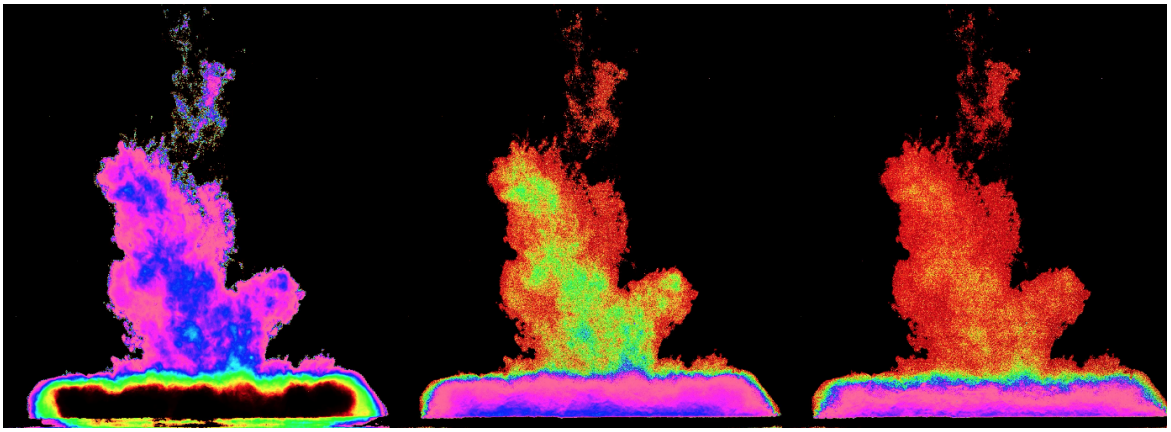

(c)

Fig. 2.15 The raw images with the weighting function applied. The black areas are where $w(I/I_0)I/I_0 = 0$.

where Δx and Δz are the sizes of the image in the $x-$ and $z-$ directions respectively, ρ_0 is the initial density of the dyed fluid, c_0 the initial concentration of dye and ch is the processed image, which is the weighted combination of the three colours with the calibrations applied. Then the vertical position of the centre of mass is given by

$$z_c = \int_0^{\Delta z} z \int_0^{\Delta x} \frac{\rho_0}{c_0} ch \, \mathrm{d}x \, \mathrm{d}z \Big/ M_{tot}.$$

The value of M_{tot} found from the average of 5 experiments performed with $L/D = 5$ at $H/D = 8$ and processed using the tricolour technique is shown in figure 2.16 and compared to the actual value of $c_0 V_0$. The dashed line shows the average of the 5 experiments, and the shaded region is plus/minus one standard deviation from the average. Unlike the total mass shown in figure 2.6 the average is now constant once the tube has finished draining for these experiments ($\hat{t} > 4$). However, as with the previous experiment there is still a difference in the measured and actual value of the mass. Hart [30] found that this difference is most likely caused by the large error in c_0 that comes from measuring such small amounts of dye, in our case from 1 to 2 ml at a time. In this case that would mean an error of 18% in the dye measurement i.e. 0.18 - 0.36 ml which is more conceivable than the 58% error seen in when using only red LEDs. However in our case it is also possible that the weighted averaging process may introduce a negative bias to the calculation of the total mass. An alternate method to combine the images has been performed, details of which can be found in appendix B, to ensure that the choice of method has no significant impact on the centre of mass measurement.

2.3 Edge Detection

From the dye attenuation images the centre of mass of a thermal can be measured, however more information about the dynamics of both the thermal and the gravity current can be obtained by detecting and tracking the edges of the dyed fluid. The edges are found by first extracting the images illuminated by the red LEDs only. The background image illuminated by the red LEDs is then subtracted, making the fluid dark and the background light. The edges of these images were then found by using the 'Canny' algorithm [14] with a sensitivity threshold to be chosen for each experiment. The threshold was chosen so that the algorithm detected only the largest structures and ignored any noise remaining in the images. The algorithm disregards all edges with strength below the lower limit, and preserves all edges with strength above the higher limit, in practice this was always approximately $[0.02, 0.1]$ where in the images 0 is white and 1 is black. The algorithm returned a matrix of the same

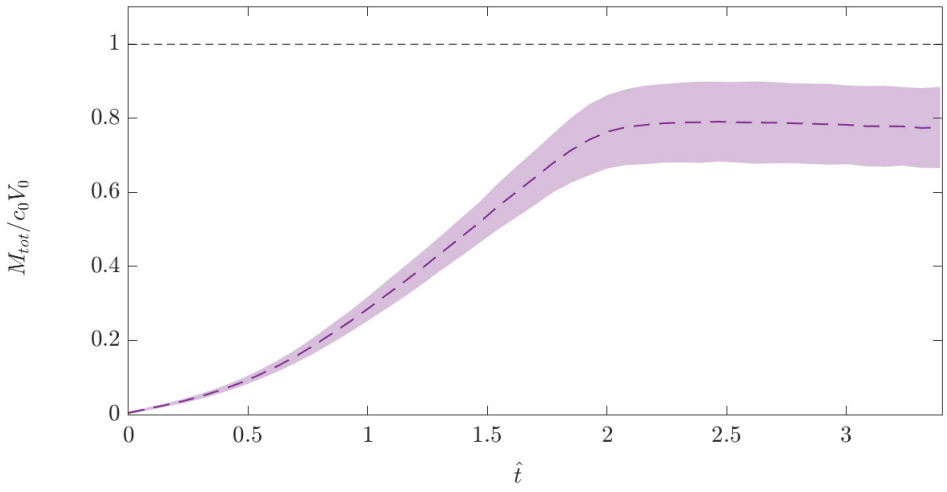

Fig. 2.16 The total mass of an experiment with $L/D = 5$ using the tri-colour LED technique.

size as the original image with 1 where there was an edge and 0 elsewhere. This binary matrix was then used to track the left most, right most and lowest edge of the dyed fluid. To track the left and right edges the binary matrices were first split in half vertically at the source center. The maximum value of each half was then taken in the vertical direction and the positions of first/last 1 i.e. the left/right most edges were found. Similarly, to find the lowest edge, the maximum of the edge image was taken in the horizontal direction and the position of the last 1 was found.

After the edges had been detected and the left/right most and lowest positions had been found these edges and positions were overlaid on to the original experimental image. As an example, an experimental image with the edges overlaid and positions marked is shown in figure 2.17. This was done for all the images in each experiment in order to check that the edges were detected and tracked correctly. The variation between the vertical position and radius when repeating experiments with notionally identical source conditions will be discussed in the following section.

2.4 Variation Between Experiments

During the descent of a thermal and spread of a gravity current turbulent structures form. The formation of these structures is not consistent between experiments and structures can be large enough to affect the measurements of both the radius of the thermal and the gravity current, the height of the gravity current, and the lowest vertical position of the thermal.

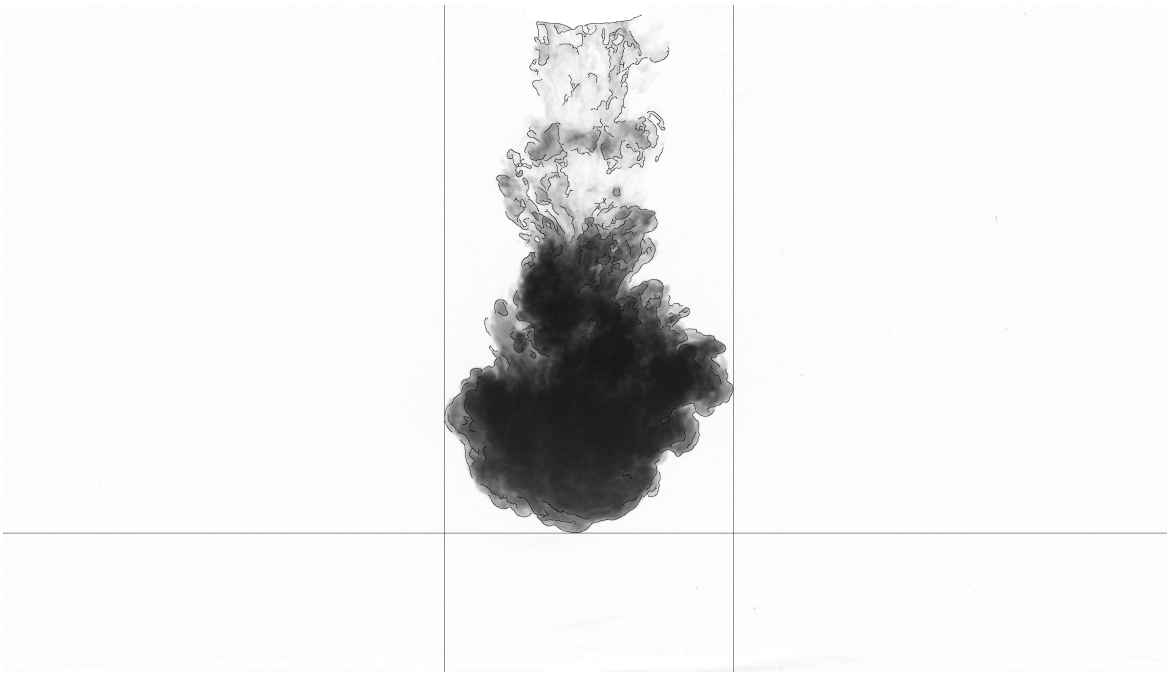

Fig. 2.17 An example experimental image with the edges and tracking of the edges overlayed.

Therefore, to obtain meaningful statistics of these quantities multiple repeats of experiments with the same L/D and H/D were performed.

To determine that the number of repeated notionally-identical experiments was sufficient, we first conducted a number of repeats. From these full sets of repeats ensemble averages were created using different subsets of the full repeats. It was observed that the measurements of the edge positions with $L/D = 1$, $H/D = 8$ were the most sensitive to these structures, and experiments with $L/D = 5$ at $H/D = 8$ the least sensitive.

For experiments with $L/D = 1$, 9 repeats were performed in total. The average and standard deviation of the 9 experiments has been found for both the lowest vertical position of a thermal and the radius of the thermal and gravity current. The shaded regions of figures 2.18 and 2.19 show $\pm$ one standard deviation (light) and half a standard deviation (dark) around the average of 9 experiments. For the lowest vertical position the maximum standard deviation is 4.05 cm, and the average standard deviation 1.78 cm. For the radius the maximum standard deviation is 13.79 cm, and the average standard deviation 2.04 cm. The average standard deviation is 4.5% of the fall height, and 8.2% of the maximum radius, when considering a set of 9 experiments.

Three random subsets of 5 and 7 experiments have been averaged and compared to the statistics from 9 experiments. Figure 2.18 shows the average lowest vertical position and radius from three subsets (marked by circles, squares, triangles) of 5 experiments. The three

subsets of 5 experiments lay within plus or minus one standard deviation from the average of 9 experiments of both the lowest vertical position and radius. However, there is a large variation between the three subsets, irrespective of how the subsets were chosen, especially at late time in the vertical position of the lowest edge of the thermal. This variation implies that the results will differ depending on the subset of experiments chosen.

For any subset of 7 experiments there was little variation between the subsets in behaviour of the average lowest vertical position and radius. Furthermore, none of the subsets of 7 experiments significantly deviate from the average of 9 experiments, lying within $\pm$ half a standard deviation from the average of 9 experiments. For the lowest vertical position the maximum standard deviation is 4.00 cm, and the average 1.90 cm. For the radius the maximum standard deviation is 10.90 cm, and the average 1.85 cm. This means that the average standard deviation of 4.8% of the fall height, and 7.4% of the maximum radius when considering a set of 7 experiments.

The average edge positions of both the thermal and the gravity current taken from any subset of 7 experiments are consistent with the averages determined from the full set of 9 experiments. Moreover their standard deviations do not differ significantly. Therefore, we determine that 7 repeats of the $L/D = 1$ experiment were sufficient to gain meaningful statistics from tracking of the edge positions.

For experiments with $L/D = 5$, 5 repeats were performed in total. The average and standard deviation of the 5 experiments were found for both the lowest vertical position of the thermal and radius of the thermal and the gravity current. The shaded regions of figure 2.20 show $\pm$ one standard deviation (light) and half a standard deviation (dark) around the average of the 5 experiments. For the lowest vertical position the maximum standard deviation is 1.86 cm, and the average 1.00 cm. For the radius the maximum standard deviation is 1.63 cm, and the average 0.87 cm. This means that the average standard deviation is 2.5% of the fall height, and 3.5% of the maximum radius when considering a set of 5 experiments.

Three random subsets of 3 experiments have been averaged and compared to the statistics from all 5 experiments. Figure 2.20 shows the average lowest vertical positions and the radius from three subsets of 3 experiments (circles, squares, triangles). The three subsets of 3 experiments lay within plus or minus one standard deviation from the average of 5 experiments for the lowest vertical position and radius. However, there is significant variation between the three subsets, especially at late time of the radius. For the lowest position the maximum standard deviation of the subset of 3 experiments is 1.97 cm, and the average 0.99 cm. For the radius the maximum standard deviation of the subset of 3 experiments is 1.61 cm, and the average 0.75 cm. Then the average standard deviation is 2.5% of the fall height, and 3% of the maximum radius when considering a subset of 3 experiments.

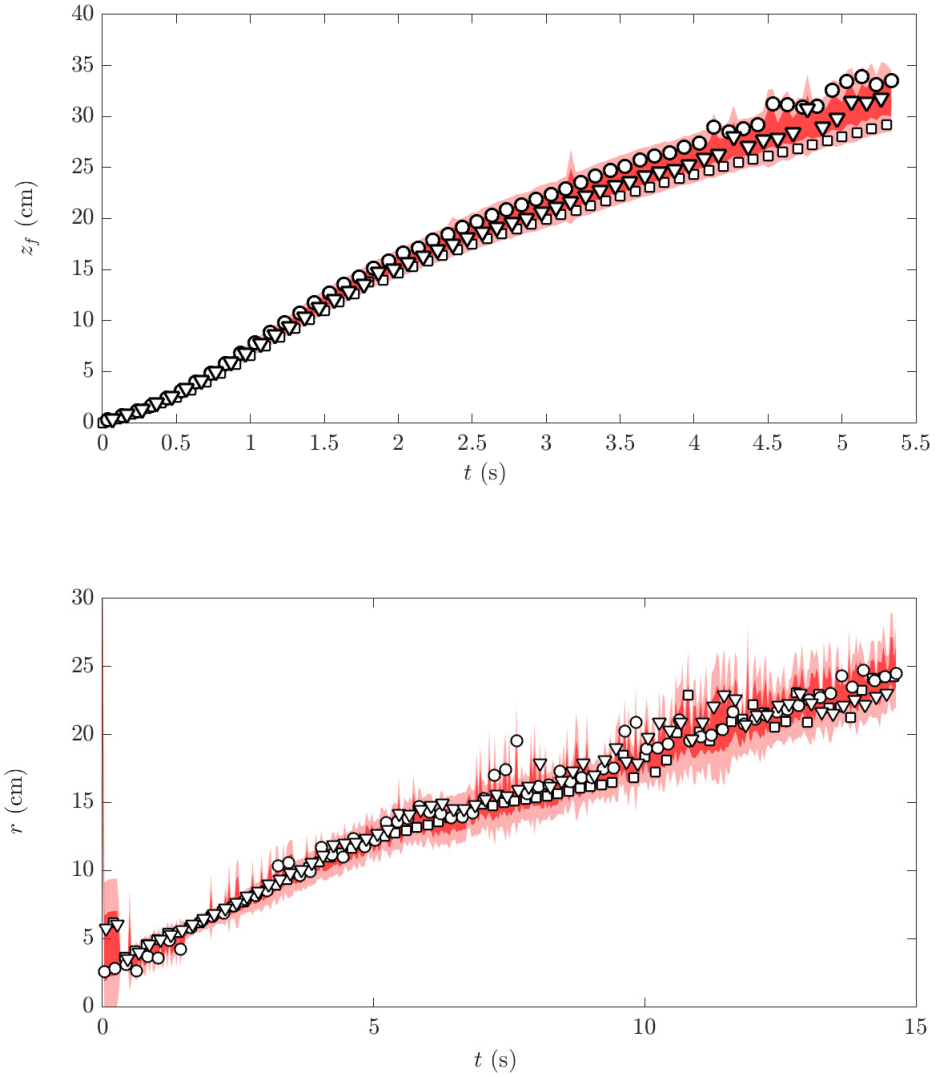

Fig. 2.18 The average of 9 experiments $\pm 0.5/1$ standard deviation denoted by the shaded region. Overlaid are averages from 3 subsets (marked by different symbols) of 5 of the 9 experiments.

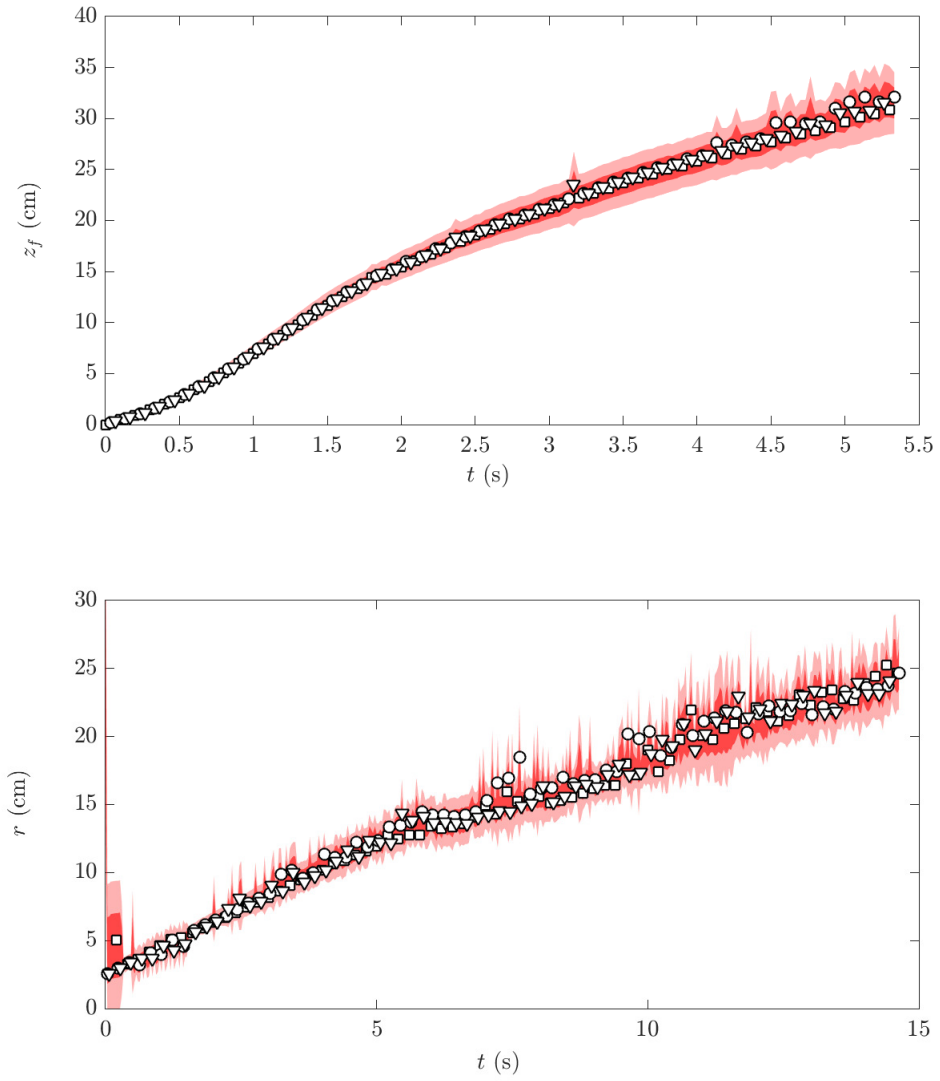

Fig. 2.19 The average of 9 experiments $\pm 0.5/1$ standard deviation denoted by the shaded region. Overlaid are averages from 3 subsets (marked by different symbols) of 7 of the 9 experiments.

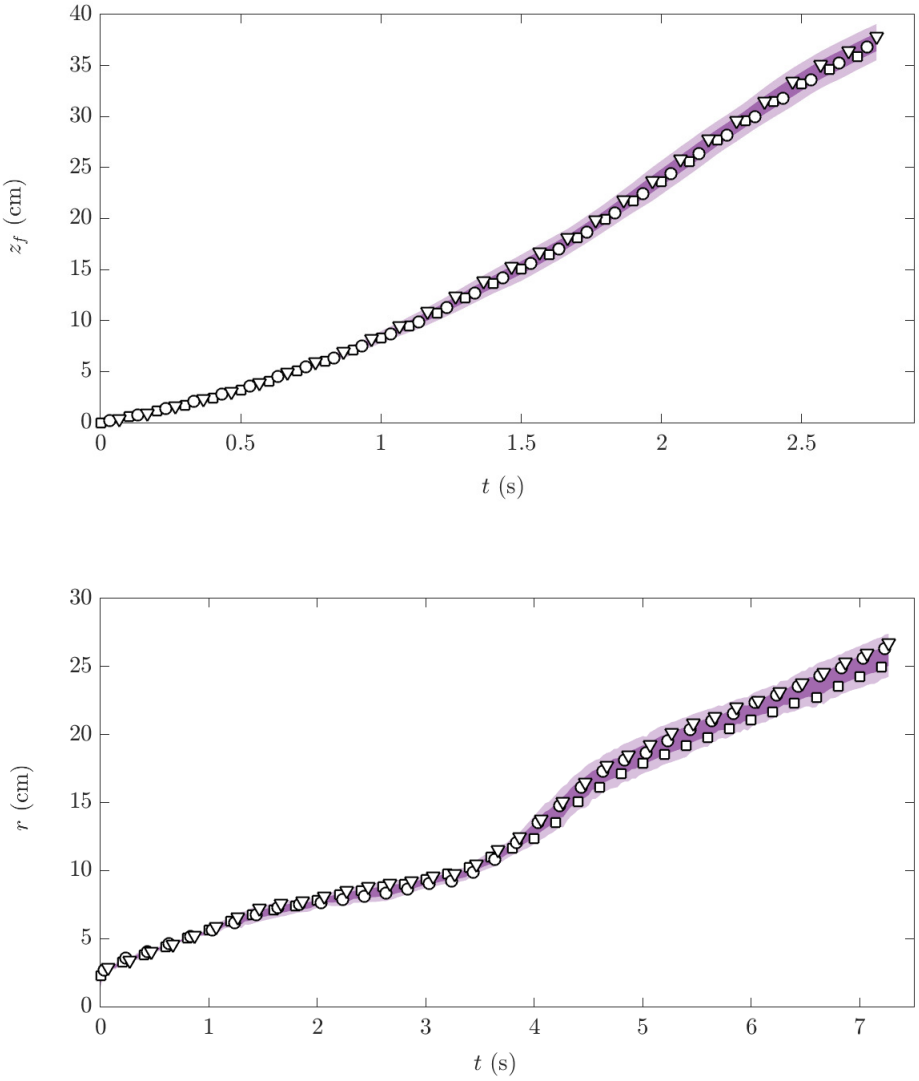

Fig. 2.20 The average of 5 experiments $\pm 0.5/1$ standard deviation denoted by the shaded region. Overlaid are averages from 3 subsets (marked by different symbols) of 3 the 5 experiments.

The standard deviations of the subsets of 3 experiments do not differ significantly from the standard deviations for 5 experiments. However, the average positions from the subsets of 3 experiments are not consistent, so the choice of subset will change the result. Therefore, for $L/D = 5$, 5 repeats will be sufficient. All the data from the experiments in the following chapters will be averages of 7 experiments for $L/D = 1,\ 2,\ 3$, and 5 experiments for $L/D = 4,\ 5$.

2.5 Conclusions

This chapter has described the challenges that occur when using dye attenuation with thermals, and the experimental set up and the measurement techniques used in this study have been proposed. We have developed a set-up and procedure that can robustly, and consistently initiate and measure both the thermal and gravity current phases of the flow. The nature of the edge statistics for the turbulent flow generated was such that a number of notionally identical experiments needed to be averaged in order to obtain reliable and repeatable statistics. The number of repeats needed was found to be 7 for $L/D = 1$, 2 and 3, and 5 repeats for $L/D = 4$ and 5. These numbers ensured that for any subset of 5/7 experiments chosen the average did not vary from the complete set of 9 experiments, and the standard deviation was also comparable to that of the full set. Two measurements techniques are used to analyse the experiments: edge detection and dye attenuation. Dye attenuation was used to measure the vertical position of the centre of mass of the thermal, and edge detection to measure the vertical position of the lowest edge of the thermal, and the radius during the descent of the thermal and the spread of the gravity current. Presented in this chapter is a novel extension to the dye attenuation technique proposed by Cenedese & Dalziel [15]. The use of three colours of LEDs enables us to measure a larger range of dye concentration than with a single colour. This was necessary due to the high dilution rates exhibited by thermals. The results from these experiments will be presented in the next two chapters.

Chapter 3

Thermals

3.1 Introduction

As discussed in chapter 1, existing laboratory studies of thermals have initiated the flow in a range of different ways. However, the resulting thermals eventually show good agreement with the similarity solutions presented by Scorer [53] when scaled using the scalings determined by Lundgren et al. [41]. Before this similarity phase is reached, measurements of the vertical positions and the radius have been shown to display an initial adjustment period, known as the acceleration phase. When using a draining tube to initiate a thermal, as we do in this study, it was found by Bond & Johari [8] and Lai et al. [37] that this phase could last between one and two times the time it takes for the tube to drain, T_d. In this chapter we are concerned with the descent of the thermal until it impacts the ground. Two release heights were chosen so that the thermals would exhibit different behaviours at impact. First we present the equations for a self-similar thermal and their derivation. As described in chapter 2, three quantities are measured directly from the experimental images: two vertical positions, and the radius. The two vertical positions are the lowest edge of the thermal, or the 'front', z_f, and the centre of mass, z_c. The horizontal radius, r, is also measured directly and the vertical radius, $h = z_f - z_c$, is calculated using the two vertical positions. As an illustration, these quantities are superimposed on an experimental image in figure 3.1. Models are then presented for the initial acceleration phase, which are compared to the measurements from laboratory experiments. Finally, using the models and the experimental data we consider the validity of the assumptions made in the derivation of the thermal equations.

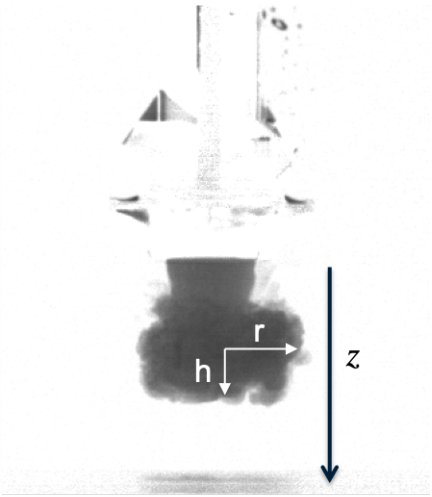

Fig. 3.1 Example experimental image of a descending thermal, with the direction of z and the positions of h and r labelled on the diagram. In this case $L/D = 4$ and $H/D = 2$.

3.1.1 Self-Similar Thermals

For the results presented in this chapter the thermals were created using the experiment methodology described in chapter 2, and an example image is shown in figure 3.1. As described in chapter 2 the experiments were performed by releasing a cylindrical volume of dense fluid into a quiescent environment of uniform density. The vertical extents, L, of these finite volumes was systematically varied so that the ratio L/D varied between 1 and 5 where D was the diameter of the cylinder. The thermals were released from two heights, H, above the ground, $H/D = 2,\ 8$. These two heights were chosen as the lower of the two, $H/D = 2$, is applicable to the geometries observed in atmospheric downdrafts, and $H/D = 8$ was chosen in order to gain measurements of the shape and dynamics of the transition from the initial acceleration phase to the self-similar phase of a thermal.

Following Lundgren et al. [41] we define length and time scales of a thermal based on R_0, the equivalent spherical radius of the initial volume of fluid in the thermal, and timescale $(R_0/g_0')^{1/2}$, where $g_0' = (\rho_0 - \rho_a)g/\rho_a$ is the value of reduced gravity at the source and ρ_0 the density of the dyed fluid in the cylinder and ρ_a the density of the ambient fluid. These length and time scales are

$$R_0 = V_0^{1/3}, \tag{3.1a}$$

$$T_0 = R_0^{1/2}(g_0')^{-1/2} = V_0^{1/6}(g_0')^{-1/2}, \tag{3.1b}$$

where $V_0 = \frac{\pi}{4}D^2L$ is the initial release volume. As discussed in chapter 1, Lundgren et al. [41] found that their experimental results compared well to data from observations of downdraughts when using these scalings. However, their experiments were somewhat

limited as they did not significantly change the aspect ratio of the source or the height above the ground, keeping $L/D \approx 1$ and $H/D \approx 2$.

In the similarity phase of the descent, when the initial conditions of a finite dense release are no longer relevant, Scorer [53] showed that the radius of a thermal spreads linearly with distance from the source, and the vertical position, z, of the thermal descends as a function of time according to

$$z \sim B^{1/4} t^{1/2}. \tag{3.2}$$

To obtain the full similarity solution Scorer [53] made the assumption, which has been widely adopted since, that the shape of an isolated thermal may be represented by an oblate spheroid. Under said assumption, the horizontal radius r (equivalent to the semi-major axis of its cross-section) and vertical extent h (equivalent to the semi-minor axis of its cross-section) determine its volume and surface area. The volume is then

$$V = \frac{4\pi}{3} h r^2,$$

and assuming the shape remains self-similar, $h = br$ for constant aspect ratio, b, then

$$V = \frac{4\pi b}{3} r^3 = m r^3,$$

where m is a constant called the 'thermal shape factor' which is unknown and to be determined by experiments. Differentiating both sides with respect to time gives the rate of increase in volume as

$$\frac{\mathrm{d}V}{\mathrm{d}t} = 3 m r^2 \frac{\mathrm{d}r}{\mathrm{d}t}. \tag{3.3}$$

As discussed in chapter 1, Morton et al. [43] determined the classical entrainment closure was appropriate for plumes. Namely that the entrainment velocity u_e of ambient fluid induced by a buoyant fluid was proportional to the vertical velocity, w. Thus the entrainment velocity can be written as $u_e = \alpha w$ where α is the entrainment coefficient. For a thermal, an equivalent assumption is that the total entrainment of ambient fluid into the thermal is proportional to its surface area, $A_s = a r^2$, multiplied by its vertical velocity $w = \frac{\mathrm{d}z_c}{\mathrm{d}t}$, where z_c is the vertical position of the centre of mass. With this entrainment assumption we can write the rate of change of volume as

$$\frac{\mathrm{d}V}{\mathrm{d}t} = \alpha a r^2 \frac{\mathrm{d}z_c}{\mathrm{d}t}, \tag{3.4}$$

It should be noted that for a spheroid a may be obtained from the value of the aspect ratio b, see appendix C for details. Equating (3.3) and (3.4) gives

$$\frac{\mathrm{d}r}{\mathrm{d}t} = \frac{\alpha a}{3m}\frac{\mathrm{d}z_c}{\mathrm{d}t} = n\frac{\mathrm{d}z_c}{\mathrm{d}t}, \tag{3.5}$$

for spreading rate n. Scorer [53] found that for their thermals (produced in the laboratory) $m = 3$ and $n = 0.25$. For $m = 3$, $\frac{a}{3m} \approx 1.1$ giving $\alpha \approx 0.23$ so n provides a reasonable approximation for the entrainment coefficient α. However, this requires that the thermal is approximately spheroidal, and that the entrainment assumption is valid.

In the unstratified case considered in this study, the total buoyancy $B = g'V = g'_0 V_0$ of the thermal is conserved, i.e. $B = B_0$, and the conservation of momentum, $M = wV$, gives

$$\frac{\mathrm{d}\left(\frac{\mathrm{d}z_c}{\mathrm{d}t} mr^3\right)}{\mathrm{d}t} = \frac{2}{3}B_0,$$

where $w = \mathrm{d}z_c/\mathrm{d}t$, $V = mr^3$ and the factor of $2/3$ comes from the added mass of a spheroids presented by Chung & Chen [16]. Therefore, since B_0 is constant, integrating with respect to t gives

$$\frac{\mathrm{d}z_c}{\mathrm{d}t} = \frac{2B_0 t}{3mr^3}. \tag{3.6}$$

Then by substituting (3.6) into (3.5) we obtain r as a function of t. It is then possible to solve for both V and z_c so that:

$$z_c = \frac{1}{n}\left(\frac{4n}{3m}\right)^{1/4} B_0^{1/4} t^{1/2}, \tag{3.7a}$$

$$r = \left(\frac{4n}{3m}\right)^{1/4} B_0^{1/4} t^{1/2}, \tag{3.7b}$$

$$V = m\left(\frac{4n}{3m}\right)^{3/4} B_0^{3/4} t^{3/2}. \tag{3.7c}$$

The thermal is released from rest and, far from the source, entrainment and drag cause the thermal to decelerate and approach a similarity state following the power laws given above. In order to obtain solutions for the equations given by (3.7) we require the values of the thermal shape factor $m = \frac{4}{3}\pi b$ and the spreading rate n. In the following section the vertical positions, radius and values of the aspect ratio b and spreading rate n found from the experiments are presented.

3.2 Results

In this section the measurements taken during the descent of the thermals created in the laboratory experiments will be presented. Qualitative images comparing the experiments at the two values of H/D for two extreme values of $L/D = 1$ and 5 will be discussed in section 3.2.1. This will be followed by the quantitative results in section 3.2.2 and section 3.2.3.

3.2.1 Qualitative Results

The raw images from four experiments are shown at two different times. The first time which is shown in figures 3.2 and 3.3 is the end of the draining phase. The second time shown in figures 3.4 and 3.5 is 1 s after the end of the draining phase. The four experiments considered comprise of two experiments from the two values of H/D considered in this study, namely $H/D = 2$ and 8. The two experiments at each height have the values of $L/D = 1$ and 5. These values were chosen since these are the shortest and longest tubes which have been considered in this study.

First consider the end of the draining phase for both lengths of tube shown in figures 3.2 and 3.3. The thermals produced by the two lengths of tube are qualitatively very different at the end of the draining phase at both heights. The most drastic difference occurs at $H/D = 2$ and with the tube $L/D = 5$, where impact with the ground has already occurred and the flow has become a gravity current before the end of the draining phase. At both heights, for $L/D = 5$ the shape of the thermal resembles a spheroid with a significant tail, the radius of the spheroidal cap of the thermal is larger than the tube radius and the sides of the tail are approximately straight and vertical. For $L/D = 1$ the shape resembles an oblate spheroid and the radius is comparable to the tube radius. For the intermediate values of L/D, i.e. $L/D = 2$, 3 and 4, the spheroid grows in radius as does the length of the tail.

Figures 3.4 and 3.5 shows 1 s after the draining of both lengths of tube. This time was chosen to illustrate the thermal after it has left the tube and for $H/D = 8$ before it has impacted the ground. At the lower release height $H/D = 2$, for both values of L/D, the thermals have transitioned into gravity currents which will be discussed further in chapter 4. However, when $H/D = 8$ there is now a significant difference between the thermals produced by the two lengths of tube. More significantly the $L/D = 5$ experiment now no longer resembles an oblate spheroid, but a prolate spheroid, whereas, for $L/D = 1$ both the vertical and horizontal radii have grown and the thermal still resembles an oblate spheroid. This deviation in shape from an oblate spheroid for the $L/D = 5$ tube brings into question

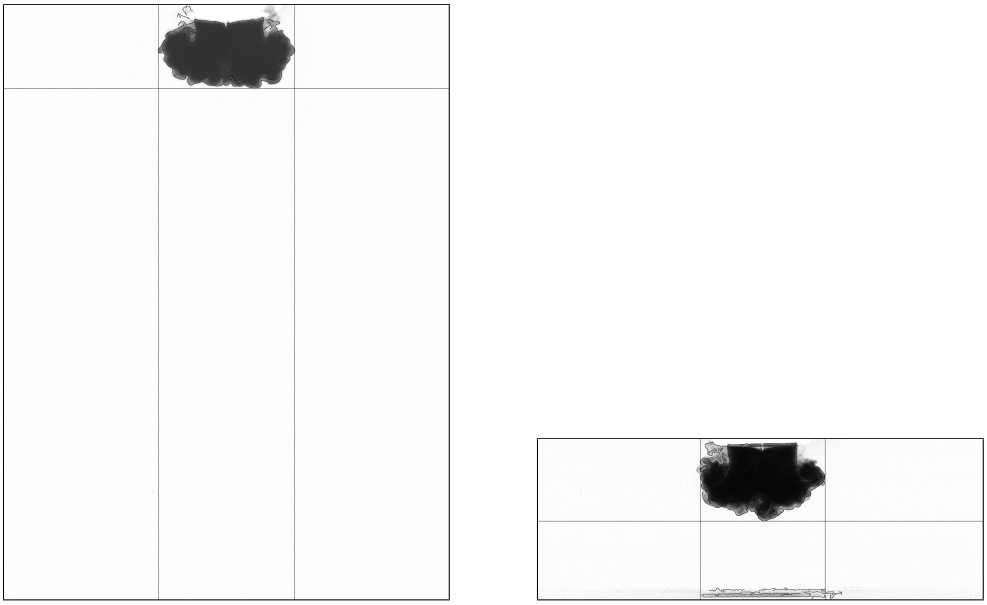

(a) $H/D = 8$ (b) $H/D = 2$

Fig. 3.2 Snapshots at the end of draining for $L/D = 1$ at both $H/D = 2,\ 8$

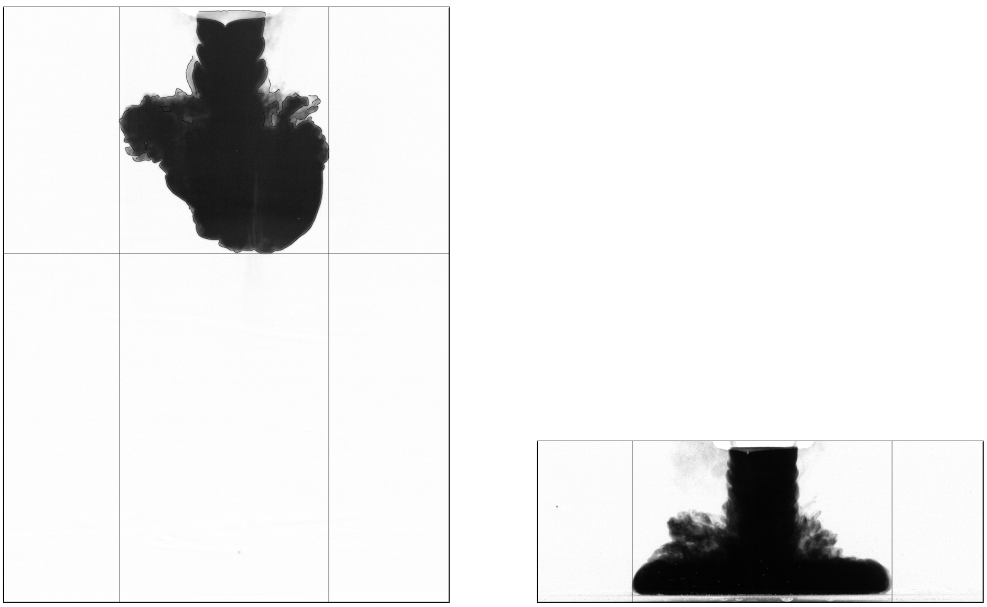

(a) $H/D = 8$ (b) $H/D = 2$

Fig. 3.3 Snapshots at the end of draining for $L/D = 5$ at both $H/D = 2,\ 8$

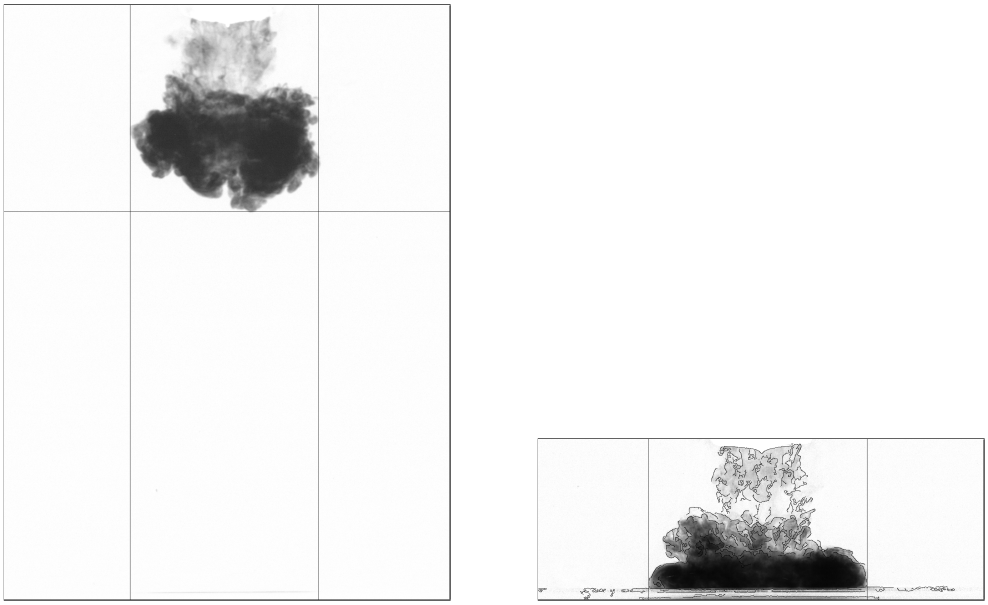

(a) $H/D = 8$ (b) $H/D = 2$

Fig. 3.4 Snapshots $1s$ after the end of draining of an $L/D = 1$ tube at both $H/D = 2,\ 8$

the validity of the self-similar shape assumption for the longer tubes which will be discussed further in section 3.5.1.

3.2.2 Centre of Mass, Front and Radii Measurements

In this section the results from the laboratory experiments are presented beginning with the lowest edge, z_f, centre of mass, z_c and the radius, r, measured during the descent from release until impact with the ground. These measurements will then be used to determine the unknown value of the aspect ratio of the thermal, b, and the spreading rate n and compare them to previously reported values. Both the radial position and vertical position of the front are measured using edge detection, while, the centre of mass data are obtained using the dye attenuation images. Both of these processes are described in Chapter 2.

Figures 3.6 and 3.7 show the mean values of z_f, the front position (circles), and z_c, the centre of mass (squares). The mean values are found by finding these positions for the individual experiments and taking ensemble averages of the positions at the same non-dimensional times. Each plot shows the data for a given value of $L/D = 1,\ 2,\ 3,\ 4$ and 5. The data for $H/D = 2$ and 8 are plotted separately. The error bars are plus/minus one standard deviation from the mean. For all experiments performed at $H/D = 2$ the vertical positions shown in figures 3.6a and 3.7a collapse onto a single curve for the different values of L/D. On the other hand, for the vertical positions for $H/D = 8$, shown in figures 3.6b

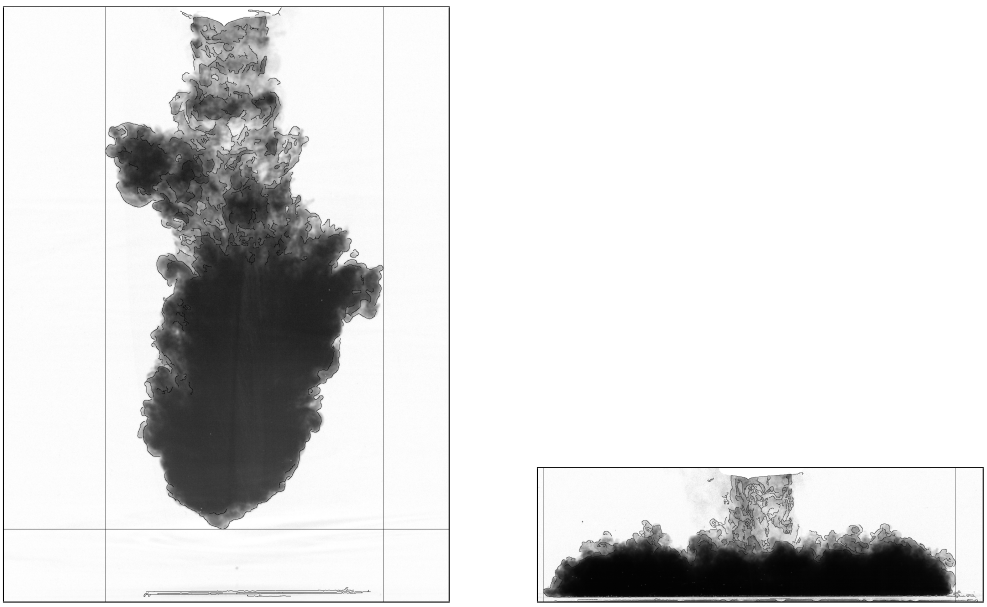

(a) $H/D = 8$ (b) $H/D = 2$

Fig. 3.5 Snapshots $1s$ after the end of draining of an $L/D = 5$ tube at both $H/D = 2,\ 8$

and 3.7b, for $L/D = 1$ and 2 experiments are significantly different from the $L/D = 3$, 4 and 5 experiments. For all experiments, both measurements of vertical position experience an initial acceleration period. The vertical positions of all experiments at $H/D = 2$, and the $L/D = 4$ and 5 experiments at $H/D = 8$, remain in the initial acceleration phase during the descent to the ground. For $L/D = 1$ and 2 at $H/D = 8$ the velocity is reduced after this initial acceleration, as the flow becomes a self-similar thermal.

Figure 3.8 shows the mean values of the maximum radius, $r - r_0$, where r_0 is the initial radius of the tube, during the descent of the thermal. Each figure gives the data for $L/D = 1$, 2, 3, 4 and 5 at $H/D = 2$ and 8, respectively. The error bars are plus/minus one standard deviation from the mean of an appropriate subset of experiments. Unlike the vertical positions the radii of the thermals do not significantly vary at $H/D = 2$ or 8 when varying L/D.

Plotted in figure 3.9 are the vertical positions of the centres of mass and radii for all lengths of tube at $H/D = 8$. Also plotted are the similarity solutions (black lines) given by (3.7) taking $m = 3$ and $n = 0.25$ the values found by Scorer [53]. The self-similar solution only qualitatively captures the dynamics of the center of mass thermal towards the end of the descent for experiments with $L/D = 1$ and 2. In order to quantitatively describe the parts of the experiments where the power laws do agree, the values of m and n cannot be 3 and 0.25 as Scorer [53] found. In the following section the values of the constants b, which is a function of m, and n are found for the experiments presented here.

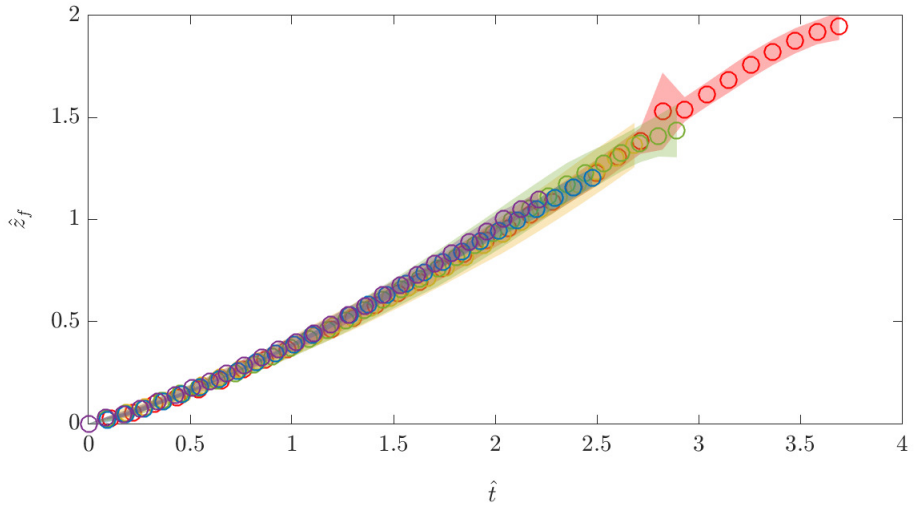

(a) $H/D = 2$

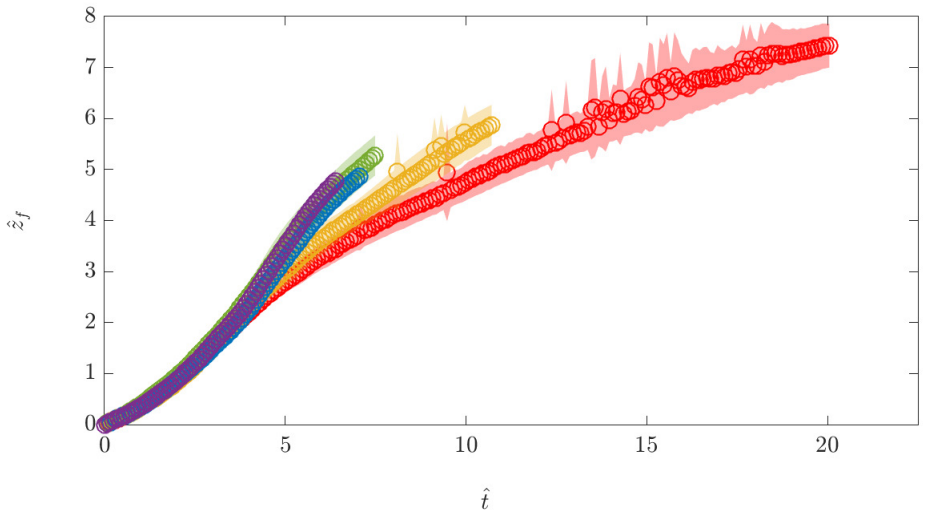

(b) $H/D = 8$

Fig. 3.6 Average vertical position of the front z_f of the thermal as a function of time for $L/D = 1$ (red), 2 (yellow), 3 (green), 4 (blue) and 5 (purple) at $H/D = 2$ and 8. The shaded region represents $\pm$ one standard deviation from the average.

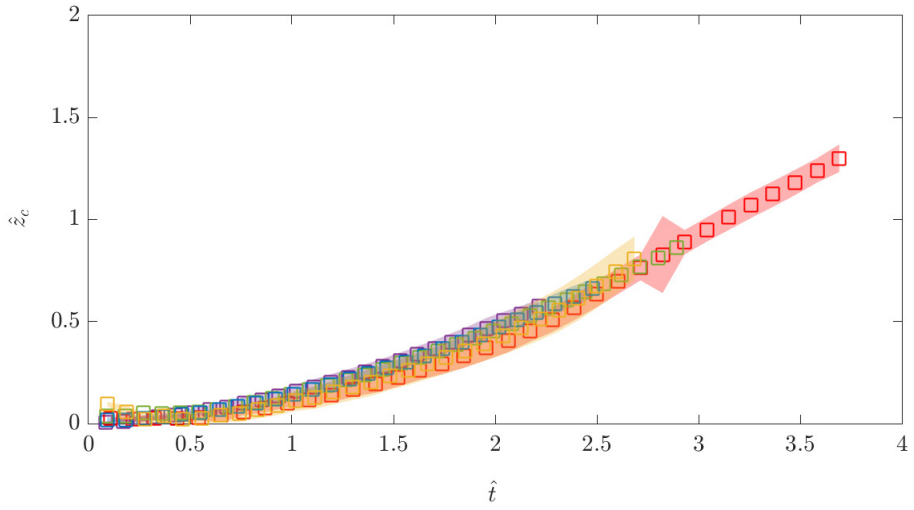

(a) $H/D = 2$

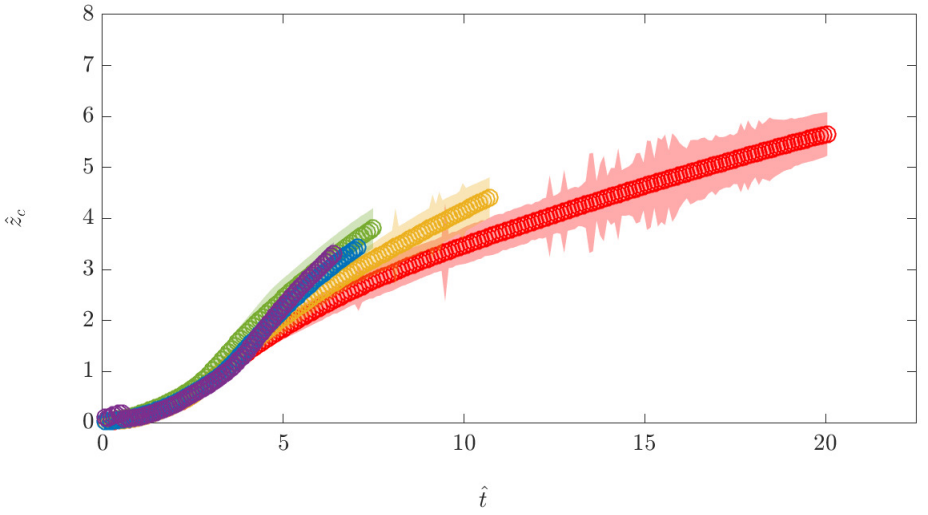

(b) $H/D = 8$

Fig. 3.7 Average vertical position of the centre of mass z_c of the thermal as a function of time for $L/D = 1$ (red), 2 (yellow), 3 (green), 4 (blue) and 5 (purple) at $H/D = 8$. The shaded region represents $\pm$ one standard deviation from the average.

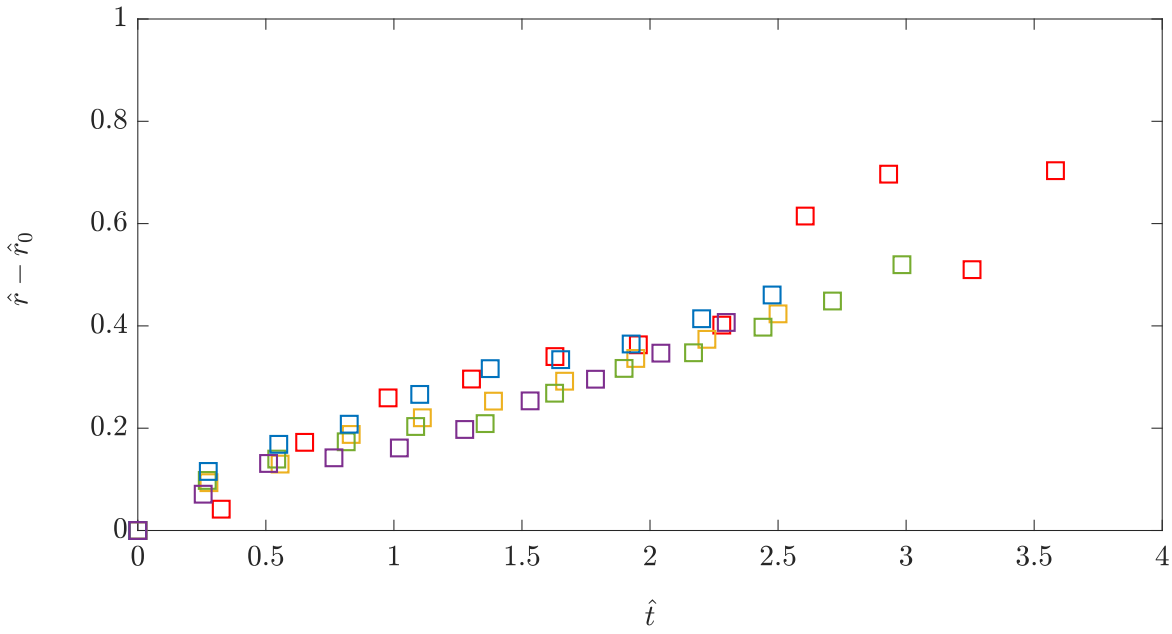

(a) $H/D = 2$

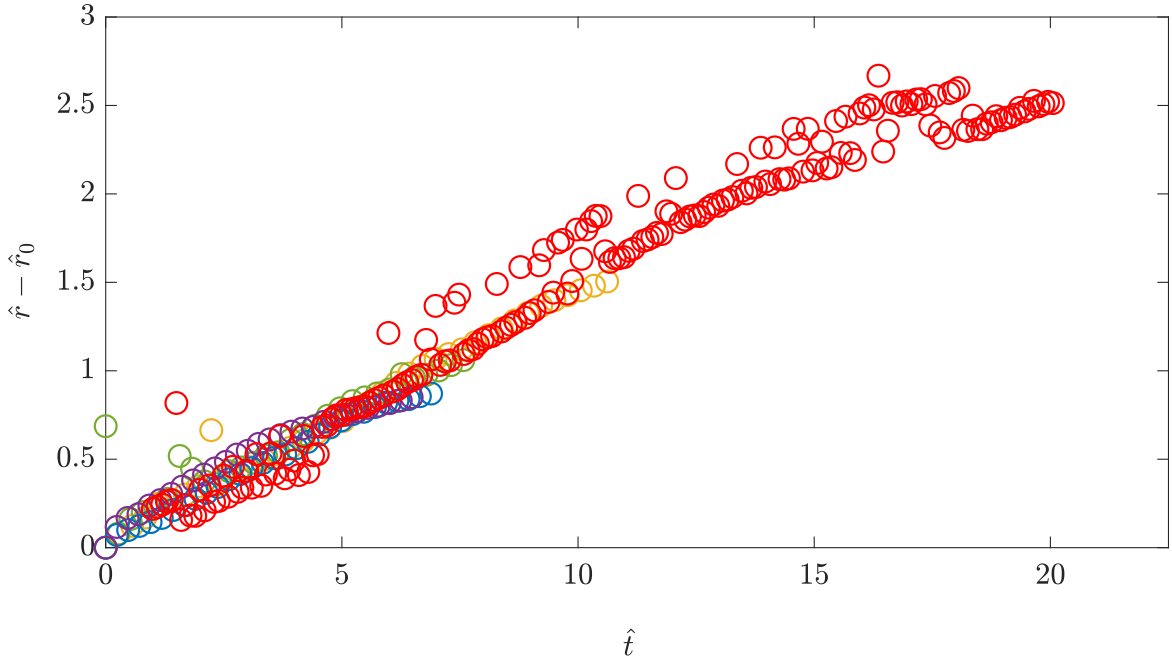

(b) $H/D = 8$

Fig. 3.8 Average radius of the thermal as a function of time for $L/D = 1$ (red), 2 (yellow), 3 (green), 4 (blue) and 5 (purple) at $H/D = 2$ and 8

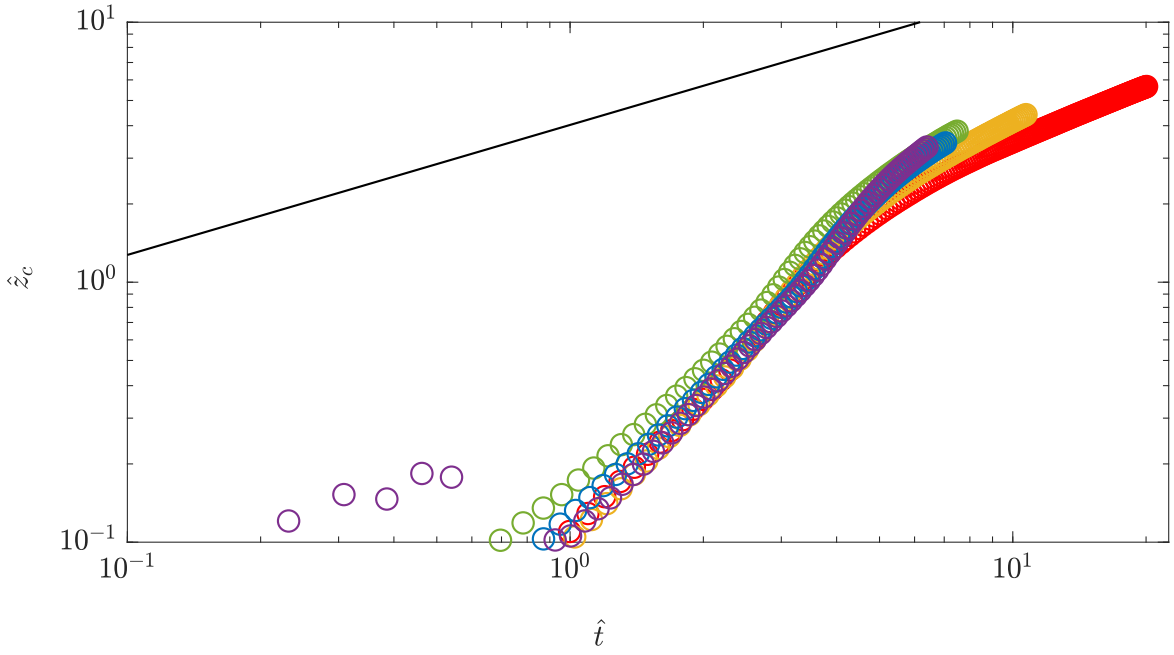

(a) $\hat{z}_c$

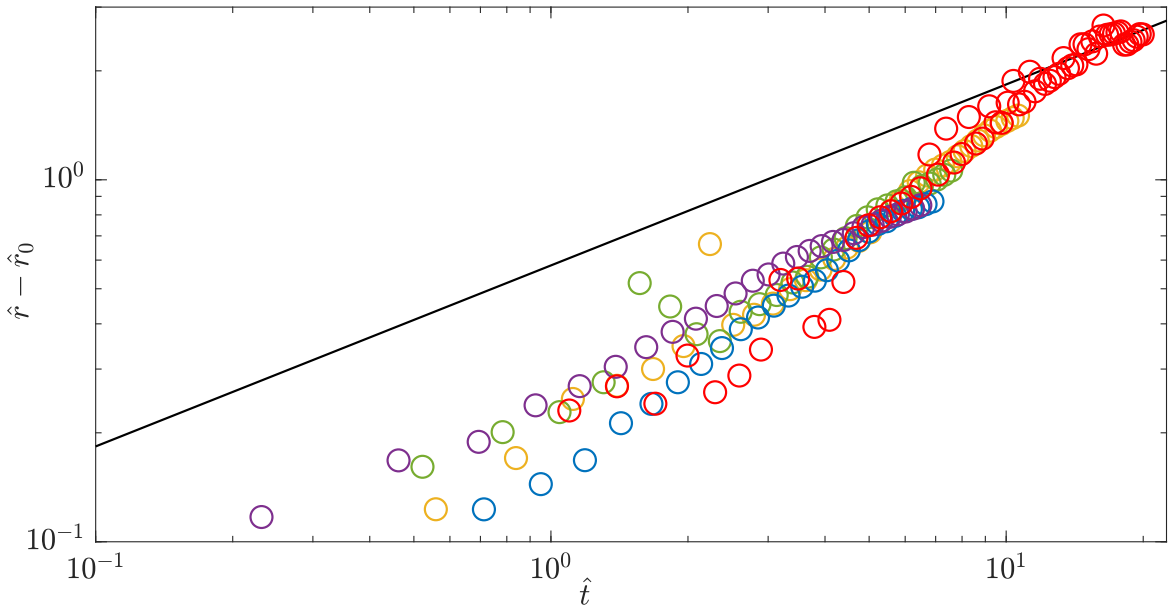

(b) $\hat{r} - \hat{r}_0$

Fig. 3.9 Vertical positions of the centres of mass and radii plotted on a log-log scale for $L/D = 1$ (red), 2 (yellow), 3 (green), 4 (blue) and 5 (purple) at $H/D = 8$. Also plotted is (3.7) (black line) with $m = 3$ and $n = 0.25$ taken from Scorer [53] where $\hat{z}_c = 2.31\hat{t}^{1/2}$ and $\hat{r} - \hat{r}_0 = 0.58\hat{t}^{1/2}$.

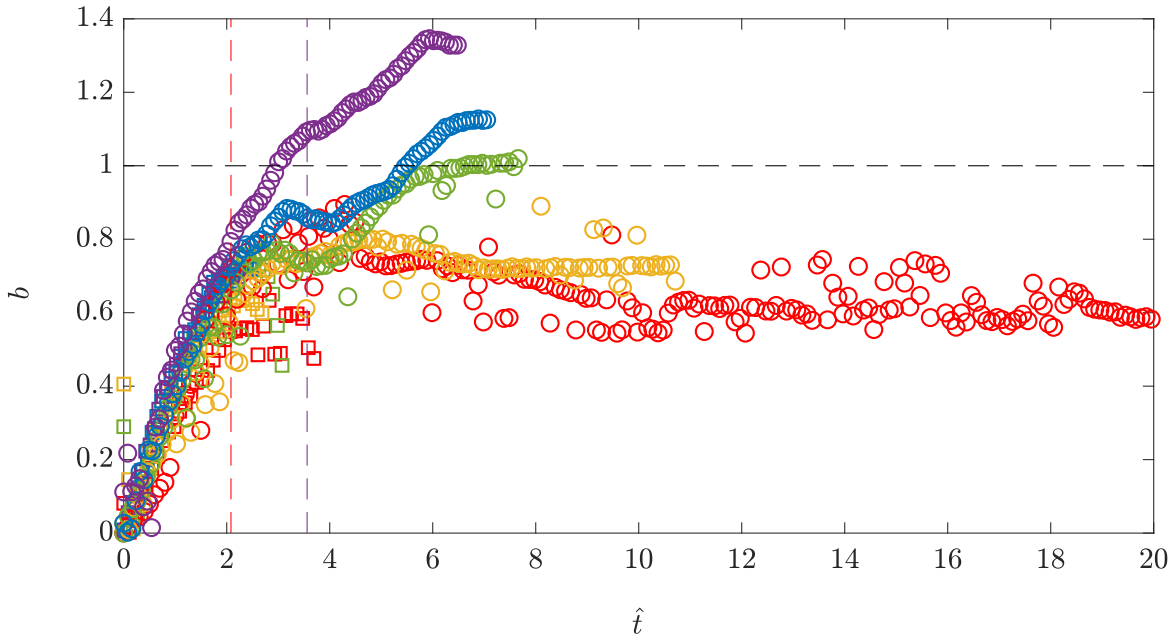

Fig. 3.10 Ratio of the vertical/horizontal radii, $h = br$ for $L/D = 1$ (red), 2 (yellow), 3 (green), 4 (blue) and 5 (purple) for the experiments performed at both $H/D = 2$ (squares) and 8 (circles). A value of $b = 1$ (horizontal dashed line) indicates that the thermal is a sphere, $b > 1$ a prolate spheroid, $b < 1$ an oblate spheroid. The draining times (vertical dashed lines) for the values of $L/D = 1$ and $L/D = 5$ are also shown.

3.2.3 Shape Factors

The values of the ratio of the semi-minor/major radii b and the spreading rates n for $L/D = 1$ to 5 at $H/D = 2$ and 8 are now considered. Figure 3.10 shows the measured value of b, found by dividing the measured values of h and r from the experiments for values of $L/D = 1$, 2, 3, 4 and 5 and for two values of $H/D = 2,\ 8$. Also plotted are the end of draining times for $L/D = 1$ and 5 (vertical dashed lines). During the draining phase, and for some time after, the ratio b initially grows at the same rate independent of L/D. For $L/D = 1$ and 2 the value of b then becomes a constant whereas, for $L/D = 3$, 4 and 5 the value of b continues to grow. This is contrary to the initial assumption that b, and therefore m, is a constant during the development of the self-similar solutions given by (3.7). In fact b varies with time during the draining of the tube and for some time after the draining has ended, before becoming a constant value.

A value of $b = 1$ (horizontal dashed line) indicates the thermal is a sphere, $b > 1$ a prolate spheroid and $b < 1$ an oblate spheroid. Hart [30] averaged the value of b over a period of 5 s for a fixed L/D and found $b = 0.86$, whereas Scorer [53] found $b = 0.72$. For a larger volume release, i.e. a larger L/D, Hart [30] found that the value of b increases. Our

results indicate that during the self-similar phase which lasts approximately 2 s for $L/D = 1$, $b = 0.62 \pm 0.05$ and for $L/D = 2$, $b = 0.73 \pm 0.04$, however for $L/D > 2$, b does not reach a constant value. For $L/D = 3$, 4 and 5, $b > 1$ indicating that the thermal resembles a prolate spheroid. As previously stated the value of b is related to m by $m = \frac{4}{3}\pi b$, this gives a value of $m = 2.60 \pm 0.21$ for $L/D = 1$, and $m = 3.06 \pm 0.17$ for $L/D = 2$. For comparison, Hart [30] found $m = 3.60$, whereas Scorer [53] found $m = 3$.

The spreading rate n can be measured in two ways: firstly, by finding the coefficient of a linear fit of edges from the time averaged images, and secondly, by directly calculating the ratio of the radius and the front position instantaneously. Figure 3.11 shows the time average of four experiments with $L/D = 1$, 2, 3 and 4 performed at $H/D = 8$. Also plotted are the linear fit to the edges of the time averaged images (dashed lines). These linear fits are found by detecting the edge of the time averaged images and performing a least squares fit to the edges. The value of the coefficient of the linear fit is plotted on figure 3.12. Also plotted on figure 3.12 are the spreading rate calculated from the instantaneous vertical and radial positions (circles/squares) and the draining times for $L/D = 1$ and 5 (vertical dashed lines). The instantaneous spreading is not constant but initially decreases independently of L/D and later reaches a constant value which depends on L/D. Our results indicate that during the self-similar phase which lasts approximately 2 s for $L/D = 1$, $n = 0.43 \pm 0.02$ and for $L/D = 2$, $n = 0.37 \pm 0.02$, however for $L/D > 2$, n continues to decrease, never reaching a constant value. This is contrary to the initial assumption that n is constant during the development of the self-similar solutions given by (3.7). The coefficients of a linear fits provide a lower bound on the instantaneous measurements. For the values of L/D considered here these bounds are given by $n = 0.34$ for $L/D = 1$, $n = 0.28$ for $L/D = 2$, $n = 0.23$ for $L/D = 3$, $n = 0.22$ for $L/D = 4$, and tend to a minimum value at 0.20 for $L/D = 5$. This variation in the value of n has been seen in previous studies with the range of spreading rate varying between 0.13 and 0.31 as the value of L/D decreases [37]. In fact the spreading rates vary with time independent of L/D during the draining of the tube and for some time after the draining has ended before becoming a constant value.

We have observed that, the values of b and n are not constant during draining or for some time after this, and that for some values of L/D and $H/D = 8$ thus never become constant. We can use these measurements of b and n along with the vertical positions of the centres of mass to estimate the times and heights at which the thermals enter each of the phases: the end of the draining phase T_d, the end of the non-constant spreading rate and shape factor phase, and the self-similar thermal phase. These three phases will be discussed further in the following section.

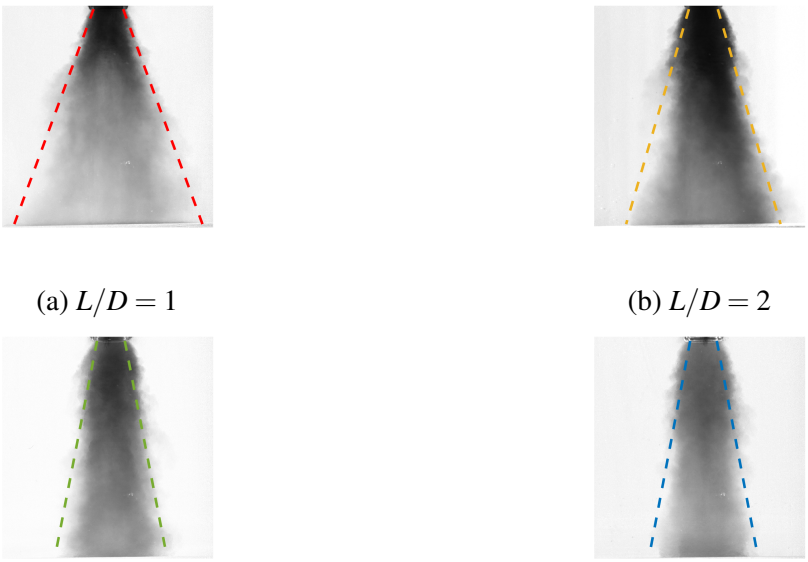

(a) $L/D = 1$ (b) $L/D = 2$

(c) $L/D = 3$ (d) $L/D = 4$

Fig. 3.11 Time averaged experimental images for $L/D = 1$, 2, 3 and 4 with the linear fit to the edges.

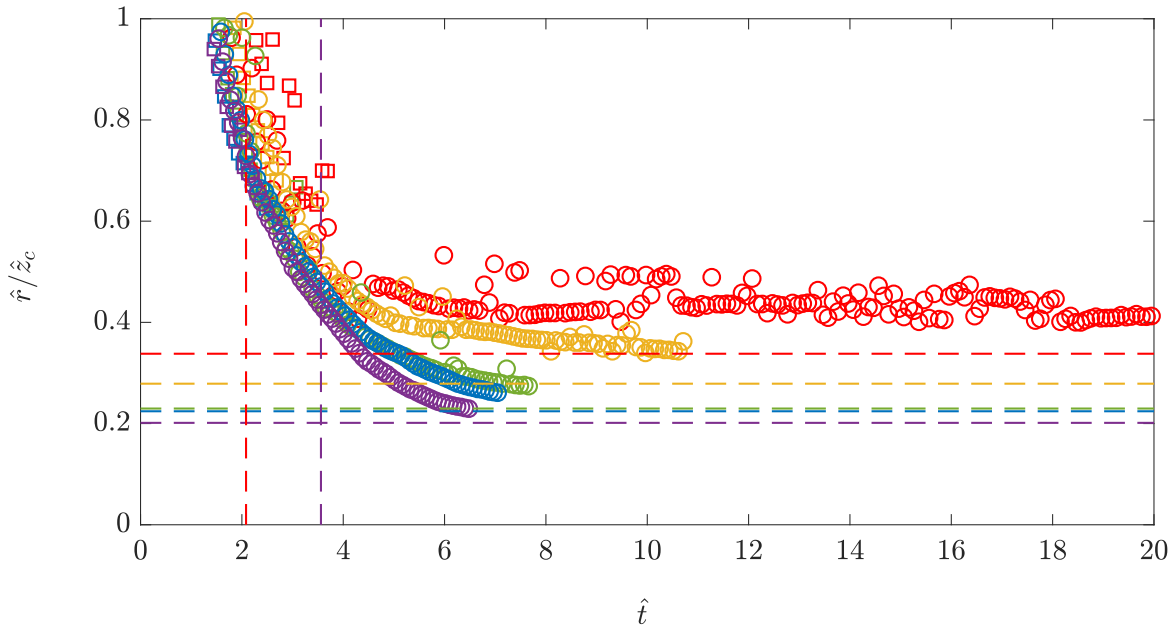

Fig. 3.12 Instantaneous spreading rate, $r = nz_f$ for $L/D = 1$ (red), 2 (yellow), 3 (green), 4 (blue) and 5 (purple) for experiments performed at both $H/D = 2$ (squares) and 8 (circles). Horizontal lines represent the fitted value of n to $r = nz_f$ for each value of L/D from figure 3.11. The draining times (vertical dashed lines) for the values of $L/D = 1$ and $L/D = 5$ are also shown.

3.2.4 Duration of Initial Acceleration Phase

As stated previously, Bond & Johari [8] found that the initial acceleration phase of a thermal, the time it takes for a thermal to become self-similar, lasted between one and two times the draining time (T_d). Figure 7 in Bond & Johari [8] shows the approximate vertical position of the front of the thermal when $z_f \sim t^{1/2}$ i.e. becomes self-similar, we call this vertical position z_T. From limited testing of this they found that z_T scales linearly with $V_0^{1/3}$, which is equivalent to z_T/D scaling linearly with $(L/D)^{1/3}$. We have observed from our measurements of the aspect ratio of the thermal b and the spreading rate n that the shape of a thermal does not become self-similar for some time after the tube has finished draining. Therefore, we chose to split the acceleration phase into two phases: the draining of the tube and a phase after draining but before the thermal becomes self-similar, known hereafter as 'the development phase'. The beginning of the self-similar phase however is unknown and occurs when the shape factors are constant, and when $z_f \sim t^{1/2}$.

For direct comparison with figure 7 in Bond & Johari [8] figure 3.13 shows the vertical position of the front, z_T, at the approximate distance from the source for $t = T_d$ and $t = 2T_d$ (squares), and at the times when the spreading rate n =constant (+), the aspect ratio of the thermal b =constant ($\circ$) and $z_f \sim t^{1/2}$ ($*$). These distances are found using the measurements from the experiments for $L/D = 1$, 2, 3, 4 and 5 with $H/D = 8$. In general, first the spreading rate becomes constant, followed by the aspect ratio of a thermal b and finally the vertical position $z_f \sim t^{1/2}$. The only experiments for which $z_f \sim t^{1/2}$ at the heights considered herein are the experiments with $L/D = 1$ and 2 at $H/D = 8$. The figure shows that for $L/D = 1$ and 2, the values of z_T for $b =$ constant, $n =$ constant and $z_f \sim t^{1/2}$ are outside the one to two draining times (between the two square markers) contrary to the measurements reported by Bond & Johari [8]. For $L/D = 1$ the vertical heights for which b and n become constant are approximately one source diameter apart, however this becomes closer as L/D increases to 2. Finally, no experiment at these heights has $z_f \sim t^{1/2}$ within one to two times the draining time as suggested by Bond & Johari [8].

As stated previously these results indicate that the initial acceleration phase of a thermal can be split up into two phases: the draining phase, and a development phase. The development phase is characterised by the time where draining has ended but when the shape factor and spreading rate are not constant. Also plotted on figure 3.13 are the two heights that experiments have been performed at $H/D = 2$ and 8 (dashed lines). This shows us which phase the thermal impacts the ground in, for each value of L/D at both heights and has been summarised below.

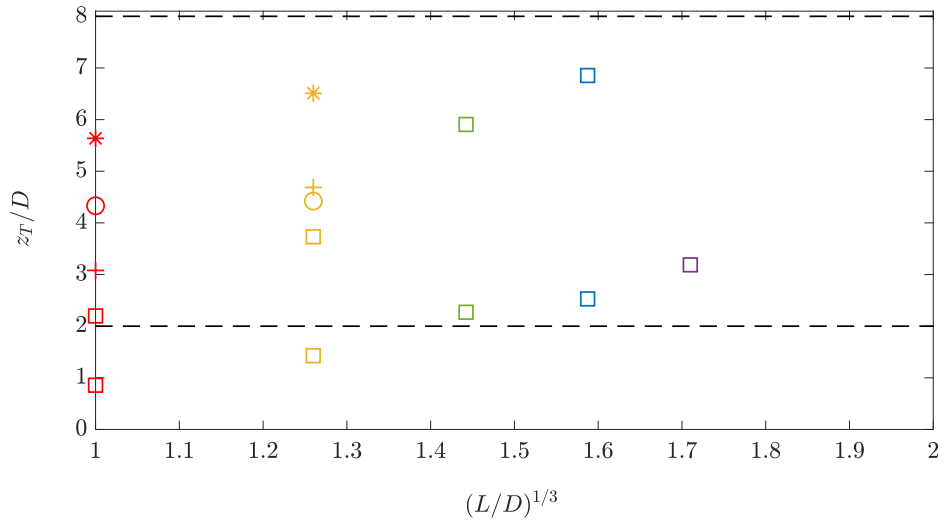

Fig. 3.13 The approximate vertical position at the points $t = T_d$ and $t = 2T_d$ (squares), when b (circles) and r/z (+) become constant, and when $z_c \propto t^{1/2}$ (*). This has been plotted for $L/D = 1$ (red), 2 (yellow), 3 (green), 4 (blue) and 5 (purple) for the experiments performed at $H/D = 8$. The two dashed lines show $H/D = 2$ and 8 the heights at which experiments have been performed at in this study.

$H/D = 2$	$L/D \leq 2$	development phase,
	$L/D \geq 3$	draining phase,
$H/D = 8$	$L/D \leq 2$	self-similar phase,
	$L/D \geq 3$	development phase.

Models for a thermal during the initial acceleration phase are presented in the following section for the draining phase and the development phase separately.

3.3 Three Phase Thermal Model

We have seen from the results presented above that the development of a thermal released from a tube can be split into three phases:

1. the draining phase: while the tube is still draining and the shape factor and spreading rates are not constant,

2. the development phase: where the tube has finished draining but the shape factor and spreading rate are not constant,

3. the self-similar thermal phase: where the shape factor and spreading rate are constant and the thermal can be described by the theory presented in section 3.1.1.

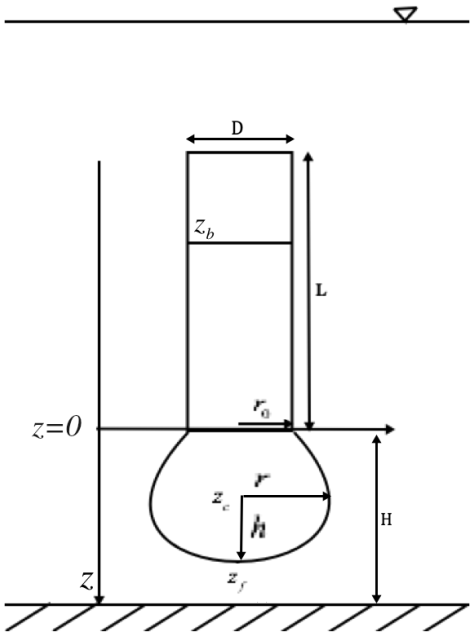

Fig. 3.14 Diagram showing the coordinate system used for the draining tube model.

In this section we propose models for the first two phases, beginning with the draining phase. The three phase model is then used to investigate the validity of assuming a constant entrainment coefficient α, and the assumption that the thermal is a self-similar spheroid.

3.3.1 Draining Equations

Figure 3.14 shows the coordinate system that will be used for this model. The model uses the thermal equations, derived previously, to represent the spheroidal mass of fluid outside the tube but these are adapted to include the volume, buoyancy and momentum gained from the draining of the tube into the spheroid. The only extra piece of information required is the velocity at the exit of the tube, $\mathrm{d}z_b(t)/\mathrm{d}t$, which will be determined by our experimental data.

As described above, the volume, buoyancy and momentum equations are adjusted to include the volume of dense fluid gained from the draining tube as well as the effects of entrainment. As the thermal drains from the tube and develops in order to account for any changes of the shape of the spheroid we allow $m = \frac{3}{4}\pi b(t)$, $a = a(t)$, where $b(t)$ is the aspect ratio of the thermal and $a(t)$ is obtained from $A_s = a(t)r^2$, the surface area. The change in volume under the assumption that the thermal is spheroidal is then given by

$$\frac{\mathrm{d}V}{\mathrm{d}t} = 3mr^2\frac{\mathrm{d}r}{\mathrm{d}t} + \frac{\mathrm{d}m}{\mathrm{d}t}r^3. \tag{3.8}$$

As with the derivation of the thermal equations we also use the entrainment assumption to describe the rate of change of the volume due to the thermal entraining ambient fluid. Then the rate of change of the volume due to entrainment and accounting for the additional volume draining from the draining of the tube can be written as

$$\frac{\mathrm{d}V}{\mathrm{d}t} = \alpha a(t) r^2 \frac{\mathrm{d}z_c}{\mathrm{d}t} + \pi r_0^2 \frac{\mathrm{d}z_b}{\mathrm{d}t}, \tag{3.9}$$

where $z_b(t)$ is the vertical position of the top of the dense fluid as it drains from the tube. The position z_b is illustrated on figure 3.14. Equating (3.8) and (3.9) we get

$$\frac{\mathrm{d}r}{\mathrm{d}t} + \frac{1}{3m}\frac{\mathrm{d}m}{\mathrm{d}t} r = n(t)\frac{\mathrm{d}z_c}{\mathrm{d}t} + \frac{\pi r_0^2}{3mr^2}\frac{\mathrm{d}z_b}{\mathrm{d}t}, \tag{3.10}$$

where $n(t) = \alpha a(t)/3m(t)$.

As source fluid drains from the tube, buoyancy and momentum are added to the thermal. It is assumed that the source fluid drains uniformly from the tube into the spheroid and so any viscous effects are ignored. In fact, during the draining a boundary layer is formed around the edge of the tube which leads to a non-uniform velocity profile over the cross-section of the tube. This boundary layer around the inner boundary of the tube has thickness $\delta \sim \sqrt{\nu T_d}$ where ν is the kinematic viscosity of the fluid. For the boundary layer to be insignificant we require that

$$\frac{\delta}{D} = \frac{\sqrt{\nu T_d}}{D} \ll 1$$

i.e. $T_d \ll D^2/\nu$. For the experiments presented here T_d ranges from 0.6 s for $L/D = 1$ to 1.6 s for $L/D = 5$ and $D^2/\nu = 2.416 \times 10^3$ s so $\delta/D \leq 3 \times 10^{-2}$. Therefore, viscous effects in the tube can be ignored and we can assume that the fluid drains uniformly from the tube. Following this the buoyancy and momentum equations can be written as

$$\frac{\mathrm{d}B}{\mathrm{d}t} = \pi r_0^2 g_0' \frac{\mathrm{d}z_b}{\mathrm{d}t}, \tag{3.11}$$

$$\frac{3}{2}\frac{\mathrm{d}(wV)}{\mathrm{d}t} = B + \pi r_0^2 \frac{\mathrm{d}}{\mathrm{d}t}\left(z_b \frac{\mathrm{d}z_b}{\mathrm{d}t}\right). \tag{3.12}$$

Modelling the Evolution of the Drainage Front $z_b(t)$

By assuming that no mixing occurs within the tube then the location of the upper boundary $z_b(t)$ in the tube can be modelled as free-fall given by

$$z_b(t) = \frac{1}{2} g_0' t^2.$$

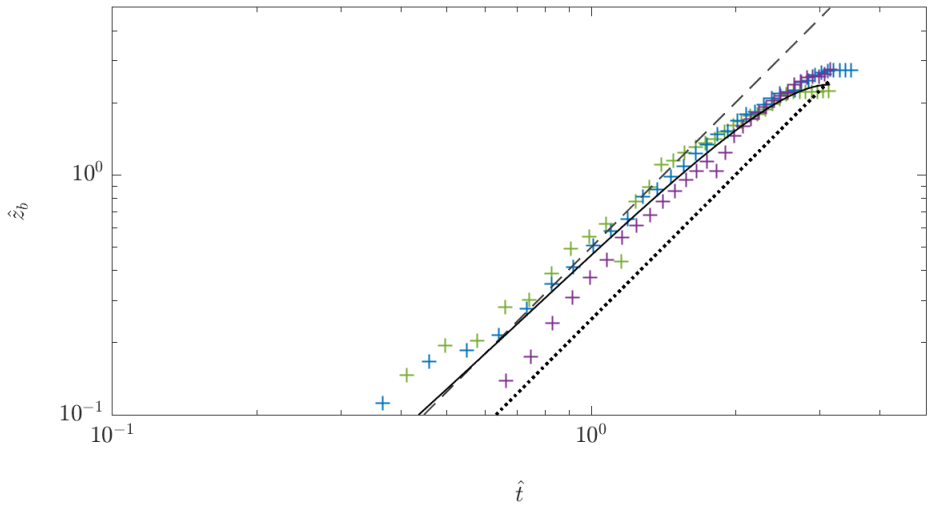

Fig. 3.15 Non-dimensional vertical position of the interface of the source fluid with the ambient fluid as it drains from the tube plotted on the log-log scale. Shown for an average of a subset of experiments for $L/D = 3$ (green), 4 (blue) and 5 (purple). Theoretical solutions of $\hat{z}_b = 0.5t^2$ (black dashed lines) and $\hat{z}_b = 0.25t^2$ (black dotted lines), also plotted is the least squares fit to the data $\hat{z}_b = 0.32t^2$ (solid black line).

Using the scalings given by (3.1a) and (3.1b), non-dimensionally

$$\hat{z}_b(\hat{t}) = \frac{1}{2}\hat{t}^2. \tag{3.13}$$

This model for the draining of the tube was compared against the experimental data. For the tubes with $L/D = 3$, 4 and 5 the interface of the source fluid and ambient fluid in the tube was tracked using edge detection and compared to this model in figure 3.15, which shows the non-dimensional mean position $\hat{z}_b$ of the top of the draining fluid with time on the log-log scale. The mean is taken over 7 ($L/D = 3$) and 5 ($L/D = 4$ and 5) experiments. Also plotted as the black dashed line is (3.13).

L/D	g_0'	$\hat{z}_b/\hat{t}^2_{avg}$
3	44.84	0.49 ± 0.32
4	55.46	0.40 ± 0.16
5	45.36	0.33 ± 0.09

Table 3.1 Comparison of the values of $\hat{z}_b/\hat{t}^2_{avg}$ for $L/D = 3$, 4 and 5 for different g_0'.

Table 3.1 gives the values of g_0' for the experiments plotted in figure 3.15 and the average values of $\hat{z}_b/\hat{t}^2$ for each value of L/D plus or minus one standard deviation. If the fluid in

the tube drained according to freefall the value of $\hat{z}_b/\hat{t}^2$ should be 0.5 (see (3.13). The actual values imply that there are other factors acting to reduce the rate of descent of the fluid in the tube, for the longest tube in particular.

The added mass represents the inertial effects added to the flow by the dense source fluid deflecting the surrounding ambient fluid as it drains from the tube. The added mass of a cylinder is $m_a = \rho_0 V_0$ [16]. Then, including the added mass in the force balance

$$F = (m + m_a)a, \tag{3.14}$$

$$= 2\rho_0 V_0 g_0'. \tag{3.15}$$

for force F and acceleration a. However, the only force acting on the fluid at the start is buoyancy and therefore $F = \Delta\rho g V_0$. By equating the two and dividing both sides by ρ_a we get

$$2\frac{\rho_0}{\rho_a} V_0 a = \frac{\Delta\rho}{\rho_a} g V_0.$$

Since it is assumed that the flow is Boussinesq we have that $\frac{\rho_o}{\rho_a} \approx 1$, and therefore the effective acceleration $a = \frac{1}{2} g_0'$. Then the equation for $z_b(t)$ becomes

$$z_b = \frac{1}{4} g_0' t^2, \tag{3.16}$$

which is also plotted on figure 3.15 (black dotted line). As can be seen from the figure $\hat{z}_b$ the coefficient of $\hat{t}^2$ lies somewhere between 0.25 and 0.5. This indicates that something not explicitly modelled is affecting the draining of the tube. To obtain the factor $1/4$ the added mass of a cylinder is used, however the shape of the thermal as it drains is complex and evolves during the draining. The evolution of the shape also depends on the value of L/D. It can be seen from table 3.1 that $\hat{z}_b/\hat{t}^2_{avg}$ ranges from 0.33 to 0.49 as L/D decreases, the variation in $\hat{z}_b/\hat{t}^2$ decreases as L/D increases. Therefore, since neither model represents the data accurately, a least-squares fit of z_b has been performed to obtain z_b. This fit of the data, $\hat{z}_b = -0.027\hat{t}^4 + 0.021\hat{t}^3 + 0.43\hat{t}^2 + 0.041\hat{t}$ with $r^2 = 0.9991$, is plotted on figure 3.15 (solid line) and will be used when solving the model in the following sections for all values of L/D.

3.3.2 Development Phase

Above we have presented models for the draining phase and the self-similar phase of a thermal. In this section we present a model for the second half of the acceleration phase: between the end of draining and the start of the self-similar phase. During this phase we

proceed in a similar manner to the draining equations by adapting the thermal equations by allowing the thermal shape to vary. By writing $m(t) = \frac{4}{3}\pi b(t)$ and $a = a(t)$. Then the increase in volume is

$$\frac{\mathrm{d}V}{\mathrm{d}t} = 3m(t)r^2\frac{\mathrm{d}r}{\mathrm{d}t} + \frac{\mathrm{d}m}{\mathrm{d}t}r^3. \tag{3.17}$$

As with the derivation of the self-similar thermal equations we use the entrainment assumption to describe the rate of change of the volume due to the thermal entraining ambient fluid. Then the rate of change of the volume due to entrainment can be written as

$$\frac{\mathrm{d}V}{\mathrm{d}t} = \alpha a(t)r^2\frac{\mathrm{d}z_c}{\mathrm{d}t}. \tag{3.18}$$

Equating (3.17) and (3.18) we get

$$\frac{\mathrm{d}r}{\mathrm{d}t} = n(t)\frac{\mathrm{d}z_c}{\mathrm{d}t} - \frac{1}{3m(t)}\frac{\mathrm{d}m}{\mathrm{d}t}r, \tag{3.19}$$

where $n(t) = \alpha a(t)/3m(t)$, as with the draining phase. Then, as with the self-similar thermal equations, using the conservation of buoyancy, $B = B_0$ and the conservation of momentum, $M = wV$, we obtain

$$\frac{\mathrm{d}(wV)}{dt} = \frac{2}{3}B_0. \tag{3.20}$$

3.3.3 Pathway to Solutions

We now have a complete set of equations for all three phases of a thermals development: the draining phase, the development phase and the self-similar phase. These three models are presented in table 3.2. The table shows the equations for the change in volume, buoyancy, vertical position of centre of mass and the radius respectively. The equations have been manipulated to form a system of coupled first order non-linear differential equations. Then using the values for m, n and z_b measured from our experiments, and discussed in section 3.2, the system was solved numerically using ode45, an explicit Runga-Kutta method, in MATLAB *ver. R2019a* [1]. The three phases were solved separately with the final values of each phase providing the initial conditions for the next phase, as outlined below

$$F(V, M, z_c, r) \tag{3.21a}$$

$$F1(0,0,0,2.5) \quad tspan1 = [0 : t_{drain}] \tag{3.21b}$$

$$F2([F1(end,1)F1(end,2)F1(end,3)F1(end,4)]) \quad tspan1 = [t_{drain} : t_{dev}] \tag{3.21c}$$

$$F3([F2(end,1)F2(end,2)F2(end,3)F2(end,4)]) \quad tspan1 = [t_{dev} : t_i] \tag{3.21d}$$

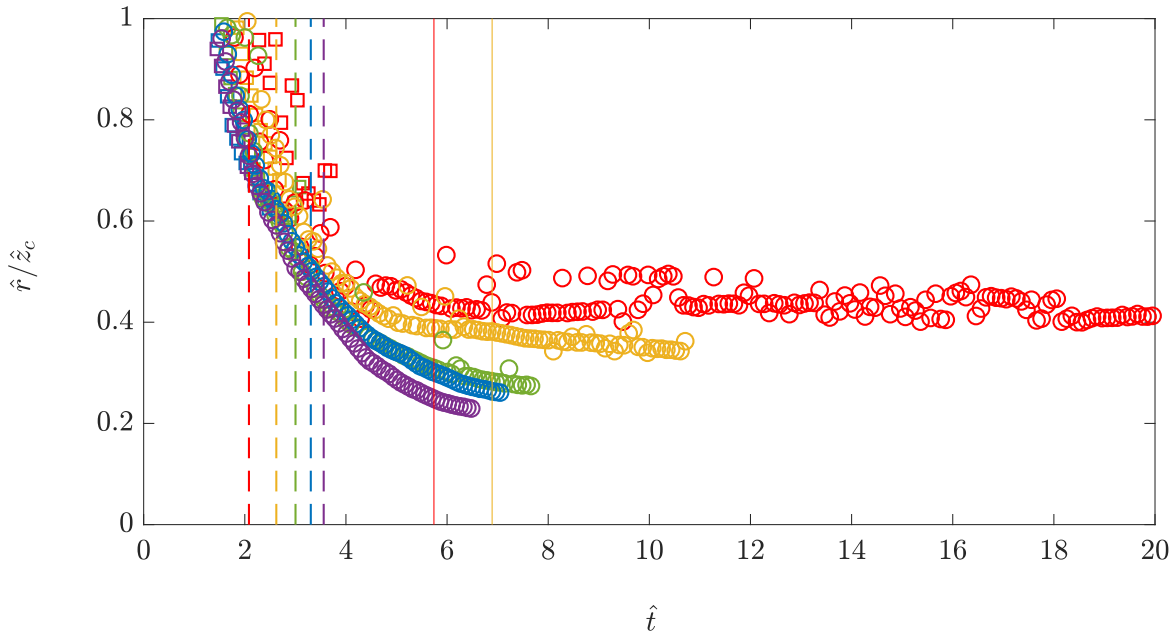

Fig. 3.16 Instantaneous spreading rate, $r = nz_f$ for $L/D = 1$ (red), 2 (yellow), 3 (green), 4 (blue) and 5 (purple) for experiments performed at both $H/D = 2$ (squares) and 8 (circles). The end of the draining phase (vertical dashed lines) for the values of $L/D = 1$ to 5, and the end of the development phase (solid lines) for the values of $L/D = 1$ and 2 are also shown.

where t_{drain}, t_{dev} and t_i are the end of the draining phase, development phase and the impact time respectively, as measured from our experiments. The end of the draining phase and the impact time are trivially found from experimental images whereas the end of the development phase is more complex. To estimate the end of the development phase the average of the value of r/z_c from between $t = t_i - \hat{2}$ and t_i. The end of the development phase was then determined by the last time r/z_c varied more than 10% of the average for $\hat{t} = 0.5$. The times t_{drain} are indicated on figure 3.16 by vertical dashed lines for $L/D = 1$ (red), 2 (yellow), 3 (green), 4 (blue) and 5 (purple). Also indicated on figure 3.16 are the times t_{dev} by vertical solid lines, for $L/D = 1$ (red) and 2 (yellow). No other value of L/D reached the criteria to indicate that the development phase ended before impact with the ground.

Draining Phase	Development Phase	Thermal Phase
$\frac{\mathrm{d}V}{\mathrm{d}t} = 3m(t)n(t)r^2\frac{M}{V} + \pi r_0^2\frac{\mathrm{d}z_b}{\mathrm{d}t}$	$\frac{\mathrm{d}V}{\mathrm{d}t} = 3m(t)n(t)r^2\frac{M}{V}$	$\frac{\mathrm{d}V}{\mathrm{d}t} = 3mnr^2\frac{M}{V}$
$\frac{\mathrm{d}M}{\mathrm{d}t} = \frac{2}{3}\pi r_0^2\left(g_0' z_b(t) + z_b(t)\frac{\mathrm{d}z_b}{\mathrm{d}t}\right)$	$\frac{\mathrm{d}M}{\mathrm{d}t} = \frac{2}{3}g_0' V_0$	$\frac{\mathrm{d}M}{\mathrm{d}t} = \frac{2}{3}g_0' V_0$
$\frac{\mathrm{d}z_c}{\mathrm{d}t} = \frac{M}{V}$	$\frac{\mathrm{d}z_c}{\mathrm{d}t} = \frac{M}{V}$	$\frac{\mathrm{d}z_c}{\mathrm{d}t} = \frac{M}{V}$
$\frac{\mathrm{d}r}{\mathrm{d}t} = n(t)\frac{M}{V} - \frac{r}{3m}\frac{\mathrm{d}m}{\mathrm{d}t} + \frac{\pi r_0^2}{3mr^2}\frac{\mathrm{d}z_b}{\mathrm{d}t}$	$\frac{\mathrm{d}r}{\mathrm{d}t} == n(t)\frac{M}{V} - \frac{r}{3m}\frac{\mathrm{d}m}{\mathrm{d}t}$	$\frac{\mathrm{d}r}{\mathrm{d}t} = n\frac{M}{V}$

Table 3.2 Full model of the draining, development and the thermal phases under the spheroidal shape assumption.

3.4 Comparison With Model

3.4.1 Constant shape factor b and constant entrainment coefficient α

Figure 3.17 and 3.18 show the centre of mass and radius of a thermal from the experiments with $L/D = 1$, 2, 3, 4 and 5 performed at $H/D = 8$ (circles). On both figures the solutions of the equations given in table 3.2 (solid lines with corresponding colours) with the assumption that both the shape factors and the entrainment coefficient are constant, i.e. m, n and α are constant. Here the values of b and α used to determine both m and n using the spheroidal shape assumption are $b = 0.72$, $\alpha = 0.25$, which correspond to the values found by Scorer [53], and $\hat{z}_b = -0.027\hat{t}^4 + 0.021\hat{t}^3 + 0.43\hat{t}^2 + 0.041\hat{t}$. These solutions over-predict the values of z_c for any value of L/D, although there is reasonable agreement for the radius. We also see that the inclusion of the draining terms has made a qualitative improvement to the solutions for the centre of mass during the draining phase, however that is not the case for the radius. The black lines plotted show the similarity solutions plotted in figure 3.9. It can also be seen that our model does indeed reach the same power laws as the similarity solutions presented by Scorer [53]. However, we know that the value of b is non-constant during the first two phases. Therefore we must look at the solutions to the model using a variable value of b but keeping the entrainment coefficient α constant.

3.4.2 Variable shape factor b and constant entrainment coefficient α

Figure 3.19 and Figure 3.20 shows the centre of mass and radius of a thermal from the experiments with $L/D = 1$, 2, 3, 4 and 5 performed at $H/D = 8$ (circles) along with the solutions for z_c and $r - r_0$ from the equations in table 3.2 (solid lines) with the assumption that only the entrainment coefficient α is constant. The values of $b(t)$ and α are used to determine both $m(t)$ and $n(t)$ for the first two phases using the spheroidal shape assumption. For the draining and development phase a least squares fit is used to determine the value of $b(t)$, and during the self-similar phase we take the value of b to be the average over this period. The least squares fits of b were each of the form $b(t) = b_1t^4 + b_2t^3 + b_3t^2 + b_4t$, and are plotted on figure 3.21, the coefficients and r^2 values for each L/D are given in Appendix E. Also, we set $\alpha = 0.25$ in all three phases which corresponds to the value found by Scorer [53], and $\hat{z}_b = -0.027\hat{t}^4 + 0.021\hat{t}^3 + 0.43\hat{t}^2 + 0.041\hat{t}$ which is the least squares fit of the measured values of z_b.

Choosing $\alpha = 0.25$ over predicts the vertical position but shows an improved fit for the intermediate values of L/D namely $L/D = 3$ and 4 for both the centre of mass and radius compared to the constant shape model. The fit with the vertical position for the other values

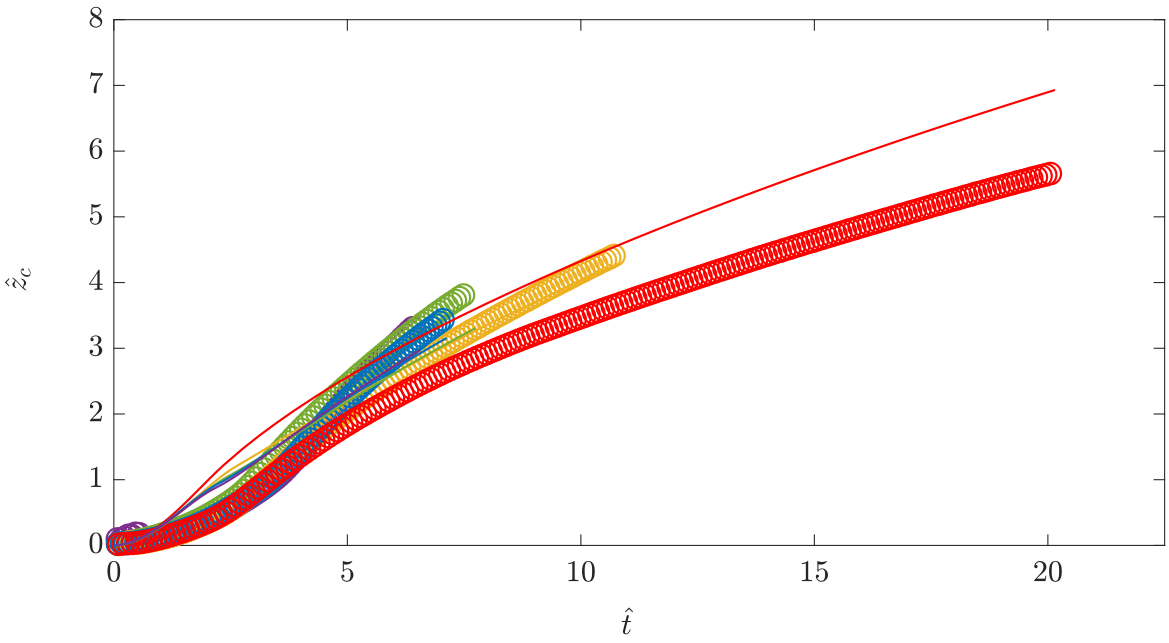

(a) $\hat{z}_c$

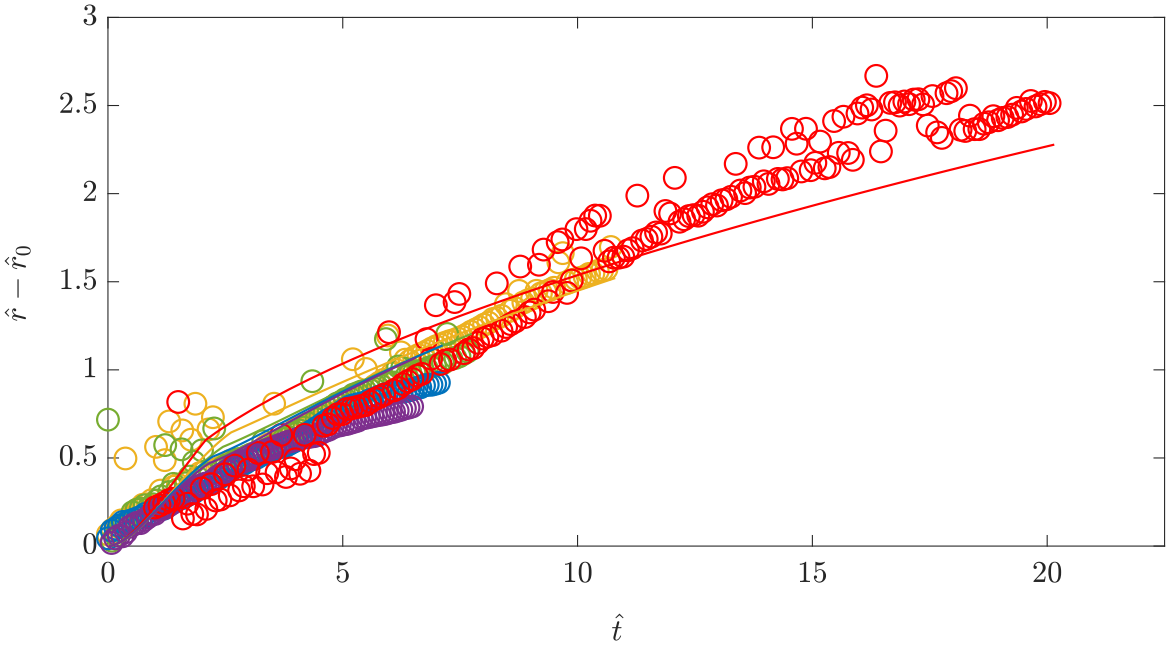

(b) $\hat{r}-\hat{r}_0$

Fig. 3.17 Vertical position of the centre of mass $\hat{z}_c$ and radius $\hat{r}-\hat{r}_0$ of the thermal for $L/D=1$ (red), 2 (yellow), 3 (green), 4 (blue) and 5 (purple) at $H/D=8$ compared to the solutions of the 3 phase model with constant shape factor b and constant entrainment coefficient α (coloured lines). The black curve is the similarity solution given by (3.7) with $m=3$ and $n=0.25$.

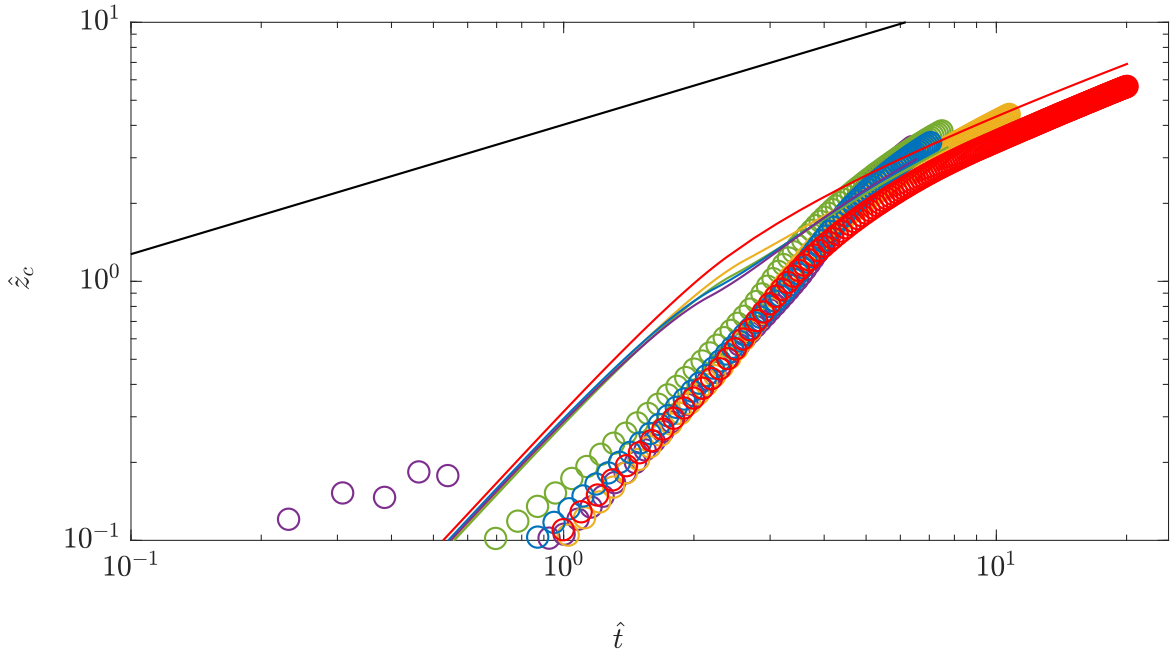

(a) $\hat{z}_c$

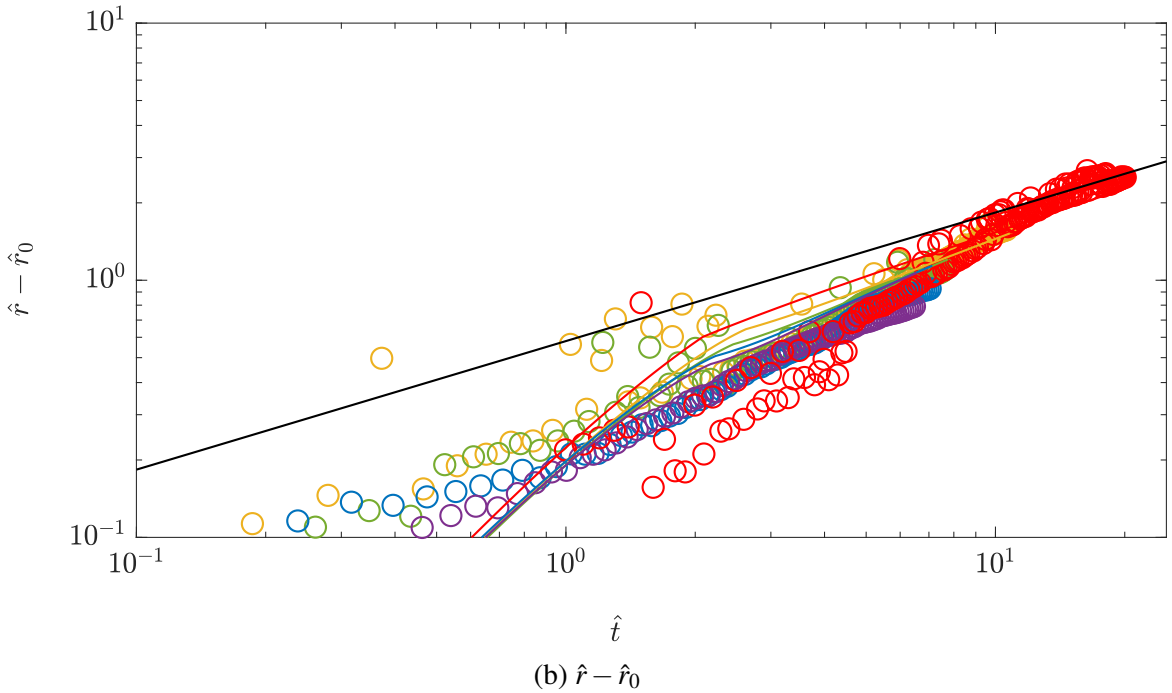

(b) $\hat{r} - \hat{r}_0$

Fig. 3.18 Vertical position of the centre of mass $\hat{z}_c$ and radius $\hat{r} - \hat{r}_0$ of the thermal for $L/D = 1$ (red), 2 (yellow), 3 (green), 4 (blue) and 5 (purple) at $H/D = 8$ compared to the solutions of the 3 phase model with constant shape factor b and constant entrainment coefficient α (coloured lines). The black curve is the similarity solution given by (3.7) with $m = 3$ and $n = 0.25$.

of L/D can be improved by increasing the value of α for $L/D = 1$ and 2 and decreasing the value of α for $L/D = 5$. However, this reduces the agreement with the radius. We are able to tune the model relatively well for z_c and r by changing α. However, it is not possible for the model to agree with both z_c and r for the same value of α. Even when using the varying shape factors the entrainment assumption using a constant value of α fails to give a good prediction for the vertical position of the centre of mass and the radius. In the case of the first two phases this is unsurprising as the entrainment closure developed by Morton et al. [43] assumes self-similarity within the flow. In the following section we will instead consider a non-constant value of the entrainment coefficient α.

3.4.3 Variable shape factor b and variable entrainment coefficient α

Figure 3.23 shows the centre of mass and radius of a thermal from the experiments with $L/D = 1$, 2, 3, 4 and 5 performed at $H/D = 8$ (circles) on a log-log scale, along with the solutions for z_c and $r - r_0$ from the equations in table 3.2 (solid line) assuming now that neither the shape nor the entrainment coefficient α are constant. In this case the values of $b(t)$ are used to determine $m(t)$ for the first two phases using the spheroidal shape assumption. The experimental measurements of $r(t)$ and $z_c(t)$ are used to determine $n(t)$ using the equations for $\mathrm{d}r/\mathrm{d}t$ for the draining and development phases. The solutions presented here use a least squares fit to determine the value of $b(t)$, $r(t)$ and $z_c(t)$, and during the thermal phase we take the average constant values of b and n found previously. The least squares fit of b was the same as used previously. The least squares fits of r and z_c are of the form $r(t) = r_1t^4 + r_2t^3 + r_3t^2 + r_4t + r_5$ and $z_c(t) = zc_1t^4 + zc_2t^3 + zc_3t^2 + zc_4t$, and are plotted on figure 3.22 respectively, the coefficients and r^2 values for each L/D are given in Appendix E. Also, as above, we set $\hat{z}_b = -0.027\hat{t}^4 + 0.021\hat{t}^3 + 0.43\hat{t}^2 + 0.041\hat{t}$ which is the least squares fit of the measured values of z_b.

Neither the radius or centre of mass have an improved fit with this model compared to the other two, and still fails to qualitatively and quantitatively capture the evolution of the radius and the centre of mass. As we saw with the experiments the modelling of the descent and spread of a thermal is more complex than can be captured by the simple model we have presented here. We saw when comparing the model to the experimental data that the entrainment coefficient is not constant during the two initial phases of the thermal development. A model that allows for this non-constant entrainment coefficient has been developed and shown not to give a good estimation for either the vertical position of the centre of mass or the radius during the draining and development phases. The other assumption made in the derivation of these equations is assuming that the shape of the thermal is spheroidal. However, from these results alone it is unclear whether this assumption

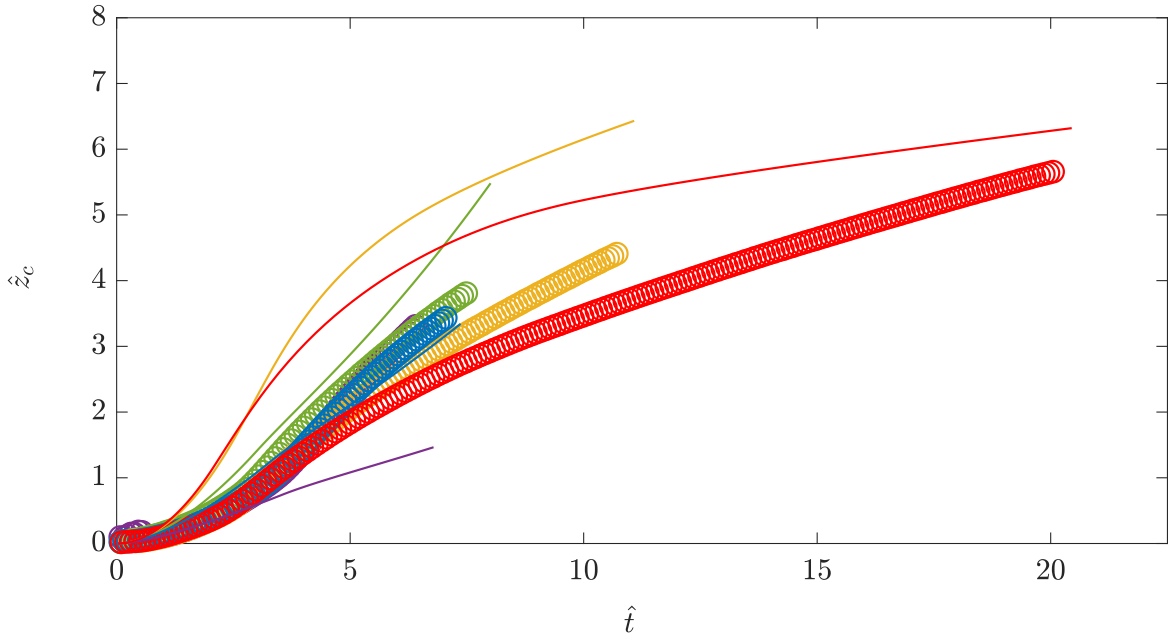

(a) $\hat{z}_c$

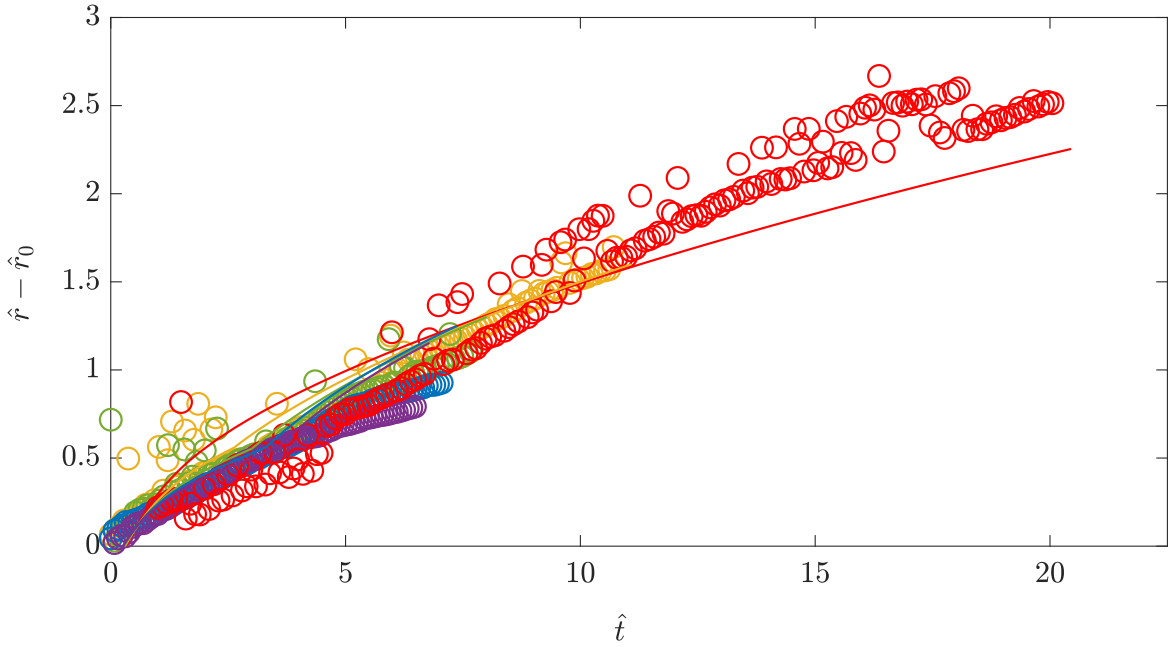

(b) $\hat{r} - \hat{r}_0$

Fig. 3.19 Vertical position of the centre of mass $\hat{z}_c$ and radius $\hat{r} - \hat{r}_0$ of the thermal for $L/D = 1$ (red), 2 (yellow), 3 (green), 4 (blue) and 5 (purple) at $H/D = 8$ compared to the solutions of the 3 phase model with variable shape factor $b(t)$ and constant entrainment coefficient α (coloured lines).

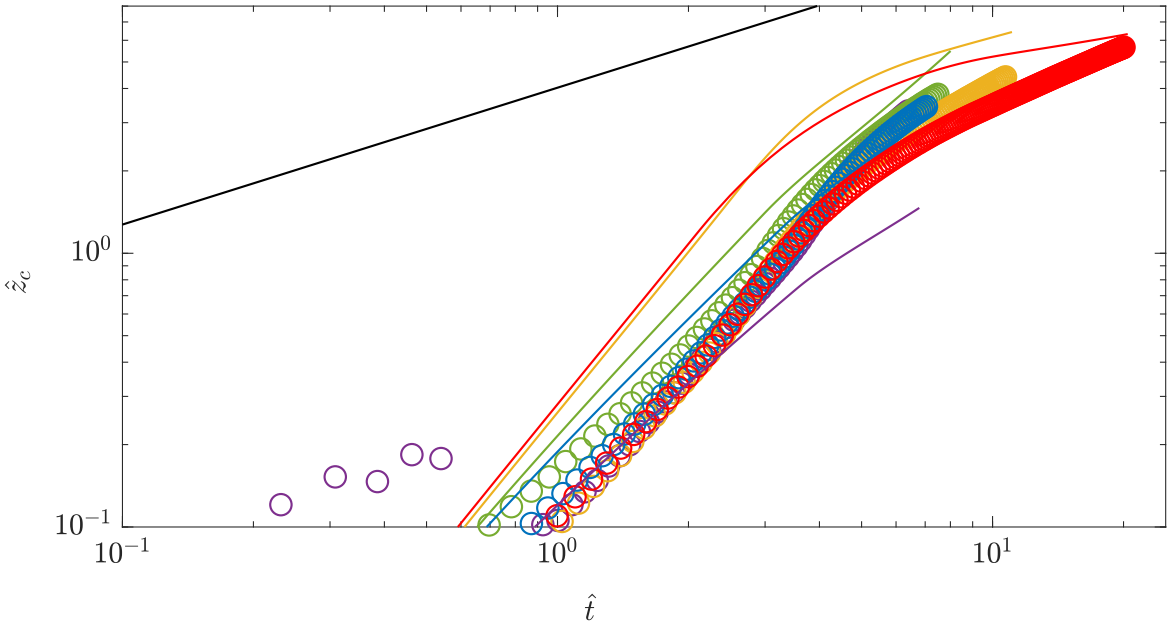

(a) $\hat{z}_c$

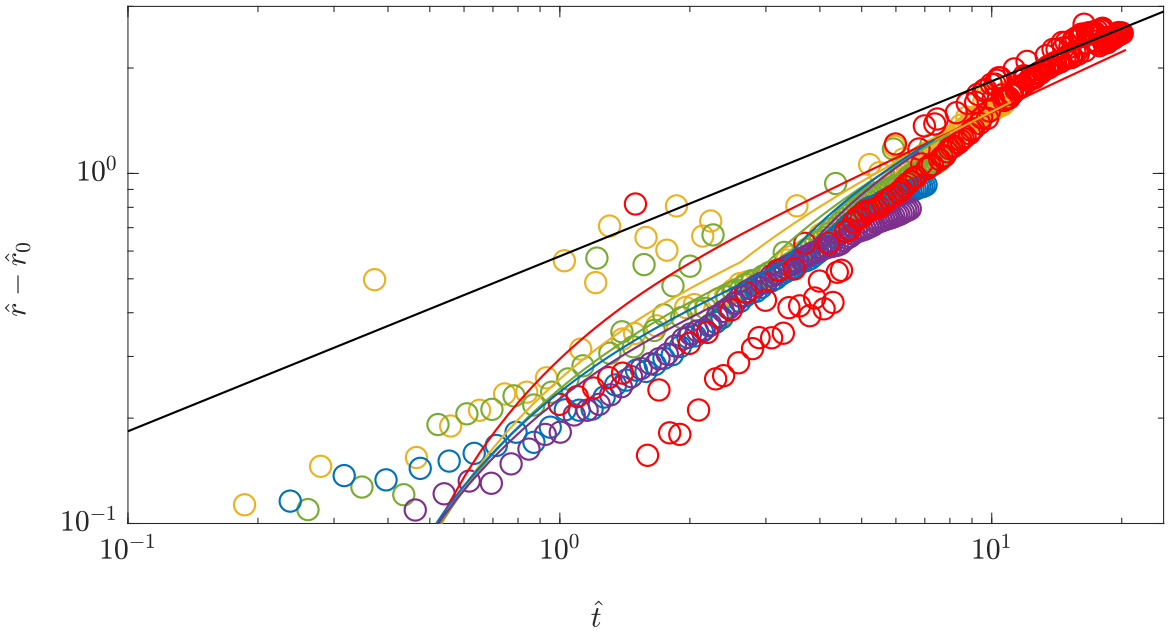

(b) $\hat{r} - \hat{r}_0$

Fig. 3.20 Vertical position of the centre of mass $\hat{z}_c$ and radius $\hat{r} - \hat{r}_0$ of the thermal for $L/D = 1$ (red), 2 (yellow), 3 (green), 4 (blue) and 5 (purple) at $H/D = 8$ compared to the solutions of the 3 phase model with variable shape factor $b(t)$ and constant entrainment coefficient α (coloured lines).

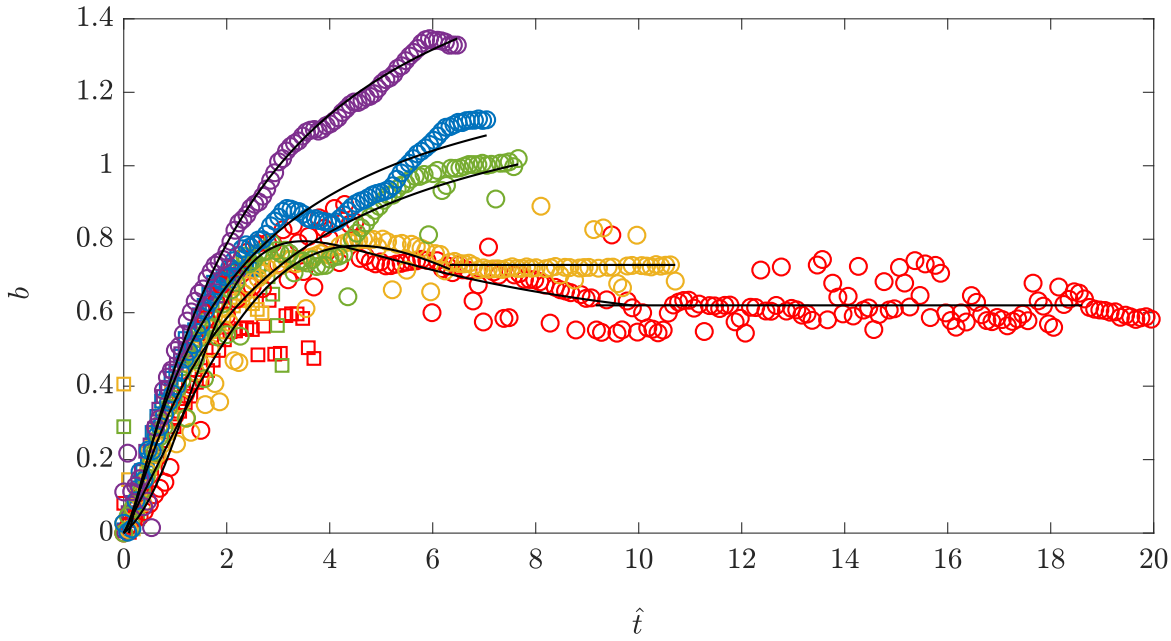

Fig. 3.21 Value of b for $L/D = 1$ (red), 2 (yellow), 3 (green), 4 (blue) and 5 (purple) at $H/D = 8$ compared to the least squares fits used to solve the three phase model. Each fit is of the form $b(t) = b_1t^4 + b_2t^3 + b_3t^2 + b_4t$.

is appropriate for any of the three phases. In the next section we will consider the validity of the shape assumption for the values of L/D considered here.

3.5 Discussion

3.5.1 Validity of Shape Assumption

Lai et al. [37] and Bond & Johari [8] found that beyond the ratio of $L/D = 2$ no further fluid can be incorporated into the spheroidal cap of a thermal and a tail of dense fluid forms behind the cap. Therefore, for $L/D > 2$ the assumption that the shape of a thermal can be represented by a spheroid becomes questionable. Instead for $L/D > 2$ the thermals have spheroidal caps with a trailing column of dense fluid or 'tail' which was seen in section 3.2.1 with the $L/D = 5$ experiment. The increase in b and m above 1 and $4\pi/3$ respectively for $L/D > 2$ in section 3.2 is indicative of this tail.

Using the experimental images it is possible to estimate the cross-sectional area A of the thermal. The experiments were backlit and therefore the image of the thermal that the camera records is integrated in the $y-$direction. Under the assumption that the thermal is an axisymmetric spheroid the images show the central cross-section of the spheroid, and

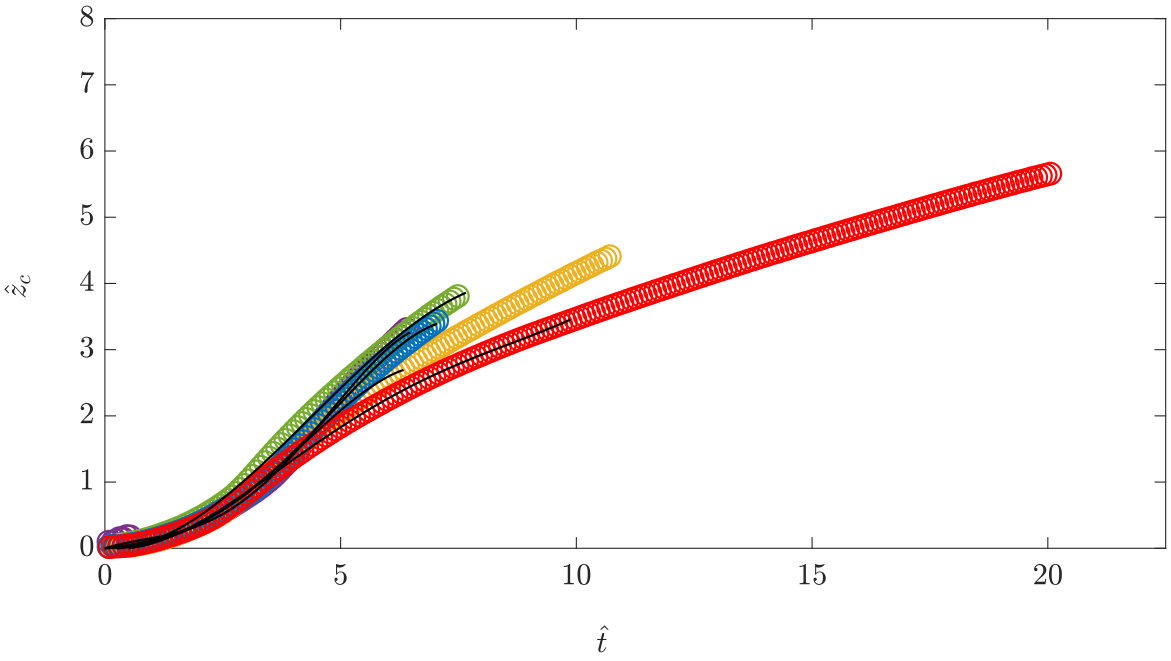

(a) $\hat{r} - \hat{r}_0$

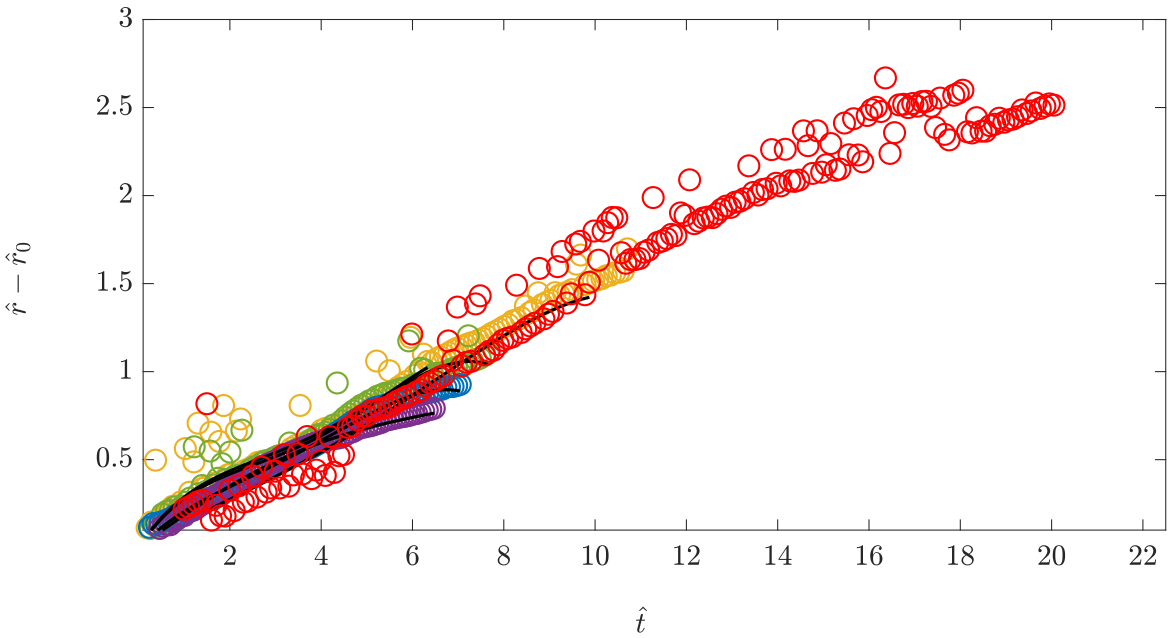

(b) $\hat{z}_c$

Fig. 3.22 Vertical position of $\hat{z}_c$ and radius $\hat{r} - \hat{r}_0$ for $L/D = 1$ (red), 2 (yellow), 3 (green), 4 (blue) and 5 (purple) at $H/D = 8$ compared to the least squares fits used to solve the three phase model. All of the fits are of the form $z_c(t) = zc_1t^4 + zc_2t^3 + zc_3t^2 + zc_4t$ and $r(t) = r_1t^4 + r_2t^3 + r_3t^2 + r_4t + r_5$.

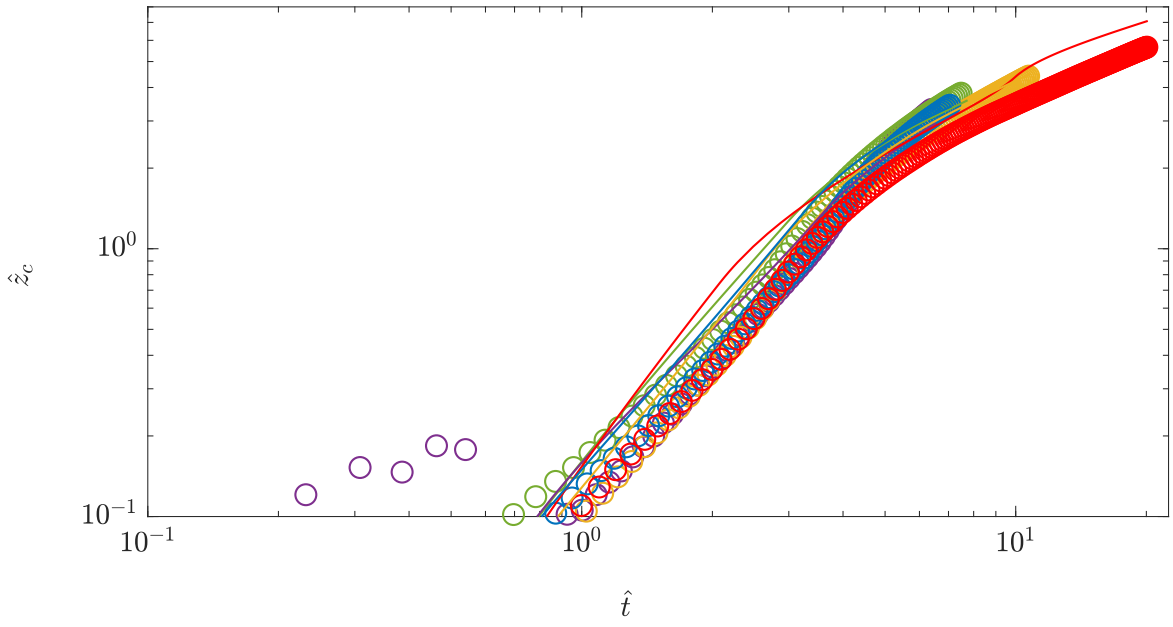

(a) $\hat{z}_c$

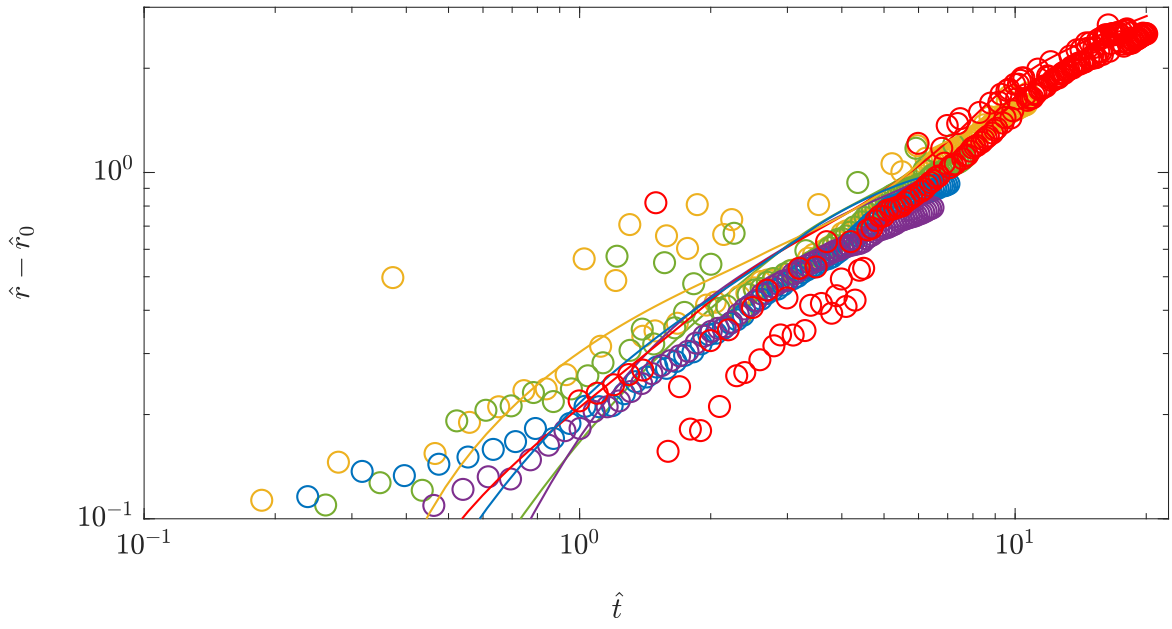

(b) $\hat{r} - \hat{r}_0$

Fig. 3.23 Vertical position of the centre of mass $\hat{z}_c$ and radius $\hat{r} - \hat{r}_0$ of the thermal for $L/D = 1$ (red), 2 (yellow), 3 (green), 4 (blue) and 5 (purple) at $H/D = 8$ compared to the solutions of the 3 phase model with variable shape factor $b(t)$ and $n(t)$ found directly from fits to z_c and r (coloured lines).

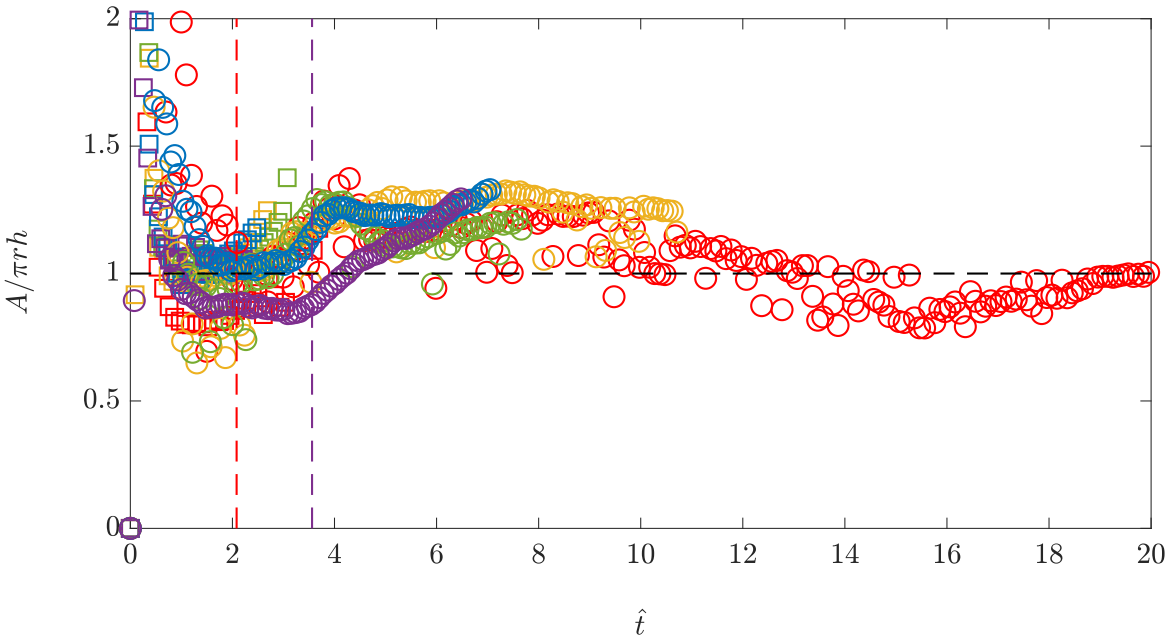

Fig. 3.24 Time dependent value of $A/(\pi rh)$ for $L/D = 1$ (red), 2 (yellow), 3 (green), 4 (blue) and 5 (purple) at $H/D = 2$ (squares) and 8 (circles).

by counting the number of pixels that have an intensity of above a certain threshold the cross-sectional area can be estimated.

Under the spheroidal shape assumption the cross-sectional area can be written as $A = \pi rh$. It is possible to measure A, r and h directly, and can therefore determine the instantaneous values of $A/\pi rh$. The values of this for the $L/D = 1$, 2, 3, 4 and 5 are shown in figure 3.24 at $H/D = 2$ and 8.

In order for the spheroidal shape assumption to be valid we require $A/(\pi rh) = 1$ (horizontal dashed line). However, in the majority of cases this condition is not satisfied. In all cases the value of $A/(\pi rh)$ initially decreases reaching a minimum value just before the end of draining has occurred (vertical dashed lines), and then continues to increase until some experiments attain a constant value. The only experiments where $A/(\pi rh)$ attains a constant value are $L/D = 1$, 2, 3 and 4 at $H/D = 8$. However, in this case when $L/D = 1$, $A/(\pi rh) = 0.91 \pm 0.07$ and when $L/D = 2$, $A/(\pi rh) = 1.3 \pm 0.07$ when averaged over 2 s. However, from the measurement of the cross-sectional area alone, it is unclear how to best model the shape of a developing thermal. For more information we require the values of both the volume and the surface area of the thermal, which requires 3-dimensional data. This data can however, be obtained from the numerical simulations performed in chapter 5 and we will return to this question there.

3.6 Conclusions

In this chapter the existing theory for thermals has been presented and compared to the experimental measurements. There are two assumptions made during the development of thermal theory:

1. that the shape of a thermal is spheroidal and therefore the volume $V = mr^3$, where m is known as the thermal shape factor,

2. and through the entrainment assumption that the radius has some spreading rate n where $n \approx \alpha$, the entrainment coefficient.

The value of m can be written as a function of b, the ratio of the semi-minor and major radii of the thermal. Both b and n have been measured directly and it has been shown that the value of these constants depends on the value of L/D. Importantly, it is also shown that neither b or n have a constant value during the draining phase and for some time after the end of draining. Three phases of a thermal development have hence been proposed: the draining phase, the development phase and the self-similar phase. We have shown the heights at which these three phases occur in our experiments and hence determined the phase of the thermal upon impact. We have also shown that the duration of the initial acceleration phase (the draining and development phase combined) does not occur between one to two draining times as found by Bond & Johari [8]. Although, constant values of b and n, and the vertical position of the thermal approaching the similarity solution were not observed for experiments performed with $L/D > 2$, experiments at larger values of H/D would be needed in order to find these heights.

A novel theory for the evolution of a thermal during the draining and development phase has been proposed. The draining equations require only that function of the position of the interface of the source fluid is known, and so can be extended to another experimental set up with different initial conditions. The three phase model has been shown to fit well with the centre of mass data from the experimental results when using the measured values of b and under the assumption that α is not constant. However, to achieve this a priori knowledge of the aspect ratio b, the centre of mass z_c and the radius $r - r_0$ is required.

However, the theory has not been able to accurately capture the evolution of both the vertical position and the radius so it is unclear as to whether the spheroidal shape assumption is valid. It was observed that the thermals produced by the tubes with $L/D = 1$ were better represented by a torus than a spheroid. The equations for the three phases have been derived under the toroidal assumption and solved and compared to the experimental results. The toroidal assumption however, did not improve the model for $L/D = 1$ and so has been omitted.

The details of how the toroidal assumption changes the three phase equations can be found in Appendix D. By looking at the cross-sectional area of the thermal we have shown that the shape assumption we initially make does not hold for $L/D > 2$, nor during the draining and development phases. It is unclear how to best model the shape of a developing thermal from the cross-sectional area alone and 3-dimensional data would be more useful. We therefore return to this question in chapter 5.

Finally, we conclude that the initial acceleration phase of a thermal observed previously can be split into two separate phases: the draining phase and the development phase, both of which assume a non-constant growth of the shape of the thermal. In the following chapter we will discuss how these three phases of the thermal upon impact affect the resulting spread of the axisymmetric gravity currents.

Chapter 4

Gravity Currents

4.1 Introduction

When studying gravity currents in the laboratory they are typically produced by a lock release experiment e.g. van der Wiel et al. [58], Hallworth et al. [29, 28], Huq [35]. A typical lock release experiments take place in a rectangular or cylindrical sector shaped tank with a gate located at one end. In both cases the fluid behind the gate has its density ρ_0 differing to the fluid on the other side of the gate, of density ρ_a. The gate is then removed and the buoyancy driven flow allowed to evolve creating a gravity current. Axisymmetric gravity currents have been produced from an elevated source of dense fluid impacting on a horizontal boundary, as is considered here. This type of experiment has been performed for gravity currents created by jets and plumes impacting a boundary by Rooney & Linden [51] and Simpson [55], and by thermals impacting a boundary by Lundgren et al. [41] and Rooney [49]. From both lock release experiments and the gravity currents produced by elevated sources, similarity solutions derived from the shallow water equations with some suitable condition at the front of the current have been shown to agree well with experiments. Similar to thermals, gravity currents also go through an initial adjustment period known as the slumping phase [34]. This phase can last between 3 to 10 times the initial radius of the release depending on the initial depth of the current compared to the depth of the ambient fluid [33]. In this chapter we compare the following model to measurements from the laboratory experiments and discuss the effects of the height and initial aspect ratio of the source has on the dynamics of the resulting gravity current, as well as on the transition from a thermal to a gravity current. Crucially, for the first time we classify the thermal on impact into one of three classes and investigate the implications for the development of the gravity current.

4.1.1 Theory

In this section we follow the derivation of an axisymmetric gravity current model used by Rooney [49] and Huq [35]. For an axisymmetric gravity current released from a lock the evolution of the leading edge is dependent on the reduced gravity g' and the vertical height of the current h. It is assumed that at the nose of the gravity current that the Froude number Fr is constant in the range of $1-1.2$ by Huq [35] and 1.4 by Rooney & Linden [51]. This result was first established by Benjamin [6] and Von Karman [56] where the Froude number

$$Fr = \frac{u}{\sqrt{g'h}} \tag{4.1}$$

where u is the radial velocity of the front of the current. In an unstratified environment buoyancy $B = g'V$ is conserved i.e. $g'V = g'_0V_0$, where V is the volume of the current and the subscript 0 denotes the initial values of reduced gravity and volume of the gravity current. By considering what is known as the box model, we assume that the gravity current evolves as a cylinder with increasing radius r and decreasing height h with no mixing. Then the volume V can be written as $V = \lambda^{-1}r^2h$ where $\lambda = \pi^{-1}$ is constant for a cylindrical release. Using this shape assumption the conservation of buoyancy can be written as

$$g'\lambda^{-1}r^2h = g'_0V_0,$$

and rearranging for $g'h$ and substituting this into (4.1) we obtain

$$u = Fr\lambda^{1/2}B_0^{1/2}r^{-1}. \tag{4.2}$$

As is the case for a thermal the entrainment process, neglected in the above derivation, determines the evolution of the volume and hence the reduced gravity and height. Hallworth et al. [29] proposed that the relative proportion of entrained fluid should be independent of g'. Experimentally they developed a relationship for V/V_0 as a function of the radius and the initial volume. This is equivalent to having the following:

$$\frac{V}{V_0} = f\left(\frac{r}{r_0}\right), \tag{4.3}$$

where r_0 is the initial radius, and the function f is an unknown function to be determined. Then, by substituting the assumption that $V = \lambda^{-1}r^2h$ into (4.3) we have the equation for the evolution of the height h

$$h = \lambda^{-1}V_0 f\left(\frac{r}{r_0}\right)r^{-2}. \tag{4.4}$$

Knowing that the total buoyancy must be conserved (4.3) gives

$$g' = B_0 \left(V_0 f \left(\frac{r}{r_0} \right) \right)^{-1}. \tag{4.5}$$

So in summary the equations that govern an axisymmetric gravity current are given by

$$u = Fr\lambda^{1/2} B_0^{1/2} r^{-1}, \tag{4.6a}$$

$$h = \lambda^{-1} V_0 f \left(\frac{r}{r_0} \right) r^{-2}, \tag{4.6b}$$

$$g' = B_0 \left(V_0 f \left(\frac{r}{r_0} \right) \right)^{-1}. \tag{4.6c}$$

The derivation of (4.6a) seemingly includes no mixing. However, if we rewrite the conservation of buoyancy using (4.3) then we obtain

$$g' f \left(\frac{r}{r_0} \right) = g'_0,$$

substituting into (4.1)

$$\begin{aligned} u =& \mathrm{Fr} f^{-1/2} \left(\frac{r}{r_0} \right) \sqrt{g'_0 h}, \\ =& \mathrm{Fr} f^{-1/2} \left(\frac{r}{r_0} \right) \left(\frac{h}{h_0} \right)^{1/2} \sqrt{g'_0 h_0}, \end{aligned}$$

then, using the assumption that $V = \lambda^{-1} r^2 h$ we obtain

$$\begin{aligned} u &= \mathrm{Fr} f^{-1/2} \left(\frac{r}{r_0} \right) \left(\frac{h}{h_0} \right)^{1/2} \sqrt{g'_0 V_0 \frac{\lambda}{r_0^2}}, \\ &= \mathrm{Fr} f^{-1/2} \left(\frac{r}{r_0} \right) \left(\frac{h}{h_0} \right)^{1/2} B_0^{1/2} \lambda^{1/2} r^{-1}. \end{aligned}$$

Equating this to the equation for u derived using no mixing assumption (4.6a) we obtain

$$\mathrm{Fr} f^{-1/2} \left(\frac{r}{r_0} \right) \left(\frac{h}{h_0} \right)^{1/2} B_0^{1/2} \lambda^{1/2} r^{-1} = \mathrm{Fr} \lambda^{1/2} B_0^{1/2} r^{-1}$$

rearranging for f gives

$$f\left(\frac{r}{r_0}\right) = \frac{hr^2}{h_0 r_0^2} = \frac{V}{V_0}$$

as assumed. However, these equations are only valid for an axisymmetric gravity current produced by a lock release. In the following section we will consider how these equations apply to a gravity current produced by a thermal.

4.1.2 Gravity Currents Produced by Thermals Impacting on a Boundary

The equations given in (4.6) are valid for an axisymmetric current produced by a lock release. By using this model to describe a gravity current produced by a thermal we ignore any momentum transferred from the thermal to the gravity current during impact with the ground, the validity of this will be discussed later in section 4.3.2. Also, the initial values of reduced gravity, volume and radius used in the model are in fact these values at the time of impact. So, the equations become

$$u = Fr\lambda^{1/2} B_0^{1/2} r^{-1}, \tag{4.7a}$$

$$h = \lambda^{-1} V_i f\left(\frac{r}{r_i}\right) r^{-2}, \tag{4.7b}$$

$$g' = B_0 \left(V_i f\left(\frac{r}{r_i}\right)\right)^{-1}, \tag{4.7c}$$

where the subscript i denotes the time of impact, and the subscript 0 the initial source conditions of the thermal. Noting that $u = \mathrm{d}r/\mathrm{d}t$ integrating (4.7a) with respect to time the radius of the gravity current is given by

$$r^2 - r_i^2 = 2Fr\lambda^{1/2} B_0^{1/2} (t - t_i). \tag{4.8}$$

For $r \gg r_i$ the radial length at impact becomes unimportant and so

$$r = \left(2Fr\lambda^{1/2} B_0^{1/2}\right)^{1/2} (t - t_i)^{1/2} \tag{4.9}$$

Both t_i and r_i are measurable quantities from our experiments, however V_i is not. V_i is needed to determine the function form of f. We can use results from thermal theory discussed in chapter 3 to calculate estimates of V_i. The volume of a thermal can be expressed as

$$V = \frac{4}{3}\pi b r^3,$$

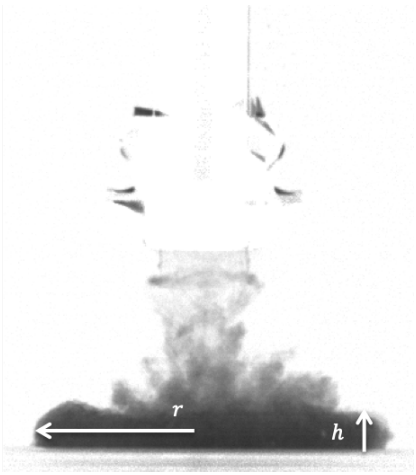

Fig. 4.1 Example image of a gravity current with the measurements of the radial spread r and the height of the gravity current h illustrated.

where r is the radial position of the thermal and b is constant only for self-similar thermals. Upon impact the thermal has volume V_i

$$V_i = \frac{4}{3}\pi b_i r_i^3.$$

However, we have seen in the previous chapter there are experiments that impact the ground while the tube is still draining, or during the development phase of a thermal. We have shown that in both of these cases it is assumed that the volume of the thermal

$$V = \frac{4}{3}\pi b(t) r^3.$$

Therefore, if the thermal has been released at a height H above the ground then upon impact the thermal has volume V_i

$$V_i = \frac{4}{3}\pi b(t_i)_i r_i^3.$$

where in both cases the values of $b(t_i)$ and r_i are to be determined by the experiments.

4.2 Results

In this section the measurements of the gravity current created by releasing a thermal in the laboratory experiments will be presented. As described in Chapter 2 two quantities are measured directly from the experimental images: the radial position, r, and the height, h. A sketch of these quantities are superimposed on an experimental image in figure 4.1.

Qualitative images comparing the evolution of the gravity currents at the two values of H/D for our two extreme values of $L/D = 1$ and 5 will be discussed in section 4.2.1. This will be followed by the measurable results in sections 4.2.2 and 4.2.3.

4.2.1 Qualitative Results

The raw images from four experiments are each shown at four times in figures 4.2 to 4.5. The four experiments considered comprise of two experiments each from the two values of H/D considered in this study, 2 and 8. The two experiments at each height have different values of L/D, 1 and 5. The values of 1 and 5 were chosen since these are the shortest and longest tubes which have been considered in this study.

The experiments performed with $L/D = 1$ at $H/D = 2$ are shown in figure 4.2, and at $H/D = 8$, figure 4.3. In both figures the top left panel shows the thermal at the point of impact with the floor, followed by the gravity currents at 1 s intervals after impact (top right). The experiments performed with $L/D = 5$ at $H/D = 2$ are shown in figure 4.4 and at $H/D = 8$, figure 4.5. Again, in both figures the top left panel shows the thermal at the point of impact with the floor, followed by the gravity current at 0.5 s (top right), and the gravity currents at 1 s intervals after impact (bottom row).

First consider the time of impact for both lengths of tube shown in the top left panel of figures 4.2 to 4.5. The thermal from the two lengths of tube are qualitatively very different at this time for both heights. The most drastic difference being for the experiment with $H/D = 2$ and $L/D = 5$ which impacts the ground before the end of the draining phase. However, even when $H/D = 8$ there is a difference between the two lengths of tube. For $L/D = 1$ the radius is $6-7$ times the tube radius and the shape resembles an oblate spheroid, whereas, for $L/D = 5$ is only 4.5 times the tube radius and the shape resembles an prolate spheroid.

The gravity currents produced by the experiments with $L/D = 5$ at both heights are shown in figures 4.4 and 4.5. After impact the height of the gravity current appears to grow between impact+0.5 s and impact+1 s. During this time the radius also appears to increase very little compared to the gravity currents at impact+2 s. To investigate this growth in height further both the radius and the height of the gravity currents are discussed in the following section.

4.2.2 Front Speed

In this section the results of the radius of the front of the gravity current measured from the experiments are presented. For all the data presented here the radius, r, is measured from the

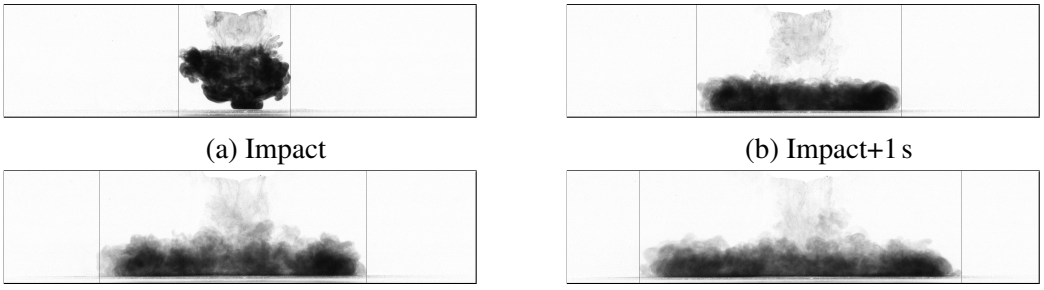

(a) Impact (b) Impact+1 s

(c) Impact+2 s (d) Impact+3 s

Fig. 4.2 Snapshots at impact with the ground for $L/D = 1$ at $H/D = 2$

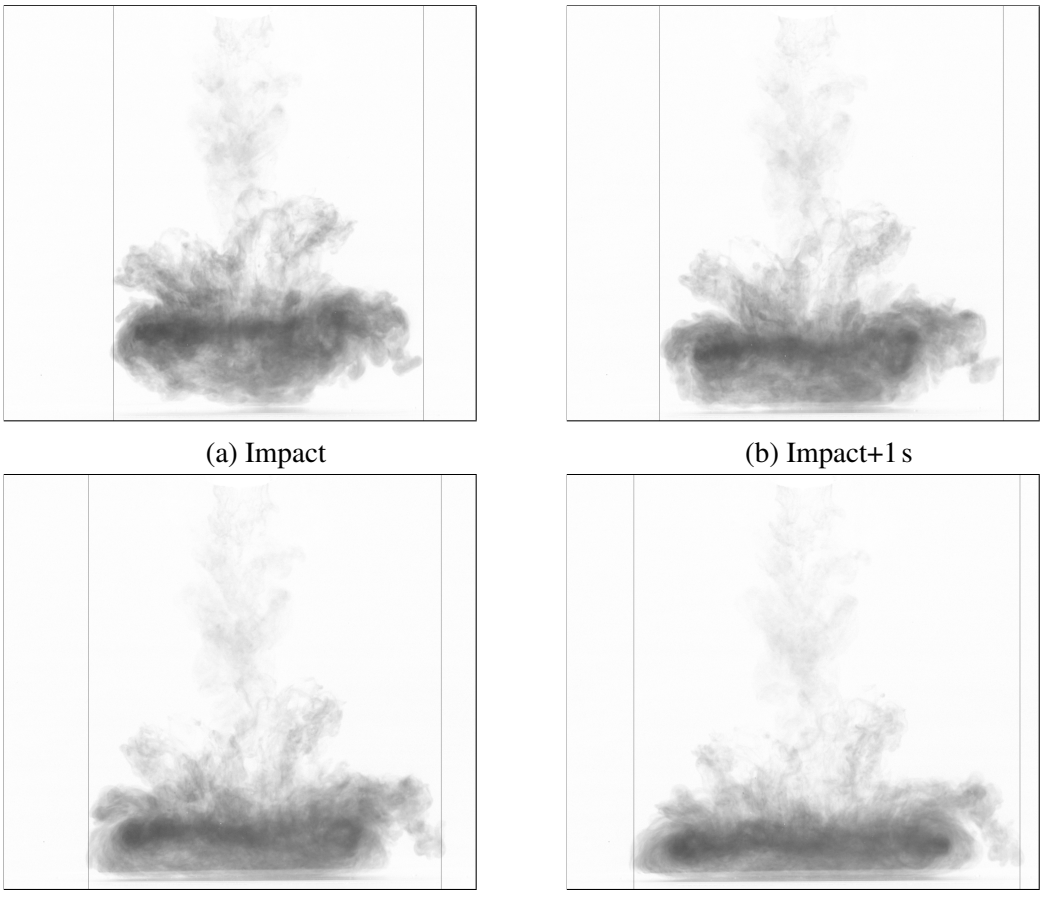

(a) Impact (b) Impact+1 s

(c) Impact+2 s (d) Impact+3 s

Fig. 4.3 Snapshots at impact with the ground for $L/D = 1$ at $H/D = 8$

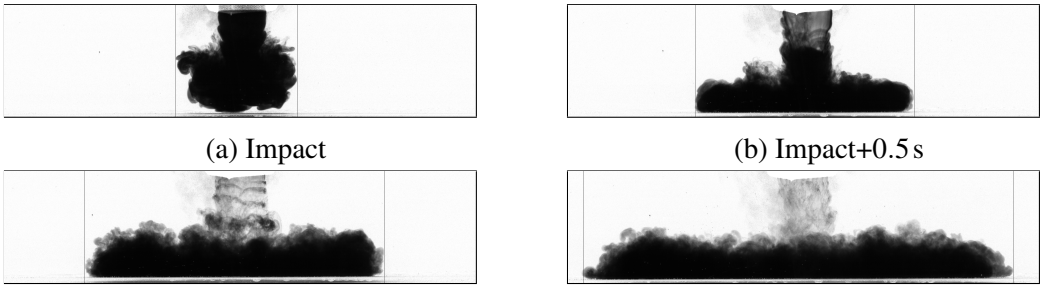

(a) Impact (b) Impact+0.5 s

(c) Impact+1 s (d) Impact+2 s

Fig. 4.4 Snapshots at impact with the ground for $L/D = 5$ at $H/D = 2$

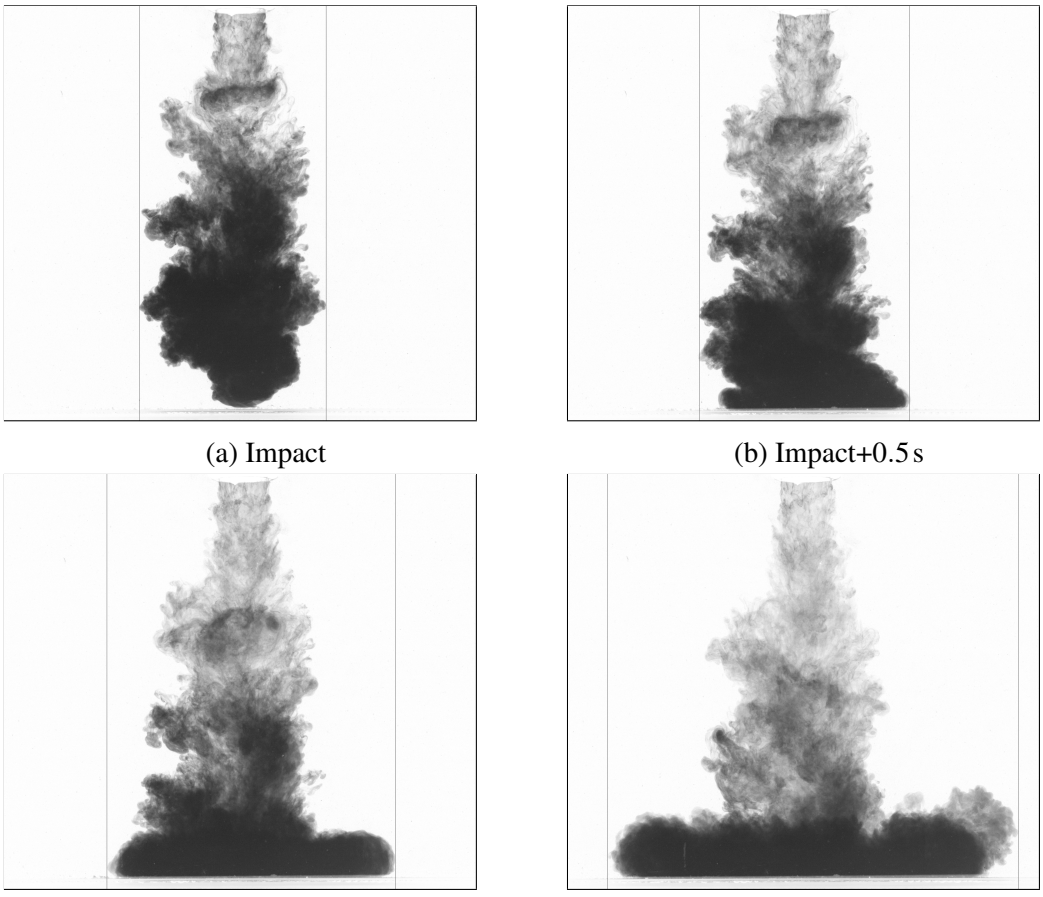

(a) Impact (b) Impact+0.5 s

(c) Impact+1 s (d) Impact+2 s

Fig. 4.5 Snapshots at impact with the ground for $L/D = 5$ at $H/D = 8$

centre of the tube. It is found by measuring both the left and right flowing current and taking the average of the two radii for each experiment. As was done for the thermals (see chapter 2) the data from each length of tube are then the ensemble average of a set of experiments of this measurement of r. In order to make comparisons between the gravity currents for different length tubes the difference between non-dimensional radial position $\hat{r}$ and the radial position of the thermal upon impact $\hat{r}_i$ is considered. The radius and time are non-dimensionalised by the same scalings used for thermals i.e. $R_0 = V_0^{1/3}$ and $T_0 = (R_0/g_0')^{1/2}$.

Firstly, we consider the radii of the experiments performed for $L/D = 1$, 2, 3, 4 and 5 at $H/D = 2$, which are shown in figure 4.6a. There are insignificant differences between the tubes of length $L/D = 3$, 4 and 5, whereas, the radius for tubes of length $L/D = 1$ and 2 indicate a slower current formed from these releases. However, the variation between the different lengths of tube is of the same order as the uncertainty as reflected by the noise in the shaded regions of figure 4.6a.

Similarly, for experiments performed at $H/D = 8$, shown in figure 4.6b, there is good agreement between the tubes of length $L/D = 3$, 4 and 5. Whereas, in contrast to the experiments performed at $H/D = 2$, for tubes of length $L/D = 1$ and 2 the radius of the gravity currents varies significantly from the other experiments. In these cases the measurements for $L/D = 1$ and 2 were difficult to track. In particular for $L/D = 1$ there was a large amount of noise in the experimental images. Despite our novel method of dye attenuation making a significant improvement, the amount by which the dye was diluted for this experiment, was sufficient that the variation in light intensity due to changes in the dye levels were comparable with the noise from the image, making edge detection difficult.

4.2.3 Heights of Gravity Currents

In this section the results of the heights of the gravity current measured from the experiments are presented. The height is measured from the moment that the thermal impacts the ground, and is measured by finding the average height across the current. The average of the left and right moving currents are taken to obtain the height measurement for each experiment. The heights of the left and right moving currents are found by first finding the edges of the flow as outlined in chapter 2. The gradients of the edges are then examined in order to identify peaks which represent the radial positions of the left and right moving currents, and the radial positions of either side of the trailing stem of the thermal. Therefore, initially the height is only the measure of the radially spreading fluid and does not include any fluid from the thermal that may still be descending. At later times, when there is no descending fluid, the height is averaged across the whole width of the gravity current. The data from each length

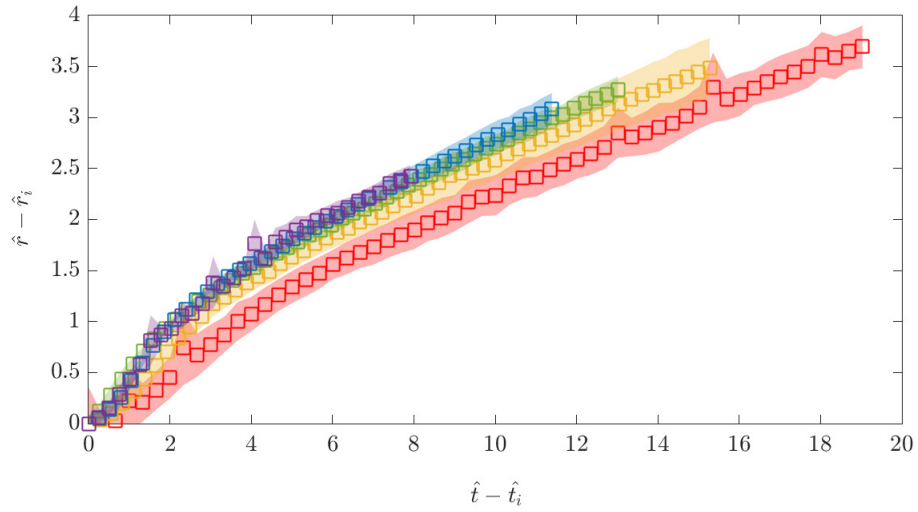

(a) $H/D = 2$

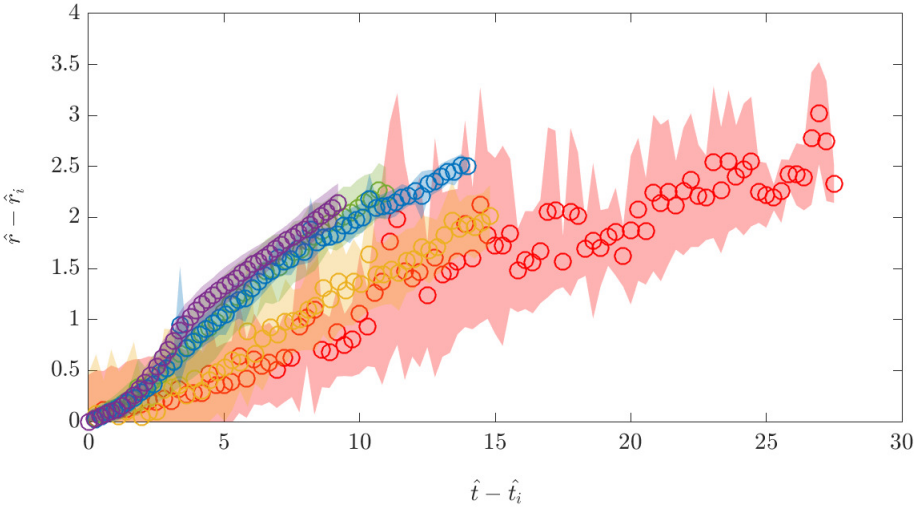

(b) $H/D = 8$

Fig. 4.6 Average radius position of the gravity current $\hat{r} - \hat{r}_i$ for $L/D = 1$ (red), 2 (yellow), 3 (green), 4 (blue) and 5 (purple) at $H/D = 2$. The shaded region represents $\pm$ one standard deviation from the average.

of tube is then the ensemble average of a set of experiments for measurements of h, as was outlined in chapter 2.

Firstly, the value of h for the experiments performed at $H/D = 2$ is plotted for $L/D = 1$, 2, 3, 4 and 5 in figure 4.7a. The height of the gravity current decreases as the value of L/D increases. It was observed from the experiments that for some initial period after impact the radial spread appeared to decrease in speed whilst the gravity currents 'fill' to a certain height, the radial spread then began to accelerate again and the height of the current decreased as expected. This effect on the height is especially clear in our measurements of h at $0 \leq \hat{t} - \hat{t}_i \leq 5$ in the larger values of L/D (e.g 3, 4 and 5) and to some extent for $L/D = 1$ and 2 at these times.

The heights of the gravity currents for the experiments performed at $H/D = 8$ are shown in figure 4.7b. The heights appear to decrease as L/D increases from 2 to 4. However, as with the experiments performed at $H/D = 2$ the height for the gravity current with $L/D = 5$ experiences the growth in height described above. The heights of the gravity currents performed with $L/D = 1$ at $H/D = 8$ have been excluded due to the large uncertainty observed in the measurements as mentioned previously there was a large amount of noise in these experimental images and despite our novel method of dye attenuation the variation in light intensity due to changes in the dye levels were comparable with the noise from the image, making edge detection difficult.

4.3 Discussion

4.3.1 Comparison with Model

The radial position of the gravity current scaled by the length scale used in the previous chapter which is based on the initial release volume is plotted for all tube lengths for both $H/D = 2$ and $H/D = 8$ in figures 4.8a and 4.8b, respectively. The dashed line drawn on the plots is $\hat{r} = 1.26(\hat{t} - \hat{t}_i)^{1/2}$, which is the similarity solution for $r \gg r_i$ given by (4.9) taking $\lambda = \pi^{-1}$ and $Fr = 1.4$ the value of the Froude number used by [51].

Figure 4.8a shows the radial position of the gravity current for the experiments performed at $H/D = 2$ for $L/D = 1$, 2, 3, 4 and 5. As we saw in the previous chapter at this height the thermals are either in the development phase, or are still draining when impact with the ground occurs. At this height the time it takes for the gravity current to reach the self-similar solution decreases as the value of L/D increases. At later times all the data reach the gradient predicted by similarity solution, i.e. $\hat{r} = 1.26(\hat{t} - \hat{t}_i)^{1/2}$. However, by taking $\lambda = \pi^{-1}$ and

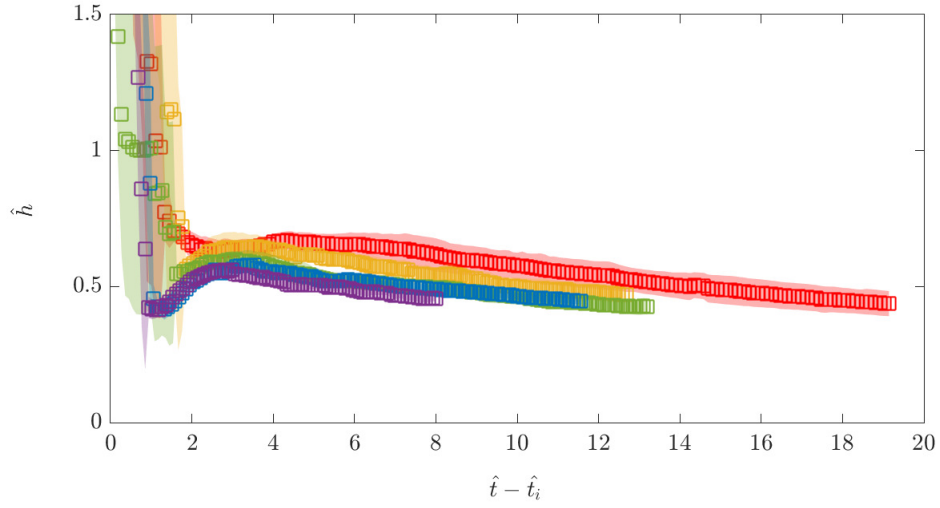

(a) $H/D = 2$

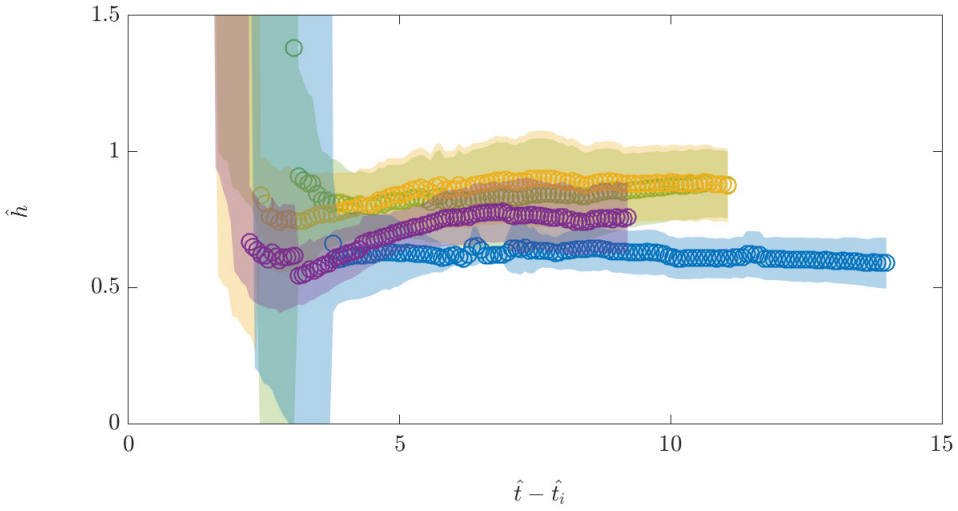

(b) $H/D = 8$

Fig. 4.7 Average height of the gravity current $\hat{h}$ for $L/D = 1$ (red), 2 (yellow), 3 (green), 4 (blue) and 5 (purple) at $H/D = 2$ (squares) and 8 (circles). The shaded regions represent $\pm$ one standard deviation from the average.

$\mathrm{Fr} = 1.4$ the similarity solution does not quantitatively represent the gravity currents at this height.

Figure 4.8b shows the radial position of the gravity current for the experiments performed at $H/D = 8$ for $L/D = 1$, 2, 3, 4 and 5. Again, as we saw in the previous chapter at this height the thermals are either in the development or the self-similar phases when impact with the floor occurs. At this height the differences in the time it takes for the gravity currents to reach the gradient of the self-similar solution is significantly increased compared to the gravity currents produced from the releases at $H/D = 2$. Similarly to $H/D = 2$ this time decreases as the value of L/D increases. As with the releases at $H/D = 2$ all the data reach the gradient predicted by similarity solution, i.e. $\hat{r} = 1.26(\hat{t} - \hat{t}_i)^{1/2}$. However, by taking $\lambda = \pi^{-1}$ and $\mathrm{Fr} = 1.4$ the similarity solution does not quantitatively represent the gravity currents at this height either.

Using the data of the position of the height of the gravity current an estimate for the function $f(r/r_i)$ can be made using (4.7b). The value of $f(r/r_i) = hr^2/V_i$ has been plotted in figure 4.9 for all tube lengths for both $H/D = 2$ and $H/D = 8$. There are two distinct groupings of experiments, the experiments performed at $H/D = 2$, (squares), and the experiments performed at $H/D = 8$, (circles). The data from the experiments performed at $H/D = 2$ fall approximately on the line $f = 0.43(r/r_i)^{1.49}$. The data from the experiments performed at $H/D = 8$ approximately fall on the line $f = 0.11(r/r_i)^{2.02}$. Both of these lines are the least squares fits of the calculated value of f.

It is to be expected that initially the gravity current does not agree with the similarity solution as, similar to thermals, gravity currents also have a development phase known as the slumping phase. Not only this but, as the equations are for a lock release experiment. They therefore do not consider the initial momentum the thermal has during impact and transition to gravity current. We have seen in the previous chapter that the radius and the shape, and therefore the volume, of a thermal upon impact is variable depending on the value of L/D and H/D which will affect the momentum of the flow that transitions from thermal to gravity current. In the following section we will discuss the transition from a thermal to a gravity current further, and the length scales over which this initial momentum provided by the thermal may affect the gravity current.

4.3.2 Transition From Thermal to Gravity Current

We have seen in chapter 3 that for the values of L/D and H/D considered, the thermal can impact the ground in one of three phases: the draining, development or the self-similar thermal phases. We also determined the vertical positions of the thermal at which these three phases occur depending on L/D (figure 3.13). For the gravity currents we have seen that

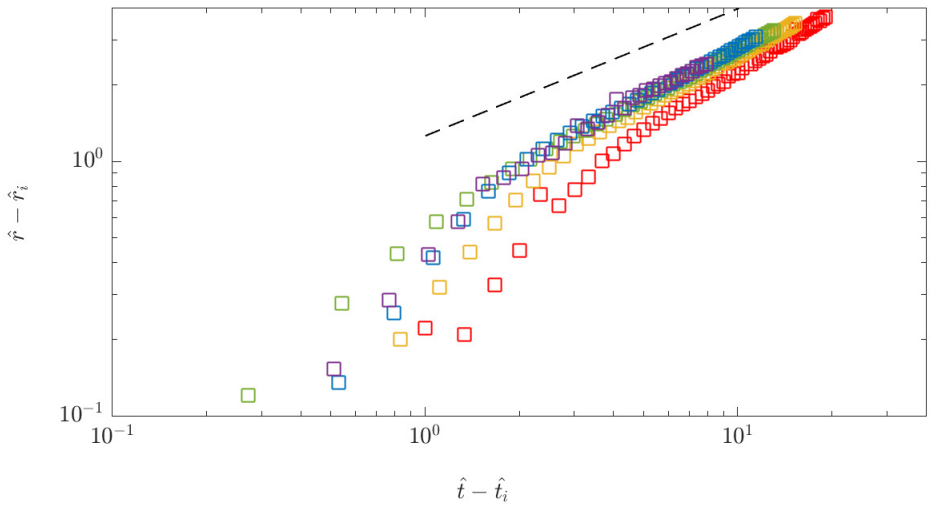

(a) $H/D = 2$

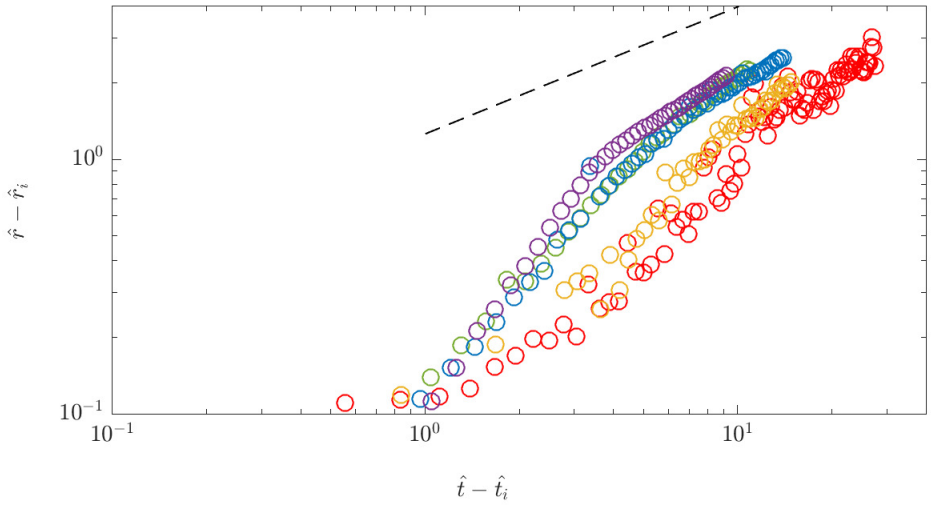

(b) $H/D = 8$

Fig. 4.8 Average radius of the gravity current for $L/D = 1$ (red), 2 (yellow), 3 (green), 4 (blue) and 5 (purple) at $H/D = 2$ and 8. The dashed line represents the similarity solution with $\lambda = pi^{-1}$ and $Fr = 1.4$ given by $\hat{r} = 1.26(\hat{t} - \hat{t}_i)^{1/2}$.

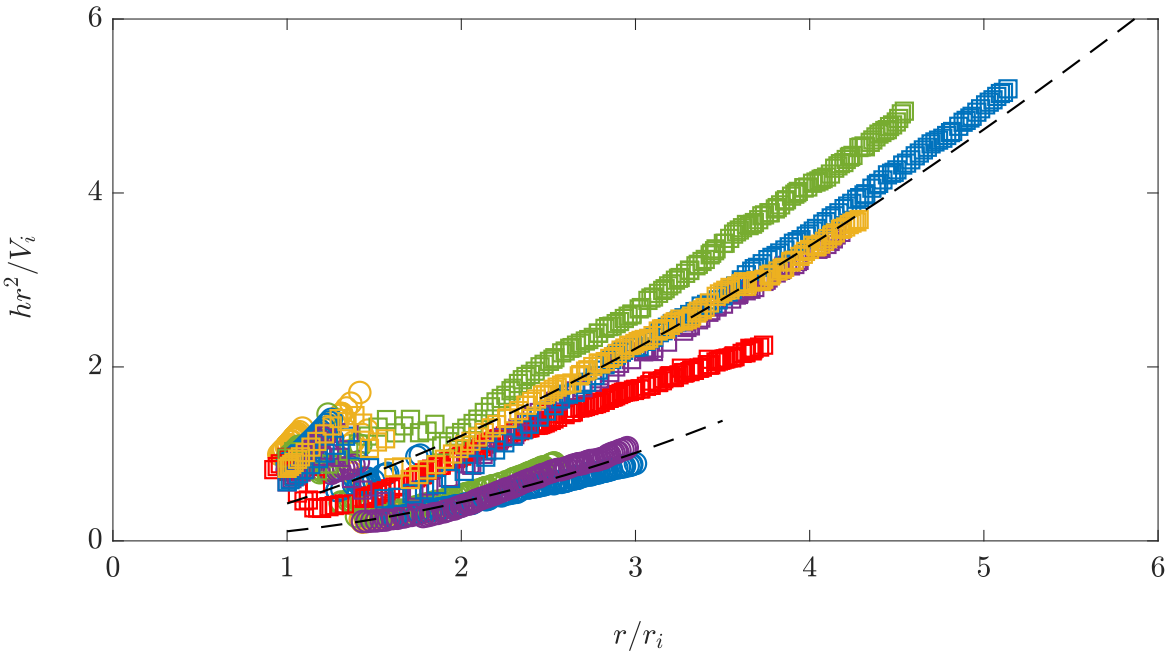

Fig. 4.9 Radius dependent value of hr^2/V_i for $L/D = 1$ (red), 2 (yellow), 3 (green), 4 (blue) and 5 (purple) at $H/D = 2$ (squares) and 8 (circles). The dashed lines are at $f = 0.43(r/r_i)^{1.49}$ and $f = 0.11(r/r_i)^{2.02}$

both the qualitative and quantitative behaviour of the radii and heights were affected by the value of L/D and H/D.

To investigate how the radial position evolves during impact, depending on the phase of the thermal at impact, we consider $\hat{r} - \hat{r}_i$ against $\hat{t} - \hat{t}_i$ so that the radius at impact lies at $(0,0)$. This is shown for $L/D = 1$, 2, 3, 4 and 5 for both $H/D = 2$ and $H/D = 8$ in figure 4.10. The colours of the symbols here represent the phase in which the thermal was in upon impact with the ground: draining (lilac), development (purple) or self-similar thermal (black).

If we zoom into the point of impact we see in figure 4.11 that prior to impact, $\hat{t} - \hat{t}_i < 0$, the evolution or the radial position is independent of the phase of the thermal upon impact. However, upon impact, $\hat{t} - \hat{t}_i = 0$, of a thermal in either the draining or development phases the radial positions are approximately stationary. The radial velocity increases at the time of impact, in the case of a thermal in the draining phase, or shortly after impact in the case of a thermal in the development phase. Then the radial position in both of these cases reaches the power law produced by the similarity solution discussed in section 4.3.1.

The experiments performed at $H/D = 8$ with $L/D = 1$ and 2 are the only experiments that reach the self-similar thermal phase. The average radial positions of these two experiments experience no change in radial velocity, $\mathrm{d}r/\mathrm{d}t$, when transitioning from the thermal to gravity

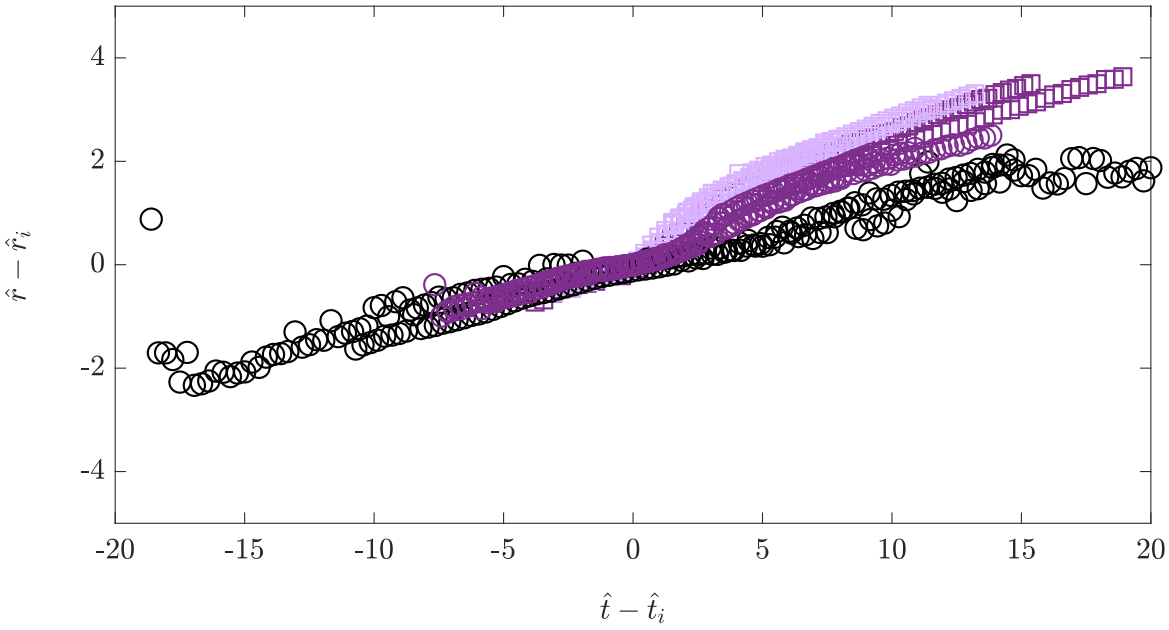

Fig. 4.10 Average radial position of the thermal and gravity current r for $L/D = 1$, 2, 3, 4 and 5 at both $H/D = 2$ and $H/D = 8$. The colours here represent the phase in which the thermal was in upon impact with the ground: draining (lilac), development (purple) or self-similar thermal (black).

current phase. Therefore, we conclude that only once a thermal is truly self-similar will the thermal-gravity current transition occur in a smooth continuous fashion.

It was observed previously, in section 4.2.3, that the gravity currents produced by thermals impacting the ground in the draining phase there is an increase in the height of the gravity current shortly after impact with the ground. Comparing figure 4.7 and figure 4.11 just after impact, between $0 \leq \hat{t} - \hat{t}_i \leq 5$, we can see that for the experiments where there is a change in radial velocity we observe the growth in height of the gravity currents. Figure 4.12 shows three individual experiments which represent the three cases of the thermal at impact. Plotted are the edges of thermals and gravity currents at 6 different times: $\hat{t} - \hat{t}_i = 0$, 1, 2, 3, 4, and 5. Also shown are the positions of $\hat{r} - \hat{r}_i = 1$ and 2 for comparison with figure 4.11. These snapshots illustrate more clearly the increase of the height of the gravity current directly after impact for the draining and development cases. Conversely, in the case of the self-similar thermal impacting the ground, figure 4.12c, we see only a small decrease in gravity current height.

As discussed previously, it is expected that the transfer of the momentum from the thermal to the gravity current during impact will affect the initial stages of the gravity current development, and will differ from that of a lock release experiment which has no momentum at the source. At the time of impact the vertical momentum M_i of the thermal is given by

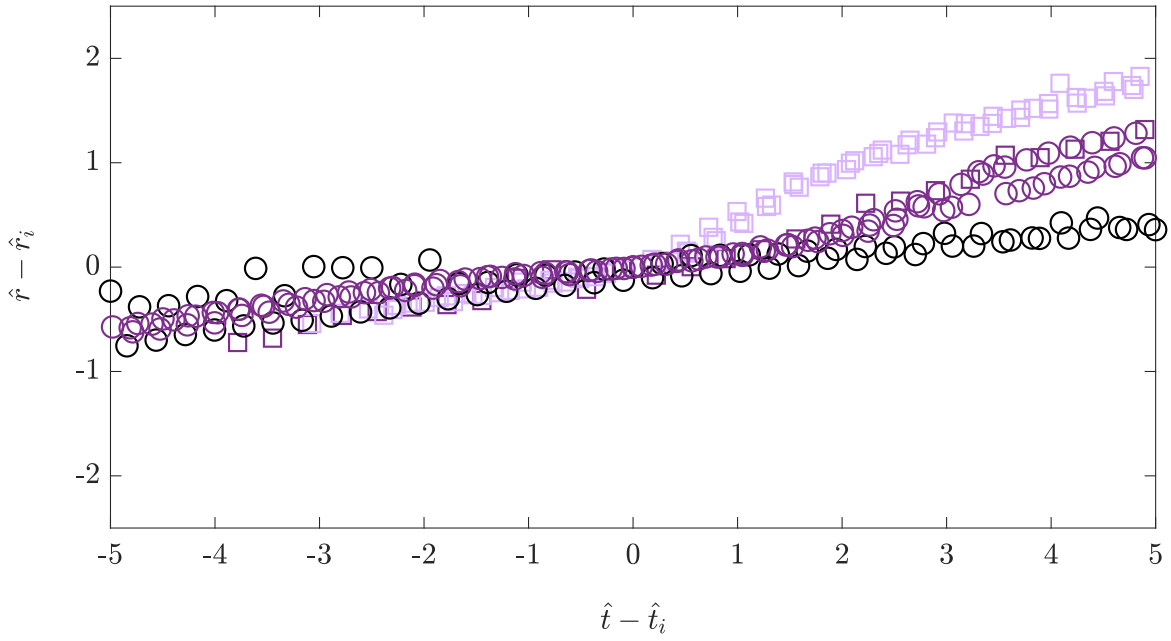

Fig. 4.11 Average radial position of the thermal and gravity current r for $L/D = 1$, 2, 3, 4 and 5 at both $H/D = 2$ and $H/D = 8$. The colours here represent the phase in which the thermal was in upon impact with the ground: draining (lilac), development (purple) or self-similar thermal (black).

$M_i = w(t_i)V(t_i)$ where $w(t_i)$ is the vertical velocity of the thermal at the time of impact, and $V(t_i)$ the volume of the thermal at the time of impact. The length scale over which the radial momentum will dominate over the buoyancy force scales with $(M_i^2/B_0)^{1/4}$. While the tube is still draining this will not hold since not all of the source fluid has exited and therefore the total buoyancy is still increasing. However, if we consider the two cases remaining, for the experiments that impact the ground in the development phase, these length scale ranges from 0.93 cm to 1.28 cm i.e. 0.10 to $0.24r_i$. In the case of the two experiments that impact the ground as a self-similar thermal, the length scale is significantly increased and ranges from 6.49 cm to 7.92 cm i.e. 0.46 to $0.64r_i$. Therefore, the phase in which the thermal impacts the ground does affect the length scale where the momentum dominates over buoyancy. For both the development and self-similar phases, these length scales are indeed less than seen in traditional lock release experiments which is between 3 and $10r_i$ [33]. However this length scale is only significant compared to the initial radius of the release when the thermal impacts the ground in its self-similar phase. Therefore, in the application to downdraughts, which we have shown will impact the ground in the draining or development phases, this initial momentum at the source of the cold pools is assumed not to play a role after impact has occurred.

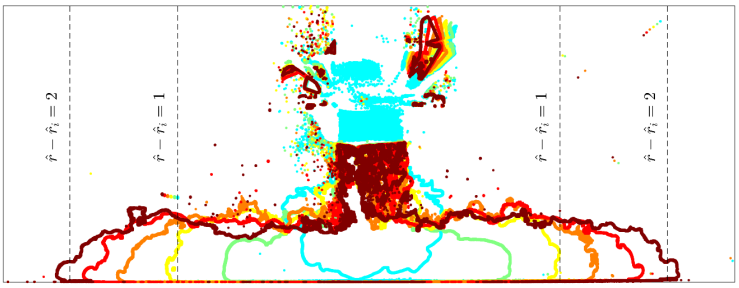

(a) Draining Phase: $L/D = 5$, $H/D = 2$

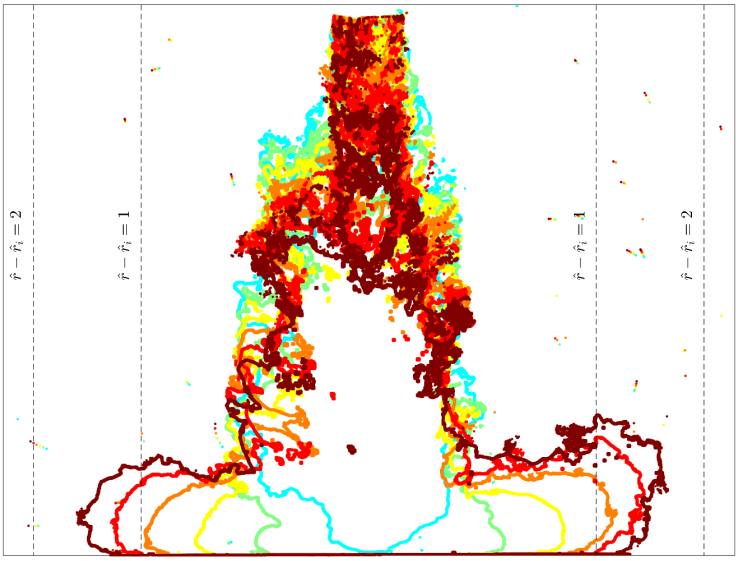

(b) Development Phase: $L/D = 5$, $H/D = 8$

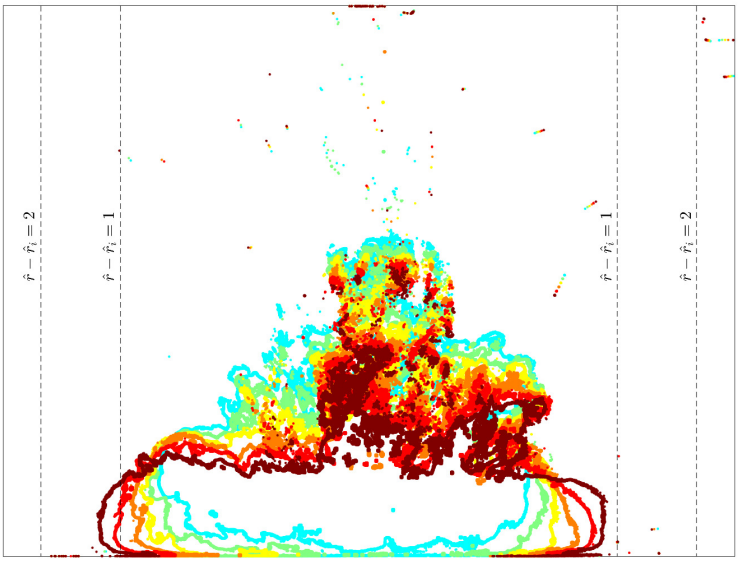

(c) Thermal Phase: $L/D = 2$, $H/D = 8$

Fig. 4.12 Edges of experimental images during the transition from thermal to gravity current from six time steps: $\hat{t}-\hat{t}_i = 0,\ 1,\ 2,\ 3,\ 4$, and 5. Three experiments are show, one from each phase of the thermal during impact i.e. draining, development and thermal.

4.3.3 Implications for Collisions

As discussed in Chapter 1, previous consideration of the collision of cold pools show that these collisions lead to an enhancement of ascending motion which causes deep convection and precipitation thereby reinforcing the storm [13, 19, 20, 58]. As such, the collisions of such expanding cold pools are thought to play a key role in the maintaining and prolonging convective storms [49].

The collisions of two-dimensional gravity currents have been produced both experimentally and numerically by van der Wiel et al. [58] and Cafaro & Rooney [13], respectively. van der Wiel et al. [58] released two gravity currents in a channel using the lock release method which propagated towards one another. They varied the density difference between the two gravity currents, and also considered the case where one was half the height of the other. They found that for the collision of notionally identical currents, i.e. same height and density, the collision front was vertical with some mixing occurring along the collision line. The collision line propagated vertically only, and the gravity currents reached a height approximately 0.9 times the depth of the tank. However, for collisions with asymmetry in the densities only the collision front was at an angle which varied with time, with the heavier release underneath the lighter. When measured from the vertical the collision angle increases with increasing asymmetry in the densities. Mixing along the collision line still occurred, however the mixing was reduced with increased asymmetry. When the asymmetry in the gravity currents was caused by a difference in the heights, the collision front was less clear where the current with the lower initial height flowed underneath the other current, and the current with the larger initial height set the direction post collision. These experiments showed a greater variation in collision heights, but no systematic trend could be found. It was found that since the collision line is stationary for symmetric gravity currents, these are conditions in which there is a greater potential for ascending motion and hence the enhancement of deep convection in convective storms.

The collisions of axisymmetric gravity currents produced from an elevated source have been considered in Droegemeier & Wilhelmson [19] and Droegemeier & Wilhelmson [20]. Both Droegemeier & Wilhelmson [19] and Droegemeier & Wilhelmson [20] used a three-dimensional numerical cloud model to produce two symmetric downdraughts, resulting in two cold pools. As the cold pools approached one another they induced lifting, warming and moistening of the air along the collision line triggering clouds to form along it. The clouds were formed either by air forced upwards by the collision, or air forced to flow over the fronts of the advancing cold pools.

For the gravity currents presented herein, there are a range of propagation speeds during the slumping phases and a range of heights that could cause asymmetry in collisions. For

the gravity currents produced by the releases from $H/D = 2$ the slumping phase is small. Therefore, unless collision occurs within this phase, asymmetry can only come from a difference in heights, initial buoyancy or different release times. The heights of the gravity currents at $H/D = 2$ have only a small variation between values of L/D. Conversely, at $H/D = 8$ the gravity currents have a more significant variation in slumping phase, so asymmetry could come from a difference in both height, speed and initial buoyancy. However, some combinations of two different values of L/D could create symmetric collision conditions providing the collision occurs after the slumping phase.

In the atmosphere it has been observed that downdraughts are formed where the value of H/D is approximately in the range of 0.25 and 2.5, with values of L/D in the same range. This implies that the downdraughts will impact the ground in either the development or draining phases of a thermal. We have seen in this section that the gravity currents produced by these experiments typically have small regions where the momentum dominates over the buoyancy force, between 0.10 and 0.24 times r_i, and therefore collisions are likely to occur when the gravity currents are in their self-similar phases. However the heights of the gravity currents at this height vary both over time and, depending on the value of L/D, making it unlikely that the heights of the currents upon collision will be symmetric. Identically forced downdraughts are unlikely to form at the same instant in time (and in close proximity) therefore asymmetric collisions are expected suggesting that the effects of collisions of asymmetric currents are sufficient to enhance deep convection in convective storms.

4.4 Conclusions

In this chapter experimental results for gravity currents produced by thermals have been compared to existing theory. The gradient of the similarity solution for the radius represents the experiments well for releases from all lengths of tube and at both heights after some initial time. We have shown that both the qualitative behaviour and quantitative measurements of the heights of gravity currents depend on both the length of the tube and the height of the release. The heights of the gravity currents at impact show qualitatively different behaviour when impacting the ground during the self-similar, development or draining phases. This has an effect on the transition of the radial position from thermal to gravity current. When considering the radius of both the thermal and gravity current the radius stalls when the thermal impacts the ground during either the development or draining phases. Whereas, when impact occurs during the self-similar thermal phase there is a smooth transition due to the fully formed vortex ring in the thermal.

Chapter 5

Numerical Simulations

5.1 Introduction

Using direct numerical simulations of turbulent flows is problematic due to the number of grid points required to obtain the spatial resolution required to resolve the full range of scales which are relevant. This requires a large amount of CPU time which is currently (and for the foreseeable future) unavailable at the scale of atmospheric dynamics. Instead in this thesis we use turbulence models to approximate their effects. One such model is a large eddy simulation (LES) otherwise known as a large eddy model (LEM). LES/LEM was founded on the observation that the small scales have a more universal character than the large scales which transport the turbulent energy [7]. The main principle of an LEM is that the large scale eddies are fully resolved and the small scale turbulence is approximated by relatively simple, so called 'subgrid models'.

The LEM used by the Met Office, referred to as 'the LEM' from now on, performs simulations by integrating the Boussinesq equations which include parameterisations of sub-grid turbulence, cloud microphysics and radiation. The prognostic variables are the three components of the velocity vector $\mathbf{u} = (u, v, w)$, the potential temperature perturbation θ' and a number of other scalar variables q_n referred to as Q fields. The flow variables are decomposed into a large scale portion which is explicitly fully resolved and an unresolved portion which is linearised around some reference state. This reference state must be specified for θ, and is constant in height [24]. The equations for the resolved portion of the flow only are then given by

$$\frac{Du_i}{Dt} = -\frac{\partial}{\partial x_i}\left(\frac{p'}{\rho_s}\right) + \delta_{i3}B' + \frac{1}{\rho_s}\frac{\partial \tau_{ij}}{\partial x_j} - \varepsilon_{ijk}\Delta_j u_k, \tag{5.1a}$$

$$\frac{\partial}{\partial x_i}(\rho_s u_i) = 0, \tag{5.1b}$$

$$\frac{D\theta'}{Dt} + w\frac{\mathrm{d}\theta_s}{\mathrm{d}z} = \frac{1}{\rho_s}\frac{\partial h_i^{\theta'}}{\partial x_i} + \frac{1}{\rho_s}\frac{\partial h_3^{\theta_s}}{\partial z} + \left(\frac{\partial \theta'}{\partial t}\right)_{mphys} + \left(\frac{\partial \theta'}{\partial t}\right)_{rad}, \tag{5.1c}$$

$$\frac{Dq_n}{Dt} = \frac{1}{\rho_s}\frac{\partial h_i^{q_n}}{\partial x_i} - \left(\frac{\partial q_n}{\partial t}\right)_{mphys}, \tag{5.1d}$$

where the subscript s represents the reference state and $'$ the perturbation to the reference state, p is the pressure, ρ the density, B' the buoyancy, δ_{i3} the Kroneker delta function, Δ the Earth's angular velocity (hereby employing the $f-$plane approximation), ε_{ijk} the alternating pseudo-tensor, the subscript *mphys* the source terms due to microphysics and subscript *rad* the source terms due to radiation. The sub-grid contribution to the flow is solely represented through the sub-grid parameterisations of the subgrid stress τ and the subgrid scalar fluxes h of θ and q_n. Details of the sub-grid parameterisation can be found in section 5.2.3 and further details of the LEM can be found in Gray & Petch [24] and Gray et al. [25, 26]. The benefit of the methodology employed by the LEM is that it requires significantly less grid points to approximate the space, so looking at higher Reynolds number flows and large spatial regions becomes more feasible, and is therefore useful for meteorology [7].

At the Met Office the LEM used in the 1980's for scientific research has since been replaced with the Met Office NERC Cloud model (MONC). MONC is a complete rewrite and re-engineering of the LEM which preserves the LEM's scientific principles. It was created to facilitate scientists who required higher spatial or temporal resolutions, which require more computational resources [9]. The LEM was not able to scale beyond a few hundred cores and so MONC was created using modern parallelisation techniques and to be able to use over 100,000 processors. For a more detailed description of MONC see Brown et al. [9, 10]. It is MONC that will be used in all the subsequent simulations.

In this chapter a detailed study into the set up of MONC has been performed. The chosen set up is then compared with exact replicas of the simulations performed by Rooney [49] in the LEM. Simulations of the laboratory experiments are then performed in order to make comparisons between the two. Finally, the data from the simulations are used to consider the validity of assumptions made in the derivation of the thermal equations.

5.1.1 Typical Numerical Set Up

As discussed above, MONC is a large eddy model designed to facilitate the resolution of higher spatial or temporal scales whilst maintaining the nature of turbulent flows. Since MONC is a large eddy model, it requires a subgrid model. MONC's subgrid model uses a

Smagorinsky representation of subgrid stress and subgrid scalar fluxes. The mixing length that relaxes to κz_0 at the surface, where $z_0 = 2.0 \times 10^{-4}$m is the roughness length and $\kappa \approx 0.4$ is von Karman's constant. In the results presented here the Smagorinsky coefficient, which relates the subgrid eddy-viscosity length scale to the model gridscale, was set to 0.23. More details of the Smagorinsky representation of subgrid stress and flux as well as the choice of Smagorinsky coefficient can be found in section 5.2.3.

The domain of the numerical experiments consisted of $402 \times 402 \times 601$ gridpoints in the $x-$, $y-$ and $z-$ directions, respectively, with a grid resolution of 10 m in all directions. This produces a domain height of 6 km and a width and length of 4.02 km. The domain is periodic in both horizontal directions with free slip and no-slip boundary conditions at the top and bottom, respectively.

The surface temperature was set to the same value as the initial background potential temperature (300K). The model was run without interaction of a humidity field. The experiments consisted of the initialisation of a cold cylinder or sphere of radius r_0, with the lowest point at height H above the surface, in an otherwise homogeneous and quiescent environment. This cold cylinder or sphere is a potential temperature perturbation, with a maximum potential-temperature perturbation $\Delta\theta_0$ from the surrounding uniform potential temperature field. The initial potential temperature perturbation then had small scale random perturbations added in order to break down the flow symmetry and promote the onset of turbulence; more details of this process can be found in section 5.2.4. A more detailed reasoning as to how the grid resolution, Smagorinsky coefficient etc. have been chosen, can be found in section 5.2.

5.1.2 Processing

After the simulations had been run, the potential temperature fields were analysed in Matlab. The potential temperature fields were integrated in the $x-$ and $y-$ directions to obtain horizontally integrated time series of the flows. The same data were collected for the simulations as for the laboratory experiments: i.e. the radial extent of the thermal, the vertical heights of the descending front and the center of mass of the thermal, the cross-sectional area of the thermal, and the radial position of the resulting gravity current. The edges of the thermal and the gravity current, and the centre of mass of the thermal are then tracked in a similar way to the laboratory experiments. To track the edges the potential temperature fields were first scaled by the minimum potential temperature at each time, then the potential temperature fields became matrices between zero and 1. This enabled us to set a threshold to determine the fluid that was part of the thermal and gravity current. It was found that when using a threshold of 0.1 the total potential temperature was less than 0.1% different to the

simulation	x/y (m)	z (m)	n$^{\text{o}}$ grid points $x \times y \times z$	symbol
L03_01	25	25	$204 \times 204 \times 241$	$\circ$
L03_07	12.5	12.5	$416 \times 416 \times 481$	$\square$
L03_11	12.5	10	$320 \times 320 \times 601$	$+$
L03_12	10	12.5	$402 \times 402 \times 481$	$\triangleleft$
L03_08	10	10	$402 \times 402 \times 601$	$*$
L03_10	10	5	$402 \times 402 \times 1201$	$\star$
L03_09	5	10	$804 \times 804 \times 601$	$\triangle$

Table 5.1 Testing the grid resolution using the recommended settings: Smagorinsky on, flow advection P-W, scalar advection TVD. All simulations done on a cylinder with radius $r_0 = 250\,\text{m}$, $L/D = 3$ and $\Delta\theta_0 = -0.1\,\text{K}$.

conserved total initial potential temperature perturbation. Therefore, a threshold of 0.1 was used for all the following analysis.

5.2 Set Up Testing

5.2.1 Grid Resolution

To test the effect of grid resolution on the release of a cylinder, we varied the resolution in the x, y and z directions from 25 to 5 m. We performed these tests on a cylinder of radius $r_0 = 250\,\text{m}$ with height $L/D = 3$ and $\Delta\theta_0 = -0.1$. The 'recommended' settings for the advection schemes and Smagorinsky are used, that is to say, the Total Variation Diminishing (TVD) advection scheme for the scalar field, and the Piasek-Williams (P-W) scheme for the velocity field were used, the details of which can be found in section 5.2.2. The Smagorinsky scheme was turned on with the Smagorinsky coefficient set to $C_s = 0.23$, where the mixing length scales with the grid size the details of which can be found in section 5.2.3. The grid scale was then decreased incrementally from 25 m in all directions to 5 m. An outline of the resolutions tests are shown in table 5.1. The finest resolution was the largest number of grid points possible to process whilst keeping all domains of the same physical dimensions.

The effects of the grid resolution were compared by measuring the vertical position and radius of the descending thermal. Figure 5.1 shows the non-dimensional position of the front edge and centre of mass of the thermal. The grid resolution does not change the qualitative behaviour of the vertical position. However, by making the resolution finer, the vertical speed of the thermal is reduced. Ultimately, making the resolution finer than $10\,\text{m} \times 10\,\text{m} \times 10\,\text{m}$ makes no significant difference to the vertical velocity indicating that some degree of resolution independence has been achieved. Similarly, for the radius of

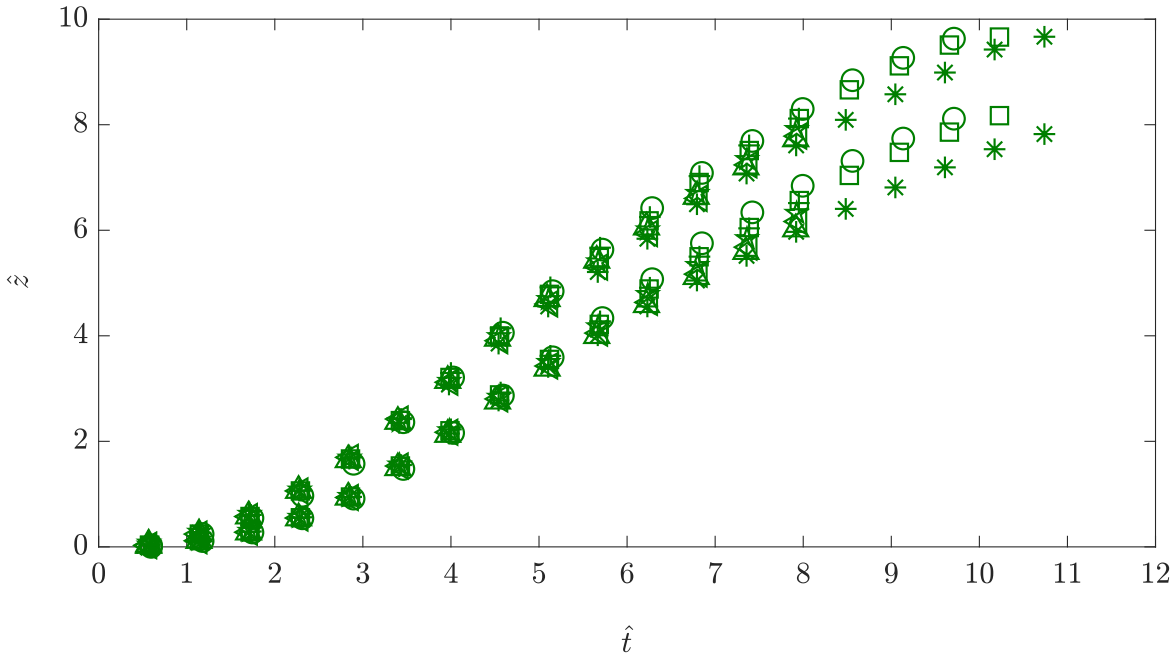

Fig. 5.1 Vertical positions of $\hat{z}_f$ and $\hat{z}_c$ during the descent for the grid resolutions outlined in table 5.1.

the thermal shown in figure 5.2 the qualitative behaviour of the radius is not affected by the grid resolution. However at 25 m (circles), which is the coarsest resolution, there is a significant variation in the radius from finer resolution simulations. This was observed to be from pulsing of the radius due to quasi-laminar behaviour of the thermal at this resolution.

5.2.2 Advection Schemes

Two advection schemes are available to choose from in MONC, they are Piacsek-Williams (P-W) first proposed by Piacsek & Williams [46] and Total Variation Diminishing (TVD) first proposed by Harten [31]. It is possible to use either advection scheme for the velocity and scalar fields.

Most finite-difference solutions of the advection equation introduce spurious oscillations, in regions of significant gradients, into the field being advected [26]. However, TVD is an upwind scheme used to remove such oscillations, for example around a sharp temperature interface or a boundary layer. The principle of TVD is that any maxima in the quantity being advected must be non-increasing, and minima non-decreasing, and so no new local extrema may be created [7]. In other words any field that is initially positive or negative will remain so [26]. The scheme works by calculating the total variation at each time step, which is a measure of the oscillations produced by the advection scheme. The scheme requires

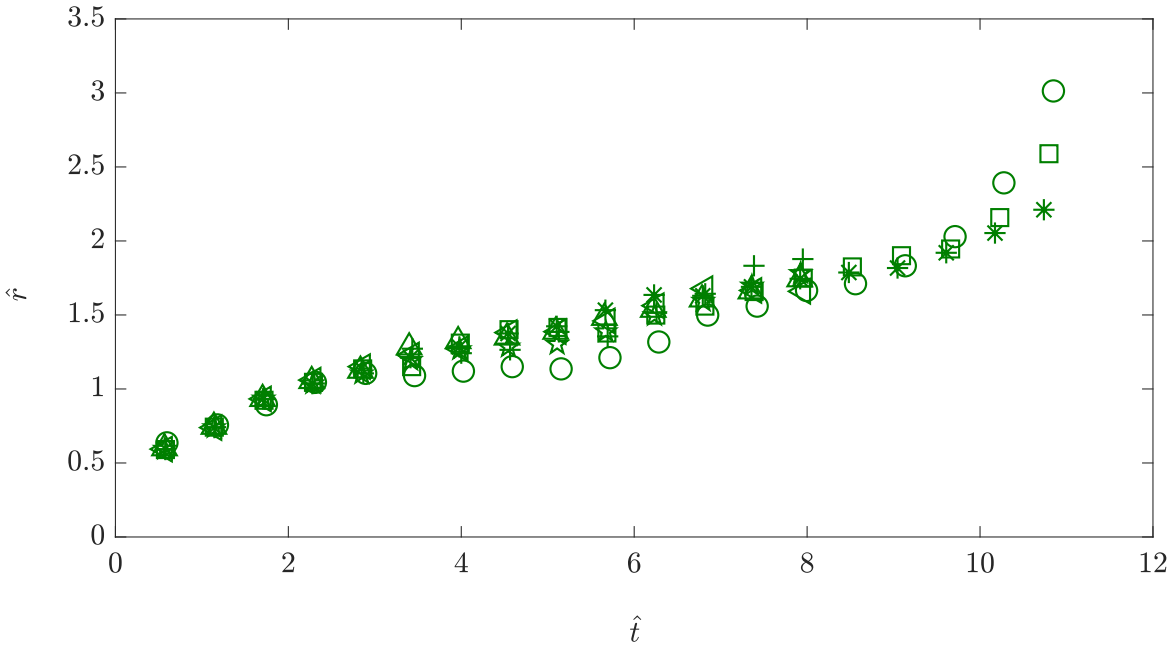

Fig. 5.2 Radius $\hat{r}$ of the thermal for the grid resolutions outlined in table 5.1.

that the total variation is less than or equal to that of the previous time step. TVD's main disadvantage is that the scheme is computationally expensive. However, the advantage of a monotonicity preserving scheme outweighs the drawbacks when considering flows that include steep gradients in velocity or scalar fields, due to the schemes preservation of such physically reasonable gradients.

P-W is the other advection scheme available; the advection term is written in flux form i.e.

$$\rho_s \mathbf{u} \nabla q = \nabla(\rho_s \mathbf{u} q) - q \nabla(\rho_s \mathbf{u})$$

using (5.1b) this becomes

$$\rho_s \mathbf{u} \nabla q = \nabla(\rho_s \mathbf{u} q)$$

The P-W advection scheme was created to reduce a weak instability produced when considering long-term time integrations that eventually led to erroneous results [46]. Unlike the TVD scheme, P-W does not act to reduce oscillations around discontinuities or sharp gradients. However, P-W is more computationally efficient to run than TVD.

To test the effects of the two advection schemes on the potential temperature and velocity fields the release of a cylinder was initiated in the same way for both schemes. A cylinder of initial radius $r_0 = 250$m and length $L = 500$m composed of air at rest was released from a height of $H = 4$km. The cylinder had an initial potential temperature perturbation of $\Delta\theta_0 = -0.1$K, where the background potential temperature was 300K. The grid resolution

simulation	velocity	scalar	L/D	symbol
L01_pw	P-W	P-W	1	$\circ$
L01_tvdpw	TVD	P-W	1	$+$
L01_pwtvd	P-W	TVD	1	$\square$
L01_tvd	TVD	TVD	1	$*$

Table 5.2 Different combinations of the advection schemes tested. All tests performed on a cylinder where $L/D = 1$.

was set to be 10m with a domain size of $502 \times 502 \times 601$ in the $x-$, $y-$ and $z-$directions respectively. The Smagorinsky diffusion scheme was turned on with the value of the Smagorinsky constant set to $C_s = 0.23$, see section section 5.2.3. As described in section 5.2.4, some initial randomisation in the potential temperature field of the release is required to promote turbulence. The associated parameter for this was set to $ampl\_frac = 0.5$.

Using the set up described four combinations of advection schemes were considered, these are outlined in table 5.2. The first two simulations use P-W advection on the scalar field and change the advection scheme used on the velocity field. The second two simulations use TVD advection on the scalar field and change the advection scheme used on the velocity field.

The effects of the advection schemes were compared by measuring the vertical position and radius of the descending thermal. Figure 5.3 shows the non-dimensional vertical position of the front edge and centre of mass of the thermal. Changing the advection scheme in either the velocity or scalar field does not significantly change the evolution of the front or centre of mass positions. The radius of the whole flow, for both the descent and spread as a gravity current, is shown in figure 5.4. The radius shows some difference for one simulation, L01_tvd (see table 5.2). This simulation uses TVD advection for both the velocity and scalar field.

To consider how the potential temperature field has been advected, the potential temperature field has been integrated in the $x-$, $y-$ and $z-$directions to give the total potential temperature, T_{tot}. Figure 5.5 shows the value of T_{tot} when using the four different advection schemes (solid lines). The potential temperature field is found using the full extent of the $z-$direction (solid line), and also with the z-direction restricted to the original release height, i.e. 4km (symbols). There is a clear difference between the simulations with P-W advection on the scalar field (circle/plus) and the simulations with the TVD advection on the scalar field (square/asterisks). For the same advection scheme on the scalar field, changing the scheme for the velocity field has little effect, especially when using TVD advection on the scalar field. This indicates that only a change in the advection scheme for the scalar field has an effect on the transport of potential temperature below the initial release height.

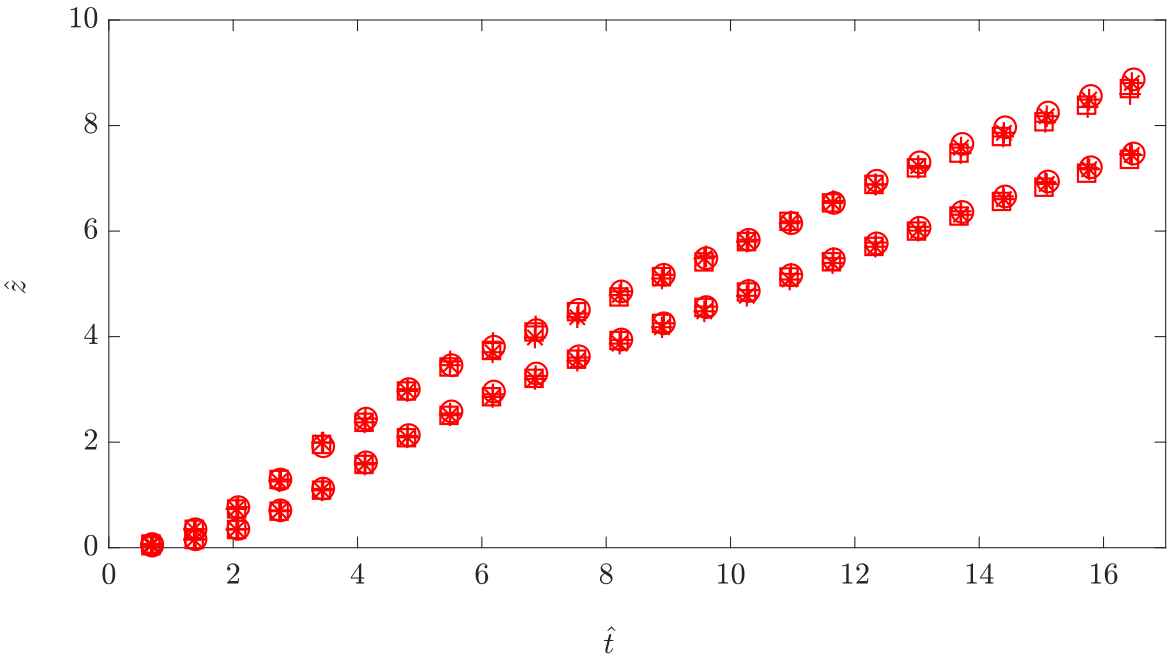

Fig. 5.3 Vertical position of the lowest point and center of mass (Z_f and Z_c). The different symbols represent the different advection schemes: P-W advection of the scalar field with P-W (circle)/TVD (plus) in the velocity field and TVD advection in the scalar field with P-W (square)/TVD (asterisks) in the velocity field, see table 5.2.

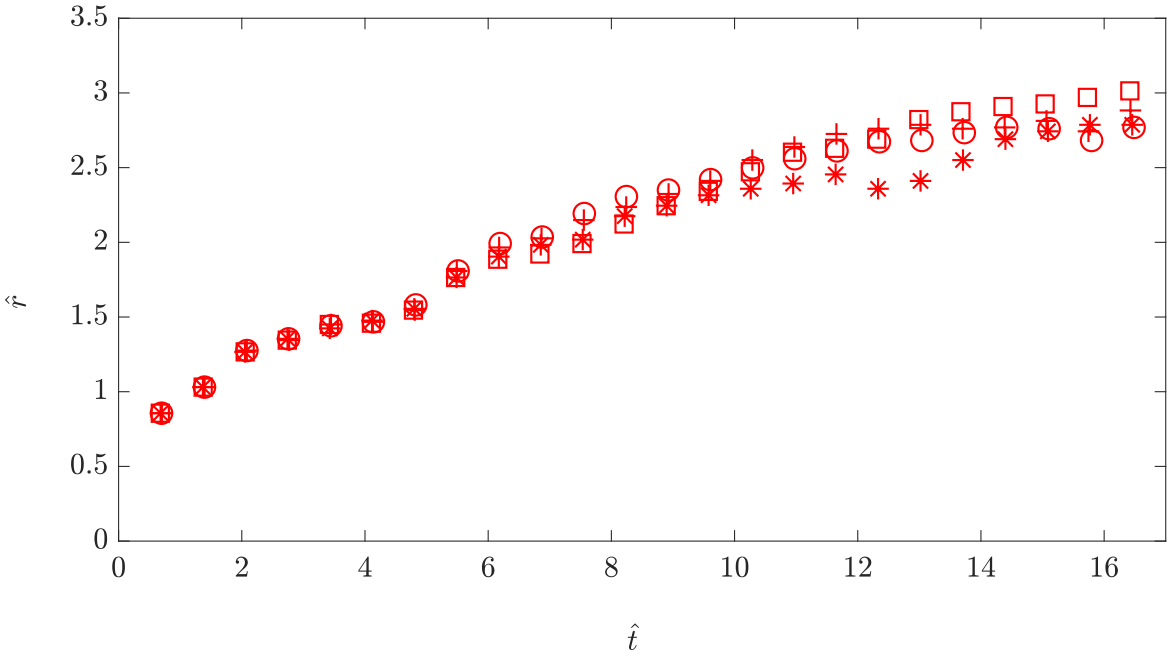

Fig. 5.4 Radial position (r). The different symbols represent the different advection schemes: P-W advection of the scalar field with P-W (circle)/TVD (plus) in the velocity field and TVD advection in the scalar field with P-W (square)/TVD (asterisks) in the velocity field, see table 5.2.

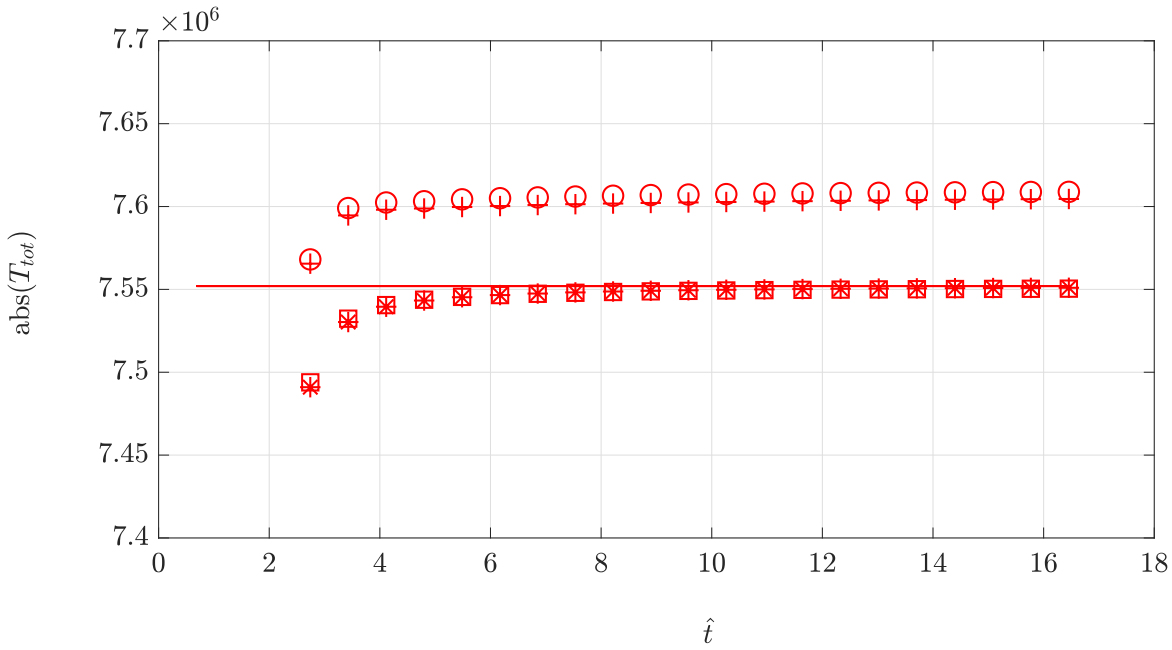

Fig. 5.5 Figure showing the integrated potential temperature field of the whole domain (solid line) and the domain cut in the horizontal direction at the base of the initiated cylinder (markers). The different shape markers represent different advection schemes: P-W advection of the scalar field with P-W (circle)/TVD (plus) in the velocity field and TVD advection in the scalar field with P-W (square)/TVD (asterisks) in the velocity field.

The absolute value of T_{tot} for all simulations, where T_{tot} is calculated with a restricted $z-$direction, increases until all the fluid is below the release height and then becomes constant. Only the simulations using TVD as the advection scheme for the scalar field reach the same absolute value of T_{tot} when it has been calculated below the source and in the whole domain. Both measures of total potential temperature being equal indicates that all the fluid has been carried in the thermal and advected below the source. However for the simulations using the P-W advection on the scalar field the absolute value of T_{tot} is conserved over the entire domain, but below the source has a larger absolute value of T_{tot}. This indicates that there has been some cooling below the source, heating above the source, or a combination of the two.

Based on the results of the tests above, for the main set of simulations TVD was chosen for the scalar field, and P-W for the velocity field. The TVD advection scheme was chosen for the scalar field due to the extra heating/cooling P-W creates in the potential temperature field, which was assumed to be due to oscillations created by the P-W scheme around sharp gradients in the potential temperature field. The P-W advection scheme was chosen for the velocity field, since as shown in figure 5.4 for the TVD advection case (stars) there were some anomalies in the radius near the lower boundary, and the P-W scheme is computationally more efficient.

5.2.3 Smagorinsky Scheme

Large eddy models are induced to resolve the large scale eddies explicitly, and approximate the small scale turbulence using a subgrid scale model. A subgrid scale model is used to parametrise the flow between grid points. If a subgrid model is not used, the model is referred to as implicit LES (ILES), in which numerical diffusion is the only source of subgrid diffusion. Whereas, if the mesh is fine enough to resolve the smaller scales then the subgrid model and associated parameters have no effect. Further details of ILES can be found in [5]. As mentioned above both the subgrid-scale tensor (SGS tensor) τ and scalar fluxes of θ and q_n, h, need to be modelled to close the filtered equations given by (5.1). The subgrid stress and scalar flux are given by

$$\tau_{ij} = \rho_s \nu S_{ij}, \tag{5.2}$$

and

$$h_{n,i} = -\rho_s \nu_h \frac{\partial q_n}{\partial x_i}, \tag{5.3}$$

where S_{ij} is the strain rate tensor given by

$$S_{ij} = \frac{\partial u_i}{\partial x_j} + \frac{\partial u_j}{\partial x_i},$$

and $\nu = \lambda^2 S f_m(Ri_p)$ is the subgrid eddy-viscosity, $\nu_h = \lambda^2 S f_h(Ri_p)$ the corresponding diffusivity for scalars. Here Ri_p is the local Richardson number, λ the mixing length scale, f_m and f_n are Richardson number dependent functions whose definition can be found in [26] and S is given by

$$S = \frac{\|S_{ij}\|}{\sqrt{2}} = \left(\frac{1}{2} \sum_{i,j=1,3} S_{ij}^2 \right)^{1/2}.$$

This an extension to the classical approach by Lilly [38], which sets $\nu = \lambda_0^2 S$ where λ_0 is the classical mixing length. Not only is ν dependent on the Richardson number dependent functions but the length scale λ is a function of λ_0 in order to provide a smooth transition between the mixing length in the interior of the flow and near the ground. Hence λ can is defined as

$$\frac{1}{\lambda^2} = \frac{1}{\lambda_0^2} + \frac{1}{(\kappa(z+z_0))^2},$$

where z_0 is the surface roughness length and κ the von Karman constant. Lilly [38] defined $\lambda_0 = C_s \Delta$ where C_s is the Smagorinsky constant and Δ the grid spacing. C_s can be considered as the ratio of the subgrid scale and the grid scale. The Smagorinsky constant is not well defined and theoretically $C_s = 0.18$ [38], however the value of the constant depends on the

simulation	L/D	grid size (m)	Smagorinsky	symbol
L01_10_smag	1	10	on	○
L01_50_smag	1	50	on	□
L01_10_nosmag	1	10	off	∗
L01_50_nosmag	1	50	off	+
L03_10_smag	3	10	on	○
L03_50_smag	3	50	on	□
L03_10_nosmag	3	10	off	∗
L03_50_nosmag	3	50	off	+

Table 5.3 Details of the simulations performed to test the effects of the Smagorinsky scheme on two different grid sizes.

type of flow - we return to this matter later in this section. If C_s is small then the fields may be rough and so discretisation errors may occur, whereas, large values of C_s could imply an inefficient use of computational resources as the gridspacing Δ could be larger [26].

A subgrid model simulates energy transfer from the large eddies to the subgrid scale. However, it is also possible for energy to be transferred from the small to large scales in a process called backscatter. It should be noted that in MONC the process of energy backscatter is not modelled, however it was modelled in the LEM. Details of the backscatter scheme can be found in Gray et al. [26].

Eight simulations, which are outlined in table 5.3, are performed in order to test the effects of the Smagorinksy scheme in the evolution of a cylinder at two different grid resolutions. Two lengths of cylinder, $L/D = 1,\ 3$, each of $\Delta\theta_0 = -0.25$ were simulated. For each length of cylinder two grid sizes have been used, 10 m and 50 m. In addition, for comparison, runs with the Smagorinsky scheme turned off for each combination of tube length and grid resolution have been simulated.

Both vertical positions, the lowest point and centre of mass, are shown in figures 5.6 and 5.7. For the cylinder with $L/D = 3$ (green) for either grid resolution turning Smagorinsky off has no effect on either the center of mass or lowest vertical position. However, for the cylinder with $L/D = 1$ (red) turning Smagorinsky off has the effect of increasing the vertical velocities at later times for both resolutions. The only exception being in the centre of mass measurement for the 50 m resolution, where it has no effect. Since the variation occurs at late times this implies that turning Smagorinsky off is inhibiting entrainment or, equivalently, that turning Smagorinsky on increases dissipation. Also, since there is variation between the vertical positions for the 10 m resolution, 10 m is not a fine enough resolution to resolve the small scales and a subgrid model is still required.

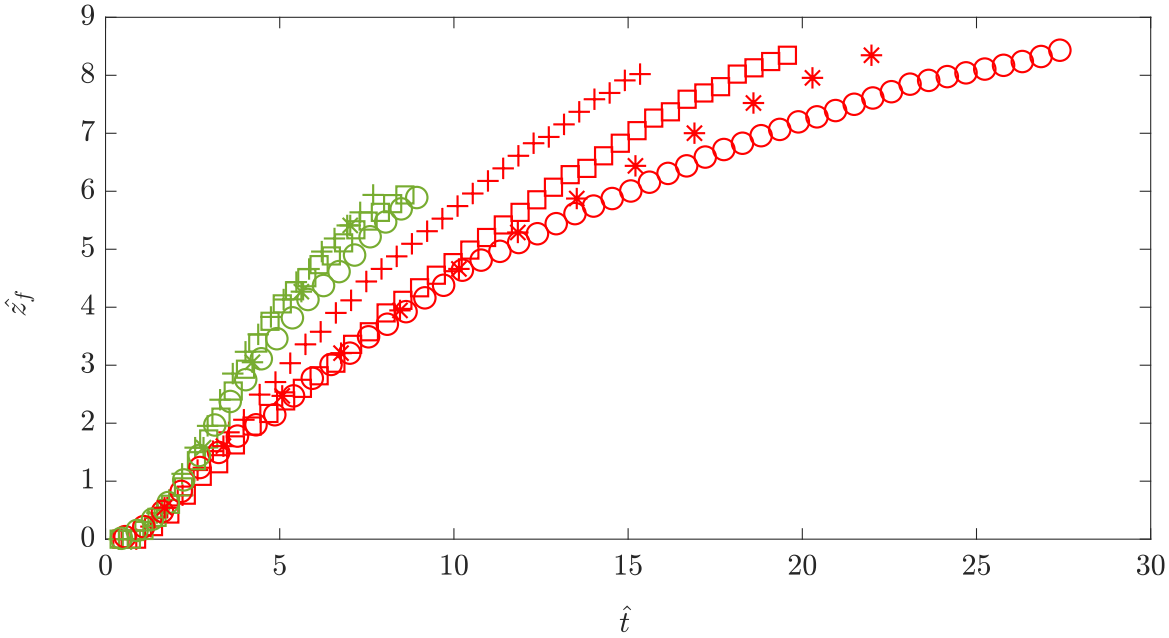

Fig. 5.6 Vertical position of the lowest point, $\hat{z}_f$, of the thermal. The details of the simulations shown can be found in table 5.3.

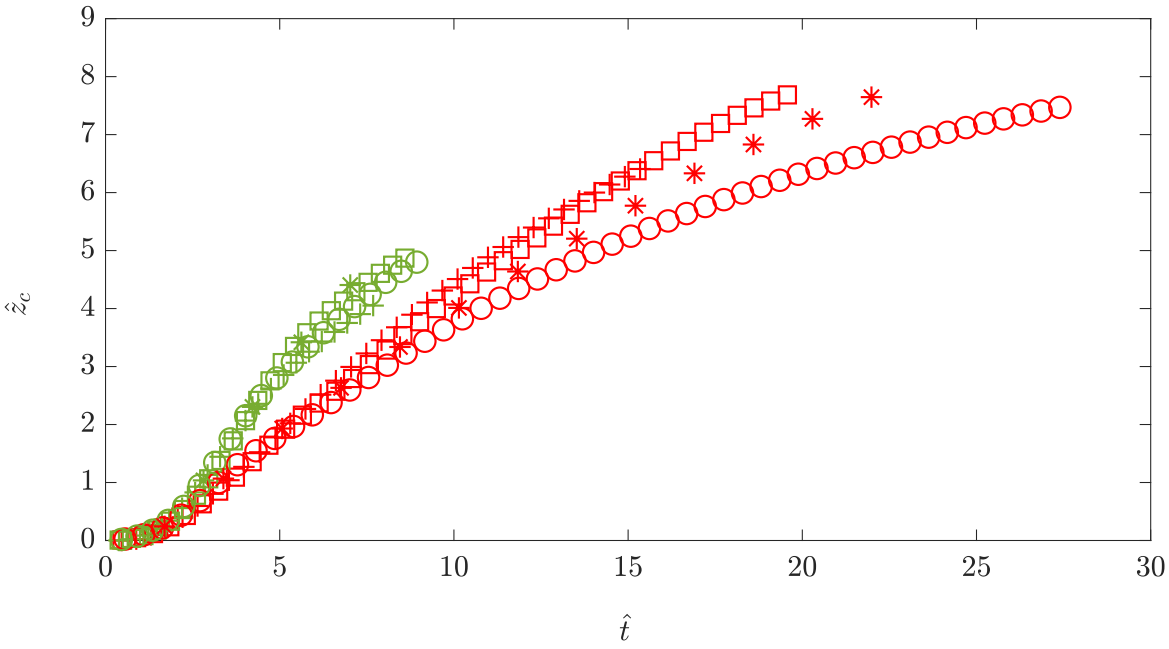

Fig. 5.7 Vertical position of the centre of mass, $\hat{z}_c$, of the thermal. The details of the simulations shown can be found in table 5.3.

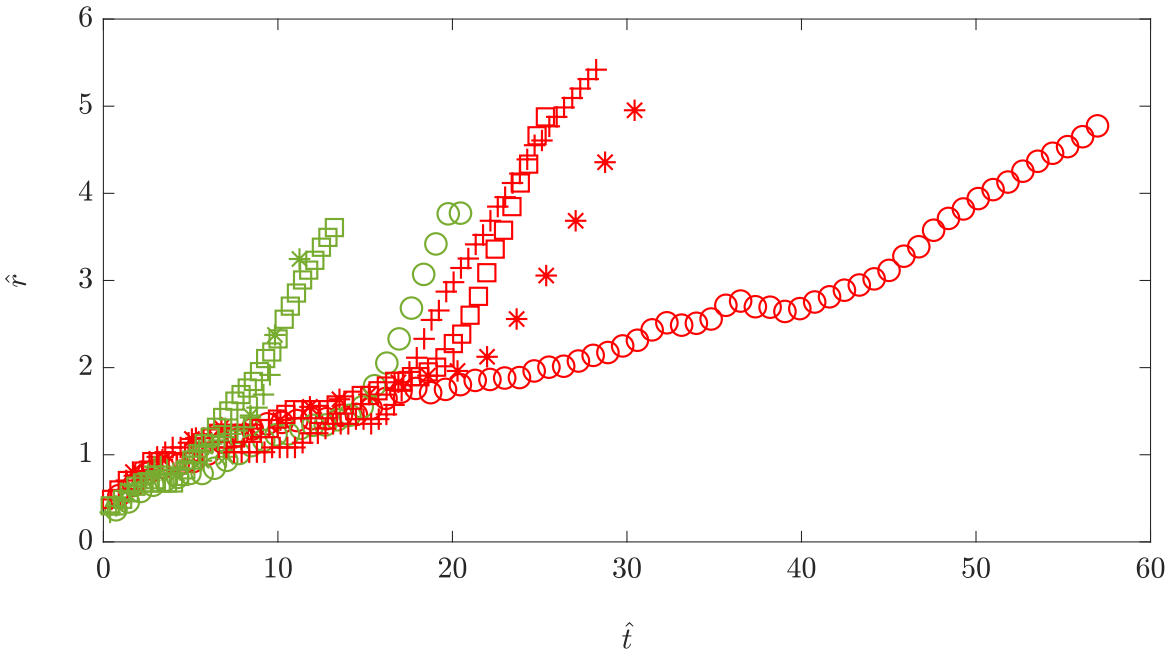

Fig. 5.8 Radial position $\hat{r}$, of the thermal and gravity current phases. The details of the simulations shown can be found in table 5.3.

The radial positions are shown in figure 5.8. For the cylinder with $L/D = 1$ and 3 for the 50 m grid resolution turning Smagorinsky off has no effect on the radial position. However, for both cylinders with 10 m resolution turning Smagorinsky off has the effect of increasing the radial velocities at later times (during the gravity current phase). Since the variation occurs at late times this implies that turning Smagorinsky off is inhibiting entrainment during the gravity current phase.

As previously stated the value of the Smagorinsky constant is not uniquely defined. Lilly [38] found theoretically $C_s = 0.18$, Rooney [49] used $C_s = 0.1$ for their simulations in the LEM, and in MONC the default setting is $C_s = 0.23$. Here four values for C_s have been considered at two different grid resolutions. These tests have been performed by releasing a cylinder with radius $r_0 = 250$ m and length $L = 1500$ m from a height $H = 4000$ m, with $\Delta\theta_0 = -0.25$ K. The details of each experiment are presented in table 5.4.

Both measures of vertical position, front edge, $\hat{z}_f$, and centre of mass, $\hat{z}_c$, are considered for the four values of C_s. These vertical positions are plotted in figure 5.9 ($\hat{z}_f$) and in figure 5.10 ($\hat{z}_c$). The vertical position of the front has very little variation between the four values, and the choice of grid resolution also has no effect on this measurement. However, the vertical position of the centre of mass has a significant difference between the values of $C_s = 0.37$ and 0.5 with 10 m grid resolution compared to the other values of C_s and all four values of C_s at 50 m grid resolution.

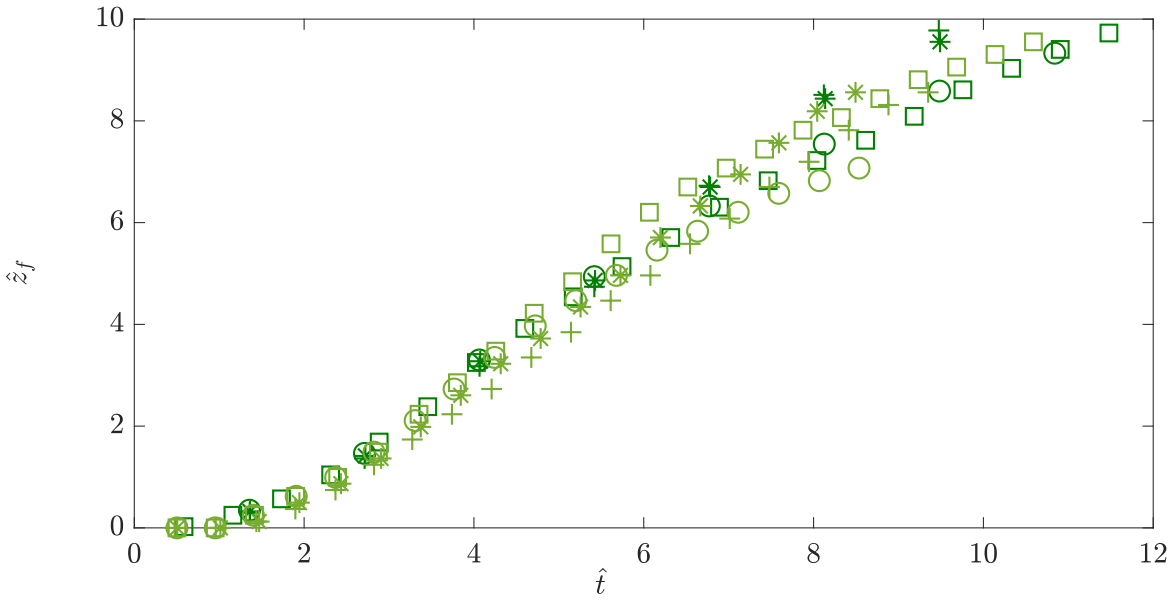

Fig. 5.9 Vertical position of the lowest point, $\hat{z}_f$, of the thermal. The details of the simulations can be found in table 5.4.

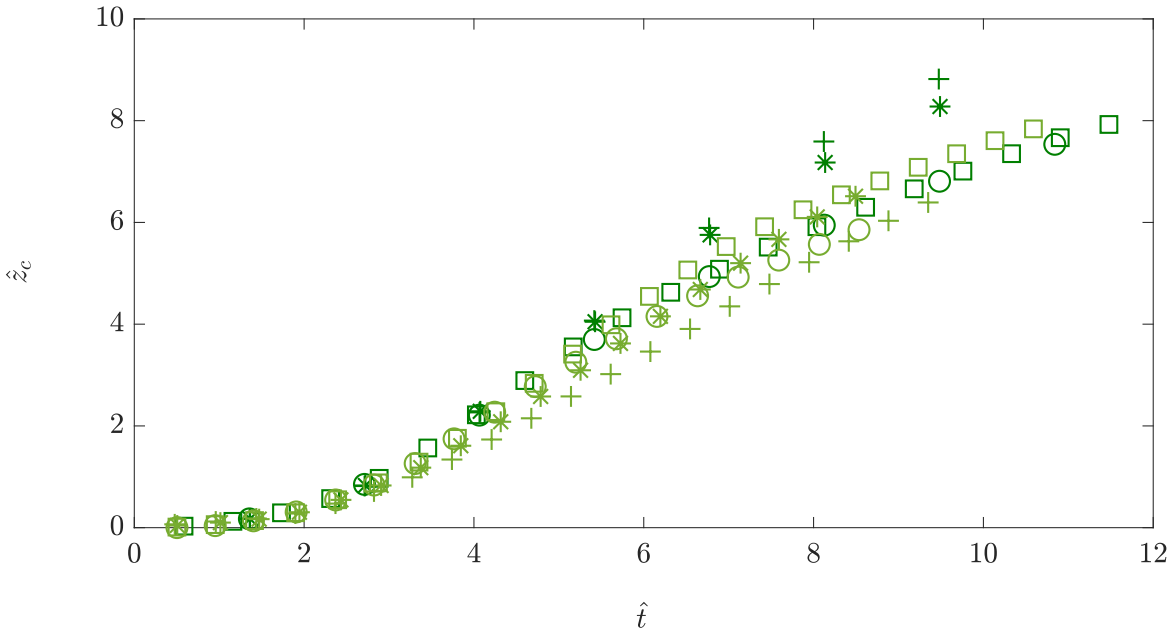

Fig. 5.10 Vertical position of the centre of mass, $\hat{z}_c$, of the thermal. The details of the simulations can be found in table 5.4.

L/D	grid size (m)	C_s	symbol
3	50	0.1	○
3	50	0.23	□
3	50	0.37	∗
3	50	0.5	+
3	10	0.1	○
3	10	0.23	□
3	10	0.37	∗
3	10	0.5	+

Table 5.4 Details of the simulations performed to test the effect of changing the Smagorinsky constant, C_s at two different grid sizes.

The radial position during both the thermal and gravity current phases is also considered for the four values of C_s. The radial positions are plotted in figure 5.11. The radial position varies significantly between $C_s = 0.1,\ 0.23$ and $C_s = 0.37,\ 0.5$ for both grid resolutions. The radial position for $C_s = 0.1$ and 0.23 varies the most between the two resolutions during the transition between thermal and gravity current at $10 < \hat{t} < 12$.

The vertical and radial positions with $C_s = 0.37$ and 0.5 were not consistent with the measurements taken using the value of $C_s = 0.1$ used by Rooney [49] or with $C_s = 0.23$ the default setting in MONC. We will therefore focus on the qualitative differences between $C_s = 0.1$ and 0.23, as the vertical and radial positions are independent of the choice between these two values at 10 m resolution.

To keep comparison with the experimental data possible, the width integrated potential temperature fields of both the thermals and gravity currents for $C_s = 0.1$ and 0.23 are shown in figures 5.12 and 5.13, respectively. We see that for the thermals the main differences between $C_s = 0.1$ and 0.23 are the shape and the width-integrated structure. The thermal with $C_s = 0.23$ is spheroidal in shape and has formed a structure akin to that observed for self-similar thermals with this initial ratio, $L/D = 3$, namely a vortex ring with a trailing stem, whereas, the thermal with $C_s = 0.1$ has not entrained as much ambient air and therefore has not formed the classic thermal structure at this height. In contrast, the gravity currents for both $C_s = 0.1$ and 0.23 have very similar structures, but different temperature profiles, both forming the bulbous gravity current head as expected. Since the measurements presented here are not significantly dependent on the value of C_s, and the descent has the desired structure of a thermal for $C_s = 0.23$, we take $C_s = 0.23$.

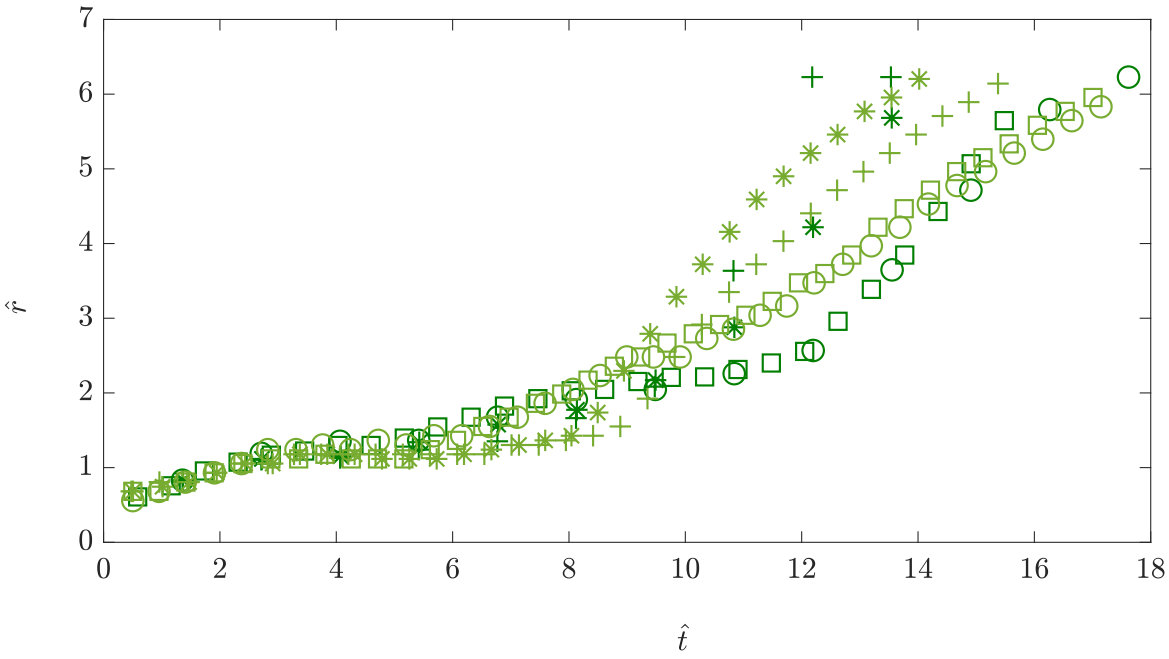

Fig. 5.11 Radial position $\hat{r}$, of the thermal and gravity current phases. The details of the simulations shown can be found in table 5.4.

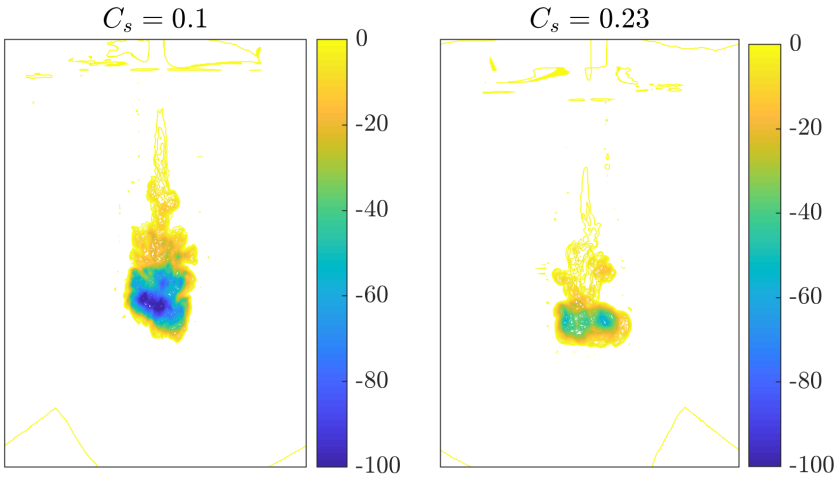

Fig. 5.12 Potential temperature field of a thermal with $L/D = 3$ at $H/D = 8$ with $C_s = 0.1$ and 0.23.

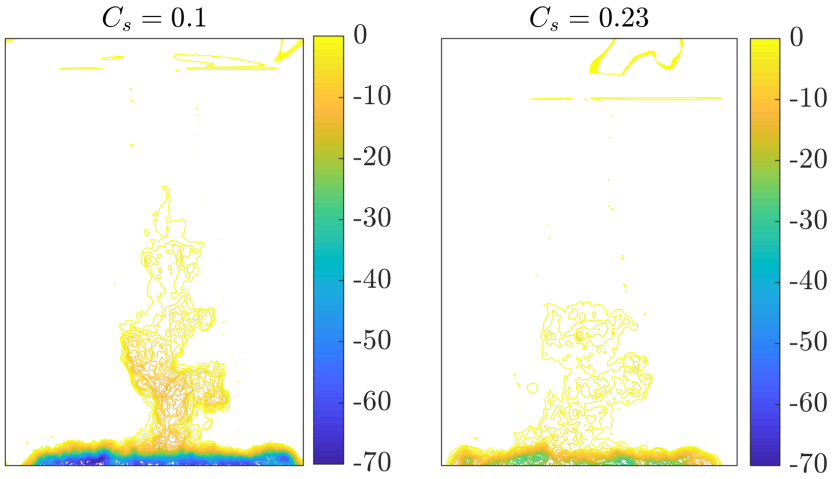

Fig. 5.13 Potential temperature field of a gravity current $L/D = 3$ at $H/D = 8$ with $C_s = 0.1$ and 0.23.

5.2.4 Initial Randomisation of Release

From early testing of MONC it was observed that the release of a cylinder from rest appeared laminar when compared to the highly turbulent laboratory experimental images. Imposing a pseudo-random perturbation in the potential temperature or momentum field is typical in order to encourage turbulence in numerical simulations by using DNS or LES methods [36]. However, there is disparity in the best way to achieve this. Kealy et al. [36] describe four common ways in which this can be done. For these simulations we randomly perturb the initial potential temperature field inside the cylinder only. This is achieved by randomly changing '*th_pert_loc*', which is the temperature perturbation at each gridpoint, by

$$th\_pert\_loc = th\_pert\_loc * (1.0 + ampl\_frac * (2.0 * random(i\_dum) - 1.0)), \quad (5.4)$$

where $ampl\_frac$ is a constant between 0 and 1, and $random(i\_dum)$ returns a random value between 0 and 1 ((0, 1) not included). Thus, $ampl\_frac$ represents the fractional amplitude of the applied random perturbations. Five values of $ampl\_frac$ have been considered, which are shown in table 5.5.

To compare the values of $ampl\_frac$ the vertical and radial positions have been compared for the release of a cylinder with $L/D = 3$ with initial potential temperature perturbation $\Delta\theta_0 = -0.25$. The Smagorinsky scheme is turned on with $C_s = 0.23$, P-W advection is used for the scalar field, and TVD for the velocity field, and the grid resolution is set as $\Delta = 10\,\text{m}$. Figure 5.14 shows a view of the potential temperature field integrated in the y-direction of

name	$ampl\_frac$	symbol
L03_0	0	○
L03_0.25	0.25	□
L03_0.5	0.5	∗
L03_0.75	0.75	+
L03_1	1	△

Table 5.5 Details of the simulations performed to test the effect of changing initial randomisation of the release.

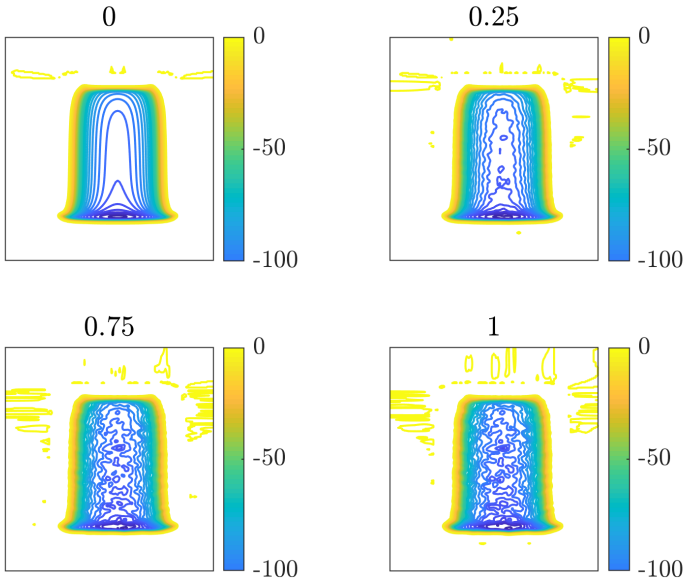

Fig. 5.14 Integrated views of the initiated cylinder for four values of $ampl\_frac = 0$, 0.25, 0.75 and 1.

the initial conditions for four values of $ampl\_frac$. These snapshots of the initial conditions show that as $ampl\_frac$ increases the interior of the cylinder exhibits more small scale structures.

The positions of the lowest vertical position and centre of mass are shown in figures 5.15 and 5.16 for the five values of $ampl\_frac$. There is little variation in the two measures of vertical position, the only differences being between $ampl\_frac = 0$, 0.25 and $ampl\_frac =$ 0.5, 0.75, 1. Similarly for the radial position shown in figure 5.17 there is little variation between the cylinders with $ampl\_frac = 0.5$, 0.75, 1. However, when $ampl\_frac = 0$, 0.25 there is a significant variation in the radial position. Therefore the first value of $ampl\_frac$ that does not significantly change any measurement is 0.5, and hence that value that will be used for the main simulations.

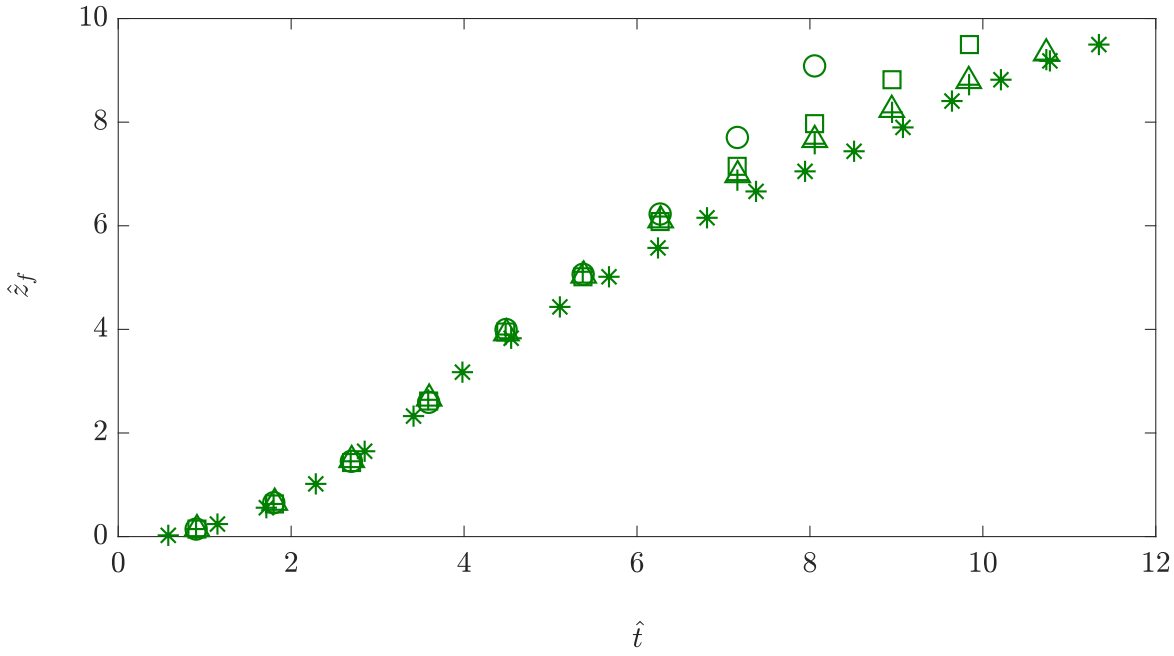

Fig. 5.15 Vertical position of the lowest point, z_f, of the thermal. The details of the simulations can be found in table 5.5.

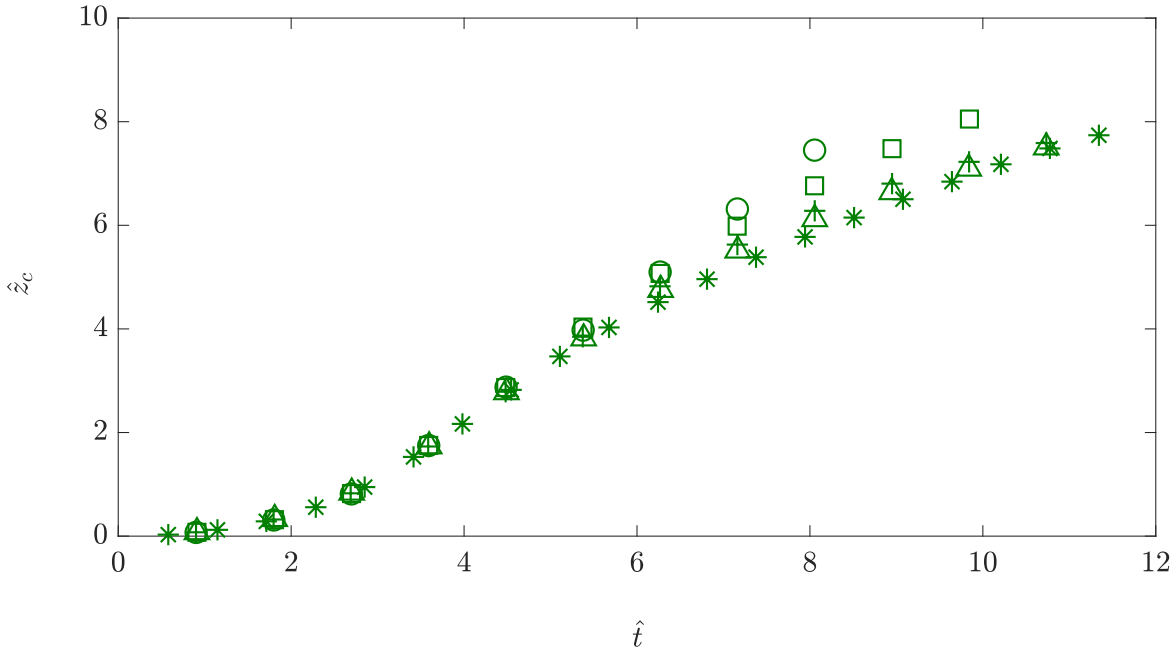

Fig. 5.16 Vertical position of the centre of mass, z_c, of the thermal. The details of the simulations can be found in table 5.5.

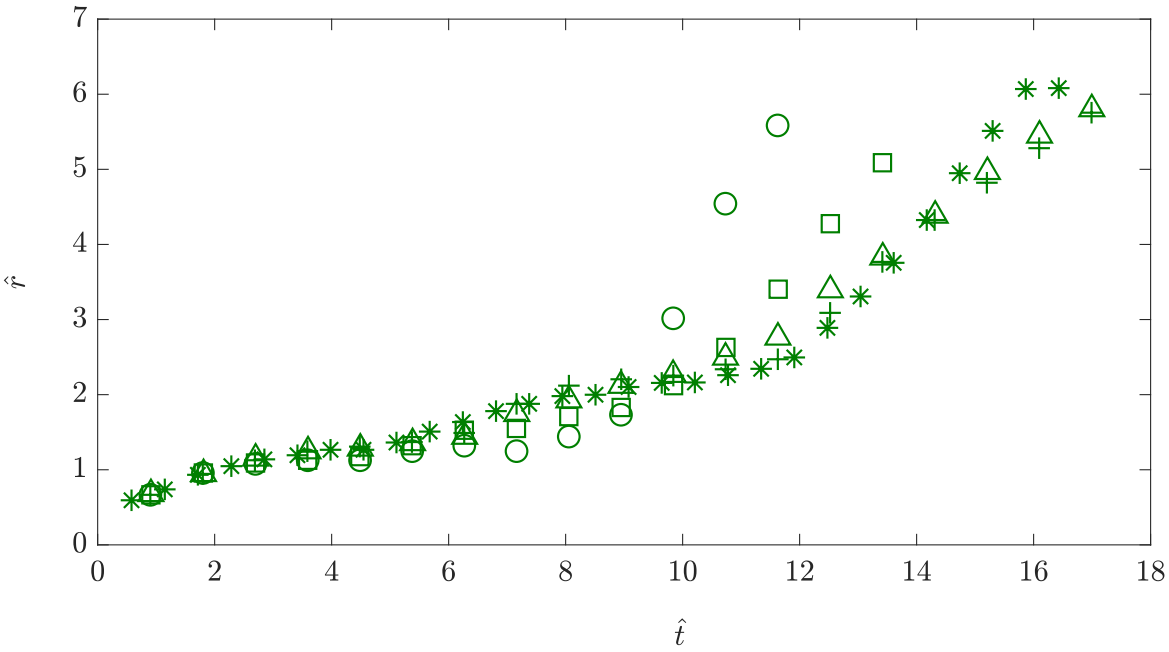

Fig. 5.17 Radial position, r, of the thermal and gravity current. The details of the simulations can be found in table 5.5.

5.3 Comparison with Rooney [49]

In comparing MONC to the LEM, we will compare exact replicas of simulations performed by Rooney [49]. Rooney initiated spheres of radii r_0 ranging from 238 m to 756 m with $\Delta\theta_0$ between -0.25 and -1 K. The domain was 512×512 gridpoints in the horizontal directions and 241 gridpoints in the vertical direction with a 50 m grid resolution. The LEM also uses a Smagorinsky subgrid model, which can also include the modelling of the backscatter process if desired. Rooney [49] ran the simulations with the backscatter and Smagorinsky schemes turned on and with the Smagorinsky constant set to $C_s = 0.1$. Rooney [49] found that running the LEM without the backscatter scheme showed the model to be more dissipative during the gravity current phase. Rooney [49] also observed that the model was not qualitatively sensitive to changes in the Smagorinsky constant C_s. The following simulations have been run with the exact conditions described in Rooney [49], unless stated otherwise. However, as mentioned previously, in MONC there is no model for the backscatter process.

Table 5.6 shows the variations of the L13 simulation performed by Rooney [49] considered here. To test the sensitivity of the simulations to changes in the Smagorinsky constant simulations with $C_s = 0.1$ (as used by Rooney [49]) and $C_s = 0.23$ have been compared to running the simulations with the no Smagorinsky scheme. It was found that when changing the value of the Smagorinsky constant from $C_s = 0.1$ (circles), to $C_s = 0.23$ (squares), the

r_0 (m)	$\Delta\theta_0$ (K)	grid size (m)	C_s	symbol
300	-0.25	50	0.1	○
300	-0.25	50	0.23	□
300	-0.25	50	off	△

Table 5.6 Direct comparison with Rooney [49] with varying values of the Smagorinsky constant, C_s

vertical position of the thermal and radial position of the gravity current varied significantly, shown in figure 5.18 and figure 5.19.

The graph of the vertical position of the thermal shown in figure 5.18, shows the replica of figure 4a from Rooney [49]. Plotted on figure 5.18 is the vertical position plus a virtual origin, $z+z_v$, against $B^{1/2}t$. Here, the virtual origin is defined as $z_v = n^{-1}r_0$ which is the vertical position of the thermal where the radius $r = 0$, and n is the spreading rate of the thermal. The dashed line plotted has equation $z+z_v = 2.8(B^{1/2}t)^{1/2}$, and is the fit of Rooney's data. For $C_s = 0.1$ (circles) the vertical position deviates from the similarity solution at late times. Since the L13 simulation being replicated here has good agreement with the similarity solution then it is possible that the absence of a backscatter scheme is the reason for the deviation from the solution in MONC. However, for the simulations with $C_s = 0.23$ and the simulation with no Smagorinsky scheme produces good agreement with the similarity solution. MONC is not able to accurately replicate the L13 simulation from Rooney [49] when using $C_s = 0.1$, it is assumed that this is due to the absence of the backscatter scheme in MONC. To mitigate this a different choice of C_s can be used in order to gain an improved agreement with the similarity solution.

The graph of the radial position of the gravity current is shown in figure 5.19 which can be compared to figure 7a in Rooney [49]. Plotted on figure 5.19 is the radial position relative to the centre of the domain, r_{max}, against $B^{1/2}(t-t_i)$, where t_i is the time at impact with the lower boundary. The dashed line plotted has equation $r_{max} = 1.7(B^{1/2}(t-t_i))^{1/2}$, and is the fit to Rooney's data. For $C_s = 0.1$ (circles) the radial position has a good agreement with the similarity solution with a reduced constant. This was also true of the L13 experiment in Rooney [49], but with an increased value of the constant. This indicates that the absence of a backscatter scheme is reducing the speed of the gravity currents. This reduction of speed is indicative of the dissipation of the gravity currents observed by Rooney [49] in the absence of the backscatter scheme in the LEM. When $C_s = 0.23$ and for the simulation with no Smagorinsky scheme there is not a good agreement with the similarity solution, especially at late times.

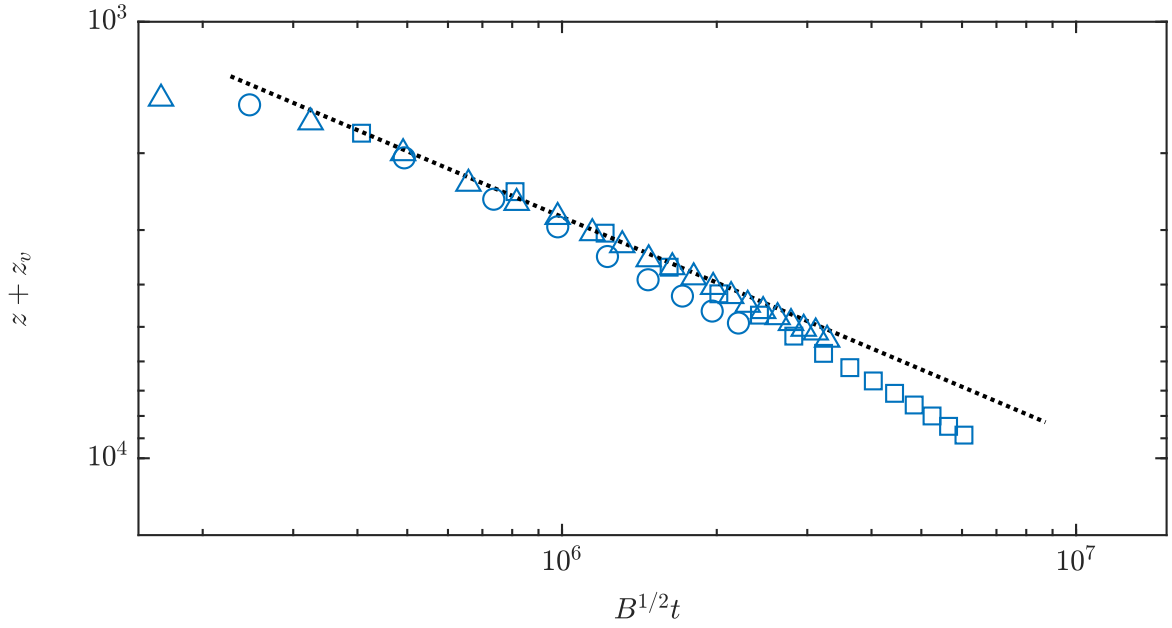

Fig. 5.18 Vertical position of the thermal produced by the simulations detailed in table 5.6. The dotted line is $z + z_v = 2.8(B^{1/2}t)^{1/2}$ which is the fit of Rooney's data.

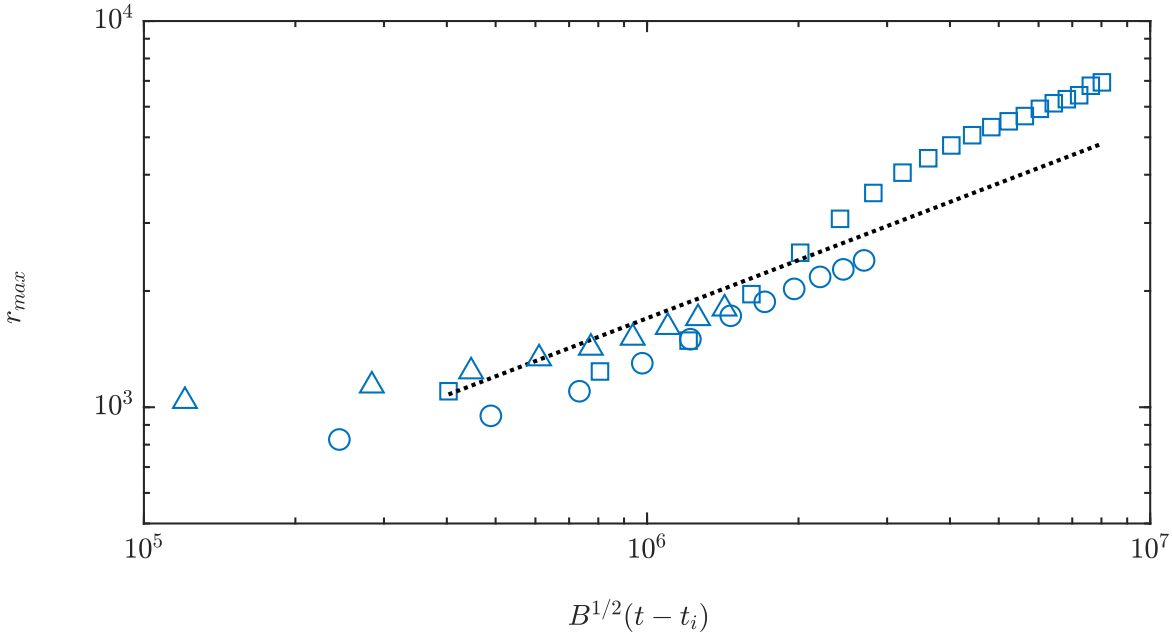

Fig. 5.19 Radial position of the gravity current produced by the simulations detailed in table 5.6. The dotted line is $r_{max} = 1.7(B^{1/2}(t - t_i))^{1/2}$ which is the fit of Rooney's data.

r_0 (m)	$\Delta\theta_0$ (K)	grid size (m)	C_s	symbol
300	-0.25	10	0.23	○
300	-0.5	10	0.23	□
300	-1	10	0.23	△
238	-1	10	0.23	○
378	-0.25	10	0.23	○

Table 5.7 Details of the simulations in MONC required in order to replicate the simulations performed by Rooney [49].

MONC was not able to replicate the L13 simulation from Rooney [49] exactly when using the exact set up used by Rooney [49]. It is assumed here that this is due to the absence of the backscatter scheme present in the LEM. In an attempt to mitigate the absence of the backscatter scheme we changed the Smagorinsky coefficient. Changing C_s improved the vertical position of the thermal but not the radial position of the gravity current. Since backscatter is the process of energy transfer from the small to the large scales, it is possible that a finer grid resolution could resolve the discrepancies with the similarity solution found by Rooney [49].

The following simulations replicate the initial conditions of experiments L11-15 from Rooney [49]. However, rather than using the domain set up used by Rooney the set up is as described in section 5.1.1. The main differences being the grid resolution, now 10 m, and the Smagorinsky constant, now $C_s = 0.23$. The details of these simulations are given in table 5.7.

The vertical and radial positions of the simulations with the present set up are shown in figures 5.20 and 5.21. Also plotted on both of these graphs are the same similarity solutions of Rooney [49] plotted in figures 5.18 and 5.19. In contrast to the previous set up for both the vertical and radial positions we now have good agreement with the similarity solutions. Therefore, to replicate the experiments performed in the LEM by Rooney [49] a finer grid resolution and adjusted Smagorinsky constant is needed to obtain the same results in MONC. This adjustment to the grid resolution and the Smagorinsky constant is needed since MONC does not have a backscatter scheme available. The code parallelisation of MONC makes it much more feasible to run at a finer resolution [10], hence coding a backscatter scheme in MONC becomes less of a priority.

5.4 Spheres vs Cylinders

The shape of the source of atmospheric downdraughts is difficult to classify. We therefore test the release from two canonical shapes: spheres and cylinders. Moreover, in a laboratory it is difficult to release spheres of fluid so cylindrical tubes of different lengths were used. In order

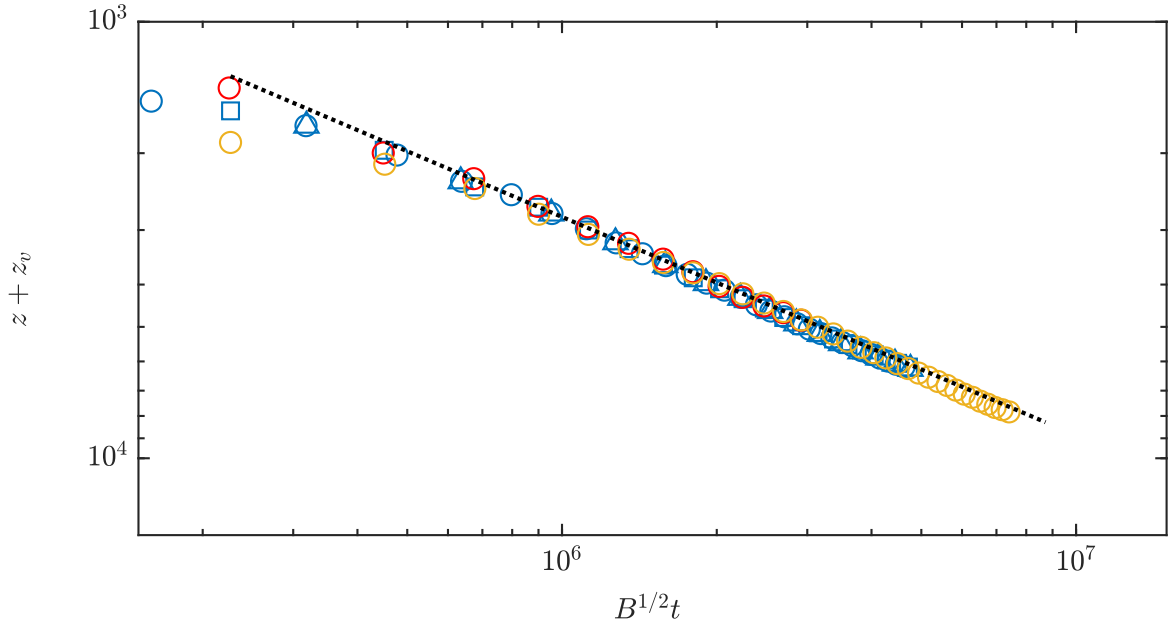

Fig. 5.20 Vertical position of the thermal produced by the simulations detailed in table 5.7. The dotted line is $z + z_v = 2.8(B^{1/2}t)^{1/2}$ which is the fit of Rooney's data.

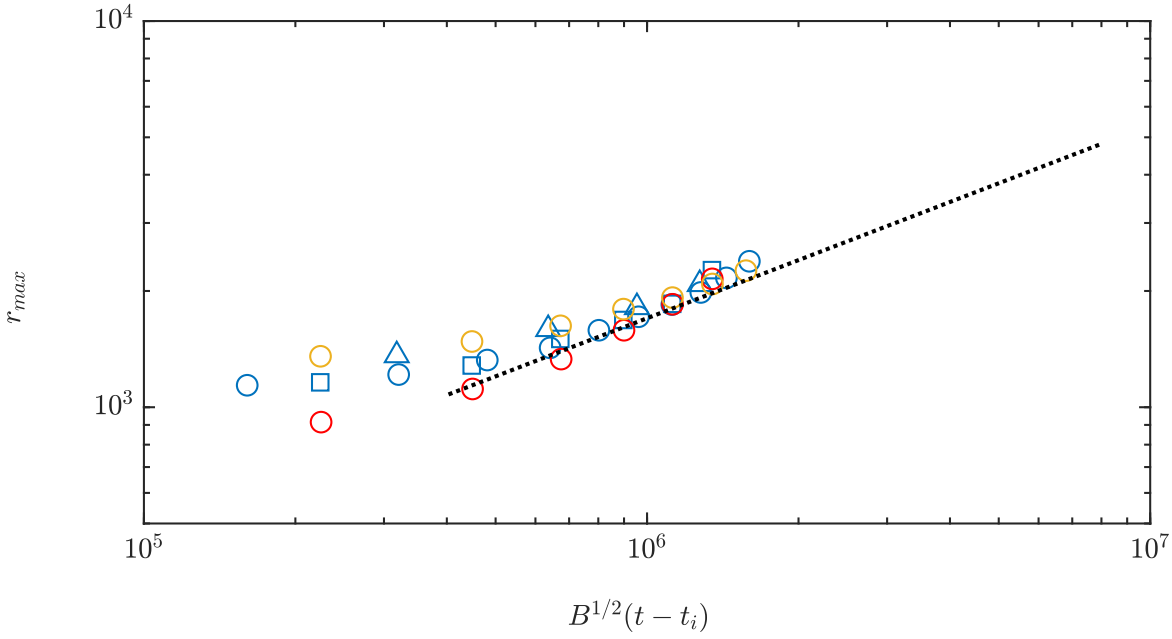

Fig. 5.21 Radial position of the gravity current produced by the simulations detailed in table 5.7. The dotted line is $r_{max} = 1.7(B^{1/2}(t - t_i))^{1/2}$ which is the fit of Rooney's data.

simulation	r_0 (m)	L (m)	$\Delta\theta_0$ (K)	$B_0(\times 10^5)$	symbol
L01c	250	500	-0.1	3.21	□
L02c	250	1000	-0.1	6.42	□
L03c	250	1500	-0.1	9.63	□
L04c	250	2000	-0.1	12.84	□
L05c	250	2500	-0.1	16.05	□

Table 5.8 Cylinder simulation details: initial radius, length, potential temperature perturbation and buoyancy of the cylinder.

Simulation	r_0 (m)	$\Delta\theta_0$ (K)	$B_0(\times 10^5)$	symbol
L01s	290	-0.1	3.34	○
L02s	360	-0.1	6.39	○
L03s	410	-0.1	9.44	○
L04s	450	-0.1	12.48	○
L05s	490	-0.1	16.12	○

Table 5.9 Sphere simulation details: initial radius, potential temperature perturbation and buoyancy of the sphere.

to make comparisons with numerical studies performed by Rooney [49] and Lai et al. [37] an understanding of how the evolution of spheres and cylinders differ is required. The time and length scales used for thermals relate to the effective spherical radius and the buoyancy. So to find comparable spheres and cylinders we will use the effective spherical radius (to the nearest 10 m) of five different lengths of cylinder. The details of the cylinder simulations are shown in table 5.8, all the cylinders have the same initial radius, $r_0 = 250$m, and potential temperature perturbation, $\Delta\theta_0 = -0.1$K, while the length varied from 500 to 2500 m i.e. $1 \leq L/D \leq 5$. For a given cylinder the radii of the spheres are calculated, to the nearest 10m (grid resolution), so as to have similar volumes as the corresponding cylinders. The spheres are also initiated with the same initial potential temperature perturbation, $\Delta\theta_0 = -0.1$K, so that the corresponding cylinders and spheres have approximately the same total buoyancy. The details of the spherical simulations are shown in table 5.9.

5.4.1 Qualitative Comparisons

To compare the evolution of a cylinder versus a sphere a vertical slice through the centre of the domain of the potential temperature field was taken for each simulation. These vertical slices were then compared at three different times. The first comparison was made just after the simulation was set running (figure 5.22). The second comparison was made at the

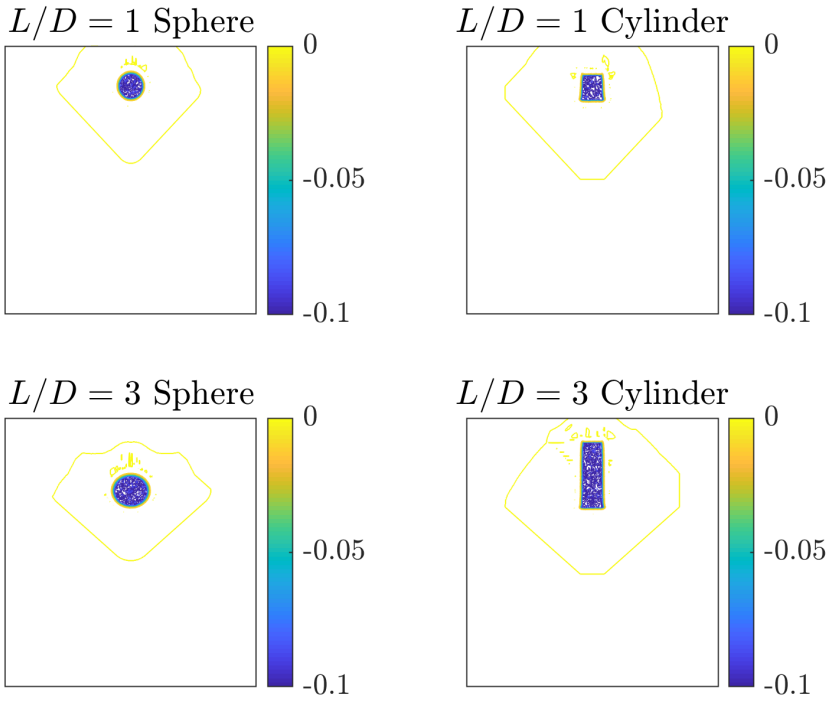

Fig. 5.22 Central slice of *L*01 and *L*03 simulations (top/bottom) and spheres and cylinders (left/right). These slices show the first time output, i.e. 200s after the sphere/cylinder was initiated.

moment the cold bubble impacted the ground, (figure 5.23), and the third comparison after the gravity current had reached the edges of the domain, (figure 5.24).

Two lengths of cylinder are compared to their respective spheres. The top rows of figures 5.22 to 5.24 show the L01 simulations, and the bottom rows the L03 simulations. The left hand columns of the figures show the spheres, and the right hand columns the cylinders of the two simulations. The L01 and L03 simulations were chosen as between them they displayed all the differences between the cylindrical and the spherical releases for $L/D = 1$ to 5.

The moments of impact for the four simulations are shown in figure 5.23. The colourbar gives the temperature scale for the images, it should be noted here that the initial temperature perturbation was $\Delta\theta_0 = -0.1\,\mathrm{K}$. Both simulations in which the initial temperature perturbations were spherical look qualitatively very similar. Both the L01 and L03 spheres have two vortex cores and a trailing wake of comparable sizes and temperatures. Similarly, the L01 simulations for both a spherical and cylindrical initiation look similar in that they have comparable internal structures and comparable sized trailing stems. The main difference

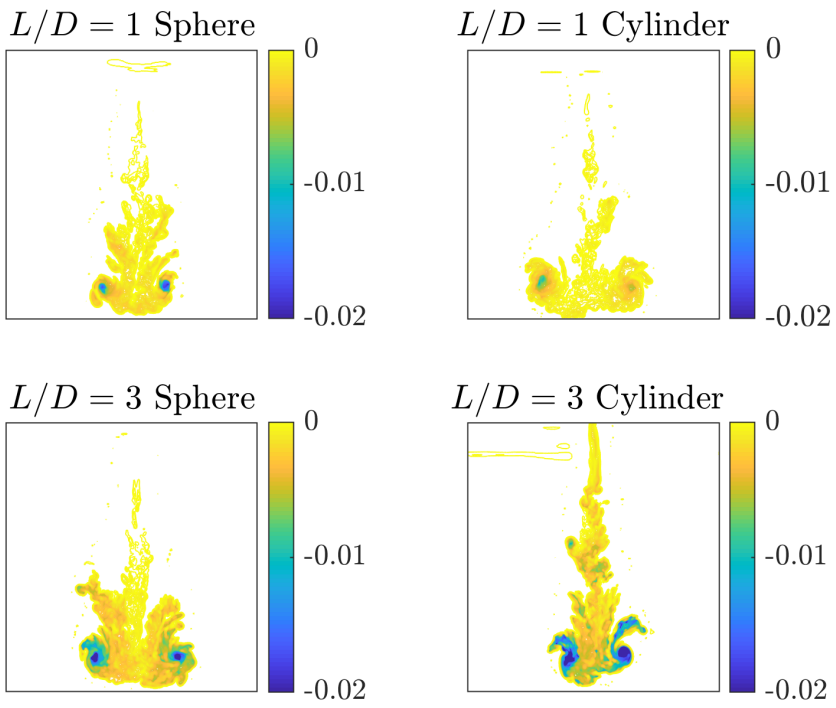

Fig. 5.23 Central slice of *L*01 and *L*03 simulations (top/bottom) and spheres and cylinders (left/right). These slices show the moment of impact of the sphere/cylinder with the lower boundary

between the L01 cylindrical and spherical releases was that the L01 cylinder has entrained more of the ambient fluid and is warmer than its spherical counterpart. There is a more significant difference between the L03 simulations and the L01 simulations. The L03 cylinder has a significantly larger wake behind it than the L03 sphere. This is similar to the qualitative results from the experiments discussed in chapter 3, where we saw that for $L/D = 5$ there was a large trailing wake.

The gravity currents for the four simulations are shown in figure 5.24. As with the impact images there is some similarity between the L01 and L03 simulations from spherical releases, with similar internal structures in the head of the gravity currents and the presence of the trailing wake. As with both simulations with $L/D = 1$ (above), we see that the cylinder has again entrained more of the ambient, making the gravity current comparably warmer than the L01 sphere. Similarly the snapshots from figure 5.23 the L03 cylinder simulation has a much larger wake than the L03 sphere simulation.

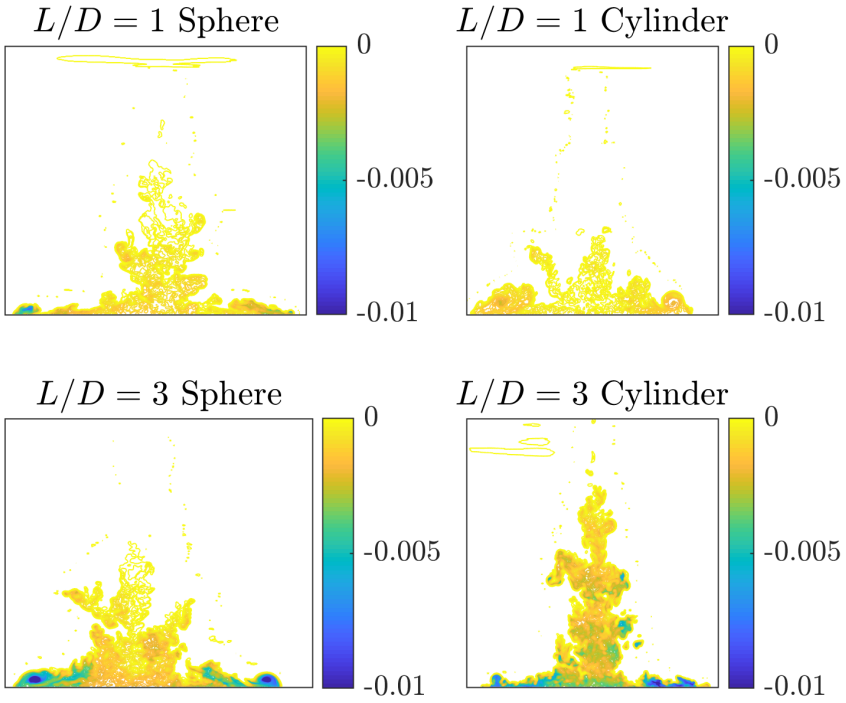

Fig. 5.24 Central slice of $L01$ and $L03$ simulations (top/bottom) and spheres and cylinders (left/right). These slices show the gravity current at least 3 source widths from the centre of the domain.

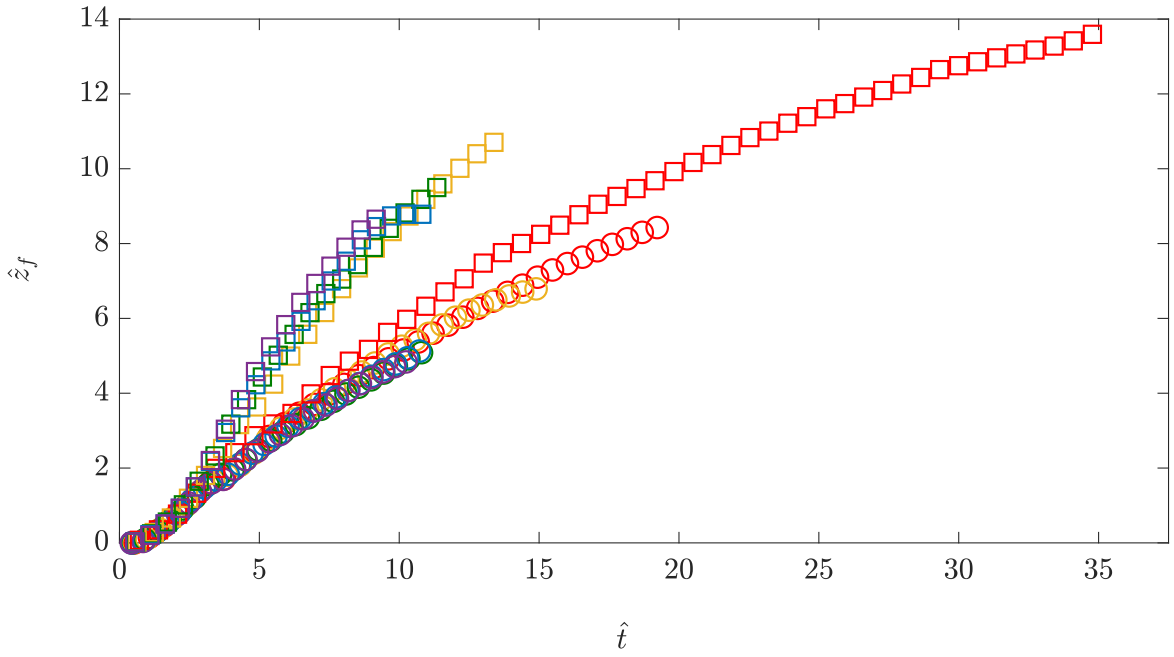

Fig. 5.25 Vertical position of the front, z_f, of the cylindrical (squares) and spherical (circles) simulations detailed in table 5.8 and table 5.9.

5.4.2 Quantitative Comparisons

From the snapshots shown in figures 5.22 to 5.24 there was a significant qualitative difference in the potential temperature field between the L03 cylinder and sphere, but less between the L01 cylinder and sphere. In this section the non-dimensional vertical and radial positions are compared for all lengths of cylinder and radii of spheres in tables 5.8 and 5.9. The lowest vertical position and centre of mass are shown in figures 5.25 and 5.26. In both measures of vertical position there is a clear variation in vertical position between the cylinder and spheres except for the L01 cylinder simulation. For the L01 simulations the vertical positions of the cylinder are much closer to those of the L01 sphere. As with the qualitative comparison this is due to the two having similar radii ($r_{0c} = 250\,\text{m}$, $r_{0s} = 290\,\text{m}$) and vertical heights ($L_c = 500\,\text{m}$, $L_s = 580\,\text{m}$).

In contrast, the opposite is true of the radial positions shown in figure 5.27 for both the cylindrical and spherical releases. The radial positions are only significantly different between the L01 sphere and cylinder simulations. With the exception of the L01 case, the radial position of the spheres and cylinders with comparable volumes and buoyancies have different qualitative and quantitative behaviours. We, therefore, would not expect our measurements of the vertical positions from the laboratory experiments to follow the results found by Rooney [49], except possibly in the $L/D = 1$ case. However, we may expect that

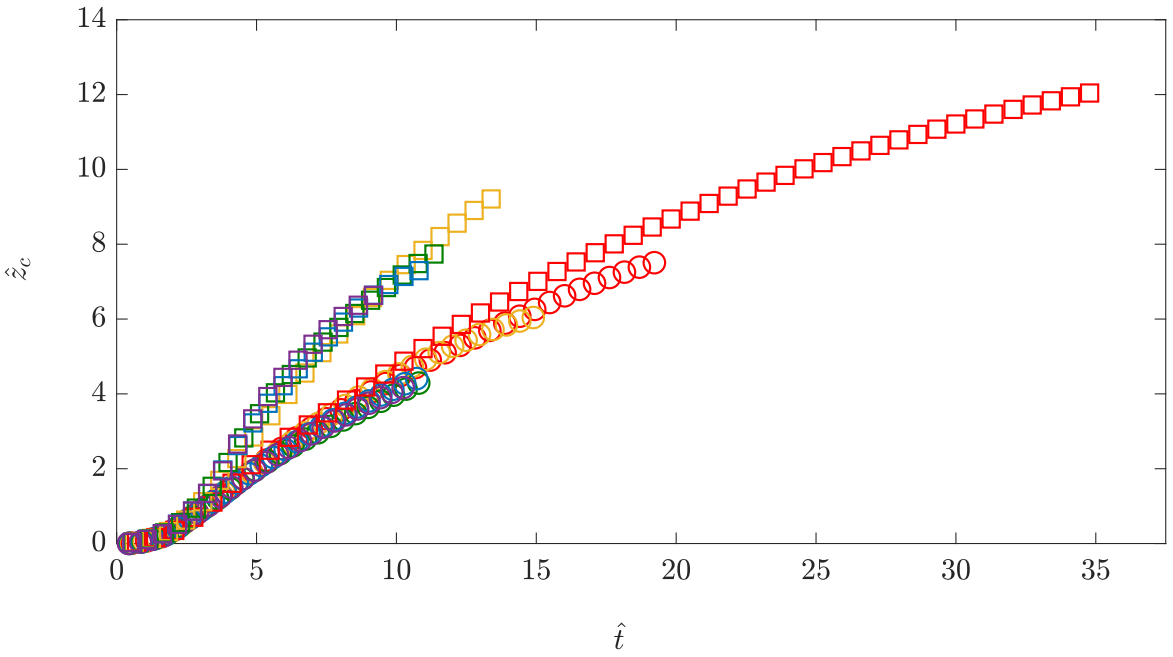

Fig. 5.26 Vertical position of the centre of mass, z_c of the cylindrical (squares) and spherical (circles) simulations detailed in table 5.8 and table 5.9.

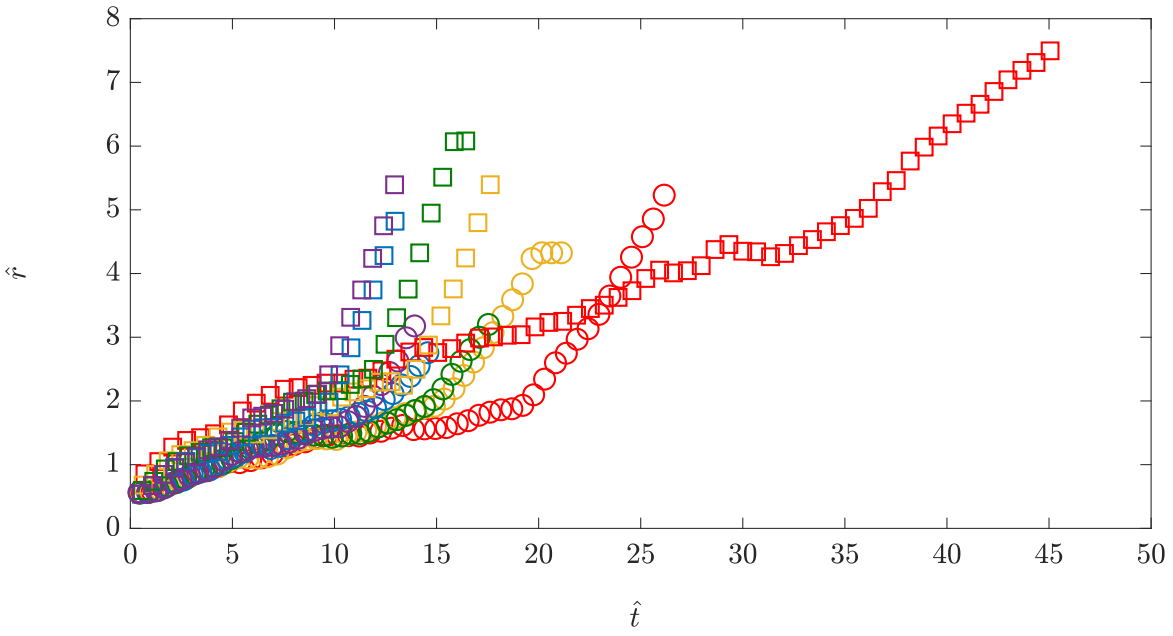

Fig. 5.27 Radial position r of the thermal and gravity currents of the cylindrical (squares) and spherical (circles) simulations, which are detailed in table 5.8 and table 5.9.

Simulation	r_0 (m)	L (m)	H (m)	$\Delta\theta_0$ (K)	grid size (m)	symbol
H02L01	250	500	1000	-0.1	10	□
H02L02	250	1000	1000	-0.1	10	□
H02L03	250	1500	1000	-0.1	10	□
H02L04	250	2000	1000	-0.1	10	□
H02L05	250	2500	1000	-0.1	10	□
H08L01	250	500	4000	-0.1	10	○
H08L02	250	1000	4000	-0.1	10	○
H08L03	250	1500	4000	-0.1	10	○
H08L04	250	2000	4000	-0.1	10	○
H08L05	250	2500	4000	-0.1	10	○

Table 5.10 Details of the simulations of cylinders released from rest performed to replicate the laboratory experiments.

the radial position of the laboratory experiments (except the $L/D = 1$ case) to follow Rooney [49]. However, this will only be true if the numerical simulations are indeed representative of the laboratory conditions.

5.5 Comparison with Experiments

In this section we compare the numerical simulations described in table 5.10 to the thermals and gravity currents produced in the laboratory experiments. The simulations mimic the 5 lengths of tube, at both of the heights that were considered in the experiments chapters. The same measurements have been taken for both the descent and gravity current phases of the simulations and are compared to the experimental data here.

5.5.1 Qualitative Comparisons

The raw images from two experiments are compared to the corresponding numerical simulations in this section. The experiments and simulations have been compared at two non-dimensional times relative to the time of impact. The first comparison is shown in figure 5.28: this experiment/simulation was performed at $H/D = 8$ with tube length $L/D = 1$. Two times compared are $\hat{t}_i \pm 5$, i.e. the thermal and the gravity current phase. The top row shows the experiment and simulation at $\hat{t} = \hat{t}_i - 5$, which is the flow during the thermal phase just prior to impact with the ground. Both the experimental and simulation at this time are qualitatively similar. However, in the experimental image there is a larger wake behind the thermal, and larger turbulent structures at the edge of the thermal. Similarly, in the gravity current phase, bottom row of figure 5.28, the experiment and simulation are very similar

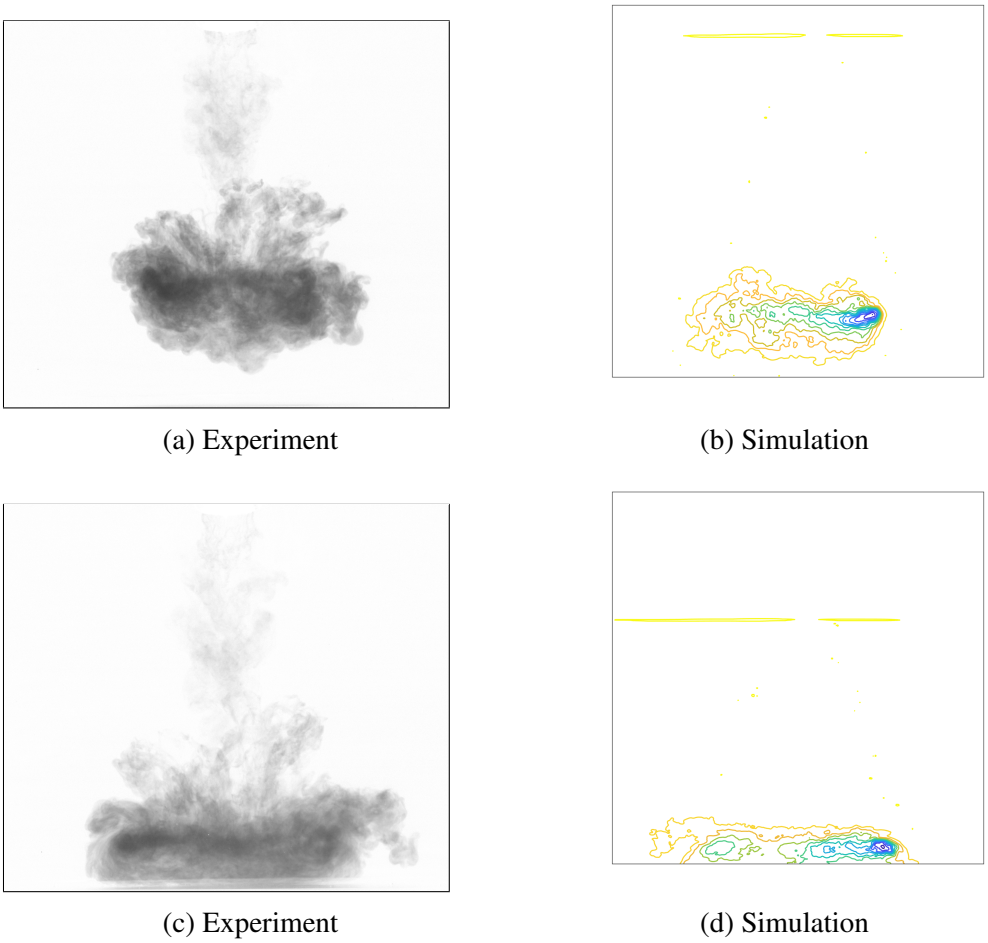

(a) Experiment (b) Simulation

(c) Experiment (d) Simulation

Fig. 5.28 Comparison of snapshots from simulations and experiments performed with $L/D = 1$ at $H/D = 8$. These images are taken at $\hat{t}_i \pm 5$.

except for the presence of a wake in the experimental image, and the head of the gravity current in the simulation is lower than in the experiment.

The second comparison is shown in figure 5.29. This experiment/simulation was performed at $H/D = 8$ with tube length $L/D = 5$. Two times compared are $\hat{t}_i \pm 2$, i.e. the thermal and the gravity current phase. The top row shows the experiment and simulation at $\hat{t} = \hat{t}_i - 2$, which is the flow during the thermal phase just prior to impact with the ground. Both the experiment and simulation at this time are qualitatively similar, but the thermal in the simulation is much closer to the floor than the experiment. In both images there is a large wake behind the thermal, but the larger turbulent structures around the thermal's edge are not present in the simulations. Similarly, in the gravity current phase, bottom row, the experiment and simulation are similar except the head of the gravity current in the simulation is lower than in the experiment.

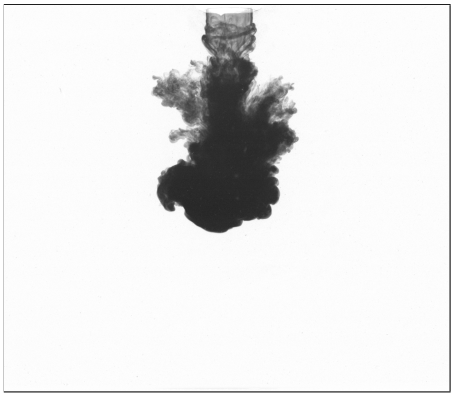

(a) Experiment

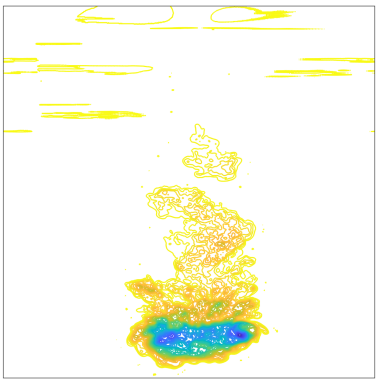

(b) Simulation

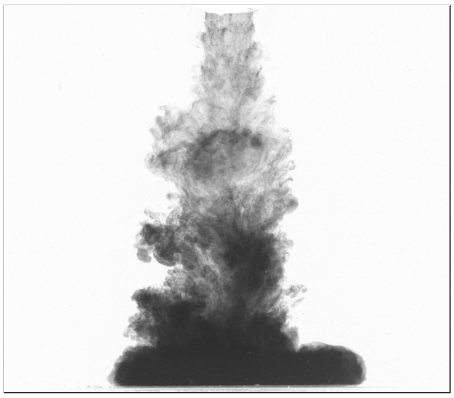

(c) Experiment

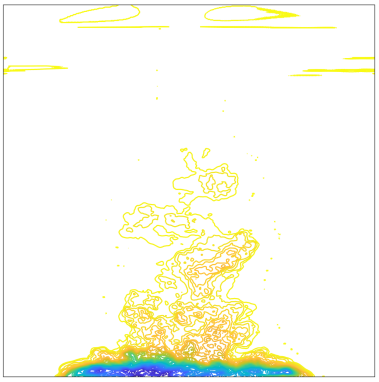

(d) Simulation

Fig. 5.29 Comparison of snapshots from simulations and experiments performed with $L/D = 5$ at $H/D = 8$. These images are taken at $\hat{t}_i \pm 2$.

We know from the study of buoyant plumes that turbulent coherent structures at the edge of the flow play a crucial role in increased entrainment Burridge et al. [12, 11]. The qualitative observation that large scale turbulent coherent structures were present in experiments and absent in simulations may hint at a difference in entrainment between experiments and numerical simulations.

5.5.2 Quantitative Comparisons

Centre of Mass and radii measurements

The vertical position of the centre of mass scaled by the length and time scales based on the initial volume are plotted for all tube lengths at both $H/D = 2$ (squares) and $H/D = 8$ (circles) in figure 5.30a. The solid line drawn on the figure is $\hat{z}_c = 2.31\hat{t}^{1/2}$ which is the

similarity solution for a thermal with $m = 3$ and $n = 0.25$. At later times we see the vertical position of the thermal reaches the expected power law, $t^{1/2}$. Also plotted (black dots) are the experimental data for $L/D = 1$ at $H/D = 8$. We see that initially the experiments and numerics agree well. This is surprising as in the experiments any initial mixing is inhibited by the presence of the tube and so we would expect the experiments to initially have an increased vertical velocity compared to the numerical simulations. This suggests that there is limited mixing in the simulations whilst the flow transitions from a cylinder to a spheroid. Moreover, after the end of draining the vertical velocity of the numerics is increased compared to the experiments. This, and the matching of the experiments and simulations during the draining phase, quantitatively indicate that there is a reduction in mixing in the simulations compared to the experiments as expected by observation.

The radius of the thermal scaled by the length scale and time scales based on the initial volume is plotted for all tube lengths at both $H/D = 2$ (squares) and $H/D = 8$ (circles) in figure 5.30b. The solid line is $\hat{r} = 0.58\hat{t}^{1/2}$ which is the similarity solution for a thermal with $m = 3$ and $n = 0.25$. Also plotted (black dots) are the experimental data where $L/D = 1$ and $H/D = 8$. We see that the radius from the numerical simulations and the experiments agree well with each other. This indicates that the reduced mixing that affected the vertical position of the centre of mass has had a less significant impact on the radial spread, contrary to the implications of simple models within the literature which suggest that $\mathrm{d}r/\mathrm{d}z \sim \alpha$.

Shape Factors

We have seen that the vertical position of the centre of mass has been affected by the reduced mixing in the numerical simulations compared to experiments. Since the values of the shape factors and the spreading rates depend on these this measurements we expect a difference in these values also.

The ratios of the semi-minor and major radius, $b = h/r$ are plotted for all tube lengths for both $H/D = 2$ and $H/D = 8$ in figure 5.31. Also plotted is the value of b for $L/D = 1$ from the experiments (black dots). The value of b shows a reduction compared to the experiments, especially with respect to the $L/D = 1$ simulations. However, the qualitative behaviour remains the same, with the value of b increasing before reaching a constant value of $b = 0.36 \pm 0.02$ and $b = 0.66 \pm 0.03$ for $L/D = 1$ and 2 respectively at $H/D = 8$.

The spreading rates $n = r/z_c$ are plotted for all tube lengths at $H/D = 2$ and $H/D = 8$ in figure 5.32. As expected n shows a reduction in value compared to the experiments, especially with respect to the $L/D = 1$ simulations. Also, as with b, the qualitative behaviour provides a good match to the experiments with n initially decreasing and then reaching a constant value of $n = 0.33 \pm 0.01$ and $n = 0.24 \pm 0.02$ for $L/D = 1$ and 2 respectively at

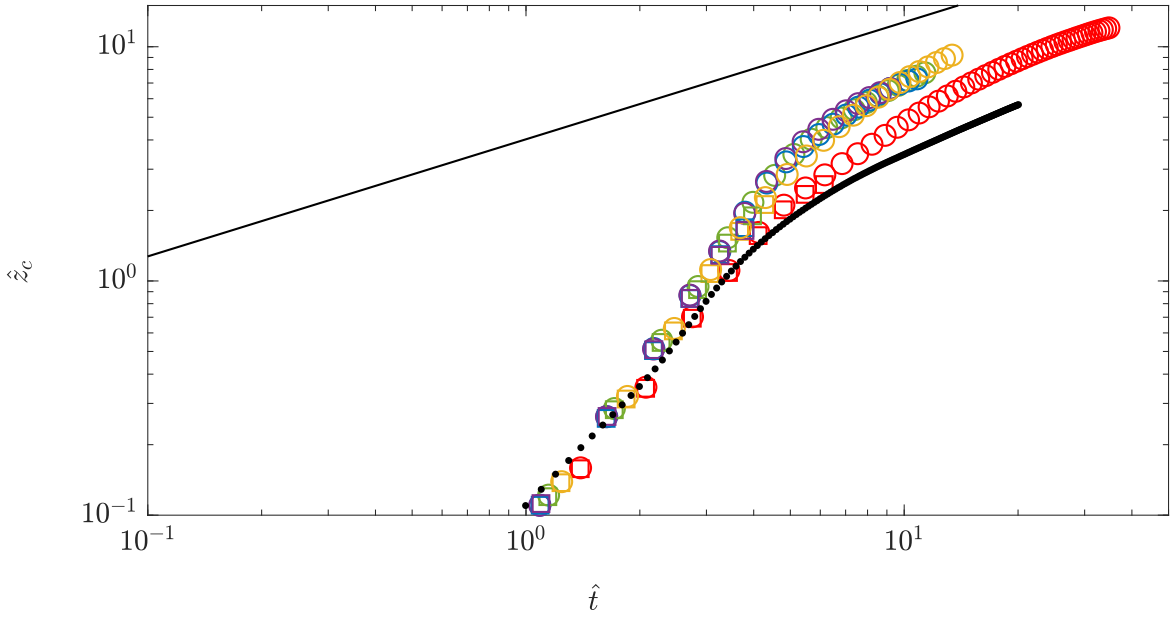

(a) $\hat{z}_c$

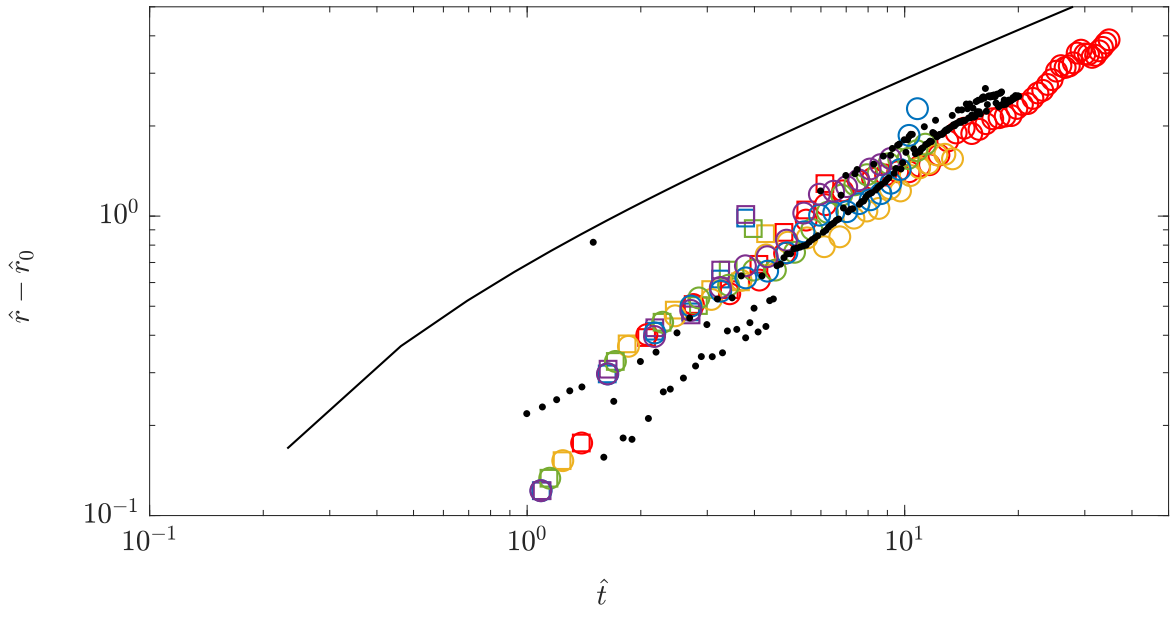

(b) $\hat{r} - \hat{r}_0$

Fig. 5.30 The vertical position of the centre of mass $\hat{z}_c$ and the radius $\hat{r} - \hat{r}_0$ of the thermal of the simulations for $L/D = 1$ (red), 2 (yellow), 3 (green), 4 (blue) and 5 (purple) at both $H/D = 2$ (squares) and 8 (circles). Also plotted is the vertical position of the centre of mass and the radius from the experiment with $L/D = 1$ and $H/D = 8$ (black dots).

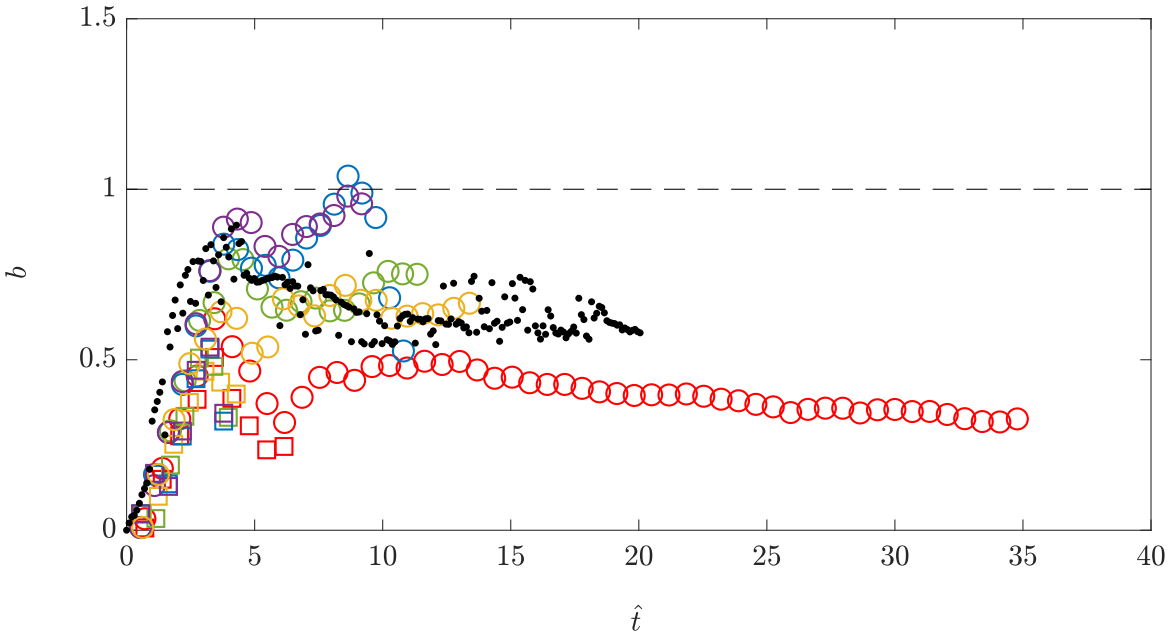

Fig. 5.31 The value of the ratio of the semi-major and minor axis of the thermal, $b = h/r$, for the simulations with $L/D = 1$ (red), 2 (yellow), 3 (green), 4 (blue) and 5 (purple) at both $H/D = 2$ (squares) and 8 (circles). Also plotted is the vertical position of the centre of mass and the radius from the experiment with $L/D = 1$ and $H/D = 8$ (black dots).

$H/D = 8$. In chapter 3 it was shown that for a simple model of a self-similar thermal the spreading rate n is related to the entrainment coefficient by $n = \alpha a/3m \approx \alpha$ for a spheroid. Therefore, a reduction in n is equivalent to a reduced entrainment coefficient and therefore a reduction in mixing compared to the laboratory experiments. This has implications for the use of MONC since it underestimates the mixing even at this fine (10 m) grid resolution.

Gravity Currents

The largest deviation between the experiments and the numerical simulations occurs in the gravity current phase. The radii of the gravity currents relative to the point of impact are plotted for all tube lengths at both $H/D = 2$ (squares) and $H/D = 8$ (circles) in figure 5.33. The dashed line drawn on the plot is $\hat{r} = 1.26(\hat{t} - \hat{t}_i)^{1/2}$. This solution is based on the similarity solution for gravity currents, using the theoretical values of λ and Fr, and shown in the previous chapter to qualitatively approximate the experimental gravity currents at late times. The gravity currents produced by the simulations travel faster than the experimental gravity currents, but in some cases (i.e. $L/D = 1$ at $H/D = 2$) do reach the same gradient as the similarity solution at late times. This is expected since there is less mixing in the simulations compared to the experiments.

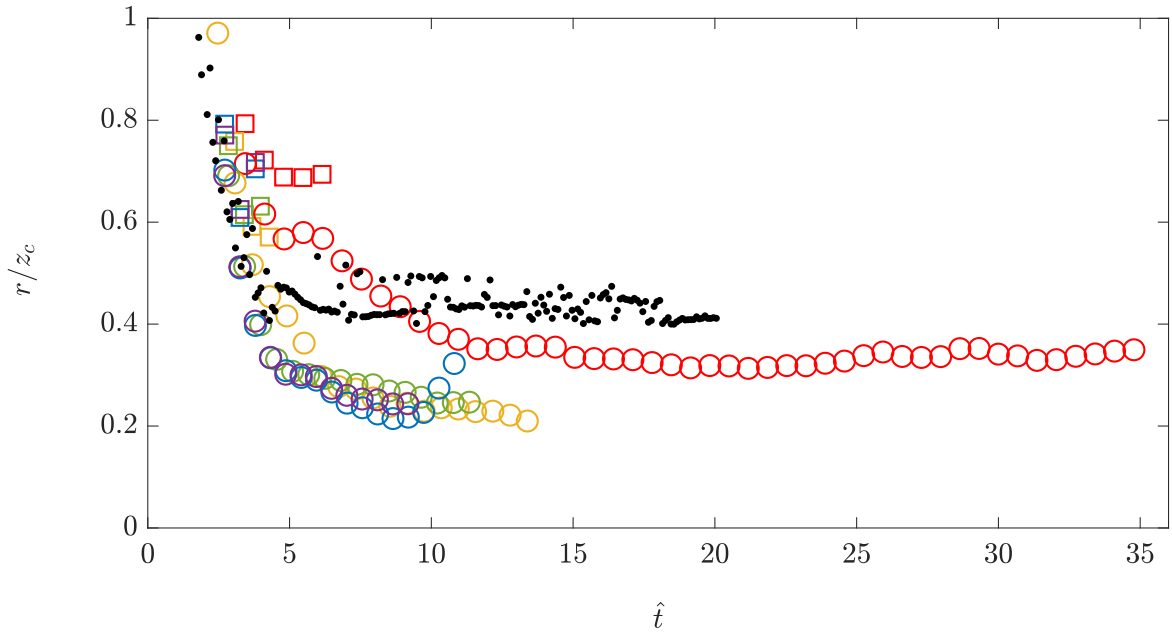

Fig. 5.32 The value of the spreading rate, n, for the simulations with $L/D = 1$ (red), 2 (yellow), 3 (green), 4 (blue) and 5 (purple) at both $H/D = 2$ (squares) and 8 (circles). Also plotted is the vertical position of the centre of mass and the radius from the experiment with $L/D = 1$ and $H/D = 8$ (black dots).

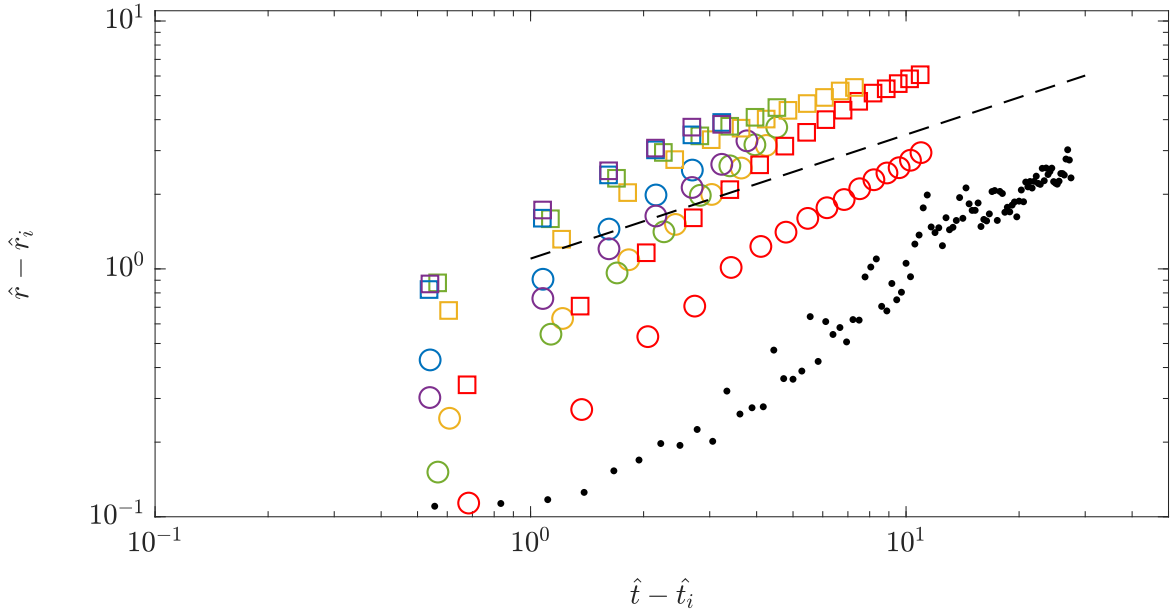

Fig. 5.33 The radius $\hat{r} - \hat{r}_i$ of the gravity current relative to the point of impact for the simulations with $L/D = 1$ (red), 2 (yellow), 3 (green), 4 (blue) and 5 (purple) at both $H/D = 2$ (squares) and 8 (circles). The dashed line represents the similarity solution with $\lambda = pi^{-1}$ and $Fr = 1.4$ given by $\hat{r} = 1.26(\hat{t} - \hat{t}_i)^{1/2}$. Also plotted is the radius of the gravity current from the experiment with $L/D = 1$ and $H/D = 8$ (black dots).

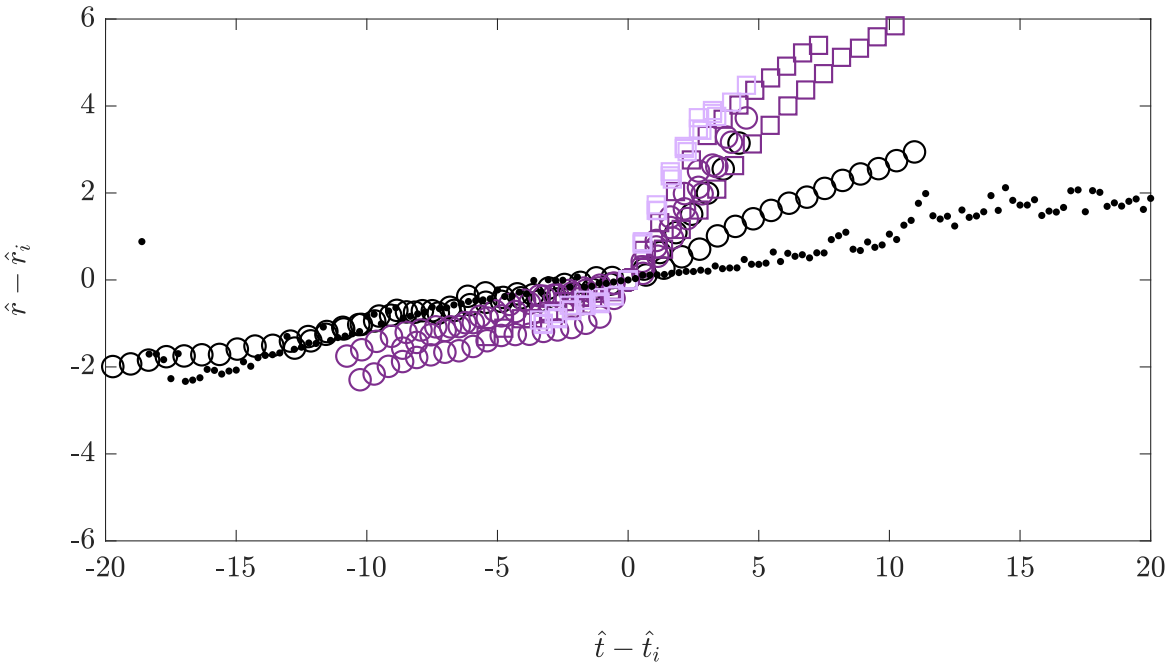

Fig. 5.34 The radius $\hat{r} - \hat{r}_i$ relative to the point of impact of both the thermal and the gravity current for the simulations with $L/D = 1$, 2, 3, 4 and 5 at both $H/D = 2$ (squares) and 8 (circles). The colours represent the phase in which the thermal was in upon impact with the ground: draining (lilac), development (purple) or self-similar thermal (black). Also plotted is the radius of the gravity current from the experiment with $L/D = 1$ and $H/D = 8$ (black dots).

In chapter 4 we showed that the radius of the gravity current evolved differently depending on the phase in which the thermal impacted the ground. Figure 5.34 shows $\hat{r} - \hat{r}_i$ against $\hat{t} - \hat{t}_i$ for the numerical simulations with $L/D = 1$, 2, 3, 4 and 5 at $H/D = 2$ and 8. The colours here represent the phase in which the experimental thermals were in upon impact with the ground: draining (lilac), development phase (purple) or self-similar thermal (black). Also plotted is the radius of both the thermal and the gravity current for the experiment with $L/D = 1$ at $H/D = 8$. As with the experiments the thermals that impact the ground during the draining or development phases have a stationary point at the time of impact. However, the simulations which impact the ground during the self-similar thermal phase do not display the same evolution of the radius as the experiments during impact. These simulations also display the stationary point at impact similar to the experiments that impacted the ground during the draining and development phases.

Draining Phase	Development Phase	Thermal Phase
$\frac{\mathrm{d}V}{\mathrm{d}t} = 3m(t)n(t)r^2\frac{M}{V} + \pi r_0^2\frac{\mathrm{d}z_b}{\mathrm{d}t}$	$\frac{\mathrm{d}V}{\mathrm{d}t} = 3m(t)n(t)r^2\frac{M}{V}$	$\frac{\mathrm{d}V}{\mathrm{d}t} = 3mnr^2\frac{M}{V}$
$\frac{\mathrm{d}M}{\mathrm{d}t} = \frac{2}{3}\pi r_0^2\left(g_0' z_b(t) + z_b(t)\frac{\mathrm{d}z_b}{\mathrm{d}t}\right)$	$\frac{\mathrm{d}M}{\mathrm{d}t} = \frac{2}{3}g_0' V_0$	$\frac{\mathrm{d}M}{\mathrm{d}t} = \frac{2}{3}g_0' V_0$
$\frac{\mathrm{d}z_c}{\mathrm{d}t} = \frac{M}{V}$	$\frac{\mathrm{d}z_c}{\mathrm{d}t} = \frac{M}{V}$	$\frac{\mathrm{d}z_c}{\mathrm{d}t} = \frac{M}{V}$
$\frac{\mathrm{d}r}{\mathrm{d}t} = n(t)\frac{M}{V} - \frac{r}{3m}\frac{\mathrm{d}m}{\mathrm{d}t} + \frac{\pi r_0^2}{3mr^2}\frac{\mathrm{d}z_b}{\mathrm{d}t}$	$\frac{\mathrm{d}r}{\mathrm{d}t} == n(t)\frac{M}{V} - \frac{r}{3m}\frac{\mathrm{d}m}{\mathrm{d}t}$	$\frac{\mathrm{d}r}{\mathrm{d}t} = n\frac{M}{V}$

Table 5.11 Full model of the draining, development and the thermal phases under the spheroidal shape assumption.

5.6 Comparison with Model

5.6.1 Thermals

In chapter 3 we developed the model given in table 5.11 that represents three phases of the thermals development for our experiments: draining, development and self-similar thermal phase. We can see from figures 5.31 and 5.32 that we once again have a portion of the flow where there exists non-constant shape factors, b, and spreading rates, n, indicating the existence of the development phase. For the $L/D = 1$ and 2 at $H/D = 8$ experiments we also have times where both b and n are constant, indicating the existence of the self-similar phase. So the existence of the development and thermal phases in the numerics are trivial. However, the main difference between the experiments and the simulations is the absence of the tube in the simulations, which allows for the cylinder to spread radially above the release height. However, the draining phase is still required due to model only considering the evolution of spheroid below the source height, as opposed to a cylinder developing into a spheroid. Therefore, the additional volume and buoyancy added by the cylinder 'draining' into the spheroid is still required. We may however expect to see the vertical position of the centre of mass being lower, and the radius of the simulations being larger than the model predicts due to the absences of the tube. If we assume that the draining phase still exists in the simulations then we require the function $z_b(t)$ which we can find by tracking the back edge of the cylinder in the simulation until it reaches the original release height. This is shown for $L/D = 2$ to 5 for both $H/D = 2$ and 8 in figure 5.35. Also shown is the least squares fit of the average (solid line) which is given by $\hat{z}_b(t) = 0.012\hat{t}^4 - 0.27\hat{t}^3 + 1.11\hat{t}^2 - 0.79\hat{t}$ with $r^2 = 0.9971$. As with the experiments this is what will be used when solving the model in the following sections.

We solve the model in the same way as outlined in chapter 3 with the three models solved individually and the final values of each phase providing the initial conditions for the following phase. The values of the end of the draining phase (t_{drain}), development phase (t_{dev}) and impact time t_i are determined from the simulations. The impact time is trivially found from the simulations. The end of the draining phase is determined as the time at which the rear of the thermal passes the release height, and the end of the development phase was estimated from the time at which the value of $\hat{r}/\hat{z}_c$ deviates more than 10% from the average value. The times for t_{drain} are indicated on figure 5.36 by the vertical dashed lines for $L/D = 1$ (red), 2 (yellow), 3 (green), 4 (blue) and 5 (purple). Also indicated on figure 5.36 is the time t_{dev} (solid line), for $L/D = 1$ (red). No other value of L/D reached the criteria to indicate that the development phase ended before impact with the ground.

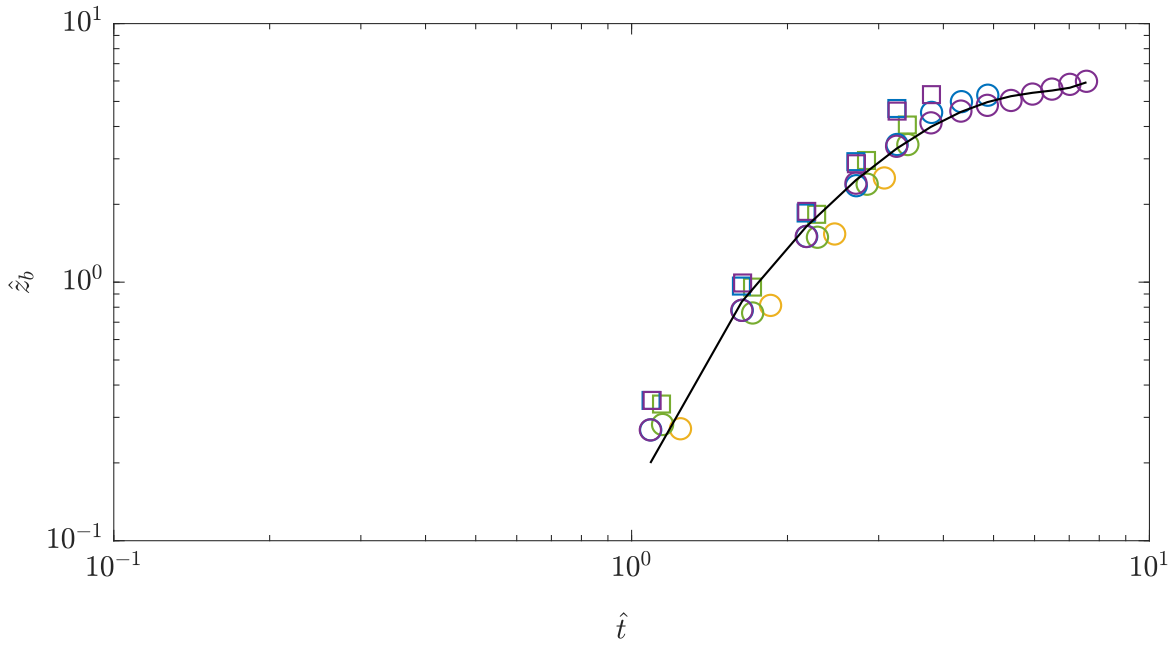

Fig. 5.35 Non-dimensional vertical position of the rear interface of the source fluid with the ambient fluid as it descends to the initial release height plotted on the log-log scale. Shown for $L/D = 2$ (yellow), 3 (green), 4 (blue) and 5 (purple). Also plotted is the least squares fit to the data $\hat{z}_b = 0.0012t^4 - 0.27t^3 + 1.11t^2 - 0.79\hat{t}$ (solid black line).

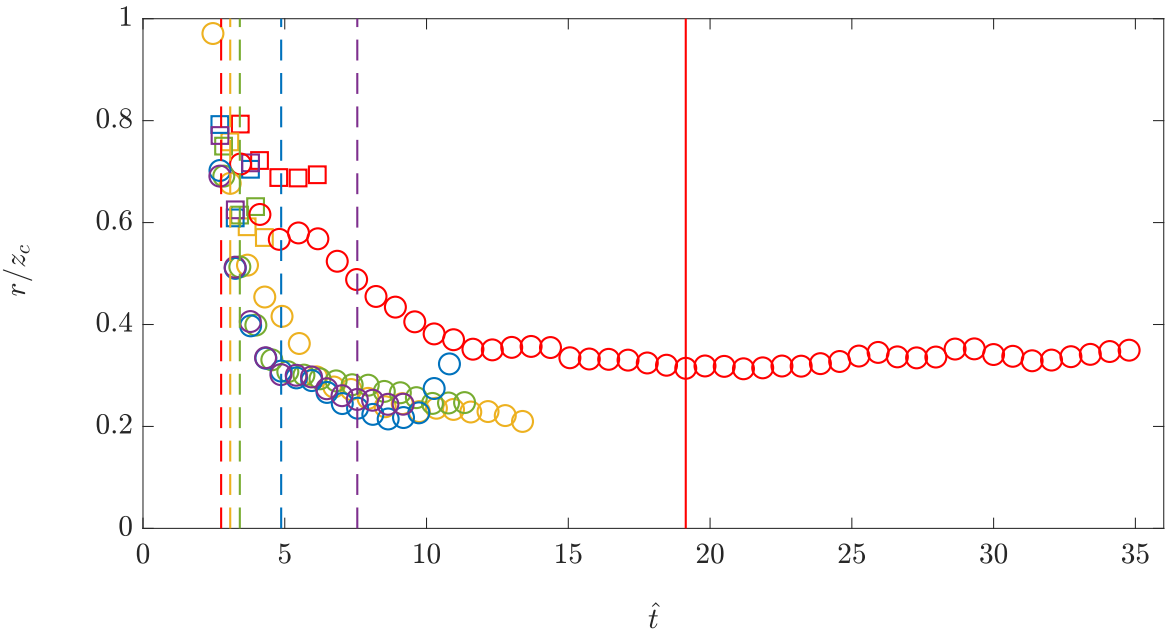

Fig. 5.36 Instantaneous spreading rate, $r = nz_f$ for $L/D = 1$ (red), 2 (yellow), 3 (green), 4 (blue) and 5 (purple) for experiments performed at both $H/D = 2$ (squares) and 8 (circles). The end of the draining phase (vertical dashed lines) for the values of $L/D = 1$ to 5, and the end of the development phase (solid line) for $L/D = 1$ are also shown.

Constant shape factor b and entrainment constant α

Figure 5.37 shows the centre of mass and the radius of a thermal from the simulations with $L/D = 1-5$ performed at $H/D = 8$. The solutions of the equations given in table 5.11 (solid lines with corresponding colours) with the assumption that both the shape factor, b, and the entrainment coefficient, α, are constant. Here the values of b and α used to determine both m and n using the spheroidal shape assumption are $b = 0.36$ which corresponds to the value found in the simulations, $\alpha = 0.25$ which is the value found by Scorer [53], and $\hat{z}_b(t) = 0.012\hat{t}^4 - 0.27\hat{t}^3 + 1.11\hat{t}^2 - 0.79\hat{t}$. As expected, due the absence of a tube, these solutions over-predict the values of z_c and under-predict the values of r during the early stages. The switch to the thermal phase, for $L/D = 1-3$ in particular, significantly under-predicts both the centre of mass and the radius. We also see that the inclusion of the draining terms has made a qualitative improvement to the solutions for both the centre of mass and the radius during early times. However, we know that the value of b is initially non-constant. Therefore, we must look at the solutions to the model using a variable value of b but keeping the entrainment coefficient, α, constant.

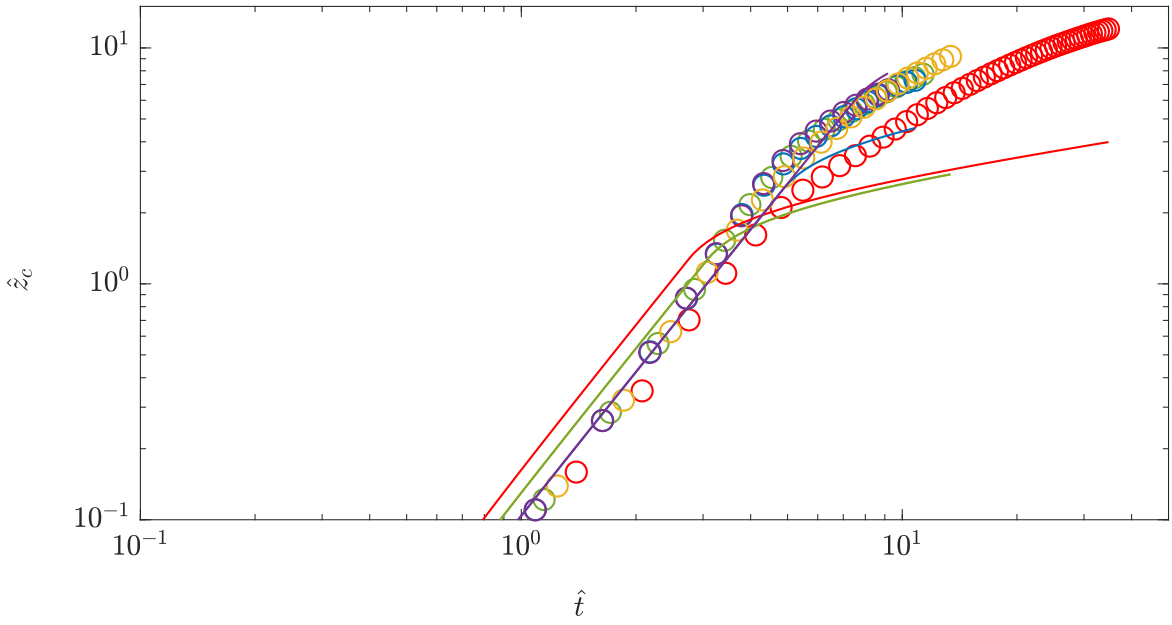

(a) $\hat{z}_c$

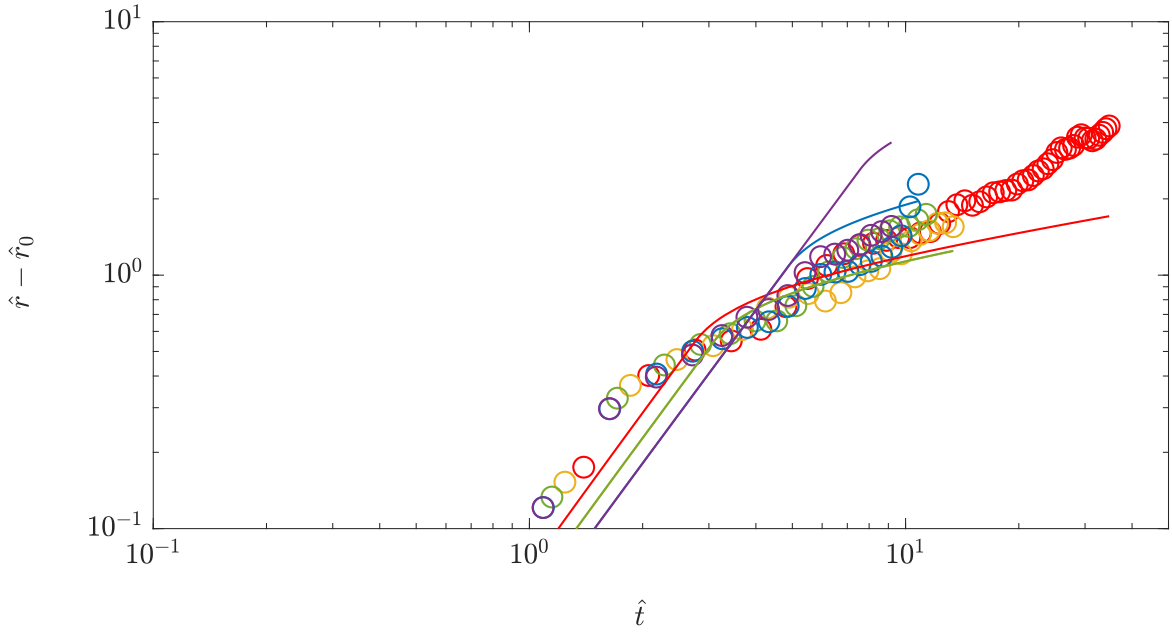

(b) $\hat{r} - \hat{r}_0$

Fig. 5.37 Vertical position of the centre of mass $\hat{z}_c$ and radius $\hat{r} - \hat{r}_0$ of the thermal for $L/D = 1$ (red), 2 (yellow), 3 (green), 4 (blue) and 5 (purple) at $H/D = 8$ compared to the solutions of the 3 phase model with constant shape factor b and constant entrainment coefficient α (coloured lines).

Variable shape factor b and constant entrainment constant α

Figure 5.38 shows the centre of mass and radius of a thermal from the experiments with $L/D = 1$, 2, 3, 4 and 5 performed at $H/D = 8$ along with the solutions for z_c and $r - r_0$ from the equations in table 5.11 (solid lines with corresponding colours) with the assumption that only the entrainment coefficient, α, is constant. The values of $b(t)$ and α are used to determine both $m(t)$ and $n(t)$ for the first two phases using the spheroidal assumption. For the draining and development phase a least squares fit is used to determine the value of $b(t)$, and during the self-similar phase we take the value of b to be the average over this period. The least squares fits of b were each of the form $b(t) = b_1t^4 + b_2t^3 + b_3t^2 + b_4t$, the coefficients and r^2 values for each L/D are given in Appendix E. Also, we set $\alpha = 0.25$ in all three phases which corresponds to the value found by Scorer [53], and $\hat{z}_b(t) = 0.012\hat{t}^4 - 0.27\hat{t}^3 + 1.11\hat{t}^2 - 0.79\hat{t}$ which is the least squares fit of the measured values of z_b.

The qualitative fit with the vertical position and radiue is improved, especially for the experiments with $L/D = 1$ and 2. The quantitative fit with the centre of mass can be improved by adjusting the value of α. However, this reduces the agreement with the radius. Moreover, we see that the inclusion of the development phase has made very little improvement to the fit of the theory with the radius. As with the experiments we are able to tune the model relatively well for the centre of mass, z_c, by changing α. However, it is not possible for the model to agree with both z_c and r for the same value of α. Even when using the varying shape factors the entrainment assumption using a constant value of α fails to give a good prediction for the vertical position of the centre of mass and the radius. In the case of the first two phases this is unsurprising as the entrainment closure developed by Morton et al. [43] assumes self-similarity within the flow. In the following section we will instead consider a non-constant value of the entrainment coefficient α.

Variable shape factor b and entrainment constant α

Figure 5.39 shows the centre of mass and radius of a thermal from the experiments with $L/D = 1$, 2, 3, 4 and 5 performed at $H/D = 8$ (circles) on a log-log scale, along with the solutions for z_c and $r - r_0$ from the equations in table 5.11 (solid line) assuming now that neither the shape factor b nor the entrainment coefficient α are constant. In this case the values of $b(t)$ are used to determine $m(t)$ for the first two phases using the spheroidal shape assumption. The experimental measurements of $r(t)$ and $z_c(t)$ are used to determine $n(t)$ using the equations for $\mathrm{d}r/\mathrm{d}t$ for the draining and development phases. The solutions presented here use a least squares fit to determine the value of $b(t)$, $r(t)$ and $z_c(t)$, and during the thermal phase we take the average constant values of b and n found previously. The

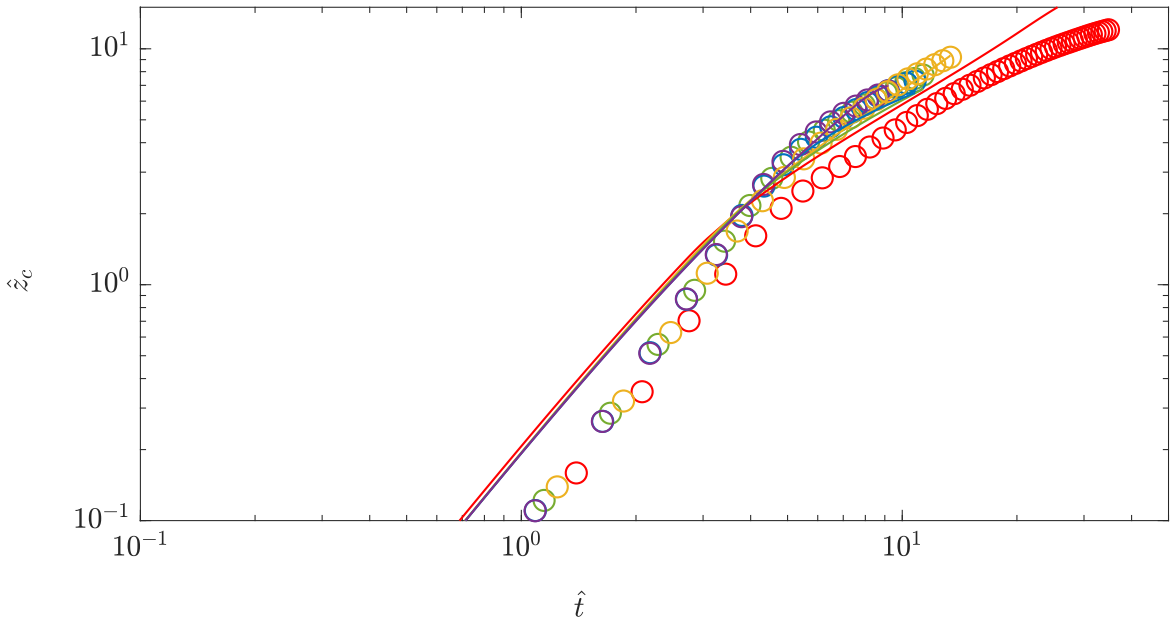

(a) $\hat{z}_c$

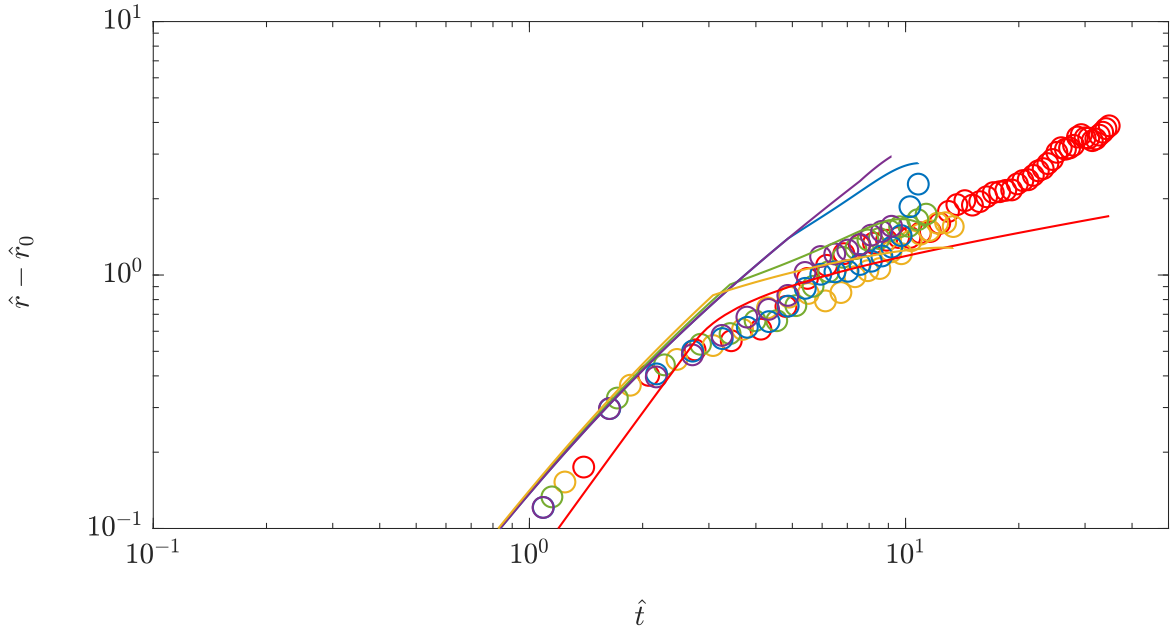

(b) $\hat{r} - \hat{r}_0$

Fig. 5.38 Vertical position of the centre of mass $\hat{z}_c$ and radius $\hat{r} - \hat{r}_0$ of the thermal for $L/D = 1$ (red), 2 (yellow), 3 (green), 4 (blue) and 5 (purple) at $H/D = 8$ compared to the solutions of the 3 phase model with variable shape factor $b(t)$ and constant entrainment coefficient α (coloured lines).

least squares fit of b was the same as used previously. The least squares fits of r and z_c are of the form $r(t) = r_1t^4 + r_2t^3 + r_3t^2 + r_4t + r_5$ and $z_c(t) = zc_1t^4 + zc_2t^3 + zc_3t^2 + zc_4t$, the coefficients and r^2 values for each L/D are given in Appendix E. Also, as above, we set $\hat{z}_b = 0.012\hat{t}^4 - 0.27\hat{t}^3 + 1.11\hat{t}^2 - 0.79\hat{t}$ which is the least squares fit of the measured values of z_b.

The experimental data of both the radius and centre of mass have an improved fit with this model compared to the other two, but still fails to quantitatively capture the evolution of both the radius and the centre of mass. The modelling of the descent and spread of a thermal has been shown to be more complex than can be captured by the simple model we have presented here. We have seen that in fact it appears that as well as the shape factor the entrainment coefficient appears not to be constant during the two initial phases of the thermal development. A model that allows for this non-constant entrainment coefficient has been developed and shown to give a good estimation for the vertical position of the centre of mass but is not able to quantitatively capture the evolution of both the radius and the centre of mass. The other assumption made in the derivation of these equations is assuming that the shape of the thermal is spheroidal. However, from these results alone it is unclear whether this assumption is appropriate for any of the three phases. In the next section we will consider the validity of the shape assumption for the values of L/D considered here.

5.6.2 Gravity Currents

The radial position of the gravity current scaled by the length scale based on the initial release volume is plotted for all tube lengths for both $H/D = 2$ (squares) and $H/D = 8$ (circles) in section 5.6.2, respectively. The dashed line drawn on the plots is $\hat{r} = 1.26(\hat{t} - \hat{t}_i)^{1/2}$, which is the similarity solution for $r \gg r_i$ given by

$$r = \left(2Fr\lambda^{1/2}B_0^{1/2}\right)^{1/2}(t - t_i)^{1/2}, \tag{5.5}$$

taking $\lambda = \pi^{-1}$ and $Fr = 1.4$ as the value of the Froude number used by [51].

Figure 5.40a shows the radial position of the gravity current for the experiments performed at $H/D = 2$ for $L/D = 1$, 2, 3, 4 and 5. At this height the thermals are either in the development phase, or are still draining when impact with the ground occurs. At this height the time it takes for the gravity current to reach the self-similar solution decreases as the value of L/D increases. At later times all the data reach the gradient predicted by similarity solution, i.e. $\hat{r} = 1.26(\hat{t} - \hat{t}_i)^{1/2}$. However, by taking $\lambda = \pi^{-1}$ and Fr $= 1.4$ the similarity solution does not quantitatively represent the gravity currents at this height.

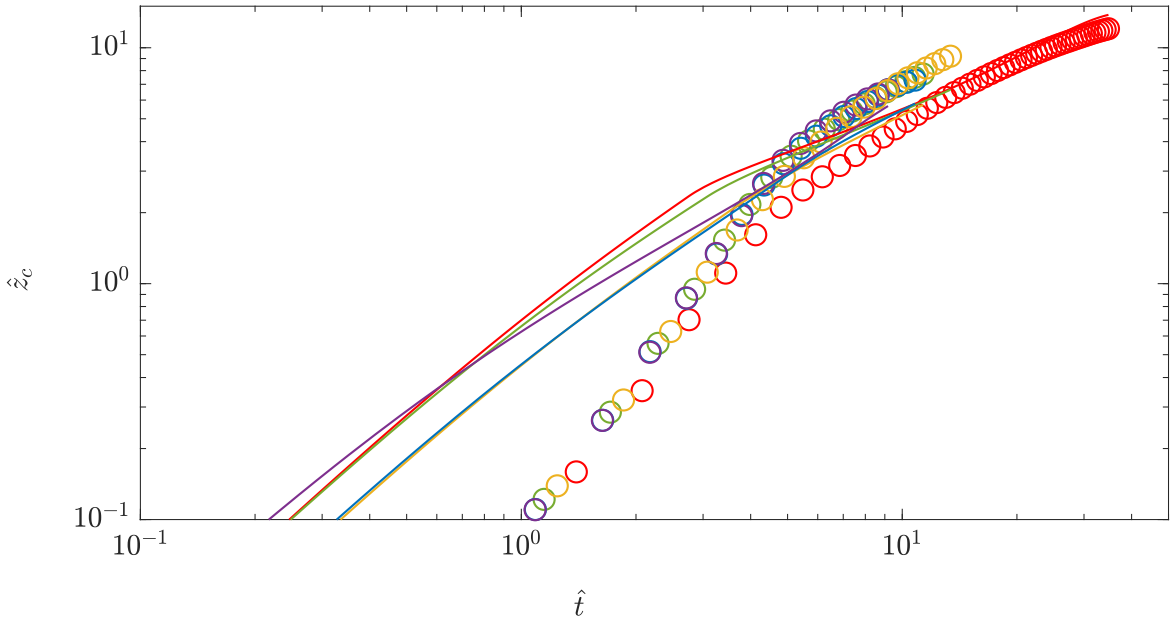

(a) $\hat{z}_c$

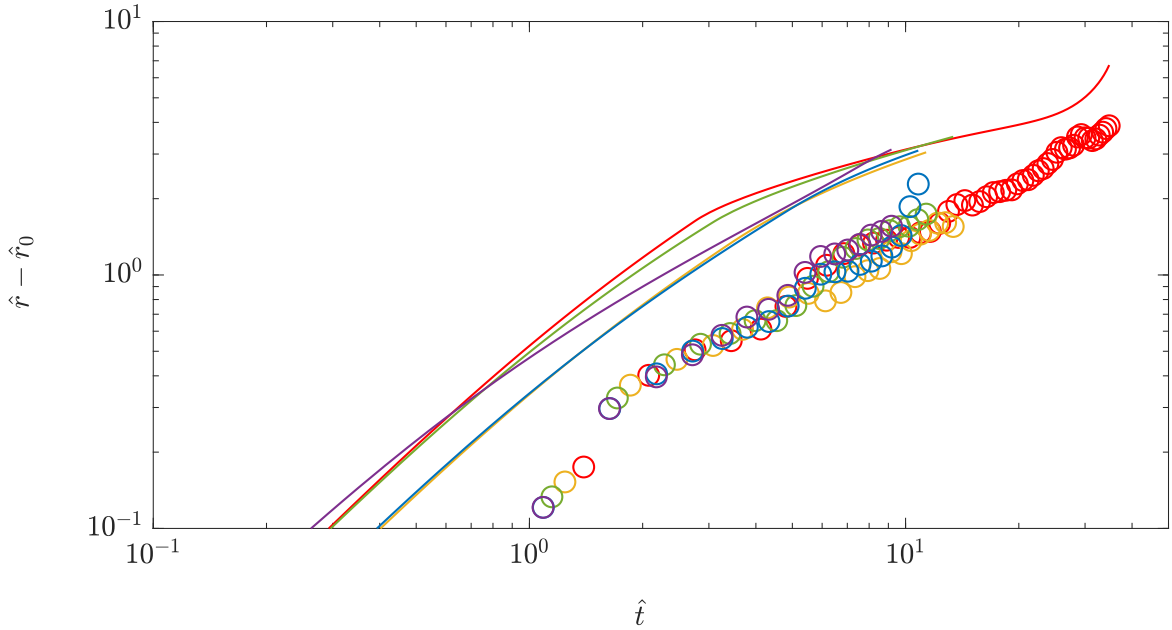

(b) $\hat{r} - \hat{r}_0$

Fig. 5.39 Vertical position of the centre of mass $\hat{z}_c$ and radius $\hat{r} - \hat{r}_0$ of the thermal for $L/D = 1$ (red), 2 (yellow), 3 (green), 4 (blue) and 5 (purple) at $H/D = 8$ compared to the solutions of the 3 phase model with variable shape factor $b(t)$ and entrainment coefficient α (coloured lines).

Figure 5.40b shows the radial position of the gravity current for the experiments performed at $H/D = 8$ for $L/D = 1$, 2, 3, 4 and 5. At this height the thermals are either in the development or the self-similar phases when impact with the boundary occurs. Unlike the releases at $H/D = 2$ no simulation reaches the gradient predicted by similarity solution, i.e. $\hat{r} = 1.26(\hat{t} - \hat{t}_i)^{1/2}$.

5.7 Discussion

5.7.1 Validity of Shape Assumption for Thermals

As stated in chapter 3, Lai et al. [37] and Bond & Johari [8] found that beyond the ratio of $L/D = 2$ no further fluid can be incorporated into the cap and a tail forms. Therefore, for $L/D > 2$ the assumption on the shape of a thermal, i.e. that it is a spheroid, is no longer valid. Instead for $L/D > 2$ the thermals have spheroidal caps with a trailing column of dense fluid or 'tail' which was seen in section 5.5.1 for example with the $L/D = 5$ experiment. The increase in b for $L/D > 2$ described in section 5.5.2 is indicative of this tail. We also saw that when solving the model developed in chapter 3, even when only the shape assumption remained the solutions to the model still could not precisely replicate both the vertical position of the centre of mass and radius. The only measurements of shape we were able to take from the experimental images were the ratio of the semi-minor and major axis and the cross-sectional area. We showed that the cross-sectional area of the experiments was not well represented by a spheroid however no further information could be obtained in order to improve the model for the shape. In order to measure the cross-sectional area, surface area and volume of the thermals, the temperature fields of the simulations were first scaled between 0 and 1. The temperature fields were then made into a binary matrix with every element above a certain threshold set equal to 1 and below equal to 0. The threshold was set to 0.001 as it was found that this initially gave the correct values of volume surface area and cross-sectional area of the cylinder. In order to find the cross-sectional area the binary matrices were then integrated in one of the horizontal directions (x or y) in order to obtain integrated views of the thermal, equivalent to the experimental images, and rescaled back to binary matrices using the same threshold has above. The measures of shape were then determined from the 3D binary matrices for the surface area and volume, and the integrated binary matrices for the cross-sectional area using 'regionprops3' and 'regionprops', respectively. Both functions count the number of '1's' in a matrix to measure the three properties.

Under the current shape assumption the cross-sectional area of a thermal can be written as $A = \pi r h$. We were able to measure A, r and h directly from the numerical simulations,

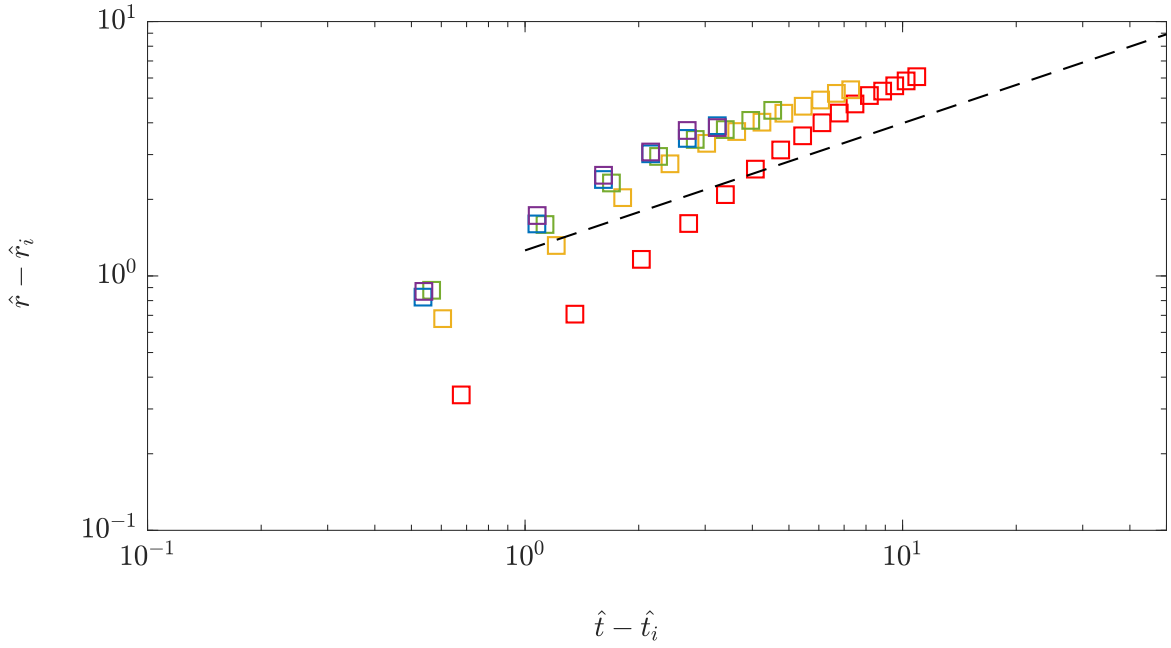

(a) $H/D = 2$

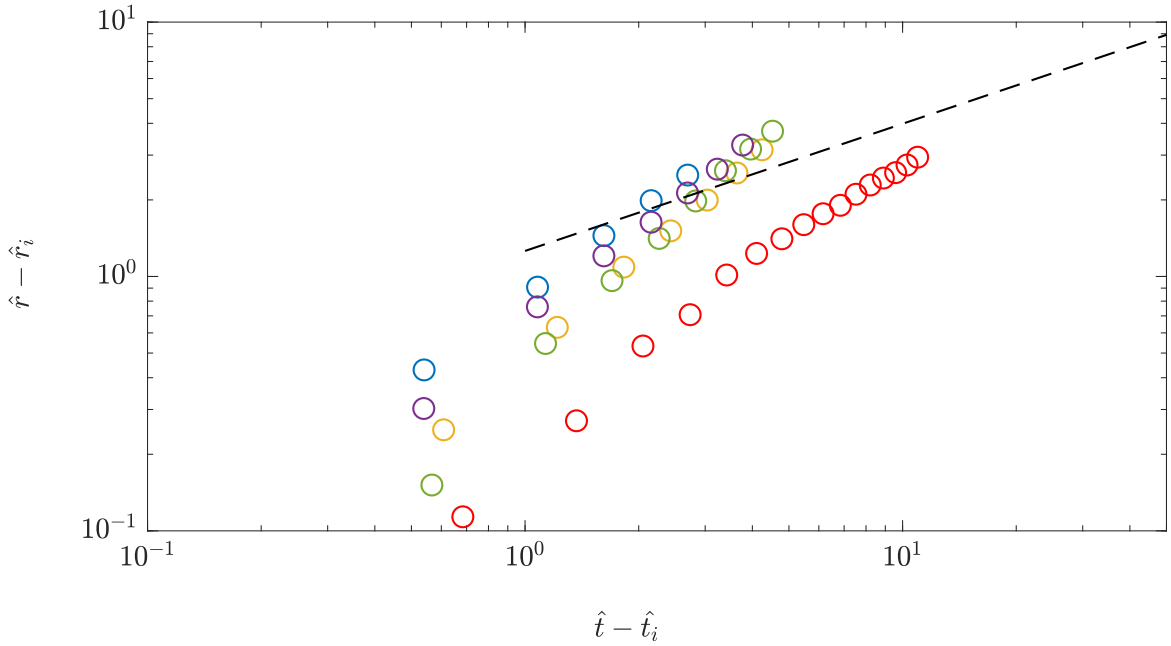

(b) $H/D = 8$

Fig. 5.40 Average radius of the gravity current for $L/D = 1$ (red), 2 (yellow), 3 (green), 4 (blue) and 5 (purple) at $H/D = 2$ (squares) and 8 (circles). The dashed line represents the similarity solution with $\lambda = pi^{-1}$ and $Fr = 1.4$ given by $\hat{r} = 1.26(\hat{t} - \hat{t}_i)^{1/2}$.

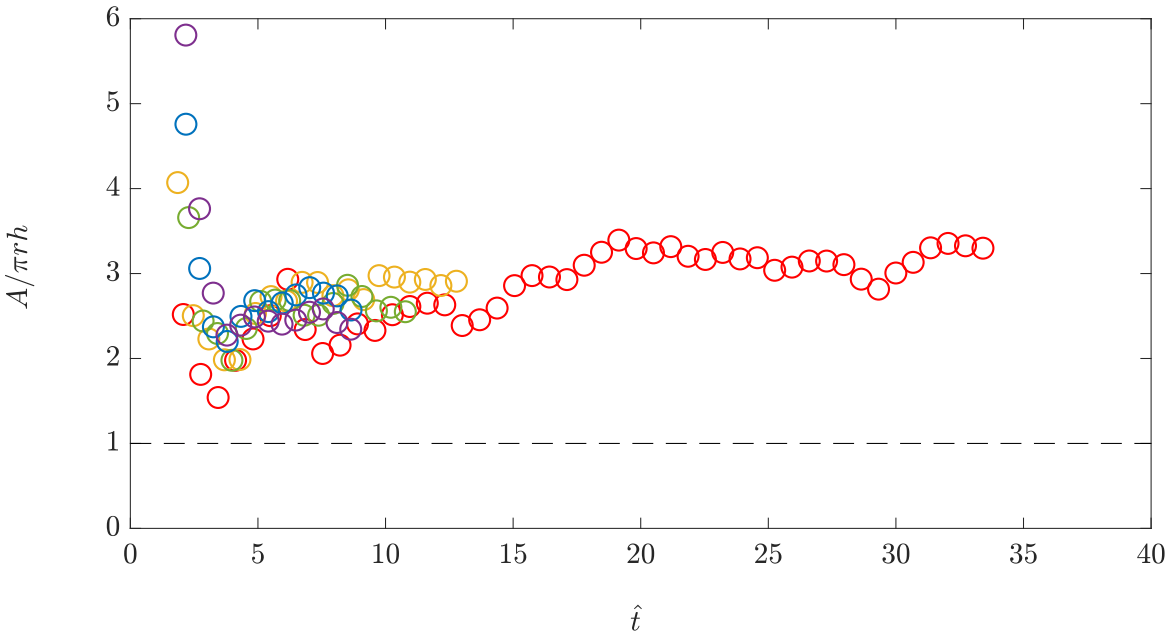

Fig. 5.41 Cross-sectional area: time dependent value of $A/(\pi rh)$ for $L/D = 1$ (red), 2 (yellow), 3 (green), 4 (blue) and 5 (purple) at $H/D = 8$.

and can therefore determine the instantaneous values of $A/(\pi rh)$. The values of this for the $L/D = 1$, 2, 3, 4 and 5 are shown in figure 5.41 at both $H/D = 2$ (squares) and 8 (circles).

In order to validate the shape assumption we require $A/(\pi rh) = 1$. However, as with the experiments, in all cases this condition is not satisfied. In all cases the value of $A/(\pi rh)$ initially decreases reaching a minimum at 2, and then continues to increase until some of the simulations performed at $H/D = 8$ attain an approximately constant value.

In order to obtain more information on the shape of the thermal using the three-dimensional data we have from the numerical simulations, both the surface area and the volume can be directly measured. As shown in appendix C the surface area of a spheroid can be written as $A_s = ar^2$, where a is a function of the ratio of the semi-minor/major axis, b. We were able to measure A_s, r and b directly, and can therefore determine the instantaneous values of $A_s/(ar^2)$. The values of this for the $L/D = 1$, 2, 3, 4 and 5 are shown in figure 5.42 at both $H/D = 2$ and 8.

As with the cross-sectional area for the thermal, to be a spheroid we require $A_s/ar^2 = 1$. However, in all cases this condition is not satisfied. In all cases the value of A_s/ar^2 initially decreases reaching a minimum at 2, and then continues to increase for all values of L/D. The simulation performed at $L/D = 1$ and $H/D = 8$ is the only simulation to attain a constant value at approximately 4.

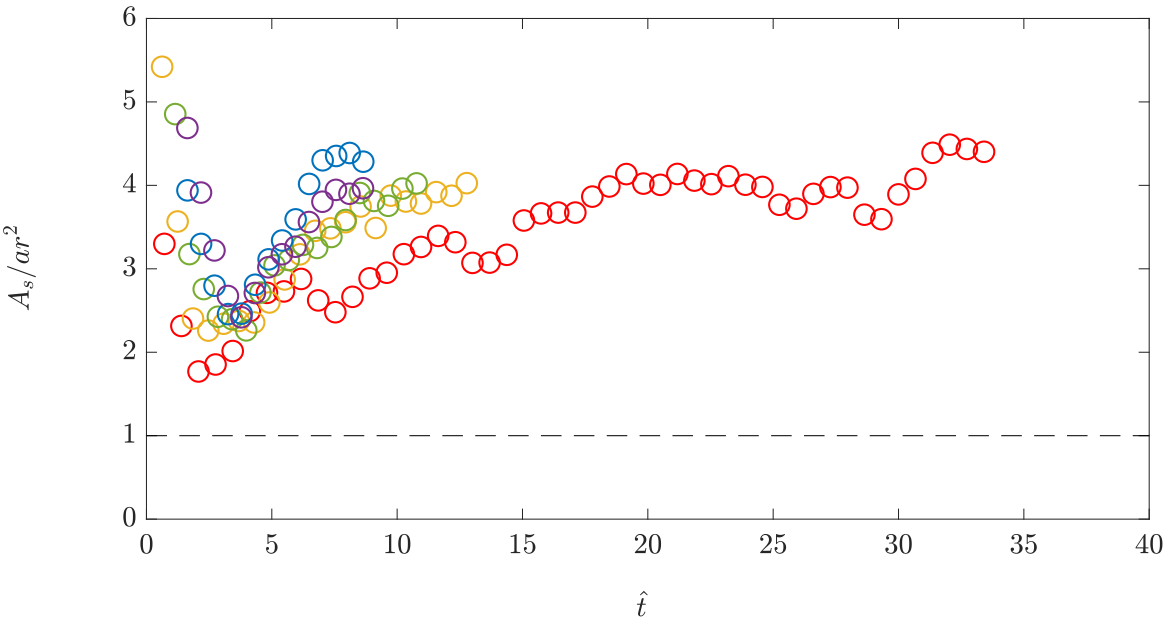

Fig. 5.42 Surface area: time dependent value of A_s/ar^2 for $L/D = 1$ (red), 2 (yellow), 3 (green), 4 (blue) and 5 (purple) at $H/D = 8$.

The volume of a spheroid can be written as $V = (4/3)\pi br^3$. We were able to measure V, r and b directly, and can therefore determine the instantaneous values of $V/((4/3)\pi br^3)$. The values of this for the $L/D = 1$, 2, 3, 4 and 5 are shown in figure 5.43 at both $H/D = 2$ and 8. Similarly, we require $V/mr^3 = 1$, which in all cases is not satisfied. Instead, the value of $V/(mr^3)$ initially decreases before attaining a constant value at approximately 1.5.

For all three measurements: cross-sectional area, surface area and volume, we have seen that only the simulations with $L/D = 1$ and 2 at $H/D = 8$ reach a constant value of $A/(\pi rh)$ and $V/4/3\pi br^3$, and this occurs after some initial adjustment. However, no experiment has a surface area that evolves with $A_s = ar^2$. This is unsurprising as for all three measures it is assumed that the thermal is a smooth spheroid, whereas, as we have seen from the qualitative images of both the experiments and simulations the thermals compromise of many large turbulent structures. The thermal can then be encased by a spheroid with little deviation in the volume or cross-sectional area however the surface area is significantly altered by assuming a smooth surface of the encasing spheroid. By increasing the threshold used to measure the surface area it may be possible to remove some of the turbulent structures effecting the surface area of the thermal. Figure 5.44 shows the value of A_s/ar^2 calculated using four different thresholds. The figure shows that only by increasing the threshold from 0.001 to 0.5 has makes the value of $A_s/(ar^2)$ approximately constant after some initial period. However, as we can see from figure 5.45, which shows $V/(mr^3)$ calculated using the same four thresholds, this has a significant impact on the measurement of the volume.

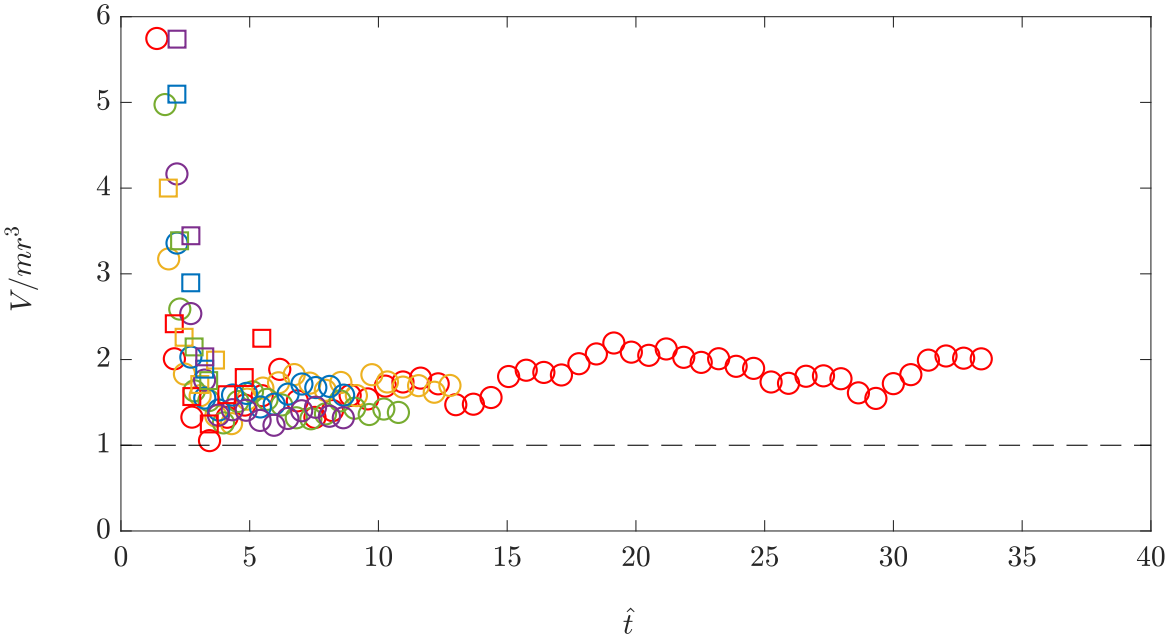

Fig. 5.43 Volume: time dependent value of V/mr^3 for $L/D = 1$ (red), 2 (yellow), 3 (green), 4 (blue) and 5 (purple) at $H/D = 8$.

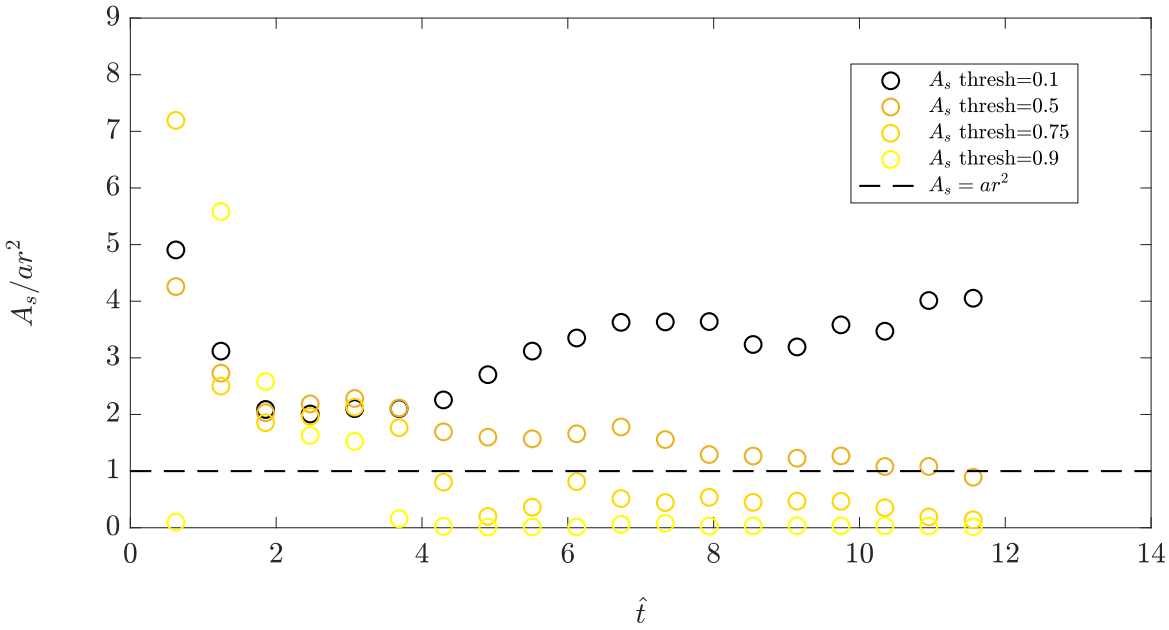

Fig. 5.44 Time dependent value of A_s/ar^2 for $L/D = 2$ at $H/D = 8$ calculated using 4 different values of the threshold.

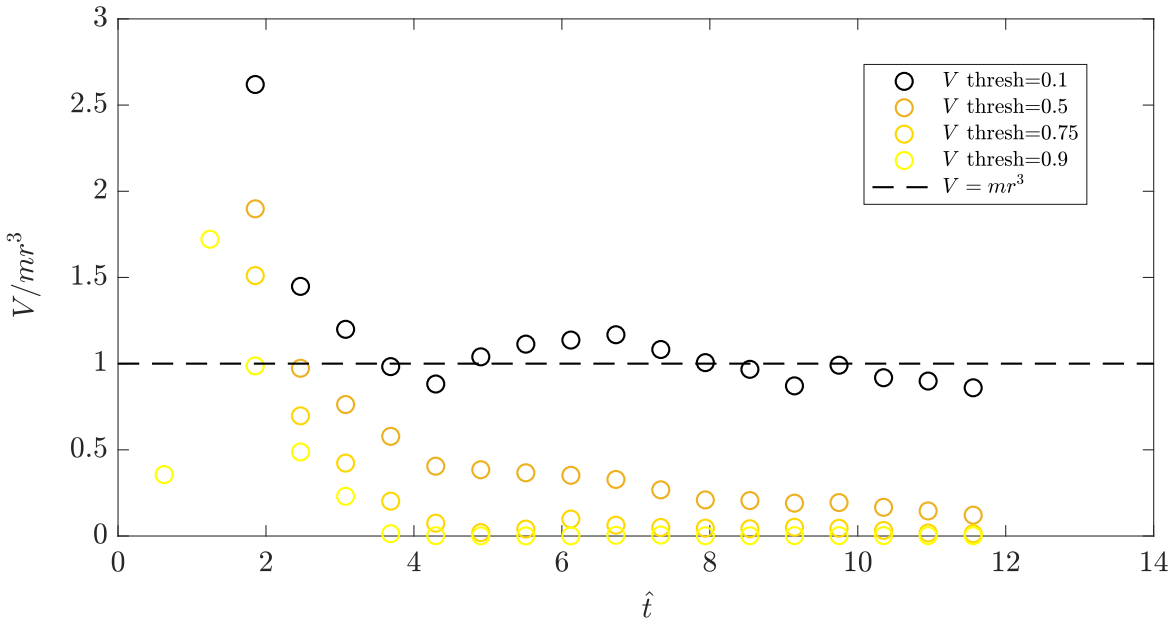

Fig. 5.45 Time dependent value of V/mr^3 for $L/D = 2$ at $H/D = 8$ calculated using 4 different values of the threshold.

5.7.2 General Entrainment Assumption for Thermals

We have seen in section 5.7.1 and in chapter 3 that the assumption that a thermal is spheroidal does not initially hold for any value of L/D nor for the surface area at any time. Morton et al. [43] assumed that the total entrainment into a thermal was proportional to the surface area and the propagation speed. Without any knowledge of the shape of a thermal the rate of change of volume can be written as

$$\frac{\mathrm{d}V}{\mathrm{d}t} = \alpha A_s \frac{\mathrm{d}z_c}{\mathrm{d}t}, \tag{5.6}$$

where α is assumed to be constant. We have directly measured the surface area and volume in the numerical simulations described in table 5.10. These measurements are used to check that the general entrainment assumption given in (5.6) holds. For the general entrainment assumption to hold we require

$$\alpha = \frac{\mathrm{d}V}{\mathrm{d}t} \Big/ \left(A_s \frac{\mathrm{d}z_c}{\mathrm{d}t} \right),$$

to be constant.

The value of α is plotted in figure 5.46. For experiments performed at $H/D = 8$, after an initial adjustment period the value of α becomes approximately constant with

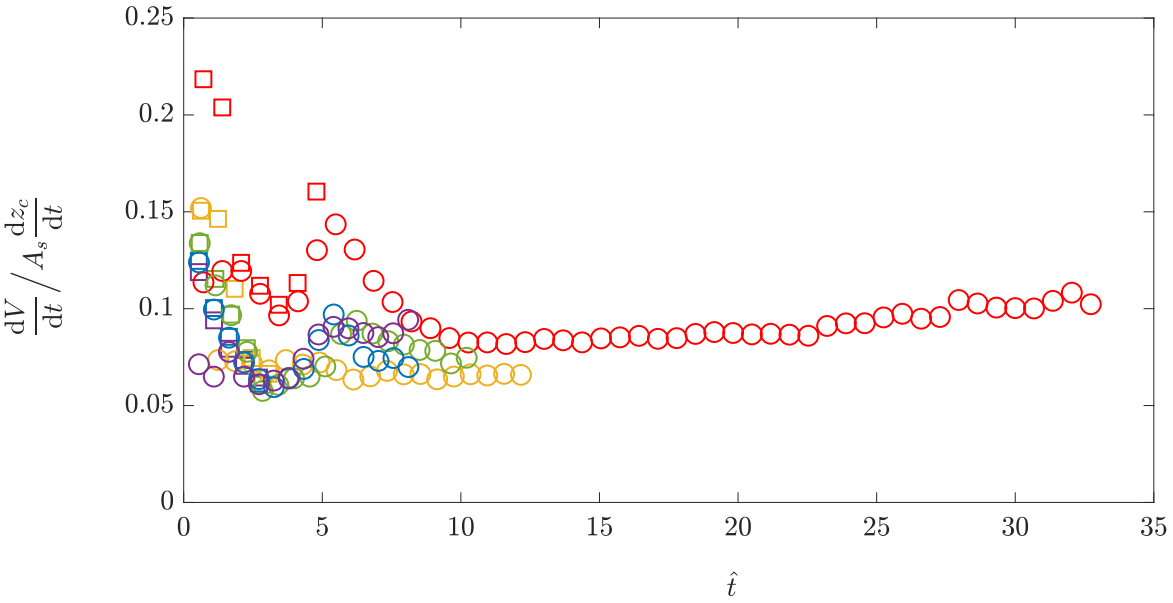

Fig. 5.46 General entrainment assumption: time dependent value of α for $L/D = 1$ (red), 2 (yellow), 3 (green), 4 (blue) and 5 (purple) at $H/D = 2$.

$\alpha = 0.099 \pm 0.010$ for $L/D = 1$. However, the values of α are different depending on L/D, with $\alpha = 0.063 \pm 0.004$ for $L/D = 2$, $\alpha = 0.075 \pm 0.006$ for $L/D = 3$, $\alpha = 0.090 \pm 0.028$ for $L/D = 4$ and $\alpha = 0.073 \pm 0.018$ for $L/D = 5$. These values are lower than the value of $\alpha = 0.13 - 0.31$ generally reported for thermals [37]. However, the reported values of α are calculated under the assumption that the surface area of the thermals are smooth and therefore are not comparable to the value of α found here.

We saw in chapter 3 the experiments at $H/D = 2$ never reach the self-similar phase, and in some cases impact the ground during draining. The values of α for these experiments are also shown in figure 5.46, in these cases α is not constant. Similar to the theory derived for the draining and development phases of a thermal, where a non-constant aspect ratio b was required, a variable entrainment coefficient is also required during the draining and development phases.

5.7.3 Transition From Thermal to Gravity Current

As we saw in chapter 4 the evolution of the radius as the flow goes from a thermal to a gravity current changes depending on the phase that the thermal impacted the ground in. In a previous section we compared the radius of the simulations to the experiments, by zooming into the point of impact we see in figure 5.47 that prior to impact, $\hat{t} - \hat{t}_i < 0$, the evolution or the radial position is no longer independent of the phase of the thermal upon impact, as

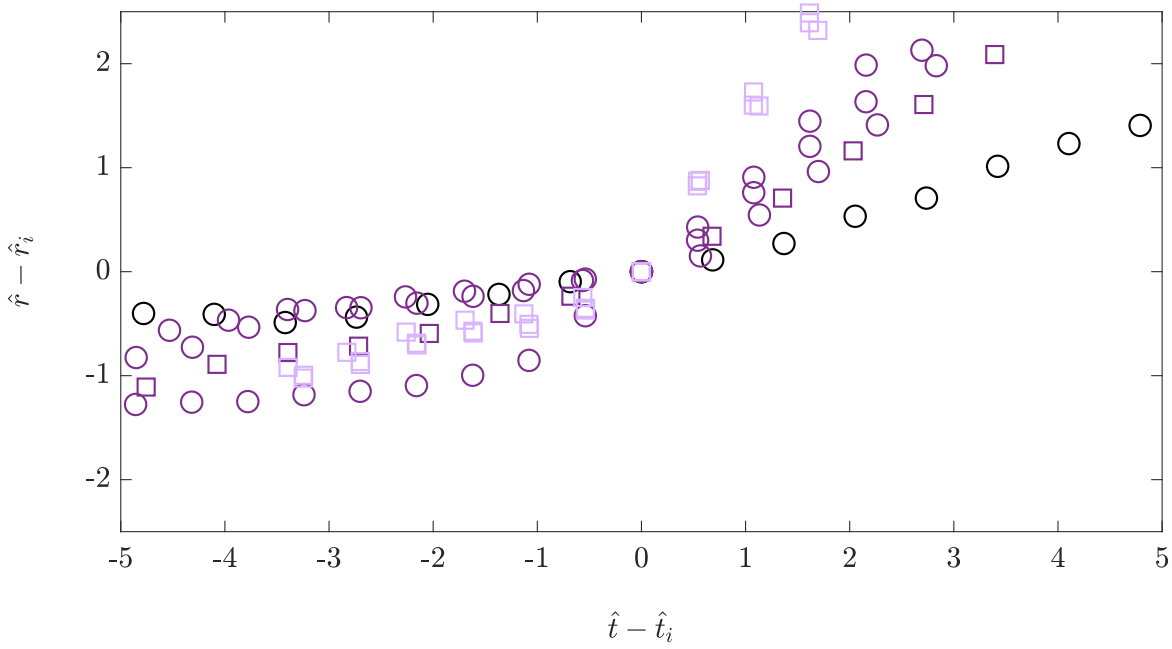

Fig. 5.47 Average radial position of the thermal and gravity current r for $L/D = 1$, 2, 3, 4 and 5 at both $H/D = 2$ and $H/D = 8$. The colours here represent the phase in which the thermal was in upon impact with the ground: draining (lilac), development (purple) or self-similar thermal (black).

it was with the experiments. However, as with the experiments, when $\hat{t} - \hat{t}_i = 0$ i.e. at the time of impact, a thermal in either the draining or development phases has an approximately stationary radial position. The radial velocity then increases at the time of impact, in the case of a thermal in the draining phase, or shortly after impact in the case of a thermal in the development phase.

The simulation performed at $H/D = 8$ with $L/D = 1$ is the only simulation that reached the self-similar thermal phase. The average radial position of this simulation experiences only a small change in radial velocity, $\mathrm{d}r/\mathrm{d}t$, when transitioning from the thermal to gravity current phase. Unlike in the experiments, where we saw no change in the radial velocity.

It was observed previously, in chapter 4, that for the gravity currents produced by thermals impacting the ground in the draining phase there is an increase in the height of the gravity current shortly after impact. Figure 5.48 shows three individual simulations which represent the three cases of the thermal at impact. Plotted are the edges of thermals and gravity currents at 6 different times: $\hat{t} - \hat{t}_i = 0,\ 1,\ 2,\ 3,\ 4$, and 5. Also shown are the positions of $\hat{r} - \hat{r}_i = 1$ and 2 for comparison with figure 5.47. Unlike in the experiments for figures 5.48a and 5.48b we see no increase in height of the gravity current directly after impact.

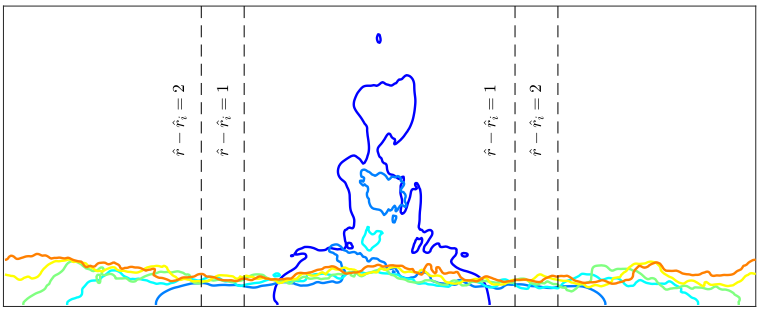

(a) Draining Phase: $L/D = 5$, $H/D = 2$

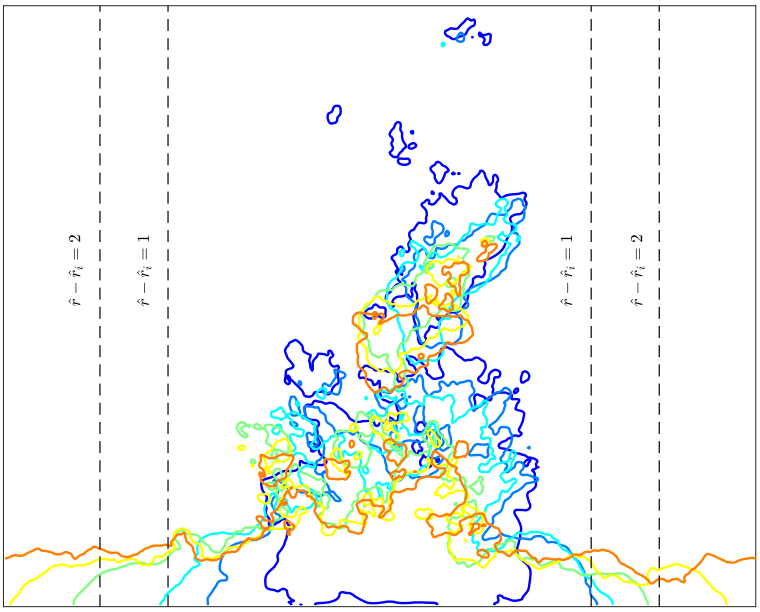

(b) Development Phase: $L/D = 5$, $H/D = 8$

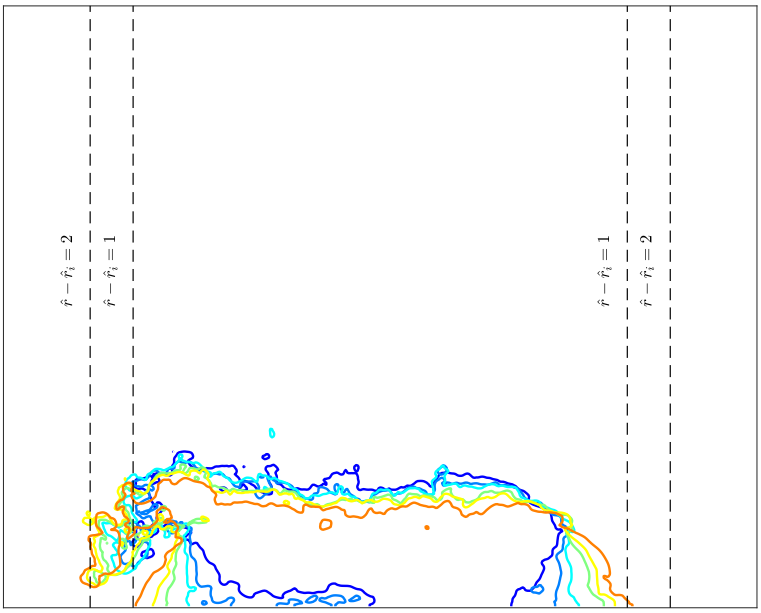

(c) Thermal Phase: $L/D = 1$, $H/D = 8$

Fig. 5.48 Edges of the simulations during the transition from thermal to gravity current from six time steps: $\hat{t}-\hat{t}_i = 0,\ 1,\ 2,\ 3,\ 4,$ and 5. Three experiments are shown, one from each phase of the thermal during impact i.e. draining, development and thermal.

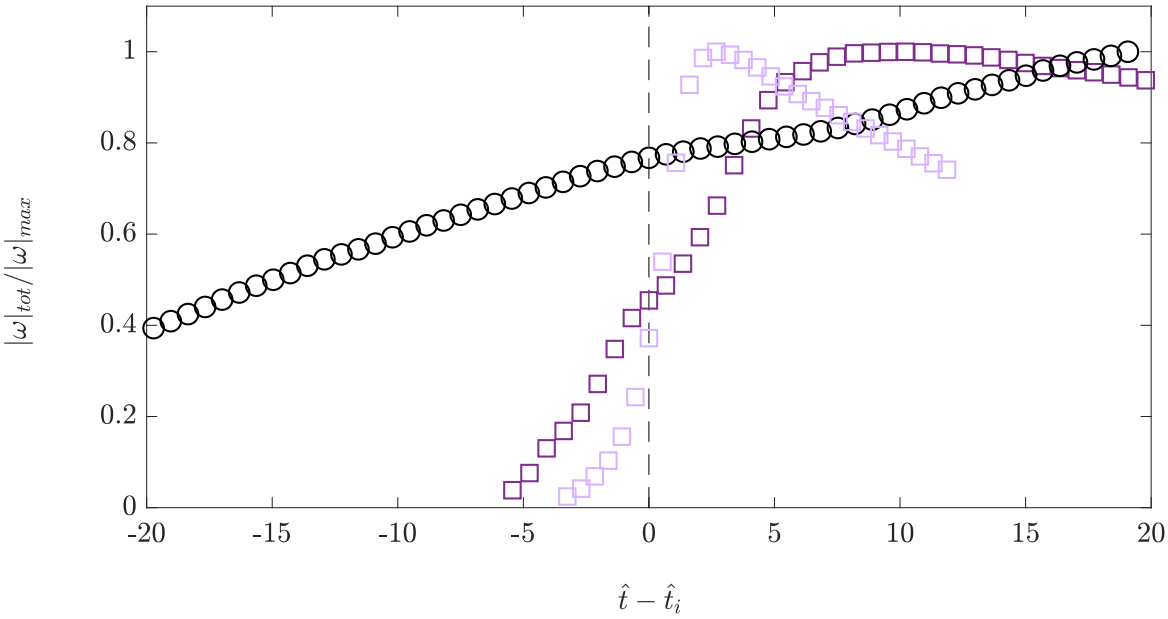

Fig. 5.49 Total vorticity relative to the point of impact of the thermal and gravity current phases of three experiments: $L/D = 1$ and $L/D = 5$ at $H/D = 8$ and $L/D = 5$ at $H/D = 2$. The colours represent the phase in which the thermal was in upon impact with the ground: draining (lilac), development (purple) or self-similar thermal (black).

Rooney [49] concluded that the gravity currents produced by self-similar thermals evolved smoothly due to their 'spun up' state. To study this further we calculate the total vorticity, the integral in the $x-$, $y-$ and $z-$directions of the vorticity $|\omega| = |(w_y - v_z, u_z - w_x, v_x - u_y)|$ where $\mathbf{u} = (u, v, w)$ is the velocity field. The total vorticity for the three cases considered above i.e. the self-similar case: $L/D = 1$ as $H/D = 8$ (black), the development: $L/D = 1$ at $H/D = 2$ (purple) and the draining: $L/D = 5$ at $H/D = 2$ (lilac) phases of the thermal upon impact. Figure 5.49 shows the total vorticity for the three cases normalised by the maximum vorticity relative to the time of impact. The figure shows that the total vorticity of the three different impacts are qualitatively different. As with the radius of the thermal that impacts the ground in the self-similar phase the vorticity evolves smoothly through the time of impact. Conversely, for the thermals the impact the ground in either the draining or development phases the vorticity significantly increases just before the time of impact. However, the thermal impacting the ground in the self-similar phase has the most relative vorticity upon impact at $0.76|\omega|_{max}$, whereas for the development phase the relative vorticity is $0.45|\omega|_{max}$ and for the draining phase $0.37|\omega|_{max}$.

5.8 Conclusions

In this chapter the set up of MONC has been tested and compared to simulations from Rooney [49] which were performed in the LEM. The vertical positions from these simulations were found to deviate from the fit of Rooney's data when using the exact set-up of Rooney [49]. The deviation of the vertical positions from the results of Rooney [49] was assumed to be due to the absence of a backscatter scheme in MONC. However, by running MONC at a 10m resolution, rather than the 50 m resolution used by Rooney [49], comparable simulations were then achieved despite the absence of a backscatter scheme in MONC. We have shown in this chapter was that the simulations compare well with the experiments during the descent. However, there is a reduction in mixing in the simulations compared to the experiments, which accounts for the small differences in b, n and the vertical position. The gravity currents in the simulations travel faster than the experiments, this was also to be expected due to the reduced mixing.

The theory proposed in chapter 3 was also tested using the measured values of b from the simulations. The three phase model has been shown to fit qualitatively well with the centre of mass and radius data from the simulations when using the measured values of b. However, to achieve this a priori knowledge of the aspect ratio b, is required. Moreover, the use of the draining phase was still required despite the absence of a tube in the simulations.

The theory has not been able to accurately capture the evolution of both the vertical position and the radius so, as with the experiments, it is unclear as to whether the spheroidal shape assumption is valid. However, unlike with the experiments the numerical simulations produce 3-D data. This allows us to consider the validity of the two assumptions made during the development of thermal theory: the shape assumption, and entrainment assumption. It was shown in chapter 3 for the experiments that during the draining and development phases of a thermal neither of these assumptions hold. In the numerical simulations the cross-sectional area, surface area and volume have been compared to the theoretical values for a spheroid. It has been shown that the surface area was the only measurement which significantly deviated from the shape assumption during all three phases of a thermals development. By considering an entrainment assumption, where there was no assumption on the shape, we have also shown that the entrainment coefficient α is not constant during the initial phases of a thermal, and after the constant value is dependent on the value of L/D which cannot be compared to to values reported in the literature as they make the smooth spheroid assumption to calculate α. This L/D dependence on the value of α has not been seen in previous studies, and is unexpected from flows which are self-similar, since initial conditions should no longer have any effect.

Chapter 6

Conclusion

The initial motivation for this study was the dynamics of downdraughts from strong convective storms and the subsequent development of cold pools, which have a significant role in the longevity and severity of convective storms [55]. During the initial investigations of a single gravity current created by the release of a thermal to represent a cold pool produced by a downdraught, it was noted that the initial geometry of the release had a significant role in the qualitative and quantitative behaviour of the resulting gravity current. This is highly relevant given that the shape and aspect ratio of the cold air initiating a downdraught are not precisely known, but are expected to vary widely. We have presented an exploration of the effects of the initial conditions on the evolution of a thermal impacting a surface and spreading as a gravity current in this thesis. We have sought to:

1. verify the assumptions made in traditional thermal theory over a range not previously considered that also included the geometries associated with downdraughts,

2. explore the effects of the initial geometries on the qualitative and quantitative behaviour of the resulting gravity currents over a range not previously considered that also included the geometries associated with downdraughts.

This has been examined using both experiments, presented in chapters 2, 3 and 4, and numerical simulations, presented in chapter 5. We have considered both experiments and simulations in the range $1 \leq L/D \leq 5$ at $H/D = 2$ and 8. Previously gravity currents produced by thermals have only been considered using experiments or simulations with $L/D = 1$, as shown in table 6.1 and figure 6.1.

Chapter 2 highlights the difficulties that occur when producing thermals in a laboratory setting. The experimental set up and the measurement techniques used in this study have been detailed. The method of release was selected to best represent the macro properties

Reference	H/D range	L/D range	description
Alahyri & Longmire [3] ×	$1.75 \leq H/D \leq 2.7$	$L/D = 1.4,\ 2$	experiments on thermals and gravity currents
Lundgren et al. [41] −−	$1.4 \leq H/D \leq 1.9$	$L/D = 1$	experiments on thermals and gravity currents
Yao & Lundgren [59] ×	$H/D \approx 2$	$L/D = 1$	experiments on thermals and gravity currents
Rooney [49] −−	$1.5 \leq H/D \leq 18$	n/a	simulations of thermals and gravity currents
Bond & Johari [8] □	$25 \leq H/D \leq 55$	$2 \leq L/D \leq 8$	experiments on thermals only
Lai et al. [37] □	$21 \leq H/D \leq 44$	$0.125 \leq L/D \leq 4$	simulations of thermals only
Huq [35] −−		$0.04 \leq L/D \leq 0.62$	experiments on gravity currents only
This Study ○	$H/D = 2$ and 8	$1 \leq L/D \leq 5$	experiments and simulations of thermals and gravity currents
Downdruaghts □	$0.25 \leq H/D \leq 2.5$	$0.25 \leq L/D \leq 2.5$	

Table 6.1 A summary of the ranges of L/D and H/D for previous works on both gravity currents and/or thermals as well as the ranges seen in the atmosphere. Also included are the symbols that represent the studies in figure 6.1.

of downdraughts without consideration of the process from which they form. Therefore, a relatively dense fluid was released without any initial momentum at the source in the most repeatable way possible. For both thermal and gravity current phases of the flow considered herein the experimental set up has been shown to produce repeatable experiments with little variation between them. Two measurement techniques are used to analyse the experiments: edge detection and dye attenuation. Also presented in this chapter is a novel extension to the dye attenuation technique proposed by Cenedese & Dalziel [15]. The use of three colours of LEDs for dye attenuation has not been previously performed and enabled us to measure a large range of dye concentration unachievable with the traditional use of a single colour. This was necessary due to the high dilution rates exhibited by thermals and it enabled us to obtain accurate measurements which are presented in chapters 3 and 4. The experimental

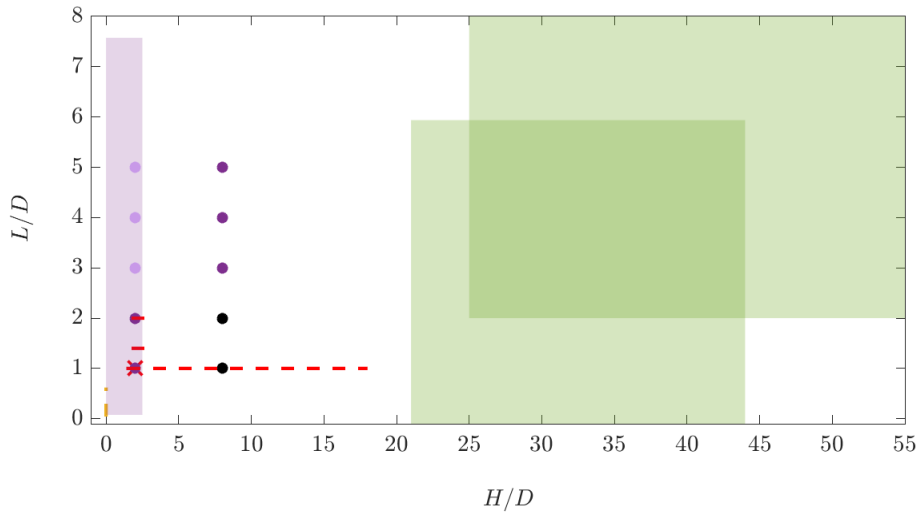

Fig. 6.1 Phase diagram showing the ranges of L/D and H/D considered by previous studies, as well as the range seen in the atmosphere. . Also plotted are the values of L/D and H/D of the experiments and simulations performed in this study (coloured dots). The colour of the markers represents the phase the thermal was in at the point of impact: draining (lilac), development (purple) and self-similar thermal (black).

measurement technique presented here could be used in future works for any flow with high dilutions rates that will require larger ranges of dye concentration. The experiments themselves are some of the few modern experiments on thermals producing gravity currents, and the only experiments that consider these combinations of L/D and H/D. These ratios were chose firstly to fill a necessary gap in the phase space shown in figure 6.1. Secondly, to explore the effects of the initial geometries on the qualitative and quantitative behaviour of the resulting gravity currents.

Chapters 3 and 5 present the existing theory for thermals and compare the experiments and numerical simulations respectively. Both the experiments and numerical simulations were shown to compare well with each other. The measurements taken were chosen in order to verify the two assumptions made during the development of existing thermal theory:

1. that the shape of a thermal is self similar and spheroidal and therefore the volume $V = mr^3$, where m is constant and known as the thermal shape factor,

2. and through the entrainment assumption that the radius has some constant spreading rate n where $n \approx \alpha$, an entrainment constant.

It is also shown that both m or n have a non-constant value during the draining and development phases. Both m and n have been measured directly and shown that the value of these

constants depends on the value of L/D. In the numerical simulations there was a reduction in mixing in the simulations, which account for the small differences in m, n when compared to the experiments. However, despite this we still saw a difference in the values of both m and n which was dependant on L/D.

A new theory for the development of a thermal during the draining phase has been proposed and shown to fit well with the experimental results, when using the measured values of m and n. The draining equations require only that the position of the interface of the source fluid is known and thus can be extended to other experimental set ups or to include other processes at the source, which may result in different initial conditions for example the inclusion of particles or an experiment with initial momentum imposed.

It is well known that two phases exist in the development of thermals: the initial acceleration phase, and self-similar phase. The initial acceleration phase has however, has not been previously studied in depth. We have shown for the first time that three phases exist during the development of thermals: draining, development, and self-similar thermal phases. We have also shown that neither the spheroidal shape assumption, nor the entrainment assumption holds during both the draining and development phases. In fact, as seen first by Bond & Johari [8], the shape assumption is not valid for any experiment or simulation for $L/D > 2$ at the two heights considered here. We encountered a problem in attempting to verify the entrainment assumptions using the experiments alone: it was not possible to measure the volume or surface area without assuming the flow is axisymmetric and so this warranted the use of the numerical simulations only. In the numerical simulations the cross-sectional area, surface area and volume have been directly measured and compared to the theoretical values for a spheroid. It has been shown that the surface area is the only measurement which significantly deviates from the shape assumption during the self-similar phase. Using the simulations we were able to consider a generalised entrainment assumption, where we have shown that, as well as m and n, α is also not constant during the draining and development phases of a thermal. Further work is needed in order to robustly model and quantify the entrainment of a thermal during the three phases. Work by van Reeuwijk & Holzner [47] and Mistry et al. [42] have mapped the entrainment from small to large scales for turbulent jets which has not as yet been extended to thermals or gravity currents.

Also presented were the vertical positions of the thermals at the end of the draining phase and development phase. We have shown that ends of these phases are not equivalent. In fact, the duration of the development phase changes depending on the criteria used to determine the end of this phase. When using the criteria $z \propto t^{1/2}$, the duration of the initial acceleration phase, the draining and development phase combined, is not one to two draining times for $L/D = 1$ and 2 as proposed by Bond & Johari [8]. Although the precise aspect ratios of

downdraughts are unknown, it is estimated that the values of both L/D and H/D lie between $0.25 \leq L/D,\ H/D \leq 2.5$, as shown in figure 6.1 by the purple shaded area. We can see from figure 6.1 that downdraughts in the atmosphere is are best represented in our experiments by the $H/D = 2$ releases. The experiments in this study are represented by dots on figure 6.1 and colour coded according the phase of the thermal upon impact: draining (lilac), development (purple) and thermal (black). The diagram shows that no release that lies within the range of downdraughts in the atmosphere reach the thermal phase. Moreover, we see that in fact the either the draining or development phases will best represent the properties of the descent of downdraughts. This may be useful to future studies that may wish to ensure they take measurements of their releases in one of the three phases.

Chapters 4 and 5 present the existing theory for gravity currents and compare the experiments and numerical simulations respectively. The similarity solution based on the shallow-water equations represents the data from the experiments well for releases from all lengths of tube and at both release heights. We have also shown that both the qualitative behaviour and quantitative measurements of the gravity currents, depend on the phase in which the thermal impacts the ground. We saw differences in both the heights and the slumping phases of the gravity currents depending on which phase impact occurred in. This also had an effect on the transition of the radial position from thermal to gravity current. The radial position is approximately stationary when the impact occurs during the draining or development phases. When impact occurs during the self-similar phase there is a smooth transition due to the fully formed vortex ring in the thermal, which had been seen previously by Rooney [49]. The gravity currents in the simulations were found to travel faster than the experiments and exhibit distinct stationary points in the radial position at the transition between thermal and gravity currents, as was seen in the experiments.

Further extensions to this work could include the collision of axisymmetric gravity currents, which have been shown to enhance deep convection, or the use of particles to either create density differences in the thermal or on the surface in order to consider dust pick up.

As well as results of the numerical simulations of the experiments, the set up of, the newly developed, MONC has been tested and compared to simulations from Rooney [49], discussed in chapter 5. The simulations tested were found to deviate, when using the exact set-up of Rooney [49] it was assumed that this was due to the absence of a backscatter scheme in MONC that was present in the LEM. However, when running MONC at a 10m grid resolution the simulations were comparable to those performed by Rooney [49]. It is important to understand how MONC and the LEM compare in order to make comparisons with existing studies in the LEM and the newer work currently being performed in MONC. Furthermore a more detailed study into the conditions at the boundary in particular, which

was not considered here, is required in order to understand the differences between the gravity currents produced in the numerical simulations and in the experiments. In this study only single simulations were considered, whereas an ensemble average of the simulations are required to ensure robust measurements, as was done in the experiments.

Overall, this thesis has presented the only experiments and simulations on thermals impacting a boundary for these values of L/D and H/D. Through these experiments and simulations we have found a number of new findings regarding the initial development of thermals and the effects on the resulting gravity currents. We have shown for the first time, using both numerical simulations and experiments, that three phases exist during the development of thermals: draining, development, and self-similar thermal phases. In particular, we have shown that for the first two phases the assumptions made regarding the shape and entrainment are only valid when using non-constant values of the shape factor m, spreading rate n, and entrainment rate α. Furthermore, depending on which of the three phases impact occurs in, there is a change in both the qualitative and quantitative behaviour of the resulting gravity currents.

Bibliography

[1] 2019 MATLAB Update 8 version 9.6.0.1335978(R2019a). The Mathworks, Inc., Natick, Massachusetts.

[2] ALAHYRI, A. & LONGMIRE, E.K. 1994 Particle image velocimetry in a variable density flow: application to a dynamically evolving microburst. Experiments in Fluids **17**, 434–440.

[3] ALAHYRI, A. & LONGMIRE, E.K. 1995 Dynamics of experimentally simluated microbursts. AIAA Journal **33**, 2128–2136.

[4] ANDREWS, D.G. 2010 2nd edn. Cambridge University Press.

[5] ASPDEN, A., NIKIFORAKIS, N., DALZIEL, S. & BELL, J.B. 2008 Analysis of Implicit LES Methods. Comm. App. Math. and Comp. Sci. **3**, 103–126.

[6] BENJAMIN, T. B. 1968 Gravity currents and related phenomena. Journal of Fluid Mechanics **31** (2), 209–248.

[7] BLAZEK, J. 2015 Computational Fluid Mechanics: Principles and Applications, 3rd edn. Elsevier.

[8] BOND, D. & JOHARI, H. 2005 Effects of initial geometry on the development of thermals. Experiments in Fluids **39**, 589–599.

[9] BROWN, N., LEPPER, A., WEILAND, M., HILL, A., SIPWAY, B. & MAYNARD, C. 2015 A directive based hybrid Met Office NERc Cloud Model. 2nd Workshop on Accelerator Programming Using Directives, WACCPD, Austin, Texas, USA.

[10] BROWN, N., WEILAND, M., HILL, A. & SHIPWAY, B. 2017 In situ data analytics for highly scalable cloud modelling on Cray machines. Concurrency and Computation: Practice and Experience **30**, 1–14.

[11] BURRIDGE, H.C., PARKER, D.A., KRUGER, E.S., PARTRIDGE, J.L. & LINDEN, P.F. 2017 Conditional sampling of a high Péclet number turbulent plume and the implications for entrainment. Journal of Fluid Mechanics **823**, 26–56.

[12] BURRIDGE, H.C., PARTRIDGE, J.L. & LINDEN, P.F. 2016 The fluxes and behaviour of plumes inferred from measurements of coherent structures within images of the bulk flow. Atmosphere-Ocean **54**, 403–417.

[13] CAFARO, C. & ROONEY, G.G. 2018 Characteristics of colliding density currents: A numerical and theoretical study. Quarterly Journal of the Royal Meteorological Society **144**, 1761–1771.

[14] CANNY, J. 1986 A computational approach to edge detection. IEEE Transactions on Pattern Analysis and Machine Intelligence **6**, 679–698.

[15] CENEDESE, C. & DALZIEL, S.B. 1998 Concentration and depth fields determined by the light transmitted through a dyed solution. In Proceedings of the 8th International Symposium on Flow Visualization, , vol. 8, pp. 1–37.

[16] CHUNG, H & CHEN, S.S 1984 Hydrodynamic mass. In Topics in Fluid Structure Interaction. ASME Pressure Vessels and Piping Conference and Exhibition, ASME,New York, NY, USA.

[17] CORNFORTH, R.J. 2013 West African monsoon 2012. Weather **68**, 256–263.

[18] DAVIES, J.M., EBERT, E., HUETE, A., NEWBIGIN, E., SILVER, J. & BEGGS, P. 2017 Aerobiological, biogeographical, and meteorological features of the November 2016 fatal thunderstorm asthma event in Melbourne, Australia. In ALLERGY, , vol. 72, pp. 803–804. WILEY 111 RIVER ST, HOBOKEN 07030-5774, NJ USA.

[19] DROEGEMEIER, K.K. & WILHELMSON, R.B. 1985 Three-Dimensional numerical modelling of convection produced by interacting thunderstorm outflows. Part I: Control Simulation of Low-Level Moisture Variations. Journal of Atmospheric Sciences **42**, 2381–2403.

[20] DROEGEMEIER, K.K. & WILHELMSON, R.B. 1985 Three-Dimensional numerical modelling of convection produced by interacting thunderstorm outflows. Part II: Variations in vertical wind shear. Journal of Atmospheric Sciences **42**, 2404–2414.

[21] FUJITA, T.T. 1985 The Downburst. The University of Chicago.

[22] FUJITA, T.T. 1986 DFW Microburst on August 2, 1985. The University of Chicago.

[23] GIANGRANDE, S.E., COLLIS, S., STRAKA, J., PROTAT, A., WILLIAMS, C. & KRUEGER, S. 2013 A summary of convetive-core vertical velocity properties using ARM UHF wind profilers in Oklahoma. Journal of Applied Meteorology and Climatology **52**, 2278–2295.

[24] GRAY, M.E.B. & PETCH, J. 2001 Version 2.3 of the Met Office Large Eddy Model: part I. user documentation. Met Office.

[25] GRAY, M.E.B., PETCH, J., BROWN, A.R. & LOCK 2001 Version 2.3 of the Met Office Large Eddy Model: part III. softare documentation. Met Office.

[26] GRAY, M.E.B., PETCH, J., DERBYSHIRE, S.H., BROWN, A.R., LOCK, A.P., SWANN, H.A. & BROWN, P.R.A. 2004 Version 2.3 of the Met Office Large Eddy Model: part II. scientific documentation. Met Office.

[27] GRUNDY, R.E. & ROTTMAN, J.W. 1985 The approach to self similarity of the solutions of the shallow water equations representing gravity-current releases. Journal of Fluid Mechanics **156**, 39–53.

[28] HALLWORTH, M.A., HUPPERT, H.E. & UNGARISH, M. 2001 Axisymmetric gravity currents in a rotating system: experimental and numerical investigations. Journal of Fluid Mechanics **447**, 1–29.

[29] HALLWORTH, M. A., HUPPERT, H. E., PHILLIPS, J. C. & SPARKS, R. S. J. 1996 Entrainment into two-dimensional and axisymmetric turbulent gravity currents. Journal of Fluid Mechanics **308**, 289–311.

[30] HART, A.C. 2008 Interacting thermals. PhD thesis, Department of Applied Mathematics and Theoretical Physics, University of Cambridge.

[31] HARTEN, A. 1983 High resolution schemes for hyperbolic conservation laws. Journal of Computational Physics **49** (3), 357 – 393.

[32] HOUZE, R.A. 1993 Academic Press.

[33] HUPPERT, H.H. 2006 Gravity currents: a personal perspective. Journal of Fluid Mechanics **554**, 299–322.

[34] HUPPERT, H.H. & SIMPSON, J.E. 1980 The slumping of gravity currents. Journal of Fluid Mechanics **99**, 785–799.

[35] HUQ, P. 1996 The role of aspect ratio on entrainment rates of instantaneous, axisymmetric finite volume releases of dense fluid. Journal of Hazardous Materials **49**, 89–101.

[36] KEALY, J. C., EFSTATHIOU, G.A. & BEARE, R.J. 2018 the onset of resolved boundary-layer turbulence at grey zone resolutions. Boundary Layer Meterology .

[37] LAI, A.C.H., ZHAO, B., LAW, A.W-K. & ADAMS, E.E. 2015 A numerical study of the effect of aspect ratio on the behaviour of a round thermal. Enviromental Fluid Mechanics **15**, 85–108.

[38] LILLY, D.K. 1967 The representation of small-scale turbulence in numerical simulation experiments. Proc. IBM sci. comp. symp. on enviromental sciences, New York, USA.

[39] LINDEN, P.F. & SIMPSON, J.E. 1989 Continuous two-dimensional releases from an elevated source. J. Loss Prev. Process Ind. **3**.

[40] LINDEN, P. F. 1999 The fluid mechanics of natural ventilation. Annual review of fluid mechanics **31** (1), 201–238.

[41] LUNDGREN, T.S., YAO, J. & MANSOUR, N.N. 1992 Microburst modelling and scaling. Journal of Fluid Mechanics **239**, 461–488.

[42] MISTRY, DHIREN, PHILIP, JIMMY, DAWSON, JAMES R & MARUSIC, IVAN 2016 Entrainment at multi-scales across the turbulent/non-turbulent interface in an axisymmetric jet. Journal of Fluid Mechanics **802**, 690–725.

[43] MORTON, B.R., TAYLOR, G. & TURNER, J.S. 1956 turbulent gravitational convection from maintained and instantaneous sources. Royal Society **234**, 1–24.

[44] NAGATA, T., OBI, S. & MASUDA, S. 2006 Statistics of velocity field in laboratory-simulated downbursts. AIAA Journal **44**, 2061–2070.

[45] OLSTHOORN, J.P. 2017 On vortex rings impacting a sharply-stratified interface. PhD thesis, University of Cambridge.

[46] PIACSEK, S.A. & WILLIAMS, G.P. 1970 Conservation Properties of Convection Difference Schemes. Journal of Computational Fluids **6**, 392–405.

[47] VAN REEUWIJK, MAARTEN & HOLZNER, MARKUS 2014 The turbulence boundary of a temporal jet. Journal of Fluid Mechanics **739**, 254–275.

[48] ROMPS, D. M. & JEEVANJEE, N. 2016 On the sizes and lifetimes of cold pools. Quarterly Journal of the Royal Meteorological Society **142**, 1517–1527.

[49] ROONEY, G.G. 2015 Descent and spread of negatively buoyant thermals. Journal of Fluid Mechanics **780**, 457–479.

[50] ROONEY, G.G. 2018 Similarity-based approximations for the evolution of a gravity current. Quarterly Journal of the Royal Meteorological Society **144** (716), 2302–2310.

[51] ROONEY, G.G. & LINDEN, P.F 2012 Radial jet due to plume impingement on a horizontal surface. Engineering and Computational Mechanics **165**.

[52] RUMBLE, J. 2019 CRC Handbook of Chemistry and Physics, 100th Edition. Taylor & Francis Limited.

[53] SCORER, R.S. 1957 Experiments on convection of isolated masses of buoyant fluid. Journal of Fluid Mechanics **2**, 583–594.

[54] SENGUPTA, A. & SARKAR, P.P. 2008 Experimental measurement and numerical simulation of an impinging jet with application to thunderstorm microburst winds. Journal of Wind Engineering and Industrial Aerodynamics **96**, 435–365.

[55] SIMPSON, J.E. 1987 Gravity Currents: In the Enviroment and the Labratory, second edition edn. Cambridge University Press.

[56] VON KARMAN, T. 1940 The engineer grapples with nonlinear problems. Bulletin of the American Mathematical Society **46** (8), 615–683.

[57] WALLACE, J.M. & HOBBS, P.V. 2006 3 - atmospheric thermodynamics. In Atmospheric Science (Second Edition), Second edition edn. (ed. John M. Wallace & Peter V. Hobbs), pp. 63 – 111. San Diego: Academic Press.

[58] VAN DER WIEL, K., GILLE, S.T., LLEWELLYN SMITH, S.G., LINDEN, P.F. & CENDESE, C. 2017 Characteristics of colliding sea breeze gravity current fronts: a laboratory study. Royal Meteorological Society .

[59] YAO, J. & LUNDGREN, T. 1996 Experimental investigation of microbursts. Experiments in Fluids **21**, 17–25.

[60] ZHAO, B., LAW, A.W.K., LAI, A.C.H. & ADAMES, E.E. 2013 On the internal vorticity and scalar concentration structures of miscible thermals. Journal of Fluid Mechanics **722:R5**.

Appendix A

Draining of full vs. partially filled tubes

To create a range of values of L/D one can either use a single tube and partially fill it, or have multiple lengths of tube. In the experiments performed by Bond & Johari [8], Hart [30], Lundgren et al. [41] the tubes were filled fully. When we carried out experiments with a partially filled tube, in the descent regime we observed a potential L/D dependence in the flow. However, this dependence was not seen when the tubes were full. We do not observe any dependence on L/D for the gravity currents for either full or partially filled tubes. The difference between experiments for the filled and partially filled tubes suggests that the experimental set up was affecting the descent.

Thermals from fixed full tubes

Figure A.1 shows the position of the front of the dense release for experiments using tubes with two different diameters and two lengths. The smaller tube had diameter of $D = 5\,\text{cm}$ and length $L = 20\,\text{cm}$. The larger tube had diameter $D = 15.5\,\text{cm}$ and length $L = 15.5\,\text{cm}$. The data from the smaller 5cm tube were from experiments where $1 \leq L/D \leq 4$ and, the data from the larger 15.5cm tube had $L/D = 1$. The only experiments using these two tubes were full were the $L/D = 4$ experiment (blue filled circle) using the smaller tube and the $L/D = 1$ experiment (red filled circle) using the larger tube. The collapse of the $L/D = 4$ data from the 5cm tube and the $L/D = 1$ data from the 15.5cm tube suggests that partially filling the tube was what was causes the data to differ for other values of L/D, and not an L/D dependence on the flow.

The gravity current from a fixed full tube

Figure A.2 shows the radial position of the gravity current experiments using tubes with two different diameters and two lengths. As above, the only cases where the tube is full are the

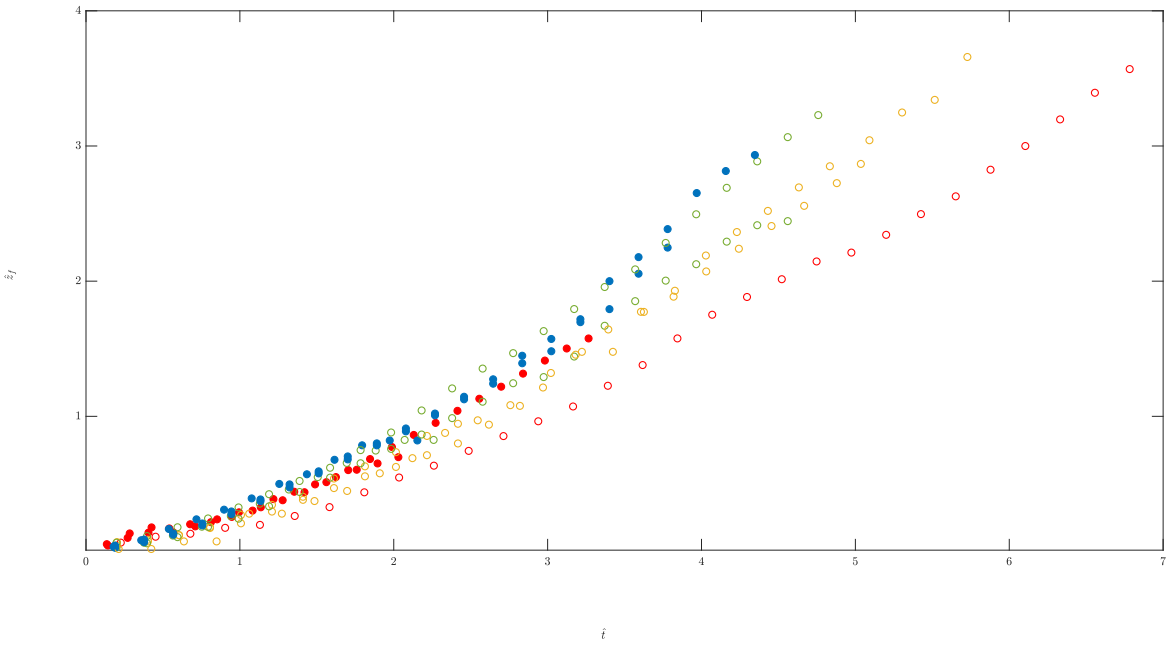

Fig. A.1 The position of the lowest vertical position. Showing data from $L/D = 1$ (red), 2 (yellow), 3 (green) and 4 (blue), from two tubes with different diameters. The experiments where the tubes are full are highlighted by filled circles.

$L/D = 4$ experiment (blue filled circle) in the smaller tube and the $L/D = 1$ experiment (red filled circle) from the larger tube. The gravity currents are affected less than the thermals by filling the tubes fully.

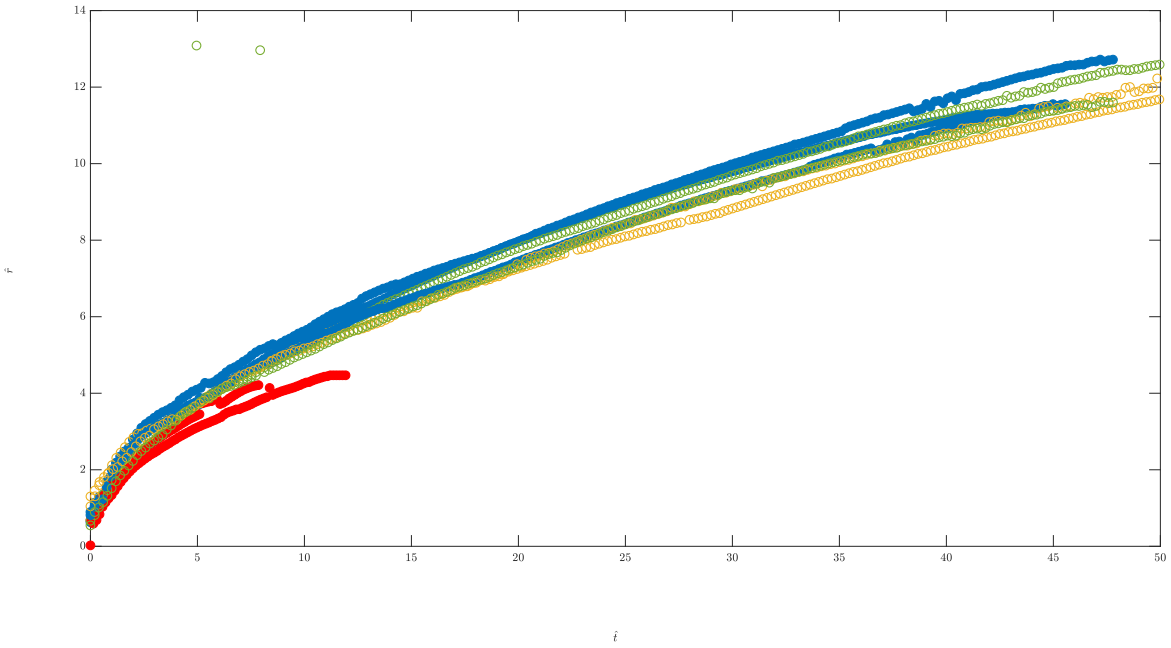

Fig. A.2 The radial position of the gravity current. Showing data from $L/D = 1$ (red), 2 (yellow), 3 (green) and 4 (blue), from two tubes with different diameters. The experiments where the tubes are full are highlighted by filled circles.

Appendix B

Combination of experimental images

As discussed in chapter 2, to combine the dye attenuation images produced using the three colours of LED we used a weighted average of the three colours. We saw that, although there was a significant improvement in the conservation of mass compared to using a single colour LED, the mass was still underestimated. To ensure that the method used to combine the dye attenuation images did not significantly affect the measurement of the centre of mass we considered an alternate method of combining the experimental images. That is to use the maximum value of *ch* from each of the three colours at each pixel, i.e.

$$ch(i,j,t) = \sum_{i,\,j=0}^{nx,\,ny} \max\left\{ch_r(i,j,t),\ ch_g(i,j,t), ch_b(i,j,t)\right\},$$

where nx, ny are the number of pixels in the horizontal and vertical directions, respectively.

Figure B.1 shows the average total mass for five experiments with $L/D = 5$ performed at $H/D = 8$ calculated using the two different methods. The crosses represent the maximum method, the circles the weighted average, and the shaded area one standard deviation from the average of each method respectively. As expected, we see that the maximum method does indeed increase the value of the total mass. However, the average of the total mass using the weighted average method lies within one standard deviation from the average of the maximum method (figure B.1a) and vice versa (figure B.1b).

Now consider the average error between the two methods for experiments with $L/D = 1-5$ shown in figure B.2 (crosses). We see that in general the average error is below 10% except for the experiments performed at $L/D = 1$ where the averaged error is 22.6%. However, we know that there also exists variation between identical experiments. So consider the percentage difference between standard deviation of the mass and the average mass from the experiments using the weighted average. This percentage error is shown on figure B.2

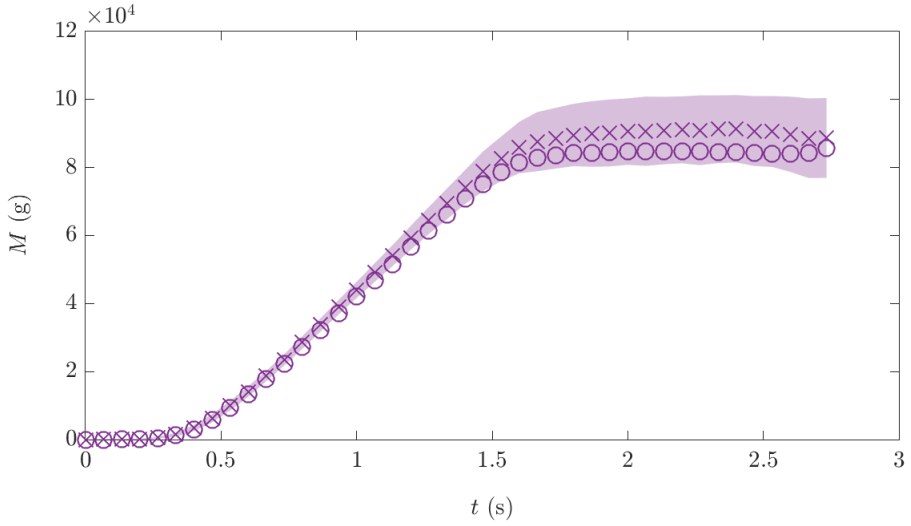

(a) standard deviation of maximum experiment

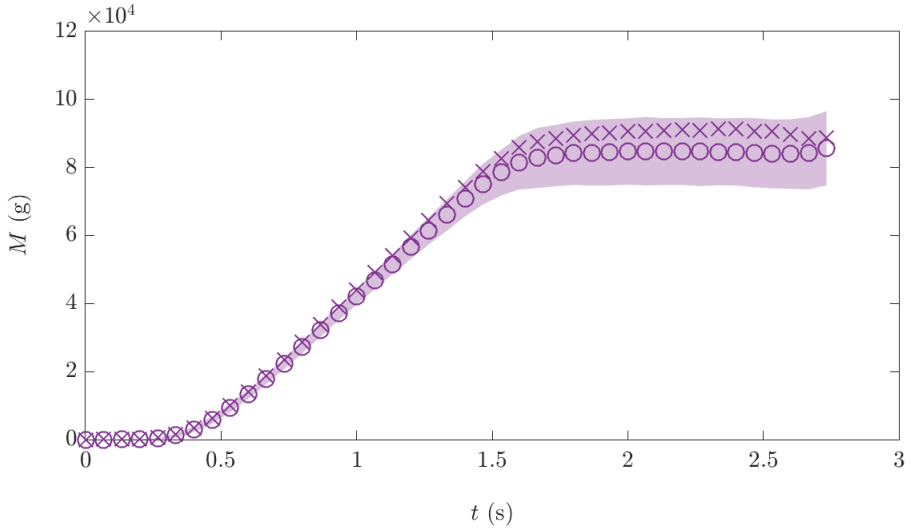

(b) standard deviation of weighted experiments

Fig. B.1 Average mass of 5 repeats of the experiments performed at $L/D = 5$, $H/D = 8$ found using the maximum method (crosses) and the weighted average method (circles). Also shown is the standard deviation of the experiments for each method (shaded area).

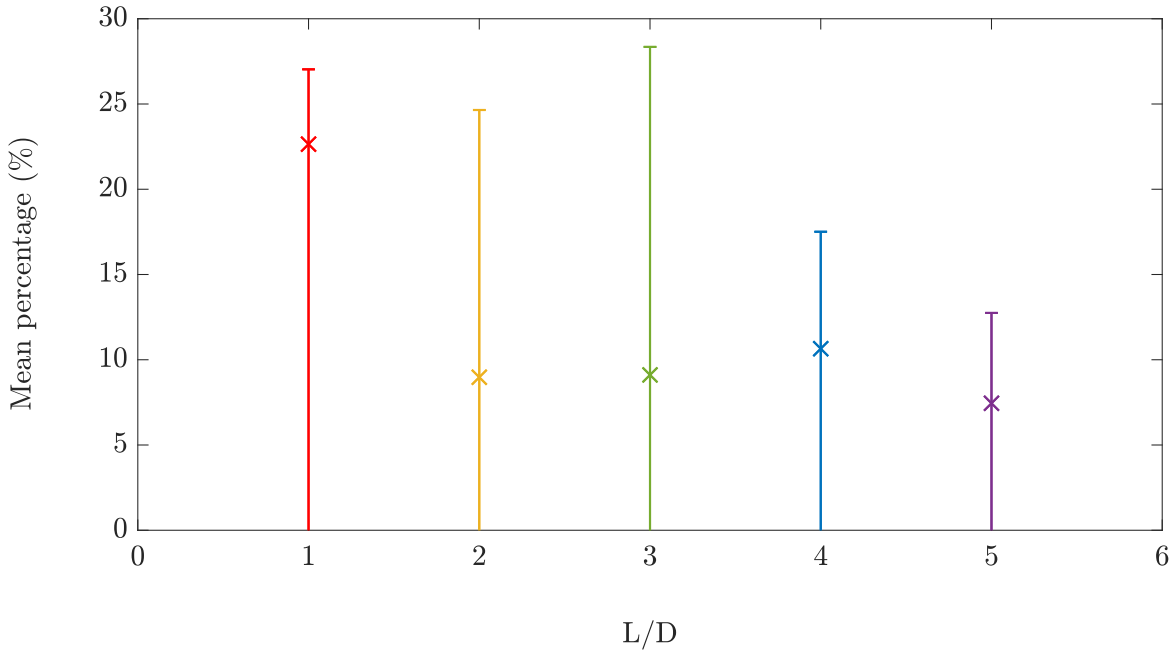

Fig. B.2 The average percentage error between the two methods of the total mass for the experiments $L/D = 1$ (red), 2 (yellow), 3 (green), 4 (blue) and 5 (purple) performed at $H/D = 8$. Also plotted is the percentage error of the variation between experiments (errorbars).

for each value of L/D as an errorbar centred on 0. We see that the average percentage error between the two methods lies within the variation between the experiments.

Although the difference in the total mass between methods is large, the total mass is only used in the calculation of the centre of mass in this study. Moreover, we would expect the maximum method to produce higher mass values than the average method. For example, consider the case of three nearly instantaneous exposures of the same color LED, the weighted averaging method would take advantage of the multiple exposures by averaging out the noise of the camera, as well as potentially removing any temporal artefacts in the image, whereas the maximum method will simply take the maximum value so always bias the results towards higher mass values. However, as it is the centre of mass that is the most important measurement. as it is used to compare to the models and calculate the shape factor in chapter 3, it is interesting to compare the sensitivity of the averaging method on these results.

Figure B.3 shows the average vertical position of the centre of mass for five experiments with $L/D = 5$ performed at $H/D = 8$ calculated using the two different methods. The crosses represent the maximum method, the circles the weighted average, and the shaded area one standard deviation from the average. We see that the maximum method decreases the vertical

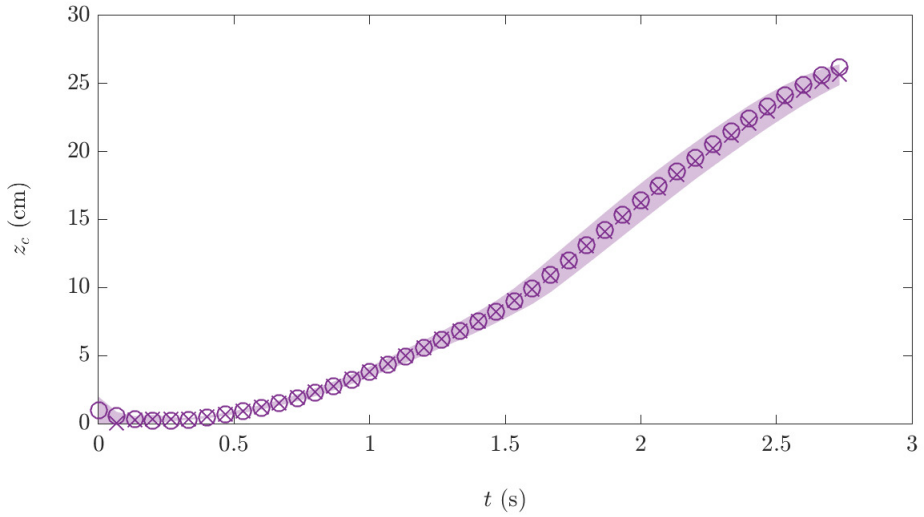

(a) standard deviation of maximum experiments

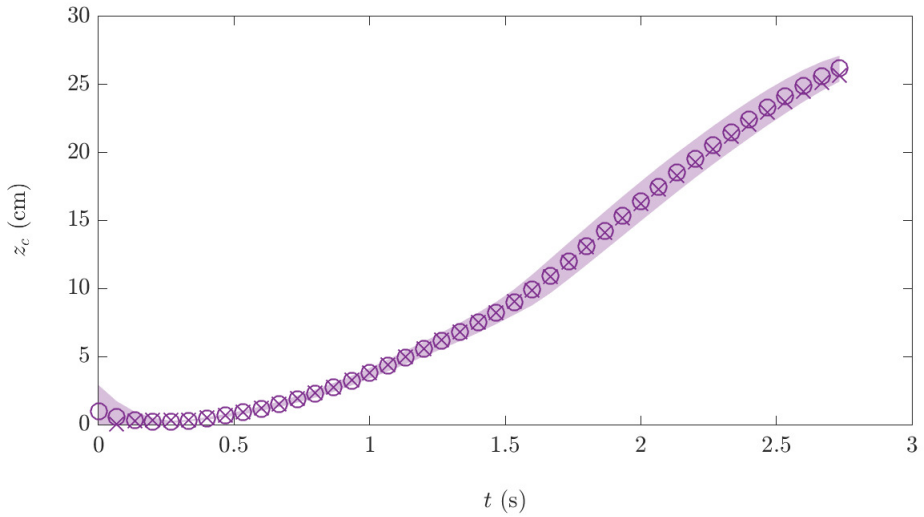

(b) standard deviation of weighted experiments

Fig. B.3 Centre of mass of 5 repeats of the experiments performed at $L/D = 5$, $H/D = 8$ found using the maximum method (crosses) and the weighted average method (circles). Also shown is the standard deviation of the experiments for each method (shaded area).

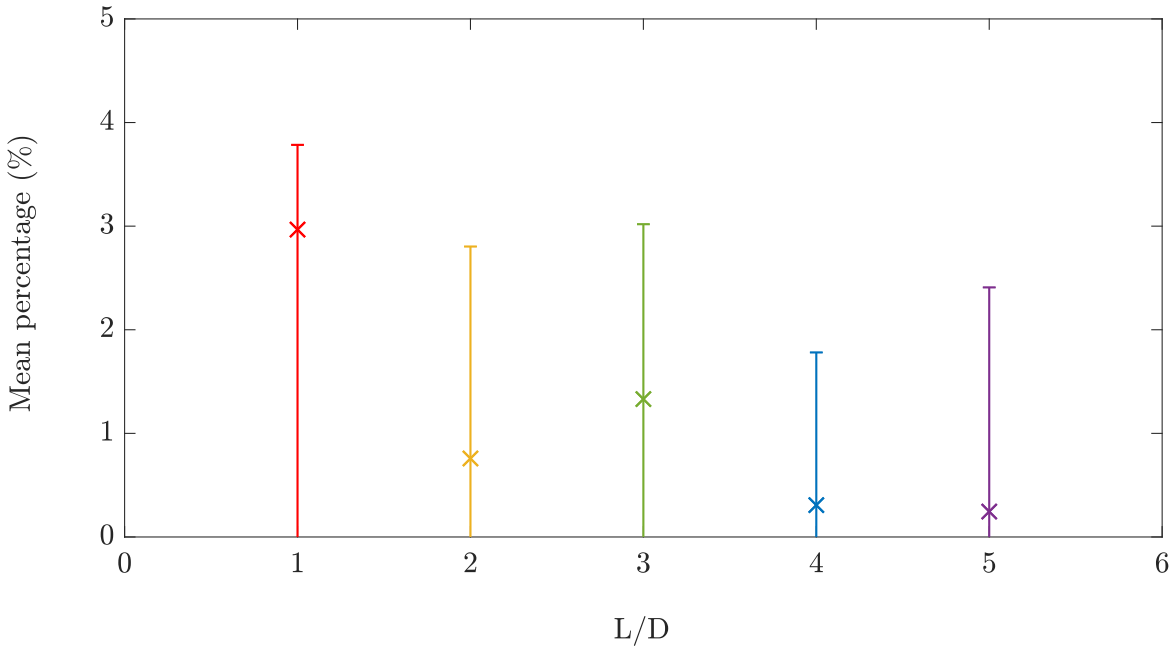

Fig. B.4 The average percentage error between the two methods of centre of mass for the experiments $L/D = 1$ (red), 2 (yellow), 3 (green), 4 (blue) and 5 (purple) performed at $H/D = 8$. Also plotted is the percentage error of the variation between experiments (errorbars).

position, but only by a small amount and only at late times. As with the total mass the average vertical position of the centre of mass using the weighted average method lies within one standard deviation from the average of the maximum method (figure B.3a) and vice versa (figure B.3a).

As with the total mass now consider the average error in the centre of mass between the two methods for experiments with $L/D = 1-5$ shown in figure B.4 (crosses). We see that in general the average error is below 1.5% except for the experiments performed at $L/D = 1$ where the averaged error is 3%. As before we compare this error associated with the variation between the experiments compared to the total release height for the different values of L/D (errorbars). We see that the average percentage error between the two methods is smaller than the percentage error from the variation between the experiments.

Although the measurement of the total mass measurements are significantly altered by the choice of method, especially in the case of $L/D = 1$, the centre of mass measurements are not. However, neither of them are altered significantly enough to be outside the range of variation between the experiments themselves. We therefore choose to combine the images using the weighted average method as theoretically it should not be affected by anomalous results caused by factors such as camera noise or debris in the tank.

Appendix C

Oblate spheroid formulae

C.1 Volume, shape factor and area

An oblate spheroid is generated by the rotation of an ellipse around its minor axis. The generating ellipse is taken to have semi-major axis r and semi-minor axis h. The eccentricity e is given by

$$e^2 = 1 - \left(\frac{h}{r}\right)^2 \tag{C.1}$$

The volume of an oblate spheroid is

$$V_s = \frac{4}{3}\pi r^2 h = mr^3 \tag{C.2}$$

where the "shape factor" $m = (4\pi/3)(h/r)$. For thermals, m has been observed or taken as approximately 3 [53], implying $b = h/r \approx 0.72$ so that $e \approx 0.5$.

The spheroid area is

$$\begin{aligned} A_s &= \left(2\pi + \pi\frac{1-e^2}{e}\ln\left(\frac{1+e}{1-e}\right)\right) r^2 \\ &= ar^2 \end{aligned} \tag{C.3}$$

where a is then a function of e, or equivalently m, only. In particular, for $m = 3$, $a \approx 11.5$.

Appendix D

Theory for Small L/D

When watching the experiments from above it was observed that for the smallest value of L/D considered, $L/D = 1$, the flow resembled a buoyant vortex ring rather than a thermal, and so would be better represented by a torus rather than a spheroid.

Using the the definition of r and h as above, and as shown in figure D.1, by assuming that the thermal is a torus rather than a spheroid, the torus has volume

$$V = 2\pi^2(1-b)b^2r^3 = mr^3$$

where r is the distance of the centre to the outermost edge and b is the ratio of the two radii, $h = br$, the two radii are illustrated in figure D.1. Then

$$\frac{\mathrm{d}V}{\mathrm{d}t} = 3mr^2\frac{\mathrm{d}r}{\mathrm{d}t}. \tag{D.1}$$

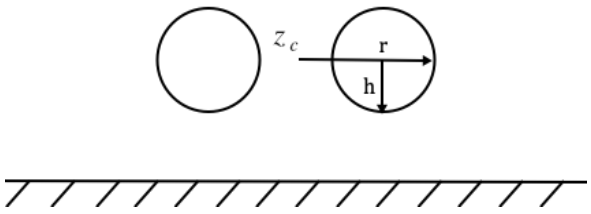

Fig. D.1 Diagram of a torus showing how the horizontal radius r and veritcal radius h are measured.

Again, we use the entrainment assumption [43] giving

$$\frac{\mathrm{d}V}{\mathrm{d}t} = \alpha a r^2 \frac{\mathrm{d}z_c}{\mathrm{d}t}, \tag{D.2}$$

where the surface area of a torus can be written in terms of b and r as

$$ar^2 = 4\pi^2(1-b)br^2,$$

and as previously α is the entrainment constant. Comparing (D.1) and (D.2),

$$\frac{\mathrm{d}r}{\mathrm{d}t} = n\frac{\mathrm{d}z_c}{\mathrm{d}t}, \tag{D.3}$$

where

$$\begin{aligned} n &= \frac{\alpha a}{3m}, \\ &= \frac{\alpha 4\pi^2(1-b)b}{6\pi^2(1-b)b^2}, \\ &= \frac{2\alpha}{3b}. \end{aligned}$$

Appendix E

Coefficients of least squares fits

The following tables present the coefficients of the fits for the values of b, z_c and r for $L/D = 1$ to 5, used to solve the equations for the draining and development phases of a thermal in chapter 3 and 5. Also presented are the r^2 values of the fits.

L/D	b_1	b_2	b_3	b_4	r^2
Experiments					
1	0	0.07	-0.59	1.25	0.8929
2	0.06	-0.27	0.09	0.79	0.9990
3	-0.05	0.34	-0.92	1.31	0.9659
4	0	0.15	-0.68	1.28	0.9890
5	0	0.05	-0.43	1.26	0.9857
Simulations					
1	0	0.00024	-0.0093	0.13	0.3744
2	0	0.00087	-0.025	0.23	0.8926
3	0.00026	-0.0037	-0.0054	0.23	0.8900
4	0.00037	-0.0057	0.0091	0.21	0.9202
5	0.0014	-0.024	0.11	0.50	0.9455

Table E.1 $b = b_1 t^4 + b_2 t^3 + b_3 t^2 + b_4 t$

L/D	zc_1	zc_2	zc_3	zc_4	r^2
Experiments					
1	0.36	-2.97	7.72	-1.24	0.9996
2	-0.81	1.75	3.13	0.14	0.9994
3	0.01	-1.57	7.78	-0.81	0.9990
4	-0.64	2.56	0.33	1.57	0.9996
5	-1.71	5.73	-4.89	3.88	0.9991
Simulations					
1	0	-0.00013	0.0007	0.47	0.9969
2	0.00061	-0.022	0.25	-0.19	0.9995
3	0.0014	-0.041	0.38	-0.40	0.9991
4	0.0011	-0.035	0.34	-0.33	0.9992
5	0.00076	-0.032	0.35	-0.38	0.9983

Table E.2 $z_c = zc_1 t^4 + zc_2 t^3 + zc_3 t^2 + zc_4 t$

L/D	r_1	r_2	r_3	r_4	r_5	r^2
Experiments						
1	-0.09	0.51	-0.77	2.21	2.5	0.8999
2	-0.59	3.37	-6.26	6.37	2.5	0.7876
3	-0.50	3.02	-6.11	6.92	2.5	0.8932
4	-0.27	1.52	-2.93	4.56	2.5	0.9954
5	0.04	-0.21	-0.21	3.51	2.5	0.9983
Simulations						
1	0	0.00024	-0.015	0.37	2.5	0.9447
2	-0.00060	0.018	-0.18	0.82	2.5	0.9789
3	-0.00092	0.023	-0.20	0.82	2.5	0.9773
4	0.00013	0.0039	-0.091	0.62	2.5	0.9665
5	-0.0015	0.031	-0.22	0.80	2.5	0.9796

Table E.3 $r = r_1 t^4 + r_2 t^3 + r_3 t^2 + r_4 t + r_5$